Effects of Composition on the Properties of Phospholipid Bilayers

By

Andrew Burley

A thesis submitted to

The University of Birmingham

for the degree of

Doctor of Philosophy

School of Chemistry

University of Birmingham

December 2011

Abstract

Membranes are an essential and ubiquitous component in biology. They are composed of a bilayer of phospholipid molecules. It is becoming clear that the membrane composition has an important effect on many processes yet it is still poorly understood how different phospholipids affect membrane properties. Dimyristoyl-phosphatidyl-serine (DMPS) and dimyristoyl-phosphatidyl-ethanolamine (DMPE) are phospholipids commonly found in cell membranes. The properties of supported bilayers composed of mixtures of these two molecules are investigated using electrochemical techniques, infrared spectroscopy and neutron reflectometry. Polarisation-modulated infrared reflectance spectroscopy (PM-IRRAS) experiments suggest that the lipid tail groups are in one conformation at 20% DMPS or below and a different conformation at 30% DMPS concentration. Differential capacity measurements show that bilayers composed of 20% DMPS in DMPE or less behave similarly to pure DMPE while at 40% DMPS concentrations or higher the bilayer behaves similarly to DMPS. Electrochemical impedance spectroscopy (EIS) indicates that bilayers containing DMPS behave as more effective barriers to the passage of anions than DMPE bilayers: the opposite is true for cations. It is speculated that the negative charge on the DMPS head group plays a major role in these changes. Neutron reflectometry data indicate that a 10% DMPS bilayer gains water and finally detach from the substrate when it is subjected to an increasing negative potential. These observations help explain the shape of the capacity curve with potential.

Acknowledgements

Firstly, a big Thank You must go to my supervisor Dr Sarah Horswell, without whose help and advice this work would not have been possible. I'd also like to thank our collaborators with the neutron reflectometry experiments, Dr Andrew Glidle and Dr Robert Cubitt at the ILL. Many thanks to Stuart Arkless for all his help over the past four years… and not being too upset when I broke things! Speaking of which, this is a good place to thank Steve Williams for mending all the glassware I broke. Thanks also go to Dr John Wilkie for all his help and patience with the molecular dynamics. An honourable mention must go to Simon, Susie, Claudine, Adrian, Jenny, Martin and everyone else of the Fridays for their role in helping to retain my sanity. Finally, I'd like to thank everyone in the group – Elena, Goy, John, Nikki and Anicetus, and not merely for putting up with me over the past four years.

Table of Contents

1. Introduction

1.1 Membranes, Phospholipids and Bilayers

The membrane is a common structure in biology. Perhaps the most obvious example is the plasma membrane that every cell possesses which serves as a barrier between the cell and its environment. Complex cells with nuclei – the eukaryotes – contain internal structures (organelles) that are partitioned off from the rest of the cell by membranes[1]. Lysosomes, for instance, contain digestive enzymes that, if released, would readily break down the essential structures of the cell if free: clearly some means of sequestering them is essential.

A striking fact is that all these membranes are remarkably similar. Biological membranes consist of amphiphilic molecules derived from lipids which consist of a hydrophilic polar head group and an acyl hydrophobic tail[1]. These molecules are arranged in a two layer structure – a bilayer, where the head groups face outwards into the aqueous environment and the hydrophobic tails are directed inwards.

The animal fats and vegetable oils that most people are familiar with in the context of nutrition are the triacyl glyercides (TAGs). These large molecules are tri-esters of glycerol with three long chain fatty acids. Typical chain lengths are 16 or 18 carbon atoms: the most common fatty acids in humans are palmitic acid with sixteen carbon residues and oleic acid with 18 carbon

atoms[2]. The ester group is polar, however, the long hydrophobic acyl chains of the fatty acids is sufficient to render TAGs immiscible in water. Hence TAGs form droplets in aqueous media with the ester groups facing outwards and a hydrophobic core. TAGs comprise the main energy storage molecule of almost all animals and are usually found as large single droplets within adipocytes[3].

Lipids found in membranes are phospholipids derived from TAGs. A phospholipid differs from a tri-acyl glyceride in that one of the fatty acids is replaced by a phosphate group. A usually highly polar head group is attached to the phosphate. Most commonly, the fatty acid attached to the first glycerol carbon is saturated and the second, attached to the centre glycerol carbon, is unsaturated[2].

This work looks closely at two phospholipids: 1,2-Dimyristoyl-sn-Glycero-3-[Phospho-L-Serine] (DMPS) and 1,2-Dimyristoyl-sn-Glycerol-3-Phosphoethanolamine (DMPE). The structures of DMPS and DMPE are shown in Figures 1.1 and 1.2 respectively. Both phospholipids have the same tail group, the fourteen carbon residue of myristic acid. Myristic acid is a minority component in human lipid makeup, comprising 3% of the total[2]. This residue was used for reasons of convenience: saturated fatty acids are stable with respect to oxidation especially compared to unsaturated fatty acids. Furthermore, phospholipids with this acyl chain are readily available at high purity. This is thus a good choice for the construction and investigation of biomimetic membranes.

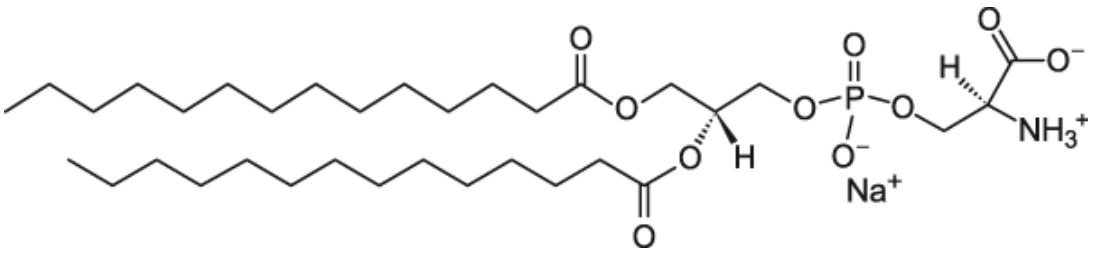

Figure 1.1: Structure of the DMPS molecule.

There are differences between the phosphatidylserine (PS) and phosphatidylethanolamine (PE) head groups. The PE head group is slightly smaller than PS, and is zwitterionic. PS, by contrast, is an anion. There are similarities too, of course: both head groups are highly polar and thus hydrophilic. DMPE is similar in some ways to 1,2-Dimyristoyl-*sn*-Glycero-3-Phosphocholine (DMPC), a zwitterionic phospholipid which is commonly used in biomimetic films. The DMPC head group is larger than that of DMPE, however (Figure 1.3).

The difference between the polar head group and hydrophobic tail of a phospholipid exerts a controlling influence over its physical behaviour. The head groups are happy to associate with water and will gain a solvent shell of entrained water molecules about them while the non-polar tails have an affinity for each other – and a strong aversion to water[2].

This contrast in properties means that phospholipids have a significant tendency to form bilayer structures spontaneously. A bilayer comprises two planar sheets of phospholipids arranged so that the head groups face

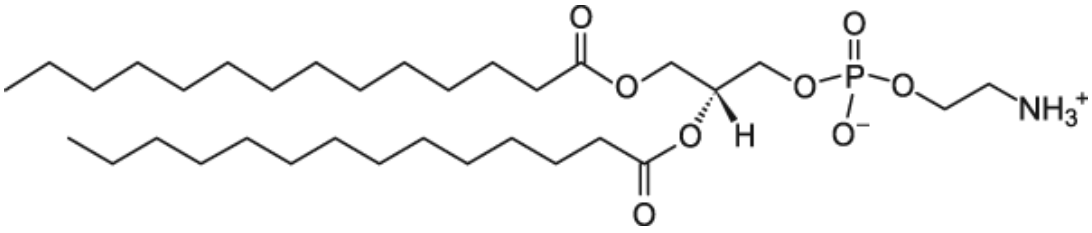

Figure 1.2: Structure of the DMPE molecule.

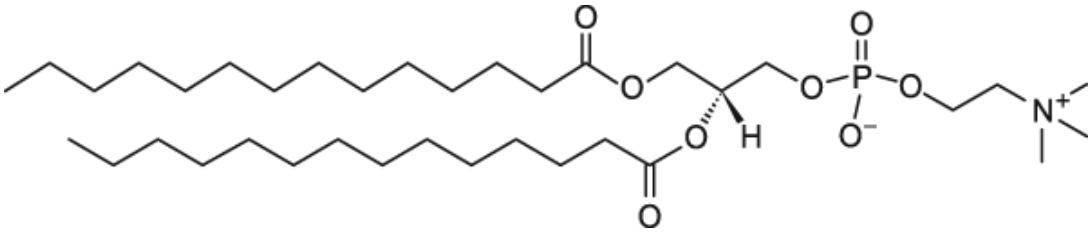

Figure 1.3: Structure of the DMPC phospholipid.

outwards into the solvent and the tail groups directed towards the central core where water is excluded (Figure 1.4). Phospholipids exhibit such a strong tendency to spontaneously organise in this fashion that it has been speculated that this is the reason that biological bilayer membrane evolved[4].

1.2 The Structure and Composition of Biological Membranes

Gorter and Grendel originally proposed the idea that a cell's plasma membrane consists of a lipid bilayer in 1925[5]. The cell membrane was thus viewed as being composed of two monolayers, or "leaflets". The inner leaflet

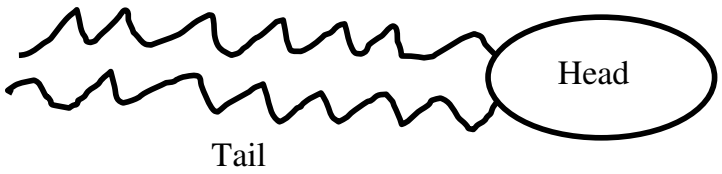

Figure 1.4 (a): A schematic cartoon of the structure of the typical amphiphilic phospholipid, with its hydrophobic tail and polar head group.

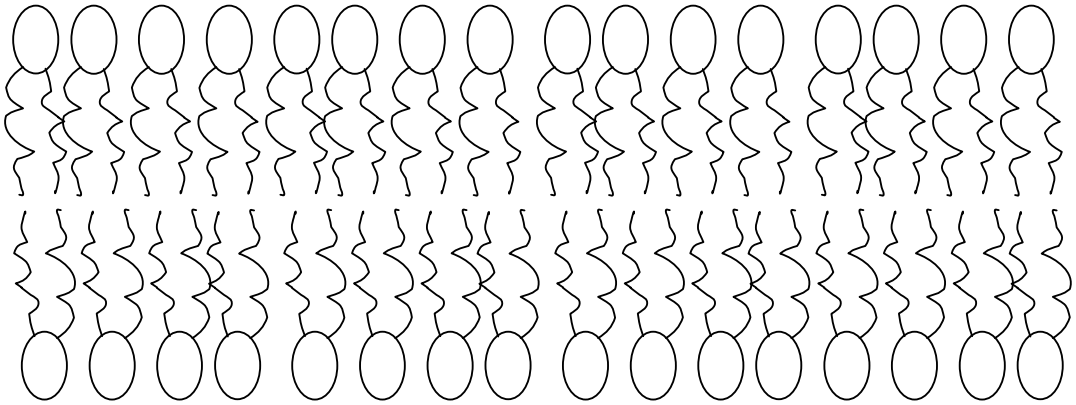

Figure 1.4 (b): A cartoon of a phospholipid bilayer, showing the typical form of the head groups directed outwards into the aqueous medium.

was arranged to that the head groups of its component lipids faced the interior of the cell, the cytosol, whilst the outer leaflet head groups were directed outwards into the cell's environment. It became clear that the cell membrane was no mere passive barrier but contained proteins and other structures that control transport across it. These proteins were assumed to be essentially immobile and held in place by the lipid matrix.

This simple model was modified by Singer and Nicolson in 1972 who proposed a considerably more dynamic picture – the fluid mosaic model[6]. The fluid mosaic model regards the cell membrane as a "sea" of lipid molecules in

which are embedded the various proteins, ion pumps and receptors, all of which "float" in the lipid matrix and possess a degree of motion (Figure 1.5). The membrane lipid matrix can itself be viewed as a viscous two dimensional fluid. Membrane fluidity is thus a key parameter.

The lipid makeup of biological membranes is such that fluidity is maintained at the temperatures encountered[1]. For instance, neural cells in carp adapt to low temperatures by modifying the composition of their cell membranes, increasing the number of short chain unsaturated phospholipids that have higher fluidity[7]. Mammals have high concentrations of cholesterol in their membranes. This relatively small molecule sits below the phospholipid head groups and acts to increase the viscosity of the lipid "sea"[8]. The importance of membrane fluidity can be observed in hibernating mammals: ground squirrels that were fed a diet high in unsaturated fats hibernated for longer periods than their fellows that were fed a saturated fat rich diet[9]. This was attributed in part to the take up of unsaturated fatty acids in the membrane phospholipids: animals that had been fed a high unsaturated fat diet were found to have higher concentrations of unsaturated fatty acids in their cell membranes, thus allowing the membranes to retain adequate fluidity at low temperatures.

The plasma membrane of all organisms consists of a number of different lipids. In humans, the most prevalent lipid is phosphatidylcholine (PC), followed by sphingomyelin (SM), PE, PS and phosphatidylinisotol (PI) (Figure

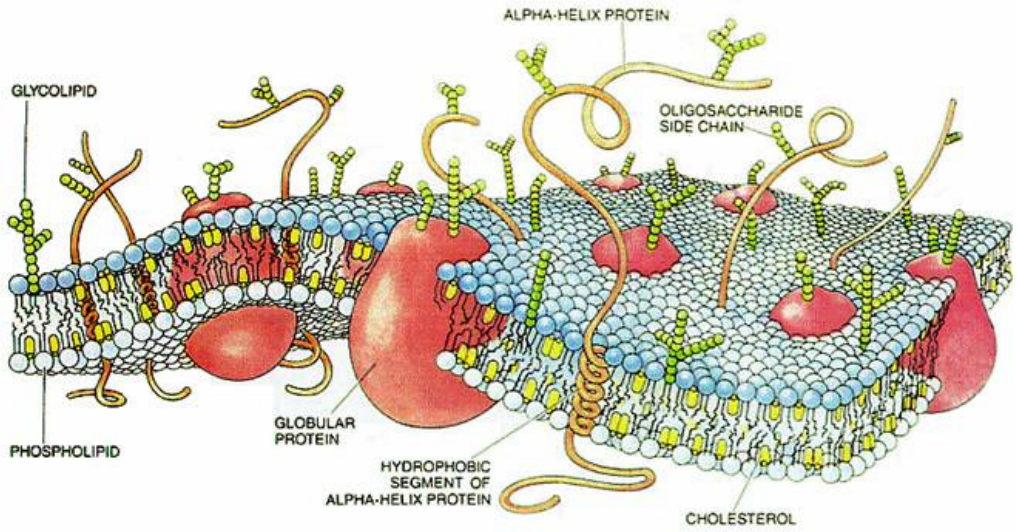

Figure 1.5: Structure of a typical mammalian cell membrane, showing both lipid leaflets and the proteins embedded within it. (After Bretscher[8]).

1.6). There is a very distinct asymmetry between the inner and outer leaflets. SM resides mainly on the outer leaflet while PE, PS and PI are distributed principally on the inner leaflet. PC is distributed fairly evenly throughout both leaflets[10].

Proteins make up approximately 50% of the typical eukaryotic cell membrane by mass[1]. Much effort has been expended to elucidate the structures and roles of membrane proteins. This is perhaps not surprising, given that half of all drug targets are membrane proteins[11].

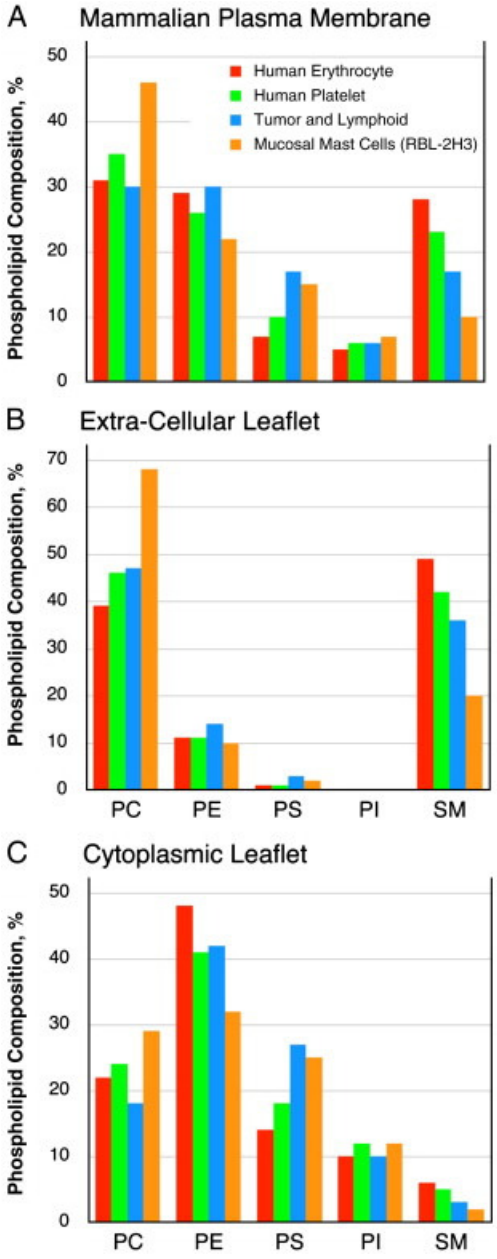

Figure 1.6: The composition of the inner (cytoplasmic) and outer (extra-cellular) leaflets of cell membranes of a number of different types of human cells (after Kiessling[10]).

A few examples may serve to emphasise the importance membrane proteins. Almost all mammalian cells maintain a higher concentration of K^+ ions than the surrounding extra-cellular fluid, and a lower concentration of Na^+. This concentration gradient is maintained by the constant pumping of ions across the plasma membrane by the Na^+/K^+ ATPase pump. The "ATPase" name refers to the fact that the pump requires the hydrolysis of ATP for its operation – that is, it consumes energy[12]. It is believed that a modified form of the Na^+/K^+ ATPase pump is responsible for some forms of microbial antibiotic resistance – the modified form is capable of pumping the antibiotic out of the cell so preventing a toxic concentration being reached[1].

The plasma membrane is the site for receptors for hormones and cytokines. There is considerable interest in these receptors as signaling molecules are a major means of regulation in most organisms. A cytokine is a signaling molecule that exerts a local effect rather than influencing remote tissues in the manner that the endocrine hormones do. Most growth factors have local – or paracrine – activity[13]. Consider that if you cut your finger, the platelets in the clot secrete a growth factor – platelet derived growth factor – which acts on the skin cells surrounding the wound to grow and proliferate[14]. It is advantageous that the healing response is mediated locally: clearly it would be undesirable if one result were to cause your ears to grow.

Problems with receptors have been implicated in a number of diseases. For example, leptin is a hormone that is produced by adipocytes: it signals that the organism has sufficient energy reserves. Female mice do not ovulate without

a sufficient concentration of leptin in their bloodstream – leptin serves as a signal that there are sufficient lipid (energy) reserves to support reproduction[3]. Leptin thus serves in the regulation of metabolism, appetite, weight and reproduction[1]. Its concentration has been found to be elevated in clinically obese adults[15], which suggests that the associated leptin receptor is defective.

In recent years, it has become increasingly clear that it is not just the proteins embedded in the plasma membrane that are important, but the lipid makeup of the membrane itself. An early hint of this was revealed with the discovery in 1980 that the neurotransmitter serotonin binds more readily to its receptor when cholesterol is present in the cell membrane[16].

As already noted, the lipid composition of mammalian cell membranes is asymmetric, with negatively charged ions preferentially located on the inner leaflet – most significantly PS. This is in marked contrast to bacteria, which have PS expressed on both leaflets of their cell membranes. Diffusion of individual phospholipid molecules between leaflets – “flip-flopping” – is slow: the polar head groups have to cross the hydrophobic core. This process requires a high activation energy[17]. Nevertheless, a mammalian cell is still required to expend energy to maintain this asymmetry. A family of enzymes – flippases – maintains this asymmetry[18].

Loss of membrane asymmetry, and in particular the appearance of PS on the outer leaflet has important consequences. An important process is apoptosis,

or programmed cell death. A severely damaged cell will in preference to turning rogue or cancerous if its genome has been damaged shut down protein synthesis, release the contents of its own lysosomes and digest itself from the inside[13]. One of the first things to occur is the activation of an enzyme, appropriately enough named “scramblase”, which scrambles the contents of its plasma membrane so that the composition of both leaflets becomes mixed together: the appearance of PS on the outer leaflet is the sign of an apoptic cell[19]. This is interpreted by cells of the immune system, the macrophages, to engulf and digest the cell.

Loss of membrane lipid asymmetry and the appearance of PS is also a key event in the clotting mechanism. To return to the example of a cut finger, one of the first things that happen is that the platelets in the wound activate a very efficient scramblase enzyme which very rapidly – within seconds – exposes large numbers of PS molecules[20] at the surface. This in turn initiates platelet aggregation[20]. The conversion of prothrombin to thrombin – the major protein causes blood to clot – requires a negatively charged surface, which is conveniently provided by the exposed PS head groups[21].

1.3 Artificial Bilayers

It can be seen that biological membranes, and the cell membrane in particular, are complex systems. In order to study the many membrane proteins and the processes that occur at biological membranes, it is desirable to examine a simpler system that can act as a convenient model. One such

system that has attracted considerable attention is the phospholipid bilayer. As these structures are composed of the entities that form a major part of biological systems, they may be considered good model systems. A further advantage is that phospholipids will readily organize themselves into bilayers spontaneously. Phospholipid bilayers have been exploited as model membranes for cellular signaling[22,23], the mechanisms of viral attack[24] and ligand-receptor interactions[25,26].

1.3.1 Supported and Unsupported Bilayers

Artificial phospholipid bilayers can be divided into two types: supported and unsupported. An unsupported bilayer is one that has solvent on both sides. The first artificial bilayer, produced by Mueller and Rudin in 1962, was of this type[27]. It was a film stretched across a one millimetre pinhole between two electrolyte compartments, somewhat akin to a soap bubble.

The unsupported bilayer system demonstrated by Mueller and Rudin[27,28] is commonly referred to as a black lipid membrane, due to its appearance under an optical microscope (interference fringes disappear and the membrane takes on a black appearance as the film spreads out and thins). Today, these films are usually made with the same method, by the use of a small paint brush to apply a 1-2% solution of phospholipid in an organic solvent (typically n-decane) across a 0.1 to 1 mm diameter pinhole[29]. The bilayer forms as the solvent evaporates. Black lipid membranes can also be formed by the spreading of a lipid monolayer in one compartment whose liquid level is then

slowly and carefully lowered and then raised again so that a bilayer is formed across the pinhole[29] (see figure 1.7).

Such black lipid membranes have advantages in that both sides of the bilayer are accessible to manipulation, the bilayer maintains full fluidity and that the lack of a supporting substrate on one side means that transmembrane proteins can easily be studied[29].

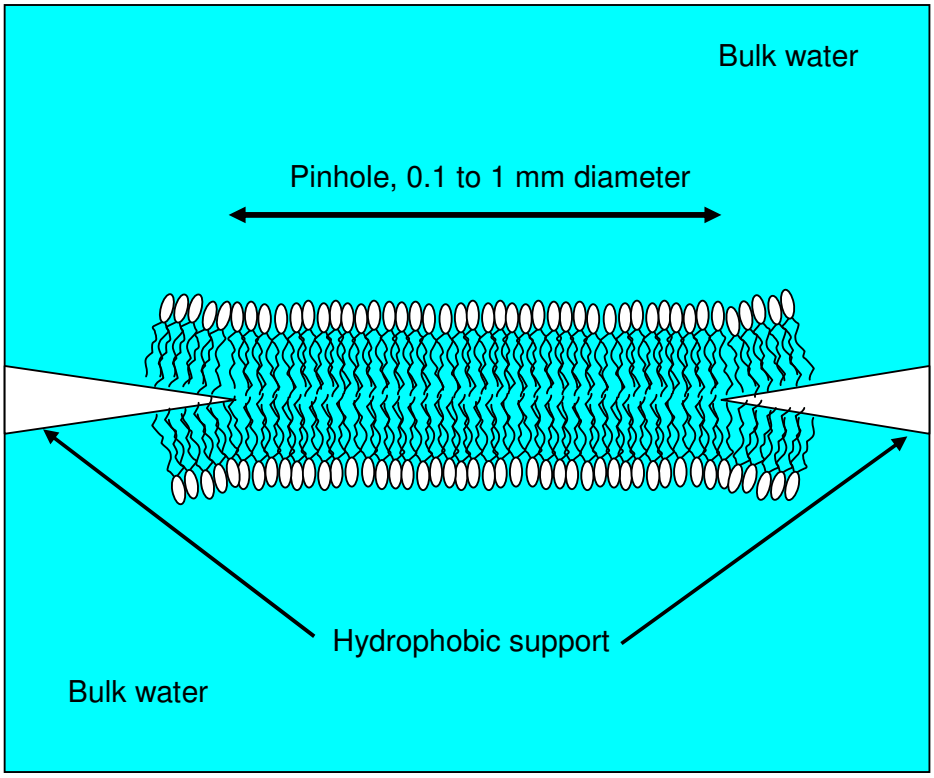

Figure 1.7: A black lipid membrane. The bilayer has been formed in a small pinhole in a hydrophobic support which separates two solvent filled compartments.

Unsupported membranes have short lifetimes and can be awkward to characterise by conventional methods such as infrared spectroscopy[29]. These problems prompted researchers to seek a more convenient model. In 1985 Tamm and McConnell reported the formation of phospholipid bilayers on the surfaces of glass, quartz and oxidised silicon[30]. These surfaces are all hydrophilic: favourable hydrophilic interactions between the surface and the lipid head groups leads to a more stable bilayer, resulting in lifetimes measurable in days rather than hours. These types of bilayer are termed supported bilayers.

There are a number of methods used to generate supported bilayers. In all cases the substrate must be clean and lack surface defects for a high quality defect free phospholipid bilayer to form. The simplest method is vesicle fusion. This involves the use small unilaminar vesicles (SUVs), which are small spherical structures typically 15-30 nm in diameter composed of a lipid monolayer enclosing a small volume of solvent. The introduction of a SUV containing solution into the electrolyte compartment allows the vesicles to attach themselves to the substrate, where they rupture and spread on the surface to form a monolayer[29]. More vesicles impacting on this monolayer will fuse and spread, forming a bilayer. This method has the advantage of being simple and versatile, being a useful technique for most phospholipids. However, the bilayer formed may have defects and/or patchy coverage[31]. Nor is it possible to form bilayers whose individual monolayers, or leaflets, are

composed of different phospholipids. Thus it is not possible to investigate asymmetric membranes – a major limitation.

A second method of forming supported bilayers is the Langmuir-Blodgett technique[32]. Here, a lipid monolayer is formed on the fluid surface of a Langmuir trough by the spreading of a dilute solution of phospholipid in solvent. The solvent is then allowed to evaporate so that a monolayer forms on the air/solvent interface. The substrate is then slowly raised from the trough while the monolayer is held under constant surface pressure so that a monolayer coats the surface. Pressing the substrate down on the monolayer (carefully!) forms the second (distal) leaflet of the bilayer. This method has the advantage that the second monolayer need not be composed of the same phospholipid as the proximal leaflet, hence more biologically relevant bilayers can be investigated. Both vesicle fusion and LB/LS methods were used in this work. A more complete description is given in Section 3.4.

The third method combines elements of the first two methods. First, a monolayer is coated on the substrate using a Langmuir trough. The substrate is then placed in a solution and vesicles introduced which will fuse and spread on top of the monolayer to form a bilayer[29]. Again, different lipids can be used for the monolayer and vesicles so that bilayers formed of dissimilar leaflets can be made.

Supported bilayers have a number of advantages over black membranes. The ease of making bilayers with dissimilar leaflets has already been mentioned.

Most supporting substrates are hydrophilic and therefore the polar head groups will readily anchor themselves to the surface. This is beneficial for bilayer stability[29]. Since the bilayer is anchored to a surface, its structure can be readily investigated using surface techniques such as attenuated total reflection Fourier Transform Infrared spectroscopy (ATR-FTIR) or surface plasmon resonance (SPR). Disadvantages arise from the close proximity of the substrate: bilayer fluidity is reduced and transmembrane proteins can also interact unfavourably with the support[29].

1.3.2 Substrates for Supported Bilayers

The surface must be both smooth and clean for the formation of a high quality bilayer with a minimum of defects. A number of materials have been used as a supporting substrate. These include hydrophilic materials such as oxidised silicon[30], borosilicate glass[33], mica[34] and silica[35]. These substrates have in common Si-O groups at the surface which under normal conditions are readily converted to Si-OH. Such a surface forms a ready host for the attachment of a lipid monolayer or bilayer as a result of the strong attraction between the OH groups and the hydrophilic lipid head groups. Furthermore, these strongly hydrophilic substrates often retain a thin 1-2 nm layer of water trapped between substrate and bilayer, which enhances bilayer fluidity[29]. However, as these substrates are nonconductive, it is not possible to conduct electrochemical investigations or subject the supported bilayer to a controlled electric field. In addition, SiO_2 substrates strongly absorb infrared radiation which makes characterization by spectroscopic techniques problematic.

Metallic substrates have also been employed such as silver[36], platinum[37], mercury[38] and gold[31]. Mercury presents a smooth, defect free surface: its high hydrogen overpotential means it can be used to investigate bilayer properties at large negative potentials. The fact that mercury possesses the most hydrophobic surface of all metals means that a lipid monolayer will readily form on the metal surface with the head groups directed outwards. In order to form a bilayer structure, the mercury surface is often pre-treated with an alkanethiol in order to provide a surface which is favourable to the attachment of the hydrophobic lipid tails[29]. 1-octadecanthiol is often used as this forms a highly ordered monolayer[38]. This technique therefore results in a hybrid bilayer with the thiol comprising the endo leaflet and the phosphoplid the exo leaflet. This cannot be considered to be a good model for biological membranes, though such bilayers are stable so are possible candidates for sensor applications. The alkanethiol can be substituted by a thiopeptide in order to form a hydrophilic surface to which a phospholipid bilayer can be attached: this has been done with gold electrodes[39].

The high electrical conductivity of metallic substrates naturally allows the electrochemical investigation of the attached bilayer. The high reflectivity of such surfaces allows the use of infrared spectroscopy techniques to be used. The use of gold as a substrate has the advantages of being usable over a wide potential range (over 1 V) and the ability to go to high positive potentials before the onset of oxide formation relative to other metallic substrates[31]. The

fact that gold has the highest infrared reflectivity of any metal is advantageous in infrared spectroscopy.

Early work using gold electrodes employed an alkanethiol monolayer to create an extremely hydrophobic surface to which a phospholipid monolayer could be attached[40,41]. Electrochemical characterisation of this hybrid bilayer revealed resistivity values close that those obtained for black lipid membranes. Addition of a peptide toxin, melittin, substantially reduced resistivity: melittin is known to induce pores in lipid bilayers which would act as channels to conduct ions[41].

The impedance of phospholipid bilayers and multilayers was investigated by Lindholm-Sethson who in 1996 used the Langmuir-Blodgett technique to sequentially build up a multilayer structure on a bare gold substrate[42]. Observed resistances were lower and capacitance higher than black lipid membranes: it was determined that this was due to defects in the first few transferred monolayers. This implied that these monolayers did not possess an ordered structure. Monolayers deposited on top of the first five layers were found to have more reproducible characteristics and thus were probably more ordered.

The first use of a gold (111) surface to investigate the absorption of a lipid monolayer was by Bizzotto and Lipkowski in 1995, who showed that films of 12-(9-anthroyloxy) stearic acid and octadecanol could be formed on the Au

(111) surface[43]. The gold (111) surface has proven itself to be an excellent surface for the depositing of high quality bilayer films[44].

The Au (111) surface is smoother than the polycrystalline gold surface, though neither can compete with mercury for surface smoothness. The maximum negative potential is limited by the onset of hydrogen reduction – again, this is inferior to Hg. For this reason, the maximum negative potential applied to Au electrodes is typically -1.2 V or less. However, gold is less hydrophobic than Hg, and thus phospholipids can adsorb to the surface by the head group, so that a normally orientated artificial bilayer may constructed where the head groups are all directed outwards. The additional alkanethiol monolayer often required with a mercury electrode can thus be dispensed with, allowing more realistic phospholipids bilayers to be used as models for biological systems.

1.4 Characterisation Methods

Even high resolution electron microscopy merely resolves biological and artificial membranes as a pair of parallel lines. The determination of their properties can be seen to be no trivial task.

Neutron reflectivity experiments allow the determination of the thickness and structure of a supported bilayer[45]. Electrochemical measurements can reveal several parameters – measurement of interfacial capacitance can reveal phase changes within the film where the molecules undergo rearrangement[31] while impedance measurements allow the determination of pores and

defects[46]. The bilayer can be imaged directly by atomic force microscopy (AFM)[47]. Information about the conformation and arrangement of the molecules comprising the film can be found through infrared spectroscopy[48].

1.5 Scope of This Thesis

The purpose of this work was to generate phospholipids bilayers by the methods of vesicle fusion and Langmuir-Blodgett / Langmuir-Schaeffer deposition. Different mixtures of DMPS and DMPE were used in order to vary the bilayer composition. Once produced, the physical properties of the bilayers were characterized by a number of different means: infrared spectroscopy, electrochemical methods and neutron reflectometry were employed. The properties of each bilayer composition were examined to determine if composition had a significant effect on the bilayer characteristics.

Polarisation modulated infrared reflectance spectroscopy can glean data on the conformation adopted by lipids adhering to a surface, the packing of those lipid molecules and the environment infrared active groups are in, such as the degree of hydration. Differential capacitance measurements allow the surface coverage of the substrate by the adsorbed film to be estimated and reveal data about phase transitions and the process of desorption induced by changes in the substrate potential. Chronocoulometry allows the surface pressure of the bilayer to be calculated. This yields data on the magnitude of adhesion between electrode and bilayer thus allowing the potential at which desorption of the film occurs to be ascertained – this can then be compared to

the differential capacitance data. Electrochemical impedance spectroscopy is capable of probing the effectiveness of a film as a barrier to the passage of anions and cations. This can be used to estimate the surface coverage and evaluate the surface roughness. Neutron reflectometry can be used to calculate the thickness of the adsorbed film and estimate its degree of hydration – and how these properties change with potential. The measurement of isotherms using a Langmuir Trough give information to phase transitions as well as how the molecules in a monolayer are organised.

Together, these techniques were used to evaluate the effect that composition had on properties. Polarisation modulated infrared reflectance spectroscopy was used to probe the conformation of the lipid head groups and tail groups. Differential capacitance and chronocoulometry were used to investigate phase transitions and desorption processes of adsorbed bilayers to develop a model of the desorption process. Electrochemical impedance spectroscopy was used to examine the permeability of bilayers of varying compositions to cations and anions, and relate permeability to surface charge. Neutron reflectometry was used to determine the structure of the bilayer along with hydration to corroborate the data acquired by electrochemical means. Isotherms were performed to investigate monolayer phase transitions and miscibility of DMPE and DMPS.

1.6 References

1. Alberts, B., Johnson, A., Lewis, J., Raff, M., Roberts, K., Walter, P., 2002, *Molecular Biology of the Cell*, 4th edition, Garland Science, US

2. McMurry, J., 1992, *Organic Chemistry*, 4th edition, Brookes/Cole Publishing Co.

3. Pond, C., 1999, *Physiological Integration*, Open University Press

4. Pulselli, R. M., Simoncini, E., Tiezzi, E., (2009), *Biosystems*, **96** 3:237

5. Gorter, E., Grendel, F., (1925), *J. Exp Med.*, **41**:439

6. Singer, S. J., Nicolson, G. L., *Science*, (1972), **175**:720

7. Buda, C., Dey, I., Balogh, N., Horvath, L. I., Matterspach, K., Juhasz, M., Yeo, Y. K., Farkas, T., *Proc. Natl. Sci. USA*, (1994), **91**:8234

8. Bretscher, M. S., (1985), *Scientific American*, **253** 4:86

9. Geiser, F., Kenagy, G. I., *Canadian J. Zoo.*, (1993), **71**:62

10. Kiessling, V, *Biochim Acta Biophys-biomembranes*, (2009), 1788,**1**, 64:71

11. Drew, J., *Science*, (1960), **287**:2000

12. Johnson, L. G., 1987, *Biology*, 2nd edition, Wm. C. Brown, US

13. Pond, C., 2002, *Size and Action*, Open University Press

14. Anitua, E, Andia, I., Ardanza, B., Nurden, P., Nurden, A. T., (2004), *Thrombosis and Haemostasis*, **91**:1

15. Considine, R.V., Sinha, M.K., Heiman, M.L., Kriauciunas, A., Stephens, T.W., Nyce, M.R., Ohannesian, J.P., Marco, C.C., McKee, L.J., Bauer, T.L., (1996), *N Engl J Med*, **334** 5:292

16. Heram, D. J., (1980), *Proc. Natl. Sci. USA*, **77**:7463

17. John, K., Schreiber, S., Kubelt, J., Herrmann, A., Mueller, P., (2002), *Biophysical J.*, **83**:3315

18. Bevers, E. M., Williamson, P. L., (2010), *FEBS Letters*, **584**, 13:2724

19. Schlegel, R. A., Williamson, P., (2001), *Cell Death and Differentiation*, **8**:551

20. Boesze-Battaglia, K., Schimmel, R. J., (1997), *J. Exp. Bio.*, **200**:2927

21. Bevers, E. M., Comfurius, P., Van Run, J. L. M. L., Henker, H. C., Zwaal, R. F. A., (1982), *Eur J. Biochem.*, **122**:429

22. Kasahara, K., Sanai, Y., (2001), *Trends Glycosci. Glycotechnol.*, **13**:587

23. Stoddart, A., Dykstra, M. L., Brown, B. K., Song, W. X., Pierce, S. K., Brodsky, F. M., (2002), *Immunity*, **17**:451

24. Xu, L., Frederick, P., Pirollo, K. F., Tang, W. H., Ralt, A., Xiang, L. M., Huang, W. Q., Cruz, I., Yin, Y. Z., Chang, E. H., (2002), *Hum. Gene Ther.* **13**:469

25. Yang, T. L., Baryshnikova, O. K., Mao, H. B., Holden, M. A., Cremer, P. S., (2003), *J. Am. Chem. Soc.*, **125**:4779

26. Plant, A. L., Brighamburke, M., Petrella, E. C., Oshannessy, D. J., (1997), *Annal. Biochem.***226**:342

27. Mueller, P., Rudin, D. O., Ti Tien, H., Wescott, W. C., (1962), *Nature* **194**:979

28. Mueller, P., Rudin, D. O., Ti Tien, H., Wescott, W. C., (1963), *J. Phys. Chem.* **67**:534

29. Castellana, T., Cremer, P. S., (2006), *Surf. Sci. Rpt.*, **61**:429

30. Tamm, L. K., McConnell, H. M., (1985), *Biophys. J.*, **47**:105

31. Bin, X., Zawisza, I., Goddard, J. D., Lipkowski, J., (2005), *Langmuir*, **21**:330

32. Lipkowski, J., (2010), *Phys. Chem. Chem. Phys.*, **12**:13874

33. Cremer, P. S., Boxer, S. G., (1999), *J. Phys. Chem. B*, **103**:2554

34. Egawa, H., Furusawa, K., (1999), *Langmuir*, **15**:1660

35. Lagerholm, B. C., Starr, T. E., Volovyk, Z. N., Thompson, N. L., (2000), Biochemistry, **39**:2042

36. Salamon, Z., Wang, Y., Tollin, G., MacLeod, H. A., (1994), *Biochim. Biophys. Acta. Biomembranes*, **1195**:267

37. Puu, G., Gustafson, I., (1997), *Biochim. Biophys. Acta. Biomembranes*, **1327**:149

38. Becucci, L., Guidelli, R., (2007), *Langmuir*, **23**:5601

39. Naumann, R., Jonczyk, A., Hampel, C., Ringsdorf, H., Knoll, W., Bunjes, N., Graber, P., (1997), *Bioelectrochem and Bioenergetics*, **42**:241

40. Plant, A. L., (1993), *Langmuir*, **9**:2764

41. Plant, A. L., Gueguetchkeri, M., Yap, W., (1994), *Biophys. J.*, **67**:1126

42. Lindholm-Stethson, B., (1996), *Langmuir*, **12**:3305

43. Bizzotto, D., Lipkowski, J., (1995), *Prog. Sur. Sci.*, **50**:237

44. Zawisza, I., Bin, X. M., Lipkowski, J., (2007), *Langmuir*, **23**:5180

45. Burgess, I., Szymanski, G., Li M., Horswell, S., Lipkowski, J., Majewski, J., Satija, S., (2005), *Biophys. J.*, **86**:1763

46. Nelson, A., (2007), *J. Electroanal. Chem.*, **601**:83

47. Xu, S., Szymanski, G., Lipkowski, J., (2004), *J. Am. Chem. Soc.*, **126**:12276

48. Bin, X, Lipkowski, J., (2006), *J. Phys. Chem. B*, **110**:26430

2. Theory

2.1 Adsorption at an Interface

The properties of matter at an interface or surface differ from the bulk. A seemingly trivial observation of this is the tendency of liquids to form spherical drops. A sphere has a minimum surface area with respect to volume. In other words, liquids exhibit a pronounced tendency to minimise surface area.

Why is this so? A molecule in the bulk is surrounded by its fellows on all sides. It therefore has the maximum of favourable interactions. On the surface, there are fewer interactions and there is a marked asymmetry resulting in a net force acting on a surface molecule that is directed into the bulk. Fewer interactions at a surface means that molecules there are unable to move to the lower energy state that molecules in the bulk possess: thus the surface possesses an excess of energy, sometimes called the surface free energy. Surface free energy can be expressed in terms of the Gibbs free energy[1]:

$$dG = \gamma dA \qquad [2.1]$$

where A is the area and γ the surface free energy and under conditions of constant temperature and pressure.

The interface between two separate phases was first modelled by Gibbs, who conjectured that there would be a narrow plane dividing the two distinct

phases with a change in concentration of chemical species across the surface, depicted in figure 2.1. Species i has a concentration N_i^{α} in phase α and concentration N_i^{β} in phase β. The concentration changes in a narrow interfacial region *S*. Adsorption at a surface will alter γ. This argument led Gibbs to derive the Gibbs Adsorption Isotherm:

$$-d\gamma = \sum_i \Gamma_i d\mu_i \qquad [2.2]$$

μ_i is the chemical potential of species i while Γ_i is the concentration of species *i* at the interface in excess of its bulk concentration and is the Gibbs excess. It is defined as:

$$\Gamma_i = \frac{N_i^S - N_i^B}{A} \qquad [2.3]$$

where A is the surface area, N_i^S the number of moles of species i in the surface s and N_i^B the number of moles of species i in the bulk.

Species can either be in excess or deficit at the interface. Inorganic salts commonly have a surface deficit: that is their concentration at the interface is less than the bulk concentration. Hence $\Gamma_i < 0$. This leads to an increase in γ. Some species have greater concentration at the surface than the bulk, $\Gamma_i > 0$. These species are surfactants. Surfactants act to decrease surface energy[2].

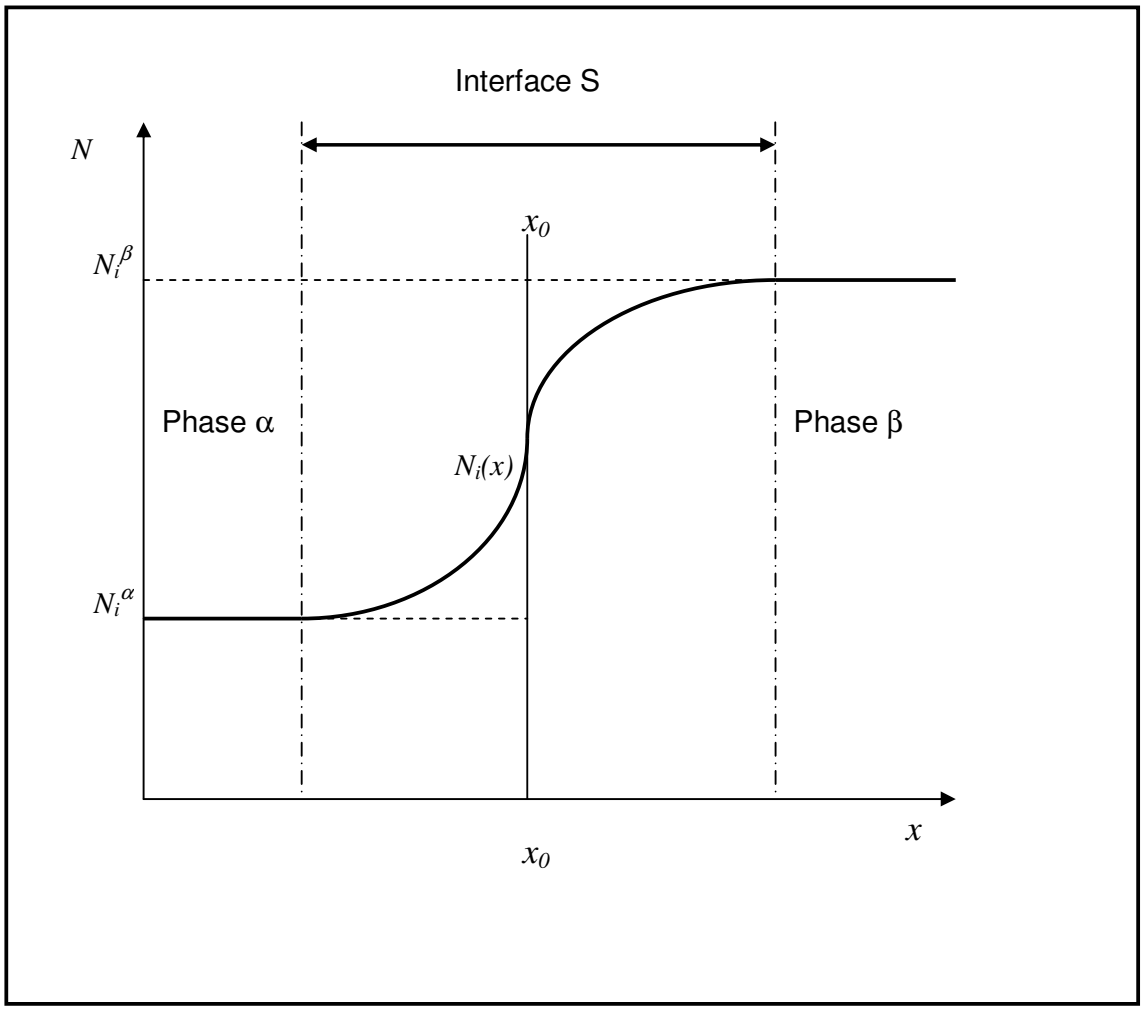

Figure 2.1: The Gibbs model of an interface. The interface *S* separates two phases α and β at the x-axis coordinate x_0. $N_i(x)$ represents the variation of concentration of species *i* across the interface.

Because an insoluble surfactant has negligible bulk concentration, it cannot be described by the Gibbs equation. An adsorbed insoluble surfactant will lower surface energy analogous to soluble surfactants. The change of surface energy is termed the surface pressure, π, and can be found from:

$$\pi = \gamma_P - \gamma_S \qquad [2.4]$$

γ_P is the surface free energy for the pure solvent while γ_S is the surface free energy of the surface in the presence of the adsorbed species[1].

2.2 The Electric Double Layer

Electrode and electrolyte have differing potentials which partly arise from the surface energy associated with the interface and also simply because the two different media can be expected to have different chemical potentials. The inevitable consequence of this is that there must be a potential difference across the interfacial region leading to the generation of an electric field.

Both electrode and electrolyte possess mobile charges: electrons in the case of the metal and ions, both positive and negative, for the electrolyte. As a consequence of Lenz's Law, these charges will move in such a direction to oppose this electric field. Hence the interfacial region is one with opposing electric charges lined up and a (usually substantial) electric field confined to this volume[3] (Figure 2.2).

This rather simple picture was first proposed by Helmholtz in 1853. In the absence of faradaic processes, the interfacial electric field would produce charge separation across the interface and the electrode charge density, q^m, matched an equal but opposite charge, q^s, in the electrolyte region next to the electrode:

$$q^m = -q^s \qquad [2.5]$$

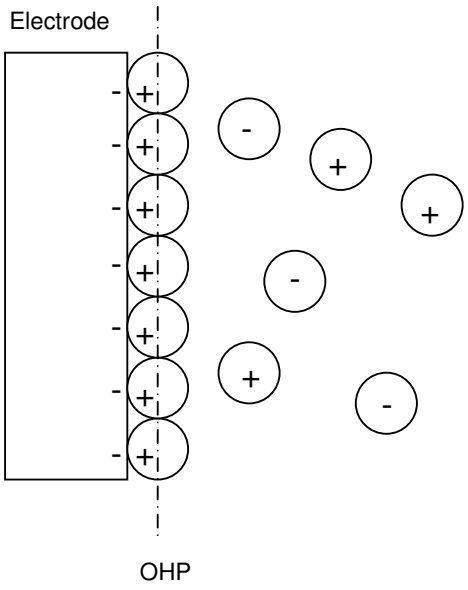

Figure 2.2: The Helmholtz model of the electrode interfacial region. All opposing charges are confined to the interfacial region. The OHP is defined by the location of the centres of the ions that are adsorbed onto the electrode surface.

The electrode charge is generated by a surfeit (negative) or deficiency (positive) of electrons at the surface. In aqueous media, most metals acquire a negative charge. The electrolyte charge is the result of redistribution of ions or solvent dipoles. Ions can approach the electrode only as far as the solvation shell they possess allows. Thus a typical Helmholtz picture would see a negatively charged electrode surface with positive ions adhering to the surface, as in figure 2.2. The centre of the positive ions defines the Outer Helmholtz Plane (OHP) with a thickness of the order of a few nanometres. The entire interfacial electric field is located in the OHP and has a linear potential drop.

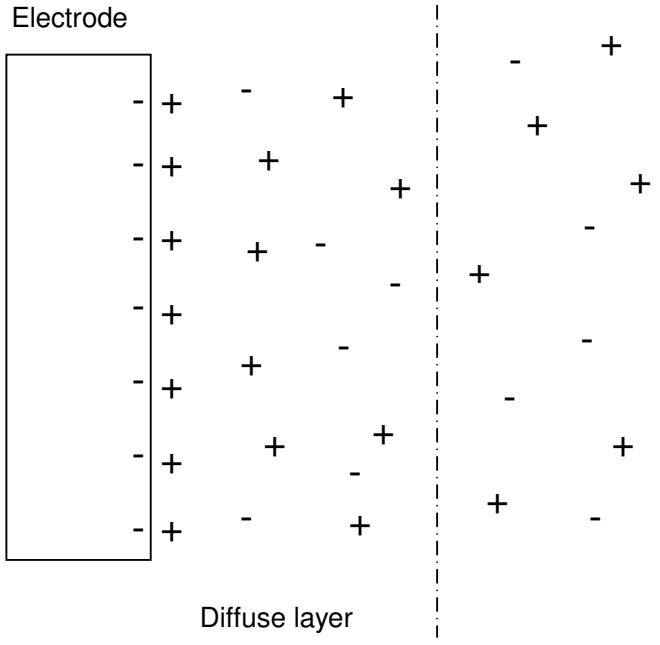

Figure 2.3: Gouy-Chapman model. Ions are modelled as point charges. The interfacial charge is carried in the diffuse layer. Beyond the diffuse layer, the electrolyte retains overall neutrality.

The Helmholtz model was modified by Gouy and Chapman. This model considered the effect of thermal fluctuations[3]. Random thermal fluctuations will have the effect that, occasionally, one or other of the ions composing the OHP will temporarily gain sufficient energy to overcome the electrostatic attraction and rejoin the bulk solution. These ions will occupy a diffuse region close to the electrode, but further out from the OHP. Thus the opposing solution charge is not concentrated in the OHP but in a larger diffuse layer close to the interface. The diffuse layer thus is the region where there is an excess of charge as opposed to the solution further from the interface which

retains overall neutrality. Likewise, the electric field also occupies a larger region as shown in figure 2.3.

In 1924, Stern produced a model which incorporated elements of both the Helmholtz and Gouy-Chapman models. It was proposed that the bulk of the solution charge existed as ions within the OHP, but Brownian motion would ensure that some charge resided in a more diffuse region. The interfacial electric field would drop sharply in the OHP but more gently in the outer diffuse region (figure 2.4). Grahame further modified the picture by pointing out that some ions may be specifically adsorbed onto the electrode surface without an accompanying solvation shell. The centres of these ions define the thickness of the Inner Helmholtz Plane (IHP)[3].

The Gouy-Chapman model allows a relation for the surface charge, σ, to be derived[4]. The Poisson equation relates electrostatic potential, ψ, to a given charge distribution:

$$\nabla^2\psi = -\frac{\sum_i z_i e c_i(r)}{\varepsilon_r \varepsilon_o} \qquad [2.6]$$

z_i is the charge on species i, e the electronic charge, $c_i(r)$, the variation of concentration of species i in the direction perpendicular to the charged interface, ε_r the relative permittivity and ε_0 the permittivity of free space.

The distribution of ions i near to the surface is given by:

$$c_i(r) = c_i \exp\left(\frac{-z_i e \psi}{k_B T}\right) \qquad [2.7]$$

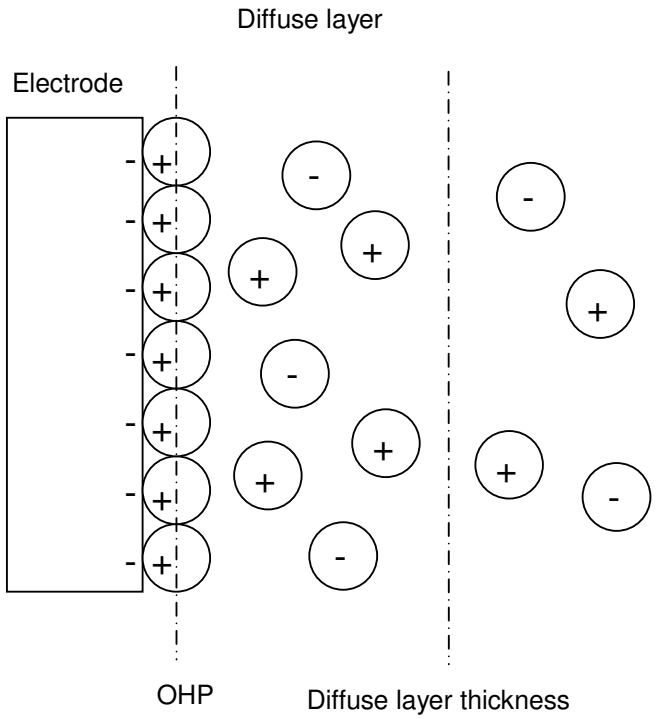

Figure 2.4: The Stern double layer incorporates elements of both the Helmholtz and Guoy-Chapman models. It combines aspects of both the Helmholtz and Gouy-Chapman models. Ions reside on the electrode surface – this defines the OHP, but there is a diffuse layer beyond this which carry some the interfacial charge density.

where T is the temperature, c_i the bulk concentration of the i-th ionic species and k_B the Boltzmann constant.

Combining both equations 2.6 and 2.7 yields the Poisson-Boltzmann equation:

$$\nabla^2\psi = -\sum z_i e c_i \exp\left(\frac{-z_i e\psi}{k_B T}\right) \qquad [2.8]$$

For neutrality to be maintained, the surface charge must be opposed by an equal and opposite charge carried by ions in the solution (equation 2.5). The potential can be assumed to tend towards zero far from the interface. It can be shown that the application of these two boundary conditions to the Poisson-Boltzmann equation produce the Grahame equation:

$$\sum_i c_i^{surf} = \sum c_i + \frac{\sigma^2}{2k_B T \varepsilon_r \varepsilon_0} \qquad [2.9]$$

c_i^{surf} is the concentration of species i at the surface.

It can be shown that for a 1:1 electrolyte such as NaCl or $MgSO_4$ that σ can be found by the following relation[4]:

$$\sigma = \sqrt{8k_B T C_{bulk} \varepsilon_r \varepsilon_0} \sinh\left(\frac{ne\psi}{2k_B T}\right) \qquad [2.10]$$

C_{bulk} is the bulk concentration of the electrolyte and n is the ionic charge of the electrolyte.

2.2.1 Double Layer Capacitance

The separation of charge in the interfacial region means that the electric double layer acts as a capacitor: a capacitor is defined as a device or structure that effects charge separation.

The capacitance, *C*, of a capacitor is given by:

$$C = \frac{q}{E} \qquad [2.11]$$

where q is the charge stored by the capacitor and E the potential difference across the capacitor.

The double layer can be approximated as a parallel plate capacitor, provided the electrode surface is flat and electrode area large compared to the thickness of the double layer. Thus the capacitance is given by[5]:

$$C = \frac{\varepsilon_r \varepsilon_o A}{d} \qquad [2.12]$$

where A is the plate (electrode) area, d the plate (double layer) separation, ε_r the relative permittivity of the electrolyte and ε_o the permittivity of free space.

The electric field across the interfacial region varies with the applied potential. From the Gouy-Chapman model, this can be expected to alter the thickness of the double layer – and hence the capacitance. The differential capacitance (DC), C_d, is a measure of how the interface capacity varies with E[6]:

$$C_d = \frac{\mathrm{d}q}{\mathrm{d}E} = \left(\frac{\partial q^m}{\partial \Delta \phi_{m/s}} \right)_{\text{constant composition}} \qquad [2.13]$$

Electrically, the electrolyte contributes resistance. Hence an electrochemical cell in the simplest terms can be modelled as a resistance in series with a capacitor (in the absence of faradaic processes).

A capacitor does not conduct direct current, but it *does* conduct alternating current, as successive cycles charge and then discharge it. An ideal capacitor produces a charging current, I, that is proportional to the rate of change to the applied voltage, E:

$$I = C\frac{dE}{dt} \qquad [2.14]$$

Considering a sinusoidal alternating current, the maximum rate of change of the potential occurs when the waveform is passing through 0 V. It therefore follows that an ideal capacitor will go through a maximum in charging current at this time. $dE/dt = 0$ at the voltage maxima and minima and hence current will fall to zero at these points. Hence the current leads the applied voltage with a phase shift of 90°.

A series RC circuit responds in a similar way to an AC current but phase shift is given by vector addition of the resistance, R, and the reactance of the capacitor, X_c, which is given by[6]:

$$X_c = \frac{1}{2\pi fC} \qquad [2.15]$$

It can be shown that the phase shift, φ, is given by:

$$\varphi = \tan^{-1}\frac{X_c}{R} \qquad [2.16]$$

The phase shift can also be expressed in terms of an imaginary current, I_{Im}, and I_{Re}:

$$C_d = \frac{I_{\mathrm{Im}}}{2\pi f V_{ac}}\left\{1+\left(\frac{I_{\mathrm{Re}}}{I_{\mathrm{Im}}}\right)^2\right\} \qquad [2.17]$$

A lock-in amplifier is a phase sensitive detector and thus can be used to separate and measure the components I_{Im} and I_{Re}. Knowing both components allows C_d to be determined from Equation 2.17.

2.3 Interfacial Charge Density

2.3.1 The Electrocapillary Equation

The separation of charge at an electrified interface gives rise to the interfacial capacitance. Clearly there must be a quantity of charge residing on the surface of the electrode. It follows that the magnitude and sign of this charge will depend on the applied potential, E. But the interfacial charge also depends on the surface energy of the interface. This leads to the possibility that measurement of the surface charge may allow the surface energy of an interface to be calculated.

The electric double layer theory outlined in the previous section is valid for an interface that is in electrostatic equilibrium. This is true only for an ideally polarisable electrode (IPE). An IPE does not experience charge transfer across the electrode/electrolyte interface. Mercury comes close to exhibiting IPE behaviour over a wide range of applied potentials – moreover its liquid state allows for the direct measurement of surface tension, and hence surface energy[6].

In the nineteenth century, Lippman derived the Lippman Equation from measurements of the surface tension of Hg in a capillary electrode as a function of potential:

$$\left(\frac{\partial \gamma}{\partial E}\right)_{T,p,\mu} = -\sigma_M \qquad [2.18]$$

γ is the surface energy of the mercury electrode and σ_M the charge density of the electrode.

The Lippman Equation led to the extension of the Gibbs adsorption isotherm to an electrified interface[6]. This yields the Electrocapillary Equation:

$$-d\gamma = SdT - Vdp + \sigma_M dE + \sum_i \Gamma_i d\mu_i \qquad [2.19]$$

where S is the entropy, T the temperature, V the volume and p is the pressure in the electrochemical cell. Γ_i and μ_i are the Gibbs excess and the chemical potential of species i at the interface, respectively. The Lippman Equation can be derived from the Electrocapillary Equation when T, V, p and μ are kept constant.

Equation 2.19 applies to a liquid IPE only. The surface energy of a solid does not merely depend on the surface area, but on the method of its creation. The energy required to create a new surface of unit area by cleavage is the superficial work, γ_c. The energy required to create a new surface of unit area by stretching solid is the surface stress Υ. These quantities are different. Appling the electrocapillary equation to a solid requires this to be taken into account:

$$-d\gamma = sdT - Vdp + \sigma_M dE + \sum_i \Gamma_i d\mu_i + (\gamma - \Upsilon) d\varepsilon_e \qquad [2.20]$$

ε_e is the elastic surface strain. It has been shown that this last term has a small value and may thus be ignored[7]. Hence the electrocapillary equation can be applied to solid electrodes.

2.3.2 Measurement of Charge Density – Chronocoulometry

The electrocapillary equation gives the conceptual foundations for the measurement of surface energy at a solid electrode. Consider the situation where an electrode is held at a constant potential E. Stepping the potential by magnitude ΔE will give rise to a current pulse as the electric double layer charges. Integrating the current over time t yields the total charge transferred, Q:

$$Q = \int_0^t I dt \qquad [2.21]$$

In the absence of any Faradaic processes, Q simply represents the charging of the double layer. As in the case of DC, modelling the cell as a resistance in series with a capacitor is useful in analysis (Section 2.2.1).

If the interfacial capacitance is constant, then the charge transferred on the application of a potential step ΔE is simply:

$$Q = C.\Delta E \qquad [2.22]$$

Current will decay in an exponential fashion:

$$I_t = I_0 e^{\left(\frac{-t}{RC}\right)} \qquad [2.23]$$

where I_0 is the initial current given by: $I_0 = R.\Delta E$. R is the total resistance of the circuit, and includes terms from the electrolyte resistance and external electric circuit resistance.

In a non-ideal situation the double layer capacitance can be expected to be dependent on E. This is particularly the case where there is an adsorbed species on the electrode: changes in capacitance can come about as a result of desorption or re-orientation of the adsorbent molecules.

Where the area of the working electrode is known, chronocoulometry thus yields the charge density, σ, of the electrode. By using different values of ΔE, it is possible to construct a plot of σ versus E. The point at which this curve crosses the x-axis is the position of zero charge (PZC). At this point, there will be no difference of potential between electrode and electrolyte, and the charge density will be zero. At the PZC, there will be no electric field across the interfacial region.

The adsorption of a species onto an electrode will change σ. A comparison of both bare electrode and electrode supporting an adsorbed layer can yield data about the adsorbed species.

Recalling that the energy, γ, stored in a capacitor is given by:

$$\gamma = \frac{1}{2} QE \qquad [2.24]$$

it is apparent that integrating the area under the plot of charge density versus E gives the energy associated with the interface:

$$\gamma = -\int_{E_0}^{E} \sigma_{M_0} dE \qquad [2.25]$$

where E_0 is the step potential. Usually E_0 is chosen so that it is negative of the desorption potential.

An adsorbed film will alter σ and hence the interfacial energy. Chronocoulometry will determine the interfacial energy due to *both* the adsorbed layer and its electrode substrate. The energy due to the adsorbed layer alone can be found by simply subtracting σ for the bare electrode[8]:

$$\pi = \gamma_0 - \gamma = \int_{E_0}^{E} \sigma_M \, dE - \int_{E_0}^{E} \sigma_{M_0} dE \qquad [2.26]$$

This measurement is thus *relative* to the bare surface. A negative value is thus not unphysical, rather it indicates that the interface has less energy than the bare surface.

2.4 Impedance at an Electrified Interface

An electrified interface presents a specific impedance to the passage of electric charge across it. This impedance is due to the capacitance of the double layer, the degree to which the solvent will transport electrons (usually a vanishingly small contribution) and the reaction kinetics of any faradaic process that takes place. This last term will have contributions from both the reaction kinetics of the electron transfer process and transport of reactive species to and from the electrode[6].

Each process that contributes to cell impedance operates over different time scales and hence will have its own characteristic time constant. It is thus possible to elucidate each process by observing the electrochemical cell's

response to an AC signal of different frequencies (and hence time scales). For example, charging of the double layer capacitance operates over short time scales and hence this process can be observed at high frequencies while diffusive transport to the electrode operates over relatively slow time scales and hence will be revealed at low frequency. Frequencies used are typically in the range 10^4 Hz down to 0.1 Hz: hence EIS can be used to investigate phenomena whose characteristic time scale spans five orders of magnitude.

The concept of impedance is essential to the understanding of EIS. We can start with the familiar Ohm's Law:

$$R = \frac{E}{I} \qquad [2.27]$$

which relates resistance, R, with the applied potential, E, and observed current, I. This may be a trivial observation, but it is important to note that Ohm's Law only applies to a resistance that behaves in an ideal fashion (a point rarely emphasised in most basic physics textbooks). An ideal resistance is one whose value is constant at all applied values of E and I, and is also constant at all AC frequencies.

Capacitors and inductors do not obey Ohm's Law. If we consider a sinusoidal AC current whose instantaneous voltage at time t is given by:

$$E = E_0 \sin(\omega t) \qquad [2.28]$$

E_0 is the amplitude and ω is the angular frequency, which is related to the frequency f by the relation $\omega = 2\pi f$. The current through an ideal capacitor, C, is given by the relation

$$I = \frac{dE}{dt}C \qquad [2.29]$$

For a sinusoidal AC signal, the quantity $\frac{dE}{dt}$ will be at a maximum when $E = 0$ and zero at the peak. Hence a capacitor imposes a positive phase shift of 90° to the current – current leads voltage. Maximum current flow occurs when the voltage is zero and it can be shown that the power dissipated in an ideal capacitor is also zero. This implies that the resistance of an ideal capacitor is likewise zero. Instead, the opposition of a capacitor to current flow is expressed by reactance, X. It can be shown that the reactance of an ideal capacitor, X_c, is given by:

$$X_c = \frac{1}{i\omega C} \qquad [2.30]$$

It can be shown that an ideal inductor, L, has a reactance, X_L, given by:

$$X_L = i\omega L \qquad [2.31]$$

In this case a negative phase shift of 90° is imposed on the current flow – current lags voltage[5].

Ideal capacitors, inductors and resistors do not exist in reality. It is possible, however, to model circuits as possessing such ideal elements in varying series and parallel combinations. It is necessary to define another quantity to model the opposition to the passage of electrical current, impedance, Z. Impedance is simply the sum of the ideal resistance and ideal reactance:

$$Z = R + X \qquad [2.32]$$

R may be considered to be the real resistance of the system. X is a phase shift term.

Impedance may be represented using complex notation:

$$Z = Z' + iZ'' \qquad [2.33]$$

It is convention to represent the real resistance as Z' and reactance (imaginary impedance) as Z'' [9].

The simple model of an electrochemical cell being represented by a series combination of a capacitor and resistor has already been used in the analysis of DC and chronocoulometry. The capacitor represents the electric double layer capacitance and is usually denoted C_{dl}. The resistor models electron transfer reactions. In this example, impedance is given by the equation

$$Z = Z' + \frac{1}{i\omega C_{dl}} = Z' - i\frac{1}{\omega C_{dl}} \qquad [2.34]$$

Impedance spectroscopy involves measuring the cell impedance at a number of different frequencies. This gives a list of real and imaginary impedances for a set of different frequencies. To aid in the interpretation of this, the results are frequently plotted as a Nyquist plot, where $-Z''$ is plotted versus Z' for each frequency measured. The shape of the plotted curve depends on the system. For instance, the Nyquist plot of a simple parallel RC circuit is simply a semicircle which crosses the x-axis at the origin and at R (Figure 2.5). The area of the semicircle is related to the value of C. An RC circuit is the simplest

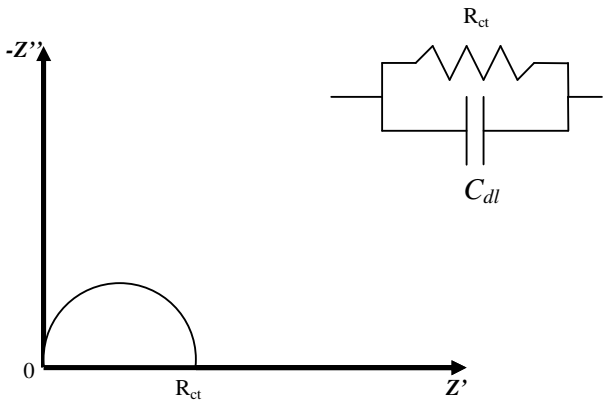

Figure 2.5: Nyquist diagram of a parallel RC circuit. The equivalent circuit is shown in the inset. For an electrochemical system, R_{ct} is the charge transfer resistance and C_{dl} the double layer capacitance. The curve on the Nyquist plot is simply a semicircle which crosses the x-axis at 0 and R_{ct}.

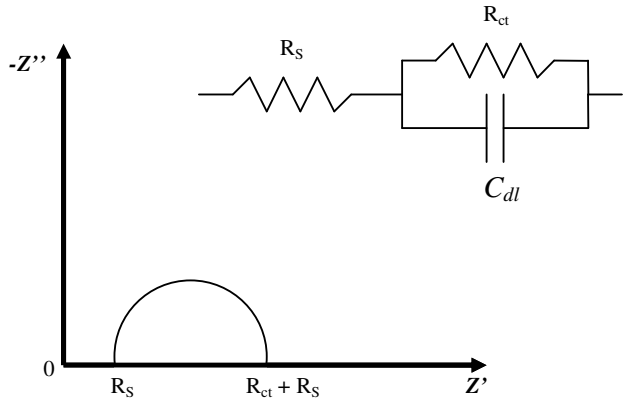

Figure 2.6: Nyquist plot of a simple electrochemical cell including solution resistance, R_s. Inset shows the equivalent circuit. The curve no longer starts at the origin but has been displaced along the axis by R_s.

electrical equivalent circuit of an electrified interface. The value of R is the charge transfer resistance and is a measure of the reaction kinetics of the faradaic process occurring. It has the symbol R_{ct}. The value of C is the double layer capacitance, C_{dl}.

A more sophisticated cell model notes that there is an additional resistance in the circuit, R_s, which can be attributed to the resistance of the electrolyte (Figure 2.6). This is the solution resistance[9]. Its effect on the Nyquist plot is to displace the semicircle from the origin: it now crosses the x-axis at R_s and R_{ct} + R_s.

Diffusion is a process that operates over longer timescales – of the order of seconds. A fast electrode reaction (small R_{ct}) will become diffusion limited over long timescales. Diffusion in EIS is modelled in the simplest manner by the infinite Warburg impedance, Z_w:

$$Z_w = \frac{\sigma}{\sqrt{\omega}} - i\frac{\sigma}{\sqrt{\omega}} \qquad [2.35]$$

σ is the Warburg coefficient. It is given by[9]:

$$\sigma = \frac{RT}{n^2F^2A\sqrt{2}}\left\{\frac{1}{\sqrt{D_O}C_O^b} + \frac{1}{\sqrt{D_R}C_R^b}\right\} \qquad [2.36]$$

D_O is the diffusion coefficient for the oxidised species, C_O^b its bulk concentration. D_R and C_R^b likewise are the diffusion coefficient and bulk concentration of the reduced species respectively, *A* the electrode area and *n* the number of electrons transferred. This is the Randles cell[10].The effect of diffusion on the Nyquist plot is shown in Figure 2.7.

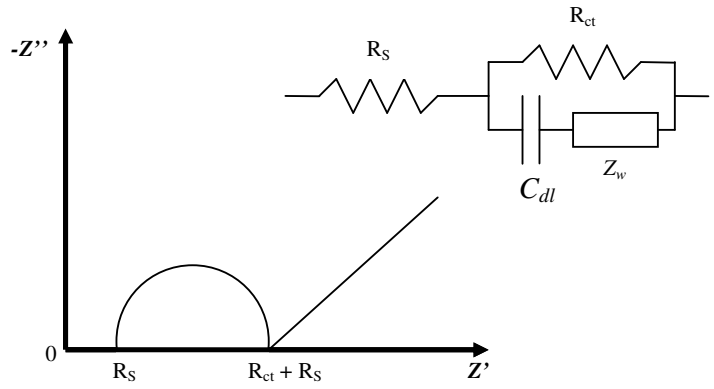

Figure 2.7: Nyquist plot of a Randles cell with the effects of diffusion. Inset shows the equivalent circuit. Z_w is the Warburg constant phase element.

So far, it has been assumed that the double layer capacitor behaves ideally – that is, it has the same value for all values of f. It is very common to find that C_{dl} varies as a function of excitation frequency. This is dispersion and is the result of the dielectric constant itself changing with frequency. A quantity, the complex dielectric constant, ε^*, may be defined as[9]:

$$\frac{\varepsilon^* - \varepsilon_\infty}{\varepsilon_s - \varepsilon_\infty} = \int_0^\infty \frac{G(\tau)}{1 + i\omega\tau} d\tau \qquad [2.37]$$

where ε_s is the dielectric constant at $\omega = 0$, ε_∞ the dielectric constant as $\omega \to \infty$ and $G(\tau)$ is a distribution function for all observed time constants τ.

In the simple case of a single time constant, $G(\tau) = \delta(\tau - \tau_0)$ and Equation 2.37 reduces to:

$$\frac{\varepsilon^* - \varepsilon_\infty}{\varepsilon_s - \varepsilon_\infty} = \frac{1}{1 + i\omega\tau_0} \qquad [2.38]$$

Where there is more than one time constant, the following equation has been modelled[11]:

$$\frac{\varepsilon^* - \varepsilon_\infty}{\varepsilon_s - \varepsilon_\infty} = \frac{1}{1 + (i\omega\tau_0)^\phi} \qquad [2.39]$$

ϕ is a constant between 0 and 1. In this case, the distribution function is a normal distribution of a function $\ln(\tau/\tau_0)$ and is given by:

$$G(\tau) = \frac{1}{2\pi\tau} \frac{\sin[(1-\phi)\pi]}{\cosh\left[\phi \ln\left(\tau/\tau_0\right)\right] - \cos[(1-\phi)\pi]} \qquad [2.40]$$

Non-ideally polarisable electrodes may be modelled in this fashion as a series of distributed time constants as given by Equation 2.40. These differing time constants are conventionally held to arise from surface roughness, chemical inhomogeneities of the surface or slow adsorption of ions. In this case, the simple model of interfacial capacitance breaks down. In such a situation C may be substituted with a constant phase element (CPE). The CPE introduces a phase shift that, unlike a capacitor, does not change with frequency. The impedance of a CPE, Z_{cpe}, can be expressed as:

$$Z_{cpe} = \frac{1}{T(i\omega)^\phi} \qquad [2.41]$$

T is a constant. On a Nyquist plot, a capacitor yields a straight line parallel to the y-axis. A CPE produces a straight line that is inclined at an angle $= 90^0(1-\phi)$. Thus when $\phi = 1$ the CPE is exhibiting ideal capacitance and

$T = C_{dl}$. $\phi = 0.5$ represents an infinite Warburg impedance while an ideal resistance yields $\phi = 0$.

Brug *et al* derived[12] a means of determining the average C_{dl}. Assuming that the electrode resistance is a sum of the solution resistance and CPE impedance, it can be shown that

$$T = C_{dl}^{\phi} R_s^{-(1-\phi)} \qquad [2.42]$$

In direct current circuit theory, the reciprocal of resistance is conductance. The analogue to conductance in AC circuit theory is admittance, Y. It, as might be expected, is the reciprocal of impedance ($Y = 1/Z$).

A series *RC* circuit has admittance:

$$Y = \frac{1}{R + \left(1/i\omega C\right)} \qquad [2.43]$$

Whitehouse *et al.*[13] showed that swapping C to a CPE means that the $i\omega$ term is exchanged for a $(i\omega)^{\beta}$ term. This term must be balanced with a dummy constant, $\omega_0^{1-\beta}$, in order for the units to be correct. ω_0 is chosen so as for this term to be unity. A capacitor with dispersion (that is, whose value depends on frequency), C_{inf}, is introduced. A further capacitance, C_s allows for the effects of dispersion due to dipole relaxation within the double layer. Dipole relaxation has a time constant τ. Dipole relaxation may have a range of values – this is modelled by introducing an exponent α. In this model admittance is given by:

$$Y = \left\{ R + \frac{1}{(i\omega)^{\beta}\,\omega_0^{1-\beta}\left[\dfrac{C_s - C_{\inf}}{1+(i\omega\tau)^{\alpha}} + C_{\inf}\right]} \right\}^{-1} \qquad [2.44]$$

Hence α models the idealness of the capacitor dielectric (the double layer, which will often be composed of a number of different elements and molecules – each of which will have its own relaxation time). β models idealness of the interface between electrode and electrolyte. When $\beta = 1$, the surface is smooth. A value of 0.5 implies that the surface is ideally porous.

It should be noted that Martin and Lasia[14] have offered an alternative explanation for ϕ. A platinum electrode was deliberately roughened by electrochemical methods - this resulted in an increase in ϕ rather than the predicted decrease. This observation was explained by attributing the decrease of ϕ from ideality to adsorbed contaminants from solution – roughening the electrode surface has the effect of increasing the surface area and hence reducing the effect of adsorbed contaminants.

2.4.1 EIS in the Absence of an Electroactive Probe

The addition of an electroactive component to the electrolyte allows its interaction with the electrode to be investigated. This is clearly of interest when the electrode is coated with a film or membrane as the ability of the electroactive prode to access to the electrode surface can be characterised. In this manner pores and defects in the membrane can be analysed or the

activity of antimicrobial peptides such as melittin which are known to open pores in phospholipid membranes be investigated[15].

But what of the membrane itself? It has been pointed out that the charge transfer resistance of the electrochemical reaction via the membrane can be determined, but not the resistance of the membrane itself[16,17]. The membrane resistance and capacitance can be determined by EIS in the absence of an electroactive probe.

In the absence of any faradaic processes, a coated electrode will exhibit capacitance due to the film covering it and the electric double layer. Surface inhomogenities and adsorbed contaminants will cause the double layer to exhibit dispersion – it must be modelled with a CPE while the membrane in the simplest approximation can be modelled as a capacitor, C_m, and a resistor, R_m, in parallel. The equivalent circuit is shown in the inset in Figure 2.8.

The impedance of the CPE is given by the formula

$$Z = A(i\omega)^{-n} \qquad [2.45]$$

This relation is empirical[18]. A is dependent upon the properties of the electrode and electrolyte while n is dependent upon the surface roughness (or more precisely, fractal dimension, where the electrode surface possesses a surface dimension greater than two, but less than three) of the electrode. Hence when $n = 1$, the CPE behaves as an ideal capacitor. As the value of n decreases, the degree of surface roughness increases. The Nyquist plot of such a circuit is shown in Figure 2.8.

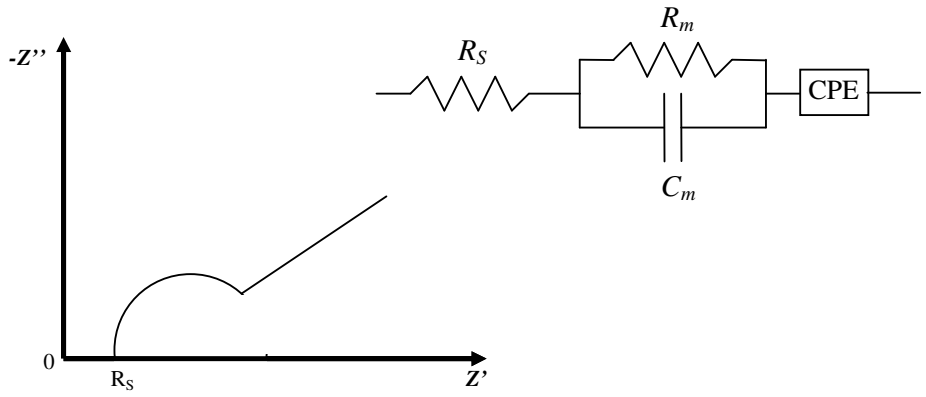

Figure 2.8: Nyquist plot for a membrane covered electrode in the absence of a faradaic reaction. The equivalent circuit is inset. As before, R_s is the solution resistance. R_m is the membrane resistance and C_m the membrane capacitance.

2.5 Principles of Polarisation Modulated Infrared Reflectance Spectroscopy

Infrared spectroscopy can give data about the conformation adopted by functional groups and their environment, such as the degree of solvation. PM-IRRAS is a surface selective technique that can provide additional information on the conformation assumed by infrared active moieties with respect to the surfaces that they are adsorbed onto.

2.5.1 Electromagnetic Waves

Electromagnetic radiation is composed of two oscillatory electric and magnetic field components arranged orthogonally to each other and perpendicular to the direction of propagation[19] (Figure 2.9).

In a vacuum, the electric field strength, E, at time t and at position x is given by the wave equation:

$$E = E_0 \cos(\frac{2\pi}{\lambda} x + \delta - \omega t) = \mathrm{Re}\left[E_0 \exp\left\{ -i\left(\frac{2\pi}{\lambda} x + \delta - \omega t \right) \right\} \right] \qquad [2.46]$$

E_0 = electric field amplitude

λ = wavelength

δ = phase shift

ω = angular frequency = $2\pi v$

v = frequency

The orientation of the electric field vector defines the polarisation. Unpolarised light may be considered to be the superposition of both horizontally and vertically polarised light.

It is also possible for the electric field vector to rotate with time: this yields circularly polarised light. The vector may rotate clockwise or anticlockwise, giving rise to clockwise or anticlockwise circularly polarised light.

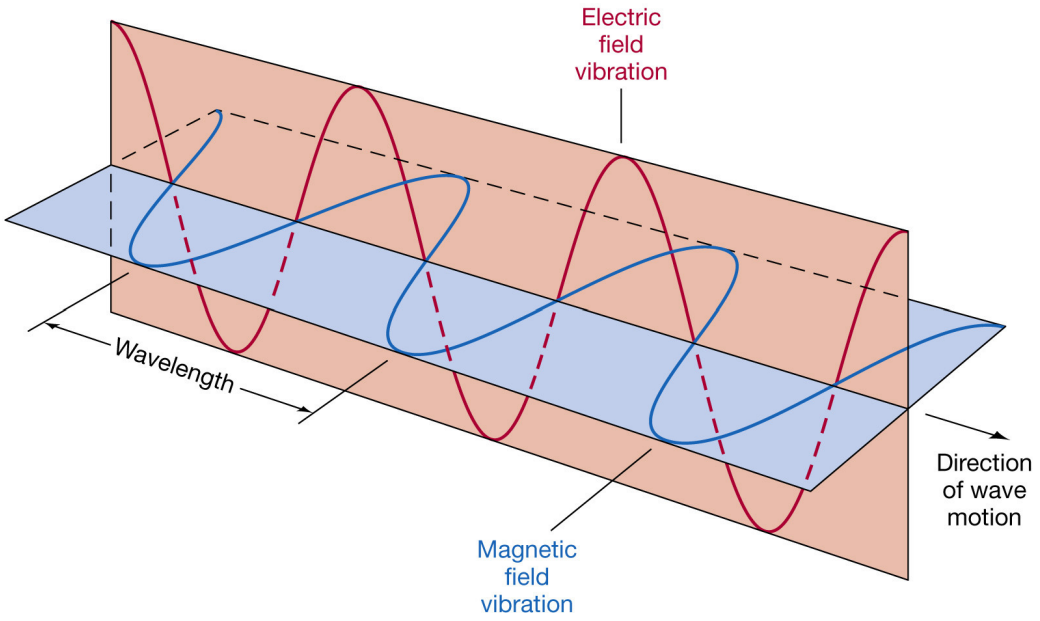

Figure 2.9: Orientation of the electric and magnetic fields of a propagating electromagnetic wave. (After Hecht[19]).

Any other medium will have electrons or other charges, hence is polarisable to some degree and thus can be expected to interact with the electric field. This has two major effects: to slow down or retard the propagation of the EM wave below that of c, the speed of light or propagation speed *in vacuo* and also to absorb some of the incident energy and hence reduce the magnitude of E_0.

The wave equation in this case becomes[19]:

$$E = \mathrm{Re}\left[E_0 \exp\left\{ -i\left(\frac{2\pi n}{\lambda} x + \delta - \omega t \right) \right\} \exp\left\{ -\frac{2\pi k}{\lambda} \right\} \right] \qquad [2.47]$$

where k is the extinction (or attenuation) coefficient and n is the refractive index.

The refractive index is determined by:

$$n = \frac{V}{c} \qquad [2.48]$$

where V is the propagation velocity. Hence the propagation velocity of light in water, where n = 1.333, is 2.00 x 10^8 m s^{-1}.

2.5.1 Electromagnetic Waves at Interfaces

At a boundary of two different media, electromagnetic radiation can either be reflected or transmitted into the second medium. In practice, both will typically occur. However, the ratio of reflected light to transmitted light depends on the angle of incidence and the difference in the refractive index across the interface (figure 2.10a).

When the interface is smooth – meaning that any surface irregularities are smaller than the wavelength of the incident light – specular reflection is observed[19]. As expected, the reflected EM wave obeys the law of reflection:

$$\theta_i = \theta_r \qquad [2.49]$$

The transmitted ray will be refracted in accordance with Snell's Law:

$$n_1 \cos\theta_i = n_2 \cos\theta_t \qquad [2.50]$$

where n_1 is the refractive index of the incident medium and n_2 that of the transmitted medium.

The amplitude of the reflected and refracted waves depends on the difference in refractive index across the interface and θ_i.

The transmission coefficient, T, is the ratio of transmitted light intensity to incident light intensity and is given by:

$$T = \frac{n_2 \cos\theta_t}{n_1 \cos\theta_r} \qquad [2.51]$$

Conservation of energy arguments allow the reflection coefficient, R, to be written as:

$$R = 1 - T = 1 - \frac{n_2 \cos\theta_t}{n_1 \cos\theta_r} \qquad [2.52]$$

In practice, infrared radiation with a wavelength greater than 3.3 μm (3000 cm^{-1}) was used in this work. This was sufficiently large compared to surface roughness that reflection remained in the specular regime.

2.5.2 Infrared Spectroscopy at Surfaces

There are a number of techniques that enable the spectra of species adsorbed at the electrode-electrolyte interface to be acquired[20].

Perhaps the simplest technique is attenuated total reflection spectroscopy (ATR). This consists of a Si or Ge hemisphere which transmits an IR beam and acts as an optical window into the cell. The radiation is totally reflected by the rear flat surface. The flat surface is coated with a very thin (several nanometres) polycrystalline metal electrode surface with the molecules of interest adhering to it. Total internal reflection causes an evanescent wave to propagate beyond the medium – hence the adsorbed molecules are subject to and can interact with the evanescent electric field.

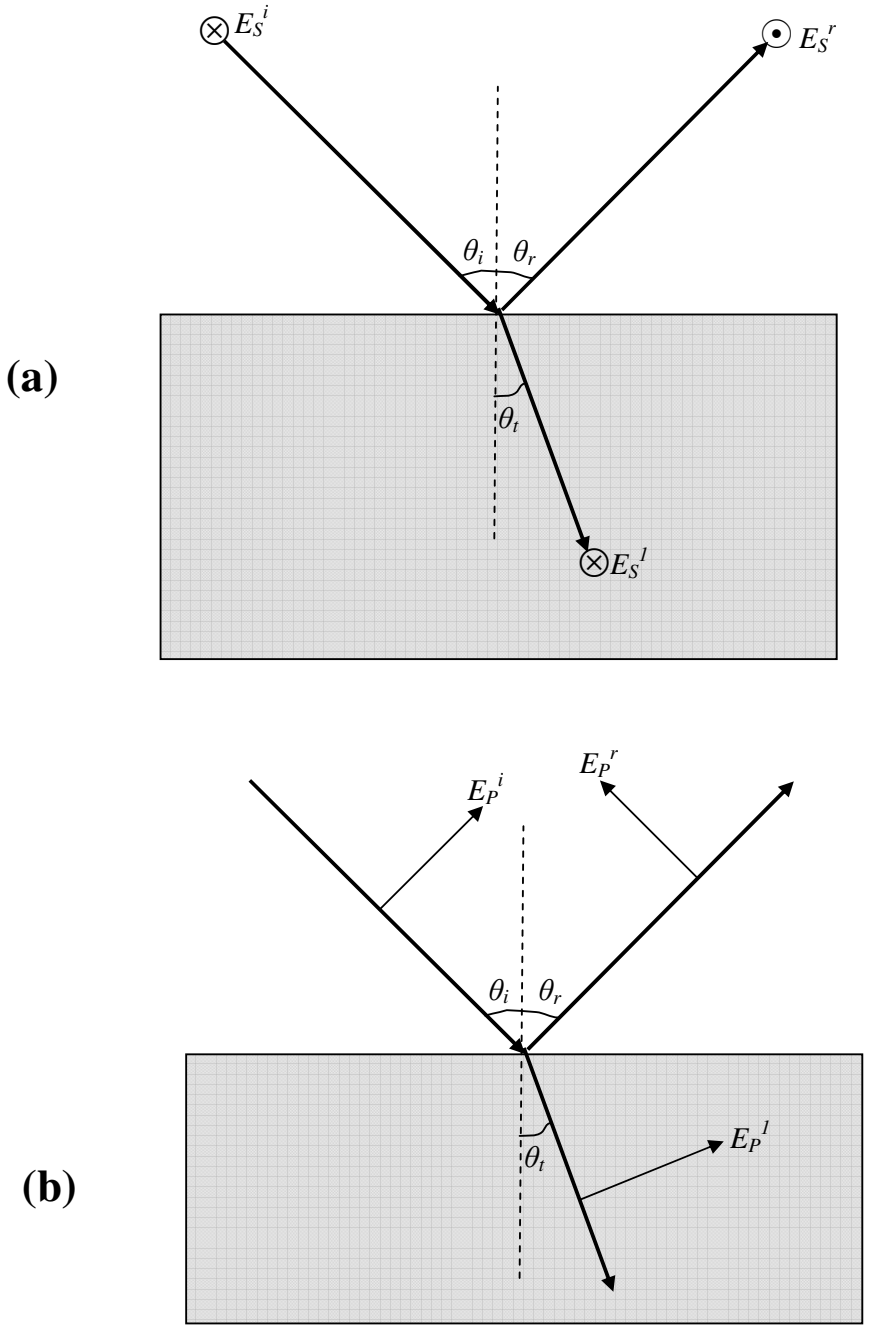

Figure 2.10: Reflection and refraction of an electromagnetic wave at an interface. (a) demonstrates the effect of s-polarised light at the same interface. Note that the electric field vector is transformed through 180°. (b) Shows the situation for p-polarised light (polarised perpendicularly to the interface).

Because the evanescent wave decays exponentially with the distance from the interface, this technique is highly selective for adsorbed species rather then the bulk electrolyte. The nature of the electrode – a metal (often Au) that has been evaporated onto the window surface and is thus polycrystalline – precludes investigations of adsorbed species on monocrystalline surfaces.

IR reflection absorbance spectroscopy (IRRAS) utilises a metal surface within a cell. In contrast to ATR, there is a gap between the electrode surface and the optical window which contains the electrolyte. In order to minimise absorption by the solvent, the gap between electrode and window is rather small – of the order of several μm. Despite this, solvent absorption still dominates in the acquired spectrum. In theory, it should be possible to acquire a background spectrum without the adsorbed species. The adsorbed species signal can then be found using the usual technique of background subtraction. In reality, it is very difficult to have conditions that are identical between both sample and background spectra.

It is possible to overcome this problem. The technique used in this work – polarisation modulated infrared reflectance absorption spectroscopy (PM-IRRAS) – is capable of selectively enhancing absorption of surface-bound species.

Upon reflection, the polarisation vector of light which is polarised parallel to the surface and perpendicular to the plane of incidence (s-polarisation) is reversed 180^{o} (figure 2.10a). Hence the incident and reflected rays will

undergo destructive interference at the metal surface. This results in an electric field magnitude that is close to zero. Thus s-polarised light will experience little absorbance at the electrode surface, but will still see absorption from the bulk solvent.

P-polarised light is parallel to the plane of incidence and thus has a vertical component to the surface. This vertical component suffers no transformation in direction upon reflection (figure 2.10b). Upon reflection, constructive interference between incident and reflected beams results in an enhancement in the electric field at the surface. Thus p-polarised light is more sensitive to adsorbed species than the bulk electrolyte. It must, however, be emphasised that the p-polarised signal will still contain absorption bands from the solvent *in addition* to those of the adsorbed species[20].

Switching rapidly between p and s-polarised light means that both signals are obtained under identical conditions. (This assumes that any changes to the system are slow compared with the switching speed of the polarisation. In practice, the polarisation direction was switched on the timescale of 10 μs, which is rapid compared with the rate of change of the phospholipid systems being investigated.) The signal from s-polarised light is sensitive to the solvent but not to the adsorbed species. Hence this signal can be used as the background signal lacking in conventional IRRAS. Simply subtracting this signal from the p-polarisation signal (which contains both the solvent background and the adsorbed species spectrum) will yield the contribution from the adsorbed molecules only.

Mid-infrared absorption absorption lines are due to vibrations of the component atoms in molecules. A trivial statement, perhaps, but not all vibrations are infrared active. To produce an absorption band, a bond must possess a permanent dipole moment. There must be an uneven distribution of charge across the atoms that compose the bond that exhibits infrared activity. The transition dipole moment is a vector quantity: it has direction as well as magnitude[21].

The dipole must be orientated parallel to the p-polarised light electric field dipole to produce an absorption band in PM-IRRAS. To take a simple example of this, consider carbon monoxide adsorbed onto a surface. The CO molecule has a permanent transition dipole (the oxygen atom has a slight negative charge relative to the carbon atom). The vector of this dipole is directed along the molecule's axis, parallel to the CO bond. Thus if the CO molecule is lying flat on the surface, the dipole vector is directed along the surface, orthogonal to the electric field vector of p-polarised light. Thus this molecule will not absorb p-polarised light and will not give rise to an absorption band in PM-IRRAS. On the other hand, a CO molecule that is vertically orientated will be active in PM-IRRAS because the charge dipole moment is directed vertically, parallel to the electric field of the incoming p-polarised light. It can thus be seen that PM-IRRAS is a powerful method for determining the orientation of surface bound molecules – or more strictly speaking, of the orientation of the transition dipole moments that give rise to the observed absorption lines.

2.5.3 Generating the Polarised Light Beams: the Photoelastic Modulator

This simple model so far outlined is idealised and omits some important details. Most importantly, the mechanism used to generate the polarised light beams introduces its own artefacts into the signal. These must be dealt with.

Some means of rapidly switching the incident beam from s to p polarisation is required. This is achieved by the use of a photoelastic modulator (PEM). The heart of a PEM is a crystal whose anisotropic optical properties can be modified at will.

An isotropic material is one whose properties are independent of direction. The refractive index experienced by an electromagnetic wave will be the same value independent of direction. Many crystals are anisotropic and their optical properties are dependent on direction. Birefringence is one effect of anisotropy. A birefringent material is one which has two different refractive indices, dependent on the polarisation of the incoming light ray. This effect causes the light ray to split into two different rays.

A birefringent material has an axis of symmetry, but no axis of symmetry perpendicular to this. This is known as the optical axis. Light which is linearly polarised parallel to the optical axis experiences a different refractive index to

light whose polarisation is orthogonal to the optical axis. Hence, an incident light ray is split into two separate rays with differing polarisations.

Isotropic materials may also exhibit birefringence when subject to an applied mechanical stress. In this case, the stress is sufficient to distort the material's symmetry so that it exhibits uniaxial anisotropy. This is the photoelastic effect[22]. A PEM makes use of this effect.

A PEM consists of an optical element that is glued to a piezoelectric transducer. Applying a voltage to a piezoelectric material causes a change in its dimensions (another example of anisotropic effects). It follows that applying a sinusoidal signal to the transducer produces a sinusoidal mechanical (acoustic) wave. The frequency of this wave is tuned to the resonant frequency of the long axis of the optical element: this allows for the greatest coupling of energy into the optical element.

A polariser is placed before the PEM and is oriented at 45^{o} to the optical axis. This produces two polarised components of equal intensity, one oriented orthogonally to the optical axis, the other parallel. With the optical element at rest – neither compressed or extended – both components pass through unchanged and the light beam emerges with its polarisation unaltered.

When the optical element is compressed, the perpendicular component remains unchanged, but the parallel polarised light ray experiences an increase in refractive index. This ray takes longer to traverse the optical

element and so emerges with a phase shift compared the unaltered perpendicular component. At maximum compression, the resultant phase shift is 90^{o} (figure 2.11). This phase shift results in a 90^{o} change in the orientation of polarisation of the emergent beam (remember that polarisation is a vector quantity, summing both components produces the change in direction). A phase shift of less than 90^{o} generates circular or elliptically polarised light.

The opposite occurs under extension: the parallel polarised component sees a decrease in refractive index at transits the PEM in a shorter time. This again results in a phase shift with respect to the perpendicular component. At maximum extension, the phase shift is 90^{o}: as with compression, this results in the exiting beam emerging with its polarisation being shifted by 90^{o}.

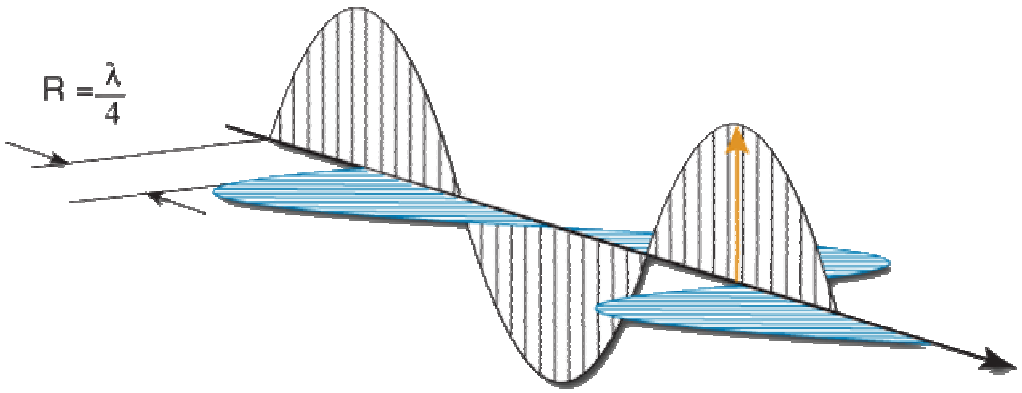

Figure 2.11: Quarter wave (90^{o}) phase shift of an electromagnetic wave by a PEM. Figure was taken from the Hinds Instruments documentation[22].

The PEM is energised by a sinusoidal acoustic wave. The optical element is compressed once in each cycle and likewise extended once per cycle. It therefore follows that the polarisation of the emergent beam changes at twice the fundamental frequency.

The static polariser in front of the PEM is oriented so that light polarised parallel to the optical bench is produced (figure 2.11). The PEM is orientated at 45° to this: the incident radiation can be considered to be composed of two perpendicularly orientated components I_{Ix} and I_{Iy} of equal magnitude. The phase shift, φ, introduced to the I_{Ix} component is given by:

$$\varphi = \varphi_0 \cos(\omega_m t) \qquad [2.53]$$

where ω_m is the operating frequency of the PEM and φ_0 the maximum phase shift, which itself depends on the wavelength, λ, and the applied voltage, V_m to the PEM. It can be found by[22]:

$$\varphi_0 = \frac{GV_m}{\lambda} \qquad [2.54]$$

G is a proportionality factor. The peak to peak amplitude of V_m is optimised to a particular frequency, λ_0 so that the maximum phase shift is π radians. Hence, substituting these into equation 2.53 yields:

$$\pi = \frac{GV_m}{\lambda_0} \qquad [2.55]$$

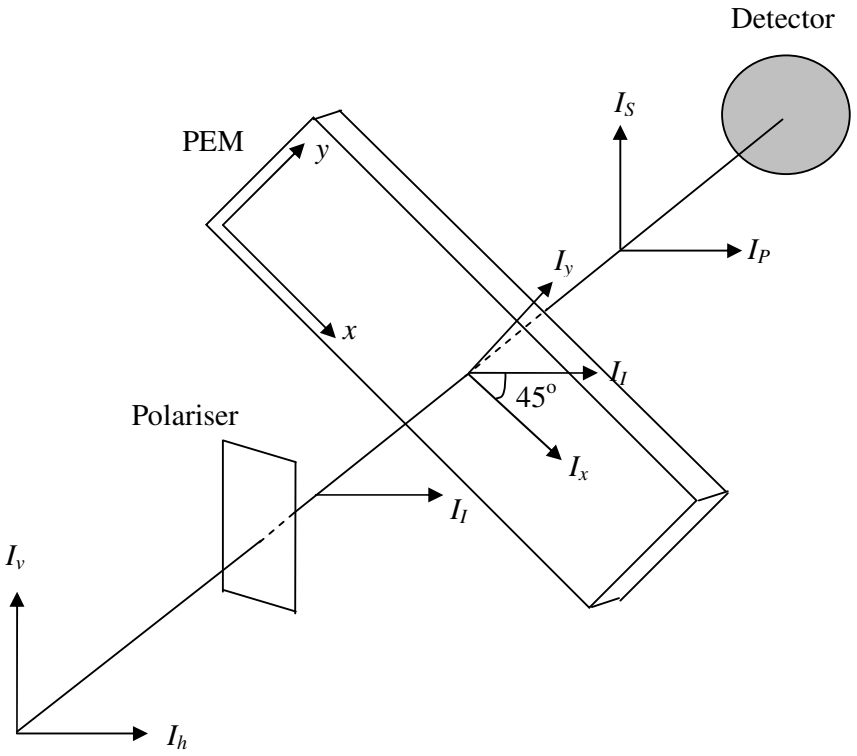

Figure 2.12: The PEM optical bench. Unpolarised light is passed through a polariser so that it becomes polarised, I_I, horizontally with respect to the optical bench. The PEM is orientated at 45°: Full retardation (or extension) results in a 90° phase shift, producing vertically polarised light.

Or, on re-arrangement: $GV_m = \pi V_m$

It can be shown that combining this with equation 2.52 gives:

$$\varphi = \frac{\lambda_0}{\lambda}\pi \cos\left(\omega_m t\right) \qquad [2.56]$$

It can also be shown that the signal at a detector, I_D, is given by the following relationship[21]:

$$I_D(\varphi) = \frac{I_s + I_p}{2} + \frac{I_s - I_p}{2}\cos(\varphi) \qquad [2.57]$$

where I_s is the component with parallel polarisation with respect to the surface and I_p the perpendicularly polarised component with respect to the surface.

Combining this expression with equation 2.56:

$$I_D(\varphi) = \frac{I_s + I_p}{2} + \frac{I_s - I_p}{2}\cos\left(\frac{\lambda_0}{\lambda}\pi\cos(\omega_m t)\right) \qquad [2.58]$$

There are two situations that need to be considered.

When $\omega_m t = (\frac{1}{2} \pm N)\pi$ where $N = 0,1,2,3,...$ [2.59]

The light beam is composed entirely of the perpendicularly polarised component: $I_D(t) = I_s$

When $\omega_m t = N\pi$ where $N = \pm 0,1,2,3,...$ [2.60]

$$I_D(t) = I_s + \frac{I_s - I_p}{2}\left[1 + \cos\left(\frac{\lambda_0}{\lambda}\pi\right)\right] \qquad [2.61]$$

In the special case that $\lambda = \lambda_0$ the second term vanishes, leaving:

$$I_D(t) = I_p \qquad [2.62]$$

Thus when the PEM has been optimised to the wavelength of the light incident upon it, the output will be linearly polarised light with p-polarisation only.

For light whose wavelength differs from λ_0, there will be an s-polarised component remaining. This will give rise to elliptically polarised light. For small departures from λ_0, this effect can be neglected.

The signal received at the detector is in theory composed of the average and difference signals between the two polarisations:

$$\frac{\Delta I}{I_{av}} = \frac{I_s - I_p}{(I_s + I_p)/2} \qquad [2.63]$$

where ΔI is the difference signal between the two polarised components and I_{av} the average signal.

In practice, the signal varies between s and p polarisation at twice the operating frequency of the PEM. This must be demodulated to recover the difference and average signals.

The simplest technique is to use a lock-in amplifier set to $2\omega_m$ to recover the second harmonic signal from the detector[23]. It can be shown[24] that this signal is related to ΔI by the following:

$$I_D(2\omega_m) = \Delta I \cdot J_2(\varphi_0) \qquad [2.64]$$

$J_2(\varphi_0)$ is the second order Bessel function of the maximum phase shift introduced by the PEM.

I_{av} can be recovered by passing the detector output through a low pass filter. Hipps and Crosby[24] derived the relationship:

$$I_D(0) = I_{av} + \frac{\Delta I}{2} \cdot J_0(\varphi_0) \qquad [2.65]$$

$I_D(0)$ is the output of the low pass filter and $J_0(\varphi_0)$ is the zero order Bessel function of φ_0.

Substituting equations 2.62 and 2.63 back into 2.61, yields:

$$\frac{\Delta I}{I_{av}} = \frac{I_D(2\omega_m)}{I_D(0)} = \frac{\Delta I \cdot J_2(\varphi_0)}{I_{av} + \frac{1}{2}\Delta I \cdot J_0(\varphi_0)} \qquad [2.66]$$

It is usual to use a highly reflective metal surface in reflectance spectroscopy (which is somewhat advantageous in ensuring adequate signal to noise). In this situation, $\Delta I << I_{av}$ and $J_0(\varphi_0) \leq 1$. This allows equation 2.64 to be simplified:

$$I_D(t) = \frac{\Delta I}{I_{av}} \cdot J_2(\varphi_0) \qquad [2.67]$$

Thus the output of this setup is the desired PM-IRRAS signal multiplied by a second order Bessel function.

When $\lambda = \lambda_0$, the phase shift is 90°, or $\pi/4$. $J_2(\pi/4) \approx 0.5$ meaning that the signal obtained using this technique is half that of the maximum theoretical signal.

$J_2(\varphi_0)$ itself varies as the wavelength:

$$J_2(\varphi_0) = J_2\left(\frac{\lambda_0}{\lambda}\pi\right) \qquad [2.68]$$

This will introduce a systematic error for all wavelengths other than λ_0. Close to λ_0, this error is small.

A second method developed by Green *et al* makes use of a synchronous sampling demodulator (SSD) to recover higher order harmonics of the PEM frequency in addition to the second order $2\omega_m$ signal[25]. The SSD is controlled by the reference oscillator signal from the PEM controller in order to determine when perpendicularly polarised light reaches the detector (when Equation 2.59 is satisfied) and when s-polarised light reaches the detector (when the conditions of Equation 2.60 are met). At these times, the detector output is sampled, generating two signals.

The first is the intensity average signal, $I_D^{av}(2\omega_m)$:

$$I_D^{av}(2\omega_m) = I_{av} + \frac{\Delta I}{2}\left\{\frac{1+\cos\varphi_0}{2}\right\} \qquad [2.69]$$

The second is the intensity difference signal, $I_D^{Diff}(2\omega_m)$:

$$I_D^{Diff}(2\omega_m) = \Delta I\left\{\frac{1-\cos\varphi_0}{2}\right\} \qquad [2.70]$$

It can be shown that the PM-IRRAS spectrum is given by:

$$\frac{\Delta I}{I_{av}} = \frac{\Delta I\{(1-\cos\varphi_0)/2\}}{I_{av} + 0.5\Delta I\{(1+\cos\varphi_0)/2\}} \qquad [2.71]$$

It can be shown that the output of Equation 2.69 approaches the ideal value given by Equation 2.63 as λ tends to λ_0. Hence the use of a SSD yields an improved signal to noise ratio over the lock-in amplifier.

The PEM introduces artefacts into the PM-IRRAS spectra that must be removed before useful data can be gleaned. It is possible, at least in theory to calculate these artefacts and hence remove them. This is not a practical proposition, as some variables, such as non-linearities in the PEM crystal are not well defined and hence impossible to model to an acceptable degree of accuracy.

The obvious approach is to take a background spectrum in the absence of any adsorbed molecules under identical conditions. The background spectrum must be normalised to the experiment spectrum. This has the obvious drawbacks that it is extremely difficult to reproduce exactly the same conditions as the experiment. In particular, the empty cell must be in the same position as the experiment cell. Deviations even of the order of a few μm will affect optical throughput sufficiently to introduce significant errors. It can be shown that under such conditions, the normalised spectrum is given by the relation[26]:

$$\frac{\Delta S}{S} = \frac{S(d) - S(0)}{S(0)} = \frac{2\eta R_P(0) R_S(0)}{R_S^2(0) - \eta R_P^2(0)} A \qquad [2.72]$$

S is the PM-IRRAS spectra normalised to the background, (d) is the experiment spectra, (0) the background. η is the optical efficiency for p-polarised light normalised to the optical efficiency of s-polarised light. R_P is the

reflectance of the metal substrate for p-polarised light, R_S the substrate reflectance for s-polarised light. A is the absorbance observed in experiment.

To obtain a solution to this equation requires precise knowledge of the optical setup. It is no trivial task to do this: in particular, the optical efficiency is difficult to measure and is acutely sensitive to the exact setup.

A superior method of handling these artefacts is to record an independent spectrum which will contain only these variables[27]. This can be done by performing an experiment where a second polariser is placed after the PEM. Buffeteau et al[25] have derived an analytical expression for this situation:

$$A = 1 - \frac{\eta R_P(d)}{R_P(0)} \approx 1 - \frac{\eta R_P(d)}{R_S(d)} = 1 - \frac{C_{PP}\left(\frac{g}{g'}C_{PS} - S(d)\right)}{C_{PS}\left(\frac{g}{g'}C_{PP} + S(d)\right)} \qquad [2.73]$$

C_{PP} and C_{PS} are calibration spectra where the polariser emplaced after the PEM is set to admit p- or s-polarised light respectively. g is the gain of the lock-in amplifier during experiment and g' the gain during acquisition of the calibration spectra.

Buffeteau[28] showed that the calibration spectra are given by:

$$C_{PP} = \frac{g'|J_2(\varphi_0)|}{1 + J_0(\varphi_0)} \qquad [2.74]$$

and

$$C_{PS} = \frac{g'|J_2(\varphi_0)|}{1 - J_0(\varphi_0)} \qquad [2.75]$$

This method was used in this work, but with modifications[27]. By taking two calibration spectra it is possible to replace the cosine terms in Equation 2.70 with acquired calibration spectra.

By running the spectrometer with the PEM switched off and a second polariser set to pass p-polarised light placed just after the PEM it was possible to measure the a reference spectrum in p-polarised light. This spectrum is the throughput of p-polarised light, I_p through the optical system.

The PEM was then turned on and two spectra were acquired. The first is the zero order calibration spectrum CJ_0 which is related to the average signal, $(I_s + I_p)/2$, while the second is the second order calibration spectrum CJ_2 which is the difference signal $(I_s - I_p)$. Hence the experiment PM-IRRAS signal is given by:

$$\frac{I_D(2\omega_m)}{I_D(0)} = \frac{\Delta I \cdot CJ_2}{I_{Av} + 0.5\Delta I \cdot CJ_0} \qquad [2.76]$$

$I_D(2\omega_m)$ is the intensity difference signal determined in experiment after demodulation and $I_0(0)$ is the experiment average signal after demodulation. Hence the acquisition of these calibration spectra allows the PM-IRRAS signal to be recovered without having to determine the exact phase shift imparted by the PEM.

2.5.4 The Fourier Transform Infrared Spectrometer

The heart of the PM-IRRAS system is a Fourier Transform Infrared Specctrometer (FTIR). This differs considerably in operation from the familiar dispersive instruments that operate in the UV-Vis. As will be seen, FTIR confers significant advantages[29].

A FTIR is constructed round a Michelson interferometer (figure 2.13)[29]. A Michelson interferometer is composed of a light source, a 50/50 beam splitter, a fixed mirror and a movable mirror.

First if the simple case of monochromatic light is considered, it is clear that constructive interference will take place if the path difference, Δd, between the two arms is zero. Altering the position of the movable mirror slightly (by less than the wavelength of the light used, λ) will change the path difference so that destructive interference occurs. Hence, if an observer peers through an eyepiece placed at the output of the interferometer, a series of interference fringes will be observed marching across the field of view. The number of fringes that appear in unit time is dependent upon the velocity of the moving mirror.

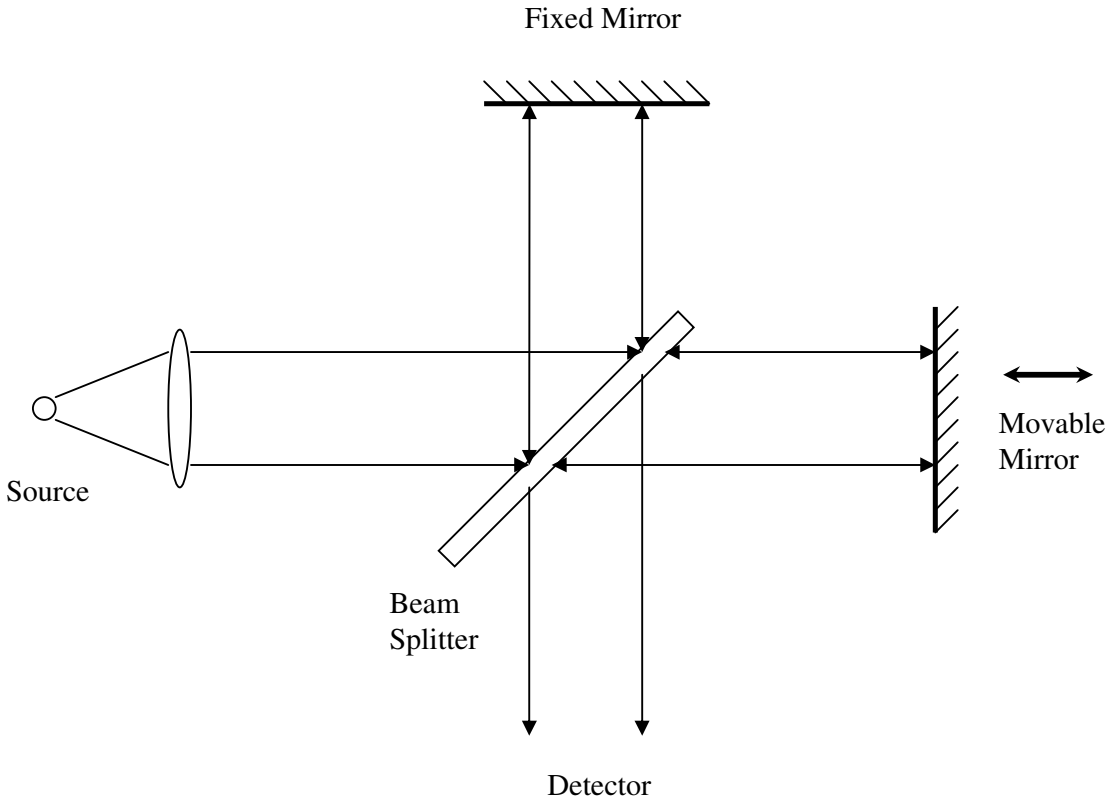

Figure 2.13: The Michleson interferometer. Light from the source is divided by the beam splitter and sent down each arm of the interferometer. A movable mirror in one arm allows the path difference to be varied.

The condition for constructive interference is:

$$\Delta d = n\lambda \qquad [2.77]$$

For destructive interference, it is simply:

$$\Delta d = \left(\frac{1}{2} + n\right)\lambda \qquad [2.78]$$

where $n = 0,1,2,3,\ldots$

If the wavelength of the light source is known, counting fringes allows the distance that the movable mirror has travelled to be determined accurately.

Should the light source emit light composed of two wavelengths, each will produce its own set of interference fringes. A broadband (or white light) source emits light of a very large number of wavelengths: each, therefore, will produce a set of interference fringes. The output of the Michelson interferometer may be considered to be a superposition of all the wavelengths present in the light source.

Placing an absorbing material in front of the detector means that the absorber superimposes its absorption spectrum on top of the light source spectrum. Hence the pattern of fringes recorded by the detector, called an interferogram, contains information about the absorption spectrum of the absorbing material.

The interferogram must be processed to recover the desired data. Firstly, it should be noted that the maximum path difference is equal to twice the maximum travel of the moving mirror, a quantity denoted d_{max}. Retardation, δ, may be defined as the path difference: that is, $\delta = \Delta d$. The interferogram intensity, I, is a function of the path difference and wavenumber of the incident light:

$$I(\delta) = \int_0^\infty B(\bar{\nu})\cos(2\pi\bar{\nu}\delta)d\bar{\nu} \qquad [2.79]$$

Spectroscopists traditionally use reciprocal units of wavelength, wavenumber, $\bar{\nu} = 1/\lambda$, rather than wavelength itself as the magnitude of this unit varies directly with energy. Units of cm^{-1} are a conveniently sized magnitude.

$B(\bar{\nu})$ denotes the intensity of the source when corrected for the distortions imposed by the beam splitter and detector. Fourier theory states that any signal can be regarded as being composed of the sum of a series of sinusoids. Hence, Fourier transformation of Equation 2.79 will recover the spectrum[29]:

$$B(\bar{\nu}) = \int_{-\infty}^{\infty} I(\delta)\cos(2\pi\bar{\nu}\delta)d\delta \qquad [2.80]$$

This assumes that $\delta \to \infty$: not quite a practical proposition. Hence real instruments produce a truncated interferogram. This truncation results in $B(\bar{\nu})$ being distorted: sharp absorption lines will display subsidiary wiggles ("ringing"). Apodization is a mathematical technique used to overcome this problem. This procedure multiplies the interferogram with a function that goes smoothly to zero at a finite value, thus values of the interferogram at high values of δ are reduced and the interferogram falls to zero at a finite value. This removes distortion, but decreases resolution somewhat.

Equation 2.80 requires the interferogram to be measured for negative values of δ. To reduce acquisition time and interferogram size, only the positive half of the interferogram is measured. It is assumed that the interferogram is symmetrical about the origin. This assumption allows Equation 2.80 to be rewritten:

$$B(\bar{v}) = 2\int_0^{\infty} I(\delta)\cos(2\pi\bar{v}\delta)d\delta \qquad [2.81]$$

Unfortunately, truncation of the interferogram distorts the symmetry about the origin. Phase correction is employed to handle this issue.

The resolution, *R*, of a FTIR is dependent upon its maximum path difference:

$$R = \frac{1}{2d_{\max}} \qquad [2.82]$$

This assumes that light rays travelling through the spectrometer are perfectly collimated. This is not achievable in practice, thus resolution will be less than that predicted by Equation 2.82.

This may all seem rather complicated but FTIR confers significant advantages: the first is that the entire spectrum is acquired simultaneously, resulting in a significant decrease in acquisition time (Fellgett's Advantage). This is of particular importance when relatively fast phenomena or short lived species are being investigated.

A FTIR does not require slits, unlike a conventional dispersive instrument. This leads to greater optical throughput. This allows for greater signal to noise, particularly in the mid to far infrared where sources are less intense and detectors less sensitive when compared with the near infrared. This is Jacquinot's Advantage.

Weak signals may be further enhanced by combining interferograms. It is common to record many hundreds or even thousands of scans and combine

the resultant interferogram into one. This has the advantage of improving the S/N ratio as this quantity is dependent upon the number of scans:

$$S/N \propto \sqrt{N} \qquad [2.83]$$

where *N* is the number of scans. Hence increasing the number of scans – and the acquisition time – by a factor of four will yield a two fold improvement in signal to noise ratio.

The path difference must be known. In practical FTIR spectrometers, it is measured by sending laser light down through the interferometer along the optical path. The fringes generated by the laser are detected and counted by the spectrometer electronics – this allows the path difference to be determined. The wavelength of the laser is known to a high degree of accuracy. Hence the determination of wavelength in the spectrometer is by reference to a frequency source of known accuracy – which means that the wavelengths of any features observed are thus accurately determined. This is the last major advantage of FTIR – Conne's Advantage.

2.6 Neutron Reflectometry

Reflectometry is a technique whereby a beam of monochromatic radiation is reflected from a surface. Clearly, information about the smoothness of the surface can be found in this manner. However, if the sample is transparent to the radiation, reflection will also occur at interfaces below the surface: thus data about the nature of any buried layers can be found. We thus have a

powerful non-destructive technique for gaining information about the structure of our sample.

The radiation need not be electromagnetic in nature – this section describes the use of neutrons in this technique – but it must be monochromatic. It thus follows that the neutrons must all possess similar kinetic energy.

There are three possible outcomes for radiation that is incident upon a surface[19]:

1) It may be reflected (elastic scattering)
2) It may pass into the bulk of the material
3) Some (or all) energy may be transferred to the sample (inelastic scattering).

Which process takes place depends on a large extent upon the incident angle of the radiation. At a grazing angle of incidence, all radiation is reflected. At some critical angle, some radiation begins to penetrate into the bulk of the material. The magnitude of this critical angle depends on the material: for visible light, it is dependent upon the change in refractive index across the surface.

Reflectometry is concerned with the first outcome, where incident radiation is reflected specularly, where the angle of incidence, θ_i, equals the angle of reflectance, θ_r. The basic premise of neutron reflectivity is that a beam of

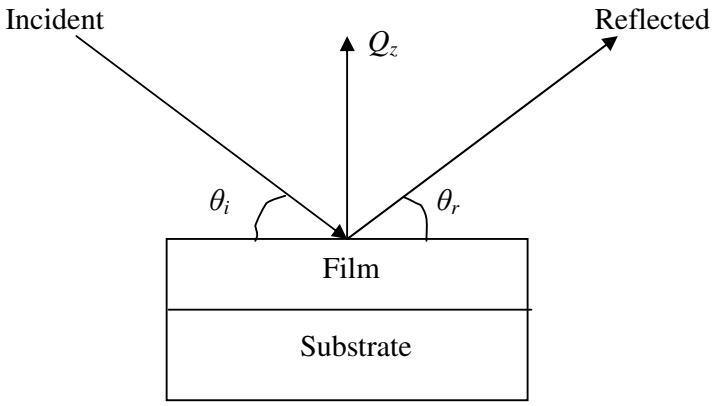

Figure 2.14: The geometry of specular reflection. $\theta_i = \theta_r$. Q_z is the resultant momentum transfer in the *z* axis and is in the plane of reflection

monochromatic neutrons is reflected by a large, flat surface and the specular reflection intensity is measured with respect to either angle or wavelength.

Mathematically and geometrically, neutron reflection is identical to optical reflection (see Figure 2.14); but it is more convenient to use scattering length density (SLD), ρ, and momentum transfer, Q.

Since momentum is a vector quantity, reflection necessarily involves a change in the momentum of the reflected neutrons: this gives rise to the observed momentum transfer. For a grazing angle of incidence, θ, momentum transfer is given by:

$$Q = \frac{4\pi \sin\theta}{\lambda} \qquad [2.84]$$

where λ is the neutron wavelength.

The SLD is related to the refractive index of the material, n, by:

$$n^2 = 1 - \frac{\lambda^2}{\pi}\rho \qquad [2.85]$$

The SLD depends on the nature and concentration of nuclei found in the sample. It can be calculated from the summation of the nuclei present:

$$\rho = \sum_i b_i n_i \qquad [2.86]$$

where b_i is the scattering length and n_i the number density of nuclear species i. The scattering length, and hence the SLD, does not vary in any regular pattern throughout the periodic table, in contrast to X-rays, where the SLD increases steadily with Z. Indeed, SLD can vary substantially by isotope of the same element. The most prominent example of this is hydrogen[30], where b_H = -3.74 x 10^{-5} Å and b_D = 6.67 x 10^{-5} Å. In practice, this means that deuterated and hydrogeneous compounds have very different contrasts – a fact that can be extremely useful when interpreting results.

In the case of specular reflection, reflection, R_f, from a smooth surface is given by Fresnel's Law[29]:

$$R_f = \left[\frac{Q_z - (Q_z^2 - Q_c^2)^{1/2}}{Q_z + (Q_z^2 - Q_c^2)^{1/2}}\right]^2 \qquad [2.87]$$

where Q_c is the critical value of momentum transfer for total reflection and Q_z the value of momentum transfer in the z direction. It can be found from the equation:

$$Q_c = \frac{4\pi}{\lambda}(1 - \cos^2\theta_c)^{1/2} = (16\pi\Delta\rho)^{1/2} \qquad [2.88]$$

θ_c is the critical angle: below this the neutron beam is reflected. $\Delta\rho$ is the change in SLD across the interface.

Most measurements are made where Q_z is much larger than Q_c. In this situation, the reflectivity can be approximated by:

$$R_k \approx \frac{16\pi^2}{Q_z^4}\Delta\rho^2 \qquad [2.89]$$

where R_k is the reflectivity in the kinematic approximation. It is immediately apparent that reflectivity declines sharply with Q above the critical edge: below the critical edge reflectivity is unity.

Structural information relating to the interface is contained in the curve above the critical edge. If the approximation where R_f is replaced by R_k, and expressed in terms of Q is used:

$$R_Q = R_f(Q)\,|\,Q_z(Q)|^2 \qquad [2.90]$$

$R_f(Q)$ is the Fresnel reflectivity term and predicts that the reflected beam intensity falls to the fourth power of Q above the critical edge. The term $Q_z(Q)$ is the film factor and is the Fourier transform of the variation of the SLD with respect to the z axis. A step change in the SLD will produce a ripple in the decreasing beam intensity as Q is increased whose period depends inversely on the thickness of the step and amplitude depends on the magnitude of $\Delta\rho$. These oscillations will be damped out with increasing Q if the interface is rough. A more complicated system with multiple layers will generate a more complicated oscillation, being the superposition of the waves produced by

each individual layer. In this case, modelling is required. A major benefit is that both the thickness and composition can be determined in this manner.

As reflectivity falls as Q^4 due to Fresnel effects, log (R) versus Q is usually plotted. Any superimposed ripples can then be readily seen. Figure 2.15 shows a typical reflectivity curve plotted against Q. The dependence of R on Q^4 can clearly be seen. The large fringes are due to a 200 Å thick gold layer.

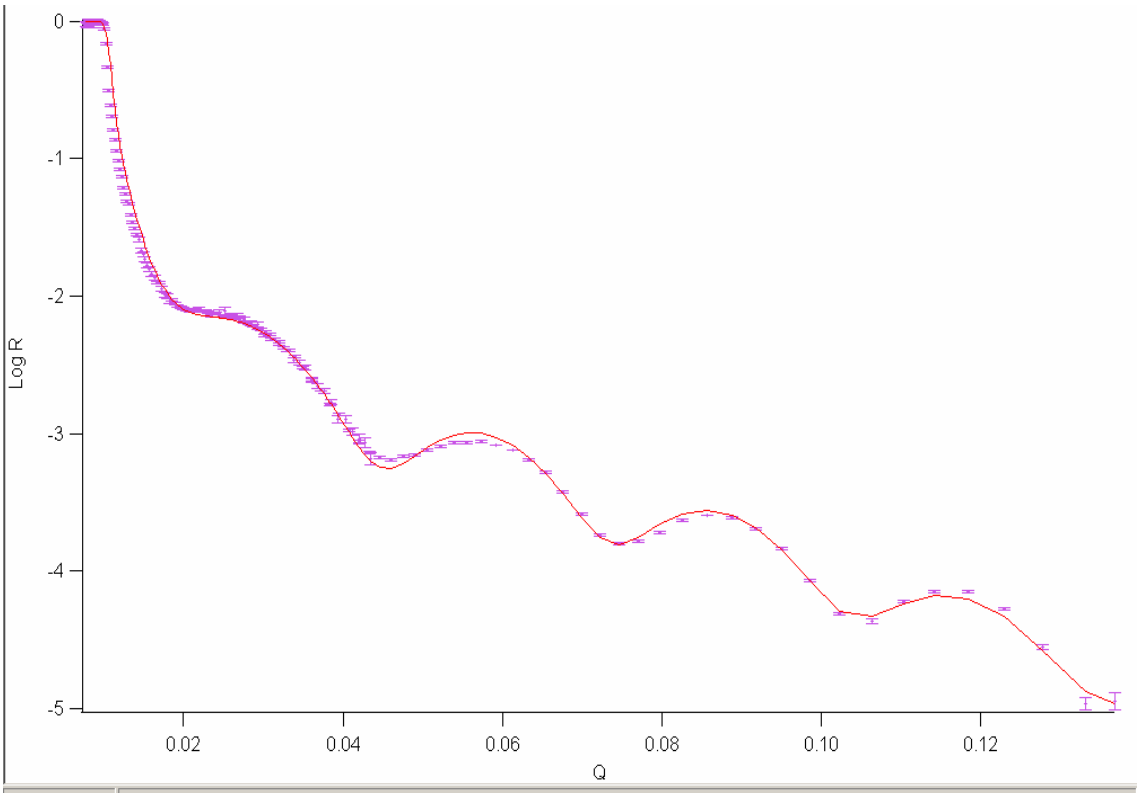

Figure 2.15: Neutron reflectivity curve for a hydrogenous DMPE/DMPS lipid bilayer in D_2O at a potential of +0.15 V (points with error bars). The solid line is a fitted curve to the data generated by *Motofit*[31].

2.7 References

1. Aveyard, R., Haydon D. A., 1973, *An Introduction to the Principles of Surface Chemistry*, Cambridge University Press

2. Rosen, M. J., 2004, *Surfactants and Interfacial Phenomena*, 3rd edition, John Wiley

3. Fisher, A. C., 1996, *Electrode Dynamics*, Oxford University Press

4. Grahame, D. C., (1947), *Chem Rev*, **41**:441

5. Halliday, D., Resnick, R., 1978, *Physics*, 3rd edition, John Wiley

6. Bard, A. J., Faulkner, L. R., 2001, *Electrochemical Methods, Fundamentals and Applications*, 2nd edition, John Wiley

7. Lipkowski, J., Schmickler, W., Kolb, D. M., Parsons, R., (1998), **452**:193

8. Lipkowski, J., Stolberg, L., 1992, *Adsorption of Molecules at Metal Electrodes*, ed J Lipkowski and P N Ross, Wiley-VCH, p171

9. Lasia, A., 1999, *Electrochemical Impedance Spectroscopy and Its Applications, Modern Aspects of Electrochemistry*, ed: B E Conway, J Bockris, R E White, Vol. 32, Kluwer Academic/Plenum p143

10. Randles, J. E. B., (1947), *Far. Discussions*, **1**:12

11. Cole, K. S., Cole, R. H., (1941), *J. Chem. Phys.*, **9**:341

12. Brug, G. J., Van Den Eeden, A. L. G., Sluyters-Rehbach, M., Sluyters, J. H., (1984), *J. Electroanal Chem.*, **176**:275

13. Whitehouse, C., O'Flanagan, R., Lindholm-Sethson, B., Movaghar, B., Nelson, A., (2004), *Langmuir*, **20**:136

14. Martin, M. H., Lasia, A., (2011), *Electrochimica Acta*, **56**:8058

15. Becucci, L., Leon, R. R., Moncelli, M. R., Rovero, P., Guidelli, R., (2006), *Langmuir*, **22**:6644

16. Lindholm-Stethson, B., (1996), *Langmuir*, **12**:3305

17. Gafni, Y., Weizman, H., Libman, J., Shanzer, A., Rubinstein, I., (1996), *Chem. Eur. J.*, **2**:759

18. Levie, R. D., (1989), *J. Electroanal. Chem.*, **261**:1

19. Hecht, E., 2003, *Optics*, 4th edition, Pearson

20. Lipkowksi, J., Ross, P. N., 1999, *Imaging of Surfaces and Interfaces*, Wiley-VCH

21. Herzberg, H., 1989, *Molecular Spectra and Molecular Structure: I. Spectra of Diatomic Molecules*, Krieger

22. Hinds Instruments, www.hindsinstruments.com/knowlege-center/technology-primer/pem-100photoelastic-modulation/principles-of-operation, retrieved on 6/8/2011

23. Golden, W. G., Dunn, D. S., Overend, J., (1981), *J. Cat*. **71**:395

24. Hipps, K. W., Crosby, G. A., (1979) *J. Phys. Chem*. **83**:555

25. Green M. J., Barner, B. J., Corn, R. M., (1991), *Rev. Sci. Instrum.*, **62**:1426

26. Buffeteau, T., Desbat, B., Turlet, J. M., (1991) *Appl. Spec*. **45**:380

27. Zamlynny, V., PhD Thesis, University of Guelph (2002)

28. Buffeteau, T., Desbat, B., Blaudez, D., Turlet J. M., (2000), *Appl. Spec*. **54**:1646

29. Stuart, B. H., (2004), *Infrared Spectroscopy: Fundamentals and Applications*, John Wiley

30. Penfold, J., Thomas, R. K., (1990), *J. Phys – Condensed Matt*, **2**:1369

31. Nelson, A., (2010), *J. Phys.: Conf. Ser.* **251**:012094

3. Materials and Methods

3.1 Materials

Sodium fluoride, Suprapur grade, was supplied by Merck. Lipids were supplied by Avanti Polar Lipids. DMPS was supplied as the sodium salt. Potassium chloride, Analar grade, was obtained from BDH.

Lipids were dissolved in a mixture of 10% methanol (HPLC grade, Fisher) in chloroform (HPLC grade, Fisher). The solution was stoppered, wrapped in aluminium foil and finally wrapped with parafilm to prevent both contamination and evaporation. The prepared solution was kept in a freezer to reduce degradation and evaporation.

Potassium ferrocyanide (ultrapure grade) was obtained from Fluka. Hexamineruthenium (III) chloride, minimum 98% purity, was supplied by Alfa Aesar. Ultrapure water was supplied by a Millipore MilliQ Elix/Gradient A10 (Millipore,France) water purifier whose output had total organic content less than 5 ppb and resistivity greater than 18 MΩ cm.

3.2 Cleaning

The molecules being investigated adsorb relatively weakly to the electrode surface. Hence it is all too possible for the lipids to be displaced by

contaminant species. Given the limited electrode area available, the possibility exists that even very low concentrations of unwanted adsorbants could mask the effects that are being investigated. Sources of contamination include fingerprints, pollen and spores from the atmosphere, organic residues and dust. Scrupulous cleanliness is therefore essential.

Two different cleaning protocols were used, depending on which cell was used. All glassware, including the cell used for differential capacitance and chronocoulometry was cleaned by immersion in an acid bath (50% concentrated nitric acid, 50% concentrated sulphuric acid, supplied by Fisher) which was then placed on a hot plate set to 250^{o}C. This process ensured any organic residue was oxidised. After cooling, glassware was carefully rinsed multiple times with ultrapure water. The cell was then assembled, filled with ultrapure water and sealed with aluminium foil from atmospheric contamination. The cell was left to soak overnight in order to remove any acid adsorbed onto the glass surface. The cell was rinsed once more immediately before use.

The Teflon impedance cell was cleaned by immersion in a solution of concentrated ammonia mixed with 30% hydrogen peroxide in a 1:1 ratio (both supplied by Fisher) and left to stand for a minimum of five hours, more often overnight. The cell was then rinsed as before with copious amounts of ultrapure water and left to stand for several hours filled with ultrapure water and wrapped in aluminium foil. Again, the cell was rinsed with ultrapure water immediately before use.

3.3 Electrode Preparation

The working electrode (WE) was a monocrystalline block of high purity (99.999%) gold with one face cut to expose the (111) surface (supplied by Metal Crystals and Oxides Ltd, Cambridge, UK). This surface is relatively hydrophilic (more so than polycrystalline Au or Hg, which are considered to be hydrophobic) with few defects and so is suitable for use as the bilayer substrate. In order to maintain a high quality surface, the working electrode was flame annealed. Annealing involves heating the surface to the point where the surface atoms become sufficiently mobile that they reorientate themselves into a clean (111) face, thereby reducing surface roughness or defects.

After being rinsed in ultrapure water, the working electrode was placed on a clean quartz plate where it was then heated with a microbunsen flame until dull red heat (approximately 550-600 ^{o}C). It was maintained at this temperature for 7 minutes. After this step, it was allowed to cool for two minutes and then flooded with ultrapure water in order to ensure the electrode was at room temperature. The working electrode was gently heated to evaporate the water then flooded a second time so that the (111) face was protected by a droplet of water to prevent atmospheric contamination. The electrode was then placed in a Teflon holder, connected to a high purity gold wire to enable electrical connection and placed in the cell.

The counter electrode (CE) was a 99.999% pure gold wire coil. It was rinsed in ultrapure water in order to remove any impurities before being flamed to red heat in a microbunsen flame and quenched with ultrapure water. It was placed in the cell immediately after this procedure in order to minimise the risk of contamination. The reference electrode was a saturated calomel electrode (SCE) supplied by Radiometrics, UK.

3.4 Bilayer Preparation

Two different methods were used to produce lipid bilayers. Both protocols are described in detail below.

3.4.1 Vesicle Fusion

The first method involved manufacturing a solution containing lipid vesicles. When introduced into the electrochemical cell, the vesicles were left to incubate and spread across the electrode surface.

It was found that 0.25 ml of 6.27 g l^{-1} (0.01 M) DMPS solution contained sufficient molecules to make a good quality bilayer. 2 g l^{-1} DMPS solution and 1.8 g l^{-1} solution of DMPE (2.8 mM for both solutions) were mixed in the appropriate proportions to make DMPE/DMPS mixtures. 0.5 ml of this mixed solution was found sufficient to produce a good quality bilayer.

This volume of lipid solution was placed in a scrupulously cleaned test tube (the cleaning protocol is outlined in Section 3.2). It was then vortexed at approximately 1800 rpm under a stream of dry nitrogen for ten minutes in order to remove the solvent and form an even lipid coating over the inner surface of the test tube.

The dry test tube was then placed in a desiccator which was then evacuated in order to remove the last traces of solvent. After a minimum of two hours the test tube was removed from the desiccator and approximately 2 cm^3 of 0.1 M NaF electrolyte was added.

The aqueous lipid solution was then incubated at 40 ^oC in an ultrasonic bath. It was sonicated for at least one hour in order to form vesicles. The success of this operation was indicated by the solution appearing clear after sonication – an indication that the vesicles are too small to scatter visible light. Sonication was continued right up to the point where the vesicle solution was introduced into the electrochemical cell by means of a clean Pasteur pipette. This ensured that the formation of large multilamellar vesicles was minimised.

Once introduced into the cell, the electrolyte was left for at least an hour in order to give the vesicles time to spread onto the surface. It is believed that a bilayer is formed through a process of vesicle fusion. Vesicles striking the exposed substrate will unravel and spread onto the surface (figure 3.1). Distribution is random so coverage cannot be expected to be complete.

The process is thus analogous to the coating of the ground with a dusting of snow: patchy distribution can be expected to be the result.

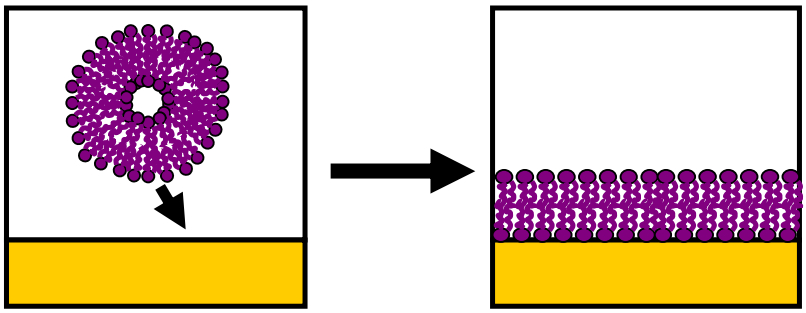

Figure 3.1: Formation of a supported phospholipid bilayer through vesicle fusion. The vesicle on impact with the gold surface has a tendency to unravel and spread across the surface, forming a bilayer patch in the process.

3.4.2 Langmuir-Blodgett Deposition

A Nima Langmuir-Blodgett Trough was used for the deposition of monolayers by Langmuir-Blodgett and Langmuir-Schaeffer deposition.

The trough had a surface area of 600 cm^2 and was constructed of Teflon. PTFE has the advantage of both being highly hydrophobic and unlikely to contaminate the subphase or monolayer.

Compression was achieved by the use of a movable Delrin barrier. A paper Wilhelmy plate was used for surface pressure measurements. The subphase was ultrapure water. A circulating water bath (Grant) was used to maintain subphase temperature at 18^{o}C.

Cleanliness is essential for good results. The trough and barrier was thoroughly cleaned beforehand with lint-free tissues (KimTech, US) soaked in a little chloroform. The aqueous subphase was then added and the paper Wilhelmy plate lowered into the subphase. The trough was then left for 30 minutes to allow the weight of the Wilhelmy plate to stabilise through water absorption.

The subphase surface was then removed by suction. The barrier was then closed and the pressure measured so that an isotherm was obtained. If the surface was free of contamination, the isotherm obtained was at zero pressure. Sometimes some contamination was present as evidenced by the increase in surface pressure. In this case, the surface was removed and another isotherm measured. This process was repeated until the surface pressure remained at zero throughout compression, indicating that all surface contaminants had been removed.

The clean gold electrode (see Section 3.3) was then placed on the dipper arm and lowered into the subphase. Once it was entirely immersed, another isotherm was measured to ensure no surface contaminants had been introduced – if it had, the cleaning process outlined above was performed.

The phospholipids, dissolved in a mixture of 10% methanol in chloroform, were then spread evenly onto the surface of the subphase using a microsyringe. It was found that 60 µl at a concentration of approximately 1.5 - 2 g l^{-1} contained sufficient lipid to obtain a good isotherm.

The trough was then left for at least 15 minutes to allow the solvent to evaporate. An isotherm was then measured to confirm the presence of lipids – and the presence of the right lipids in the correct ratio! A barrier speed of 25 cm^2 min^{-1} was used throughout.

The monolayer was then compressed to a pressure of 40 to 45 mN m^{-1} (typically, a pressure of 42 mN m^{-1} was used): this was chosen to be well above the liquid to gel phase transition but comfortably below the collapse pressure. This pressure corresponds to a molecular area of approximately 38 $Å^2$ (this depends somewhat on the monolayer composition, see Section 7.1.4). Hence a reasonably ordered well packed monolayer could be expected. The trough was set to constant pressure control so that the pressure would be automatically maintained at the desired value.

The dipper was then raised slowly – 2 mm min^{-1} to ensure good transfer to the electrode. Hence the end result was an electrode with an even phospholipid monolayer coating (Figure 3.2). The monolayer was then dried for 30 minutes under a stream of argon.

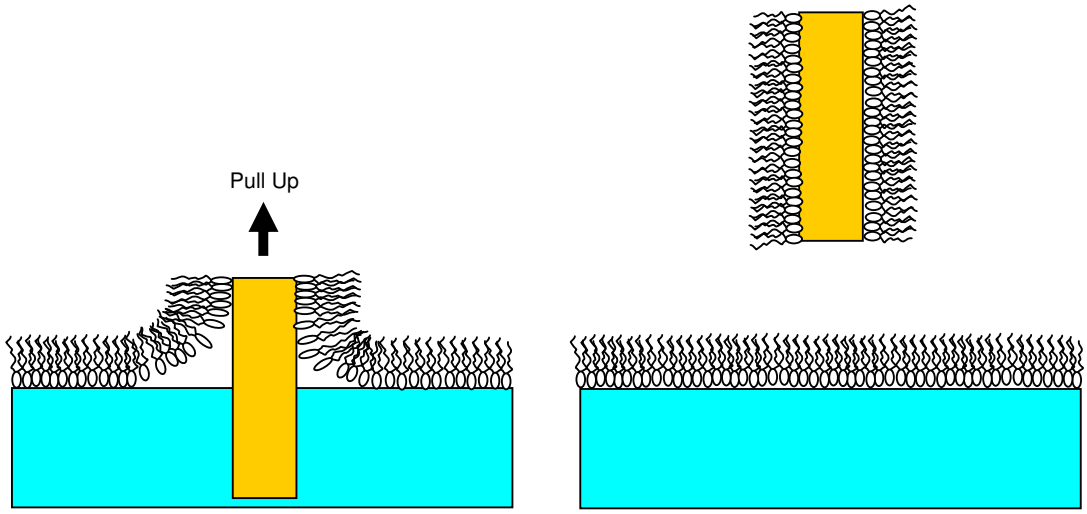

Figure 3.2: Langmuir-Blodgett deposition. The substrate is pulled through a monolayer floating at the subphase/air interface of a Langmuir Trough and gains a surfactant monolayer as it is lifted.

At this point, two methods were used to form a bilayer. The first was simply to lower the electrode back into the trough. This allowed the hydrophobic tails of the lipids to attach themselves to the now hydrophobic electrode surface (as it is now coated with a lipid monolayer with the tails facing outward). The monolayer on the subphase surface had then to be removed by suction – failure to do this essential step will result in the deposition of an undesired third lipid layer on the electrode. Once the monolayer had been removed, the dipper was raised.

The second method employed was Langmuir-Schaeffer deposition (Figure 3.3). With the trough monolayer still under constant pressure, the electrode

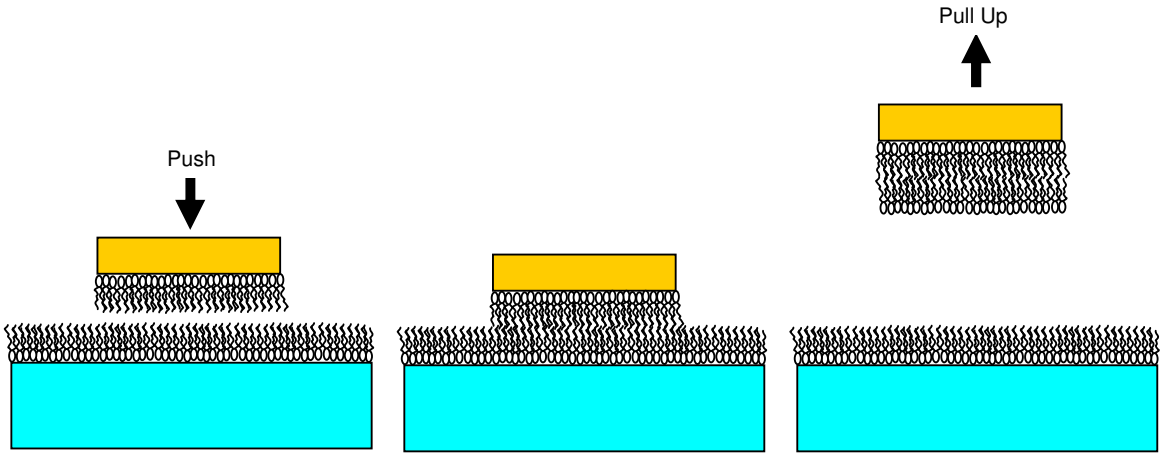

Figure 3.3: Langmuir-Blodgett/Langmuir-Schaeffer deposition. A bilayer is formed by allowing the monolayer coated substrate to contact the monolayer floating on the surface of the Langmuir Trough.

was slowly lowered at a rate of 2 mm min^{-1} to contact the surface. This transfers a second layer onto the existing monolayer. The electrode was then raised at the same rate.

3.5 Differential Capacitance

3.5.1 The Electrochemical Cell

The electrochemical cell consisted of two parts connected by a ground glass joint. It is shown schematically in Figure 3.4. The top half contained quickfit ground glass joints that served as ports for the electrodes, salt bridge and gas

ports. There were two gas ports which could be used to purge the cell with argon to remove oxygen. One port admitted Ar into the air space above the electrolyte so that this space could be purged, the other purged the electrolyte by means of a long glass bubbler. The cell was placed in a thermostatically controlled water bath (Grant).

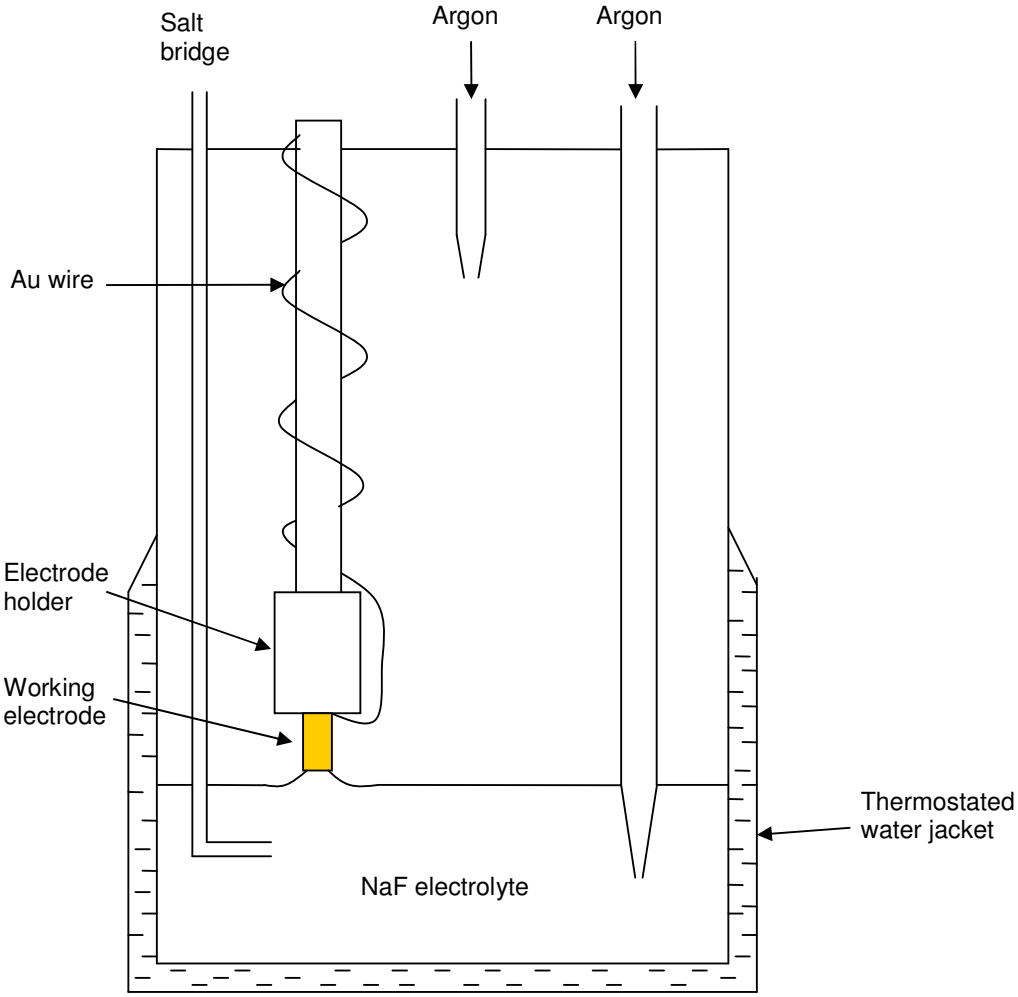

Figure 3.4: The electrochemical cell. The salt bridge led to a separate compartment containing the reference electrode (not shown). The working electrode was used in the hanging meniscus configuration.

A saturated calomel electrode (SCE) was used as the reference electrode ($E^{\ominus}$ = 0.2412 V). All potentials quoted in this work are referenced to the SCE unless otherwise stated. It was housed in a separate reference compartment connected to the electrochemical cell by a salt bridge. The electrolyte solution in this compartment was saturated KCl. The salt bridge was designed to be long with a small cross section in order to reduce the diffusion rate of chloride ions along it: chloride has a high affinity for gold, so contamination by this ion must be avoided. A three way tap was employed to fill the bridge with electrolyte. The entire assembly was placed in a Faraday cage in order to screen out electromagnetic interference. A Heka PG590 potentiostat was used to precisely control the potential applied between the RE and WE. A three electrode system was used.

3.5.2 Differential Capacitance (DC) Measurements

A schematic diagram of the apparatus used is shown in Figure 3.5. In operation, the cell was filled with 0.1 M NaF electrolyte. The water bath temperature was set to 35.0 ^{o}C with a quoted stability[1] of ±0.1 ^{o}C – at this temperature, lipid bilayers can be expected to be fully liquid. The working and counter electrodes were prepared and placed in the cell, which was then purged with Ar for at least one hour. The working electrode was used in a hanging meniscus configuration. This entailed lowering the working electrode until it touched the electrolyte surface and then lifting it so that the meniscus was bowed upwards to ensure only the (111) face of the working electrode was in contact with the electrolyte.

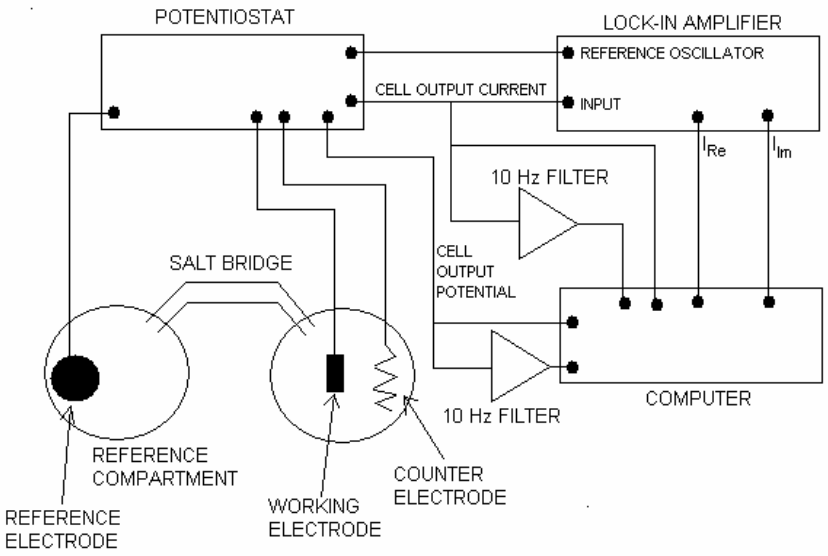

Figure 3.5: Schematic diagram of the chronocoulometry and differential capacitance measurement system.

The internal oscillator of a Signal Recovery 7265 lock-in amplifier was used to generate a 20.000 Hz sinusoidal signal at 5 mV rms amplitude: this was fed into the potentiostat which superimposes this signal on top of the cell voltage (the potential difference between the reference and working electrodes). The current output of the potentiostat was fed back into the lock-in amplifier and used to recover the in phase I_{Re} and out of phase (90^0 phase shift) I_{Im} signals.

The cell potential and current was filtered and recorded along with the I_{Re} and I_{Im} signals by a computer via a National Instruments data acquisition board. The unfiltered current and potential signals were also recorded so that it was possible to check that the filters were not distorting the signal.

The potentiostat was set to scan linearly over the range +0.4 V to -0.8 V at a ramp rate of 5 mV s^{-1} when investigating LB/LS bilayers and a range of +0.4 V to -1.2 V when vesicle-formed bilayers were being investigated. A background capacitance scan was performed to check the quality of the working electrode surface and cleanliness of the cell before lipid deposition.

The vesicle solution, prepared as outlined in Section 3.3.1, was then introduced into the cell, which was left to purge for one hour with Ar. This time was required to allow the vesicles the opportunity to spread on the working electrode and form a bilayer. During this period, the cell voltage was cycled – this was found to aid bilayer formation. The progress of vesicle deposition could be monitored by recording changes in the capacity during this time – the measured differential capacitance could be expected to drop as vesicles adhered to the electrode. Figure 3.6 illustrates this process for a DMPC bilayer. This shows four voltage cycles over the range of -0.75 to +0.45 V for a solution of DMPC vesicles. Each successive cycle displays a decreased capacity as more vesicles adhere to the electrode and coverage increases. In practice, it was usually sufficient to observe the fall in the real and imaginary currents as displayed by the lock-in amplifier: a decrease to less than 30% of the bare electrode value indicated that a bilayer was forming on the electrode surface. Once this point was reached, differential capacitance scans could be commenced. The scan range used was +0.45 V to -1.2 V.

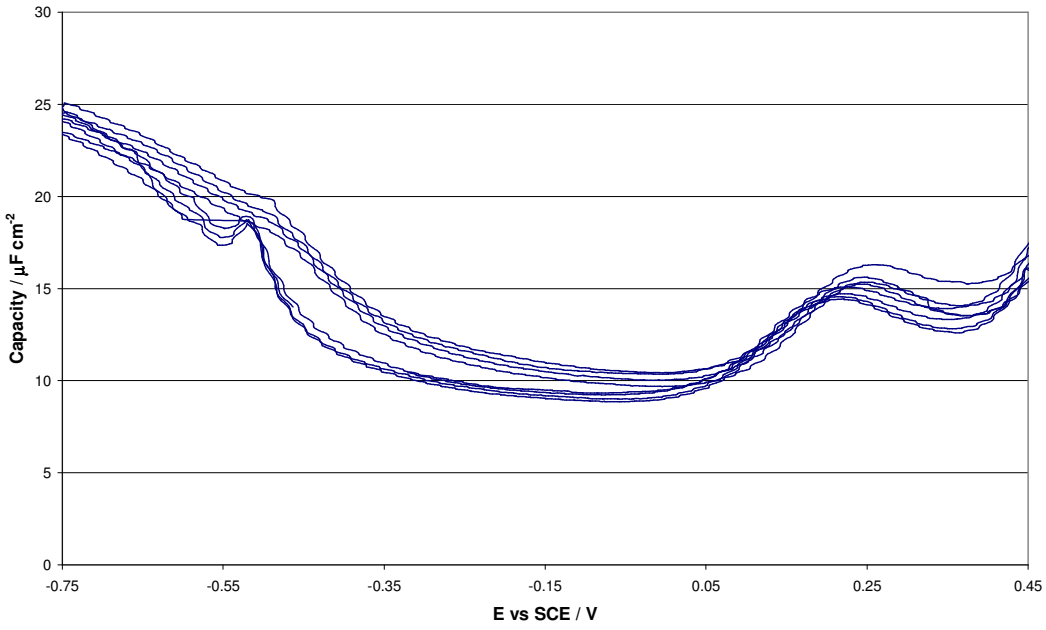

Figure 3.6: Deposition of DMPC vesicles onto an Au (111) substrate. This was recorded 10 minutes after DMPC vesicles had been introduced thus a film had already formed on the electrode. The fall in capacity with each successive cycle indicates that bilayer coverage is increasing.

When a LB/LS bilayer was being investigated, the coated electrode (see Section 3.3.2) was placed in the cell but not lowered to touch the electrolyte surface. The cell was purged for at least 30 minutes to remove oxygen after which the electrode was lowered into the hanging meniscus configuration. Data acquisition could be started after the cell was purged of oxygen. Once obtained, the data were exported into a spreadsheet where the capacitance for each data point was evaluated and then plotted.

3.6 Chronocoulometry

The same setup was used for chronocoulometry measurements as differential capacitance. The 111 face of a monocrystalline gold block was used, and was prepared as before by flame annealing. The vesicle solution was prepared as outlined in Section 3.4.1. For experiments involving Langmuir-Blodgett Langmuir-Schaeffer bilayers, the procedure is given in section 3.4.2.

Once the electrode had been flame annealed, it was introduced to the cell. The cell was then purged with Ar for an hour to remove oxygen. A DC scan was then carried out to check that the electrode surface was clean and free of defects: a poor surface could be detected by an unusually high capacitance values at negative potentials and a feature at +0.2 V. If the surface was deemed to be of insufficient quality, the electrode was removed and flame annealed a second time.

Once the electrode surface was of satisfactory quality, vesicles were introduced to the cell, which was purged for 30 minutes in order to remove any dissolved oxygen. The working electrode could then be lowered to the 0.1 M NaF electrolyte surface in the hanging meniscus configuration, as before.

The cell water jacket was maintained at 37±0.1 ^{o}C and the cell voltage cycled for one hour to encourage the formation of a bilayer. A DC scan was performed to confirm the existence of a bilayer, then the water jacket was set to 25^{o}C and allowed to equilibriate for 30 minutes. A further DC curve was recorded, followed by cyclic voltammetry to confirm the absence of oxygen. Oxygen must be excluded, otherwise it will be reduced during the experiment, thus contributing to the charge measured during chronocoulometry. If oxygen was determined to be present, further purging of the cell with Ar was performed.

The double step chronocoulometry technique was used. This involved holding the electrode at -0.10 V for 60 s to allow the bilayer to equilibrate. The potential was then stepped to the potential of interest and held for 210 s, again to allow the bilayer to equilibrate at this new potential. The potential was then briefly stepped to the desorption potential of -1.2 V for 0.15 s in order to strip the bilayer from the electrode. The current transient was recorded. The potential was then reduced to the resting potential of -0.10 V so that the cycle could be repeated at the next potential of interest. A desorption potential of -1.2 V was chosen as DC measurements indicate that the bilayer is fully desorbed at this potential.

A macro in Igor Pro was used to integrate the current transient in order to yield the total charge transfer[2]. This gives the relative charge density referenced to the desorption potential. In other words, this allows the

determination that a bilayer at 0.3 V has (say) 50 μC cm^{-2} higher charge density than at the desorption potential of -1.2 V.

It is the difference between the electrode surface with and without the adsorbed bilayer that is of interest. This requires knowledge of the properties of the Au (111) surface. The charge density of the electrode has itself been measured: the value obtained agrees with measurements performed by Lipkowski's laboratory[2]. From this it is known that the Au (111) surface has a charge density of -41 μC cm^{-2} at the desoprtion potential. Assuming the bilayer is fully desorbed at -1.2 V, it is possible to calculate σ_m for the bilayer by the addition of -41 μC cm^{-2} to the relative charge density.

3.7 Impedance Measurements

The impedance cell was machined from a Teflon block and equipped with a glass side arm for the reference electrode, as shown in Figure 3.7. The cell was sealed by a Teflon lid and o-ring. A small hole in the lid admitted the counter electrode. The working electrode was clamped to the side and sealing was again achieved with an o-ring.

The working electrode was high purity, 99.999% polycrystalline gold evaporated onto a glass substrate. The thickness was 20 nm. The counter electrode was a high purity (99.999%) gold wire and a SCE was used as the reference electrode. The cell was connected to an Autolab PG12 potentiostat

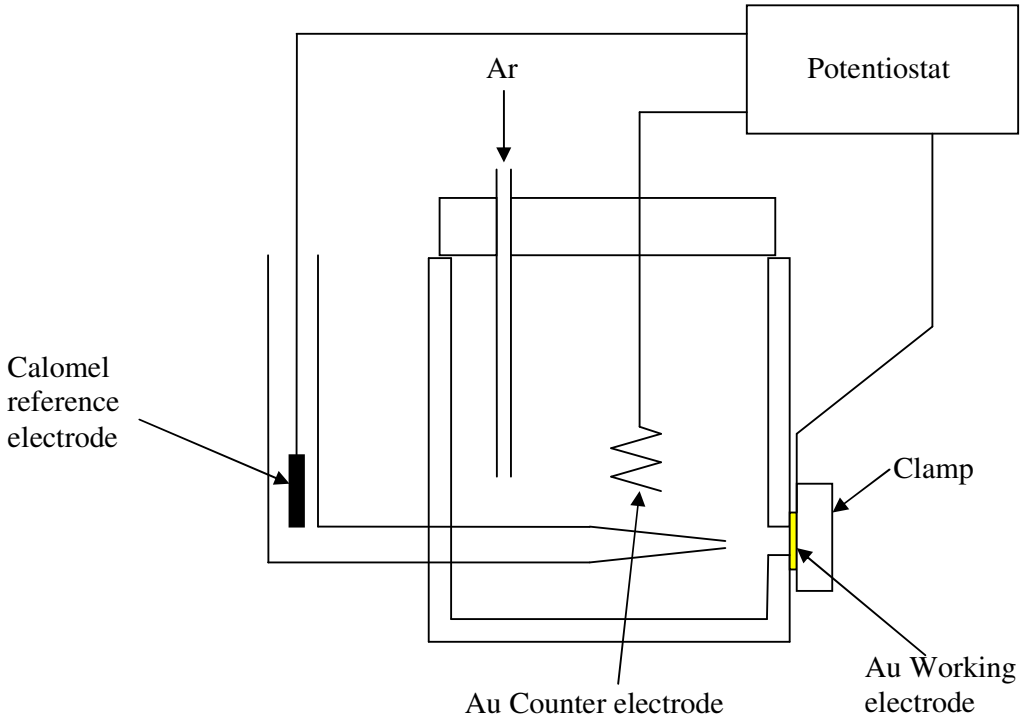

Figure 3.7: The impedance cell. The SCE reference electrode was held in a glass side arm while the counter electrode was a coil of gold wire. The working electrode was a glass slide coated with gold, held down by a clamp and sealed with an o-ring.

with a FRA module and controlled via GPES software for CV and FRA software for impedance (Electrochemie, NL).

experiments. The point of zero charge (PZC) for polycrystalline gold is -0.05 V referenced to the SCE[3]. Figure 3.8 compares the difference capacity plots for both electrode surfaces. The polycrystalline gold data in Figure 3.8 is derived

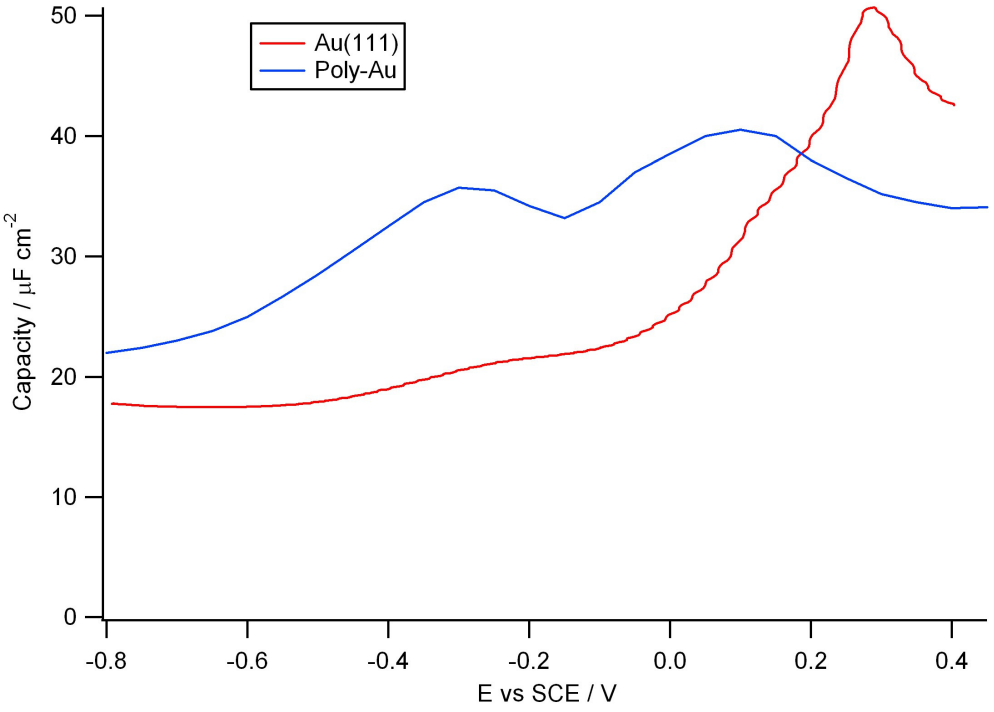

Figure 3.8: A comparison between the differential capacity curves of the gold (111) face (red) and a polished polycrystalline gold surface (blue). The monocrystalline surface has the lower capacity at negative potentials. Polycrystalline Au data extracted from Safonov[4].

from Safonov *et al*. for a 0.05 M NaF electrolyte[4]. It is evident that a polycrystalline Au electrode has the higher capacitance at potentials below +0.2 V. The reverse is true above this value, where the Au (111) surface exhibits a peak in capacity at the pzc.

Impedance spectroscopy with an electroactive probe was chosen in order to investigate bilayer quality. It is assumed that the electroactive species can

only access the electrode surface through pores and defects in the bilayer. Hence a comparison with the bare electrode can yield data as to how effective a barrier the film acts towards the electroactive ions.

An electrolyte of 0.1 M NaF, or 1 mM potassium hexaferrocyanide in 0.1 M NaF was used. The electrolyte was purged of oxygen by bubbling a stream of Ar through it before being placed in the cell. The counter electrode was flame annealed to red heat before use. The working electrode was rinsed in ultrapure water, gently flame annealed and rinsed a second time before being placed in the cell. The system was evaluated by cyclic voltammetry. A range of 0 to 0.4 V was used with a scan rate of 50 mV/s. On a bare gold working electrode the reduction peak of the reaction:

$$Fe(CN)_6^{4-}(aq) \rightarrow Fe(CN)_6^{3-}(aq) + e^-$$

was found to be +0.12 V, or +0.36 V relative to the standard hydrogen electrode (SHE). This compares well with the literature value[5] of +0.36 V. The oxidation peak occurs at +0.24 V. The midpoint between the reduction and oxidation peaks is +0.18 V. This was used as the origin for impedance studies. The impedance of the reduction of potassium hexaferrocyanide was measured in the range 0.08 V to 0.28 V in 0.02 V steps.

A frequency range of 10 kHz to 0.1 Hz was used. Data points were distributed logarithmically so that each decade had the same number of data points. There were 51 points in total. A sinusoidal signal with 0.010 V rms amplitude was used.

Impedance spectroscopy using hexaammineruthenium (III) chloride was performed under similar conditions as the potassium hexaferrocyanide, except that the potential used was in the range -0.08 V to -0.28 V. The impedance of the system was recorded in 0.02 V steps as before. The electrolyte was a solution of 0.1 M NaF, where 1 mM of hexaammineruthenium (III) chloride had been added. $Ru[(NH_3)_6]^{3+}$ is reduced according to:

$$Ru[(NH_3)_6]^{3+}(aq) + e^- \rightarrow Ru[(NH_3)_6]^{2+}(aq)$$

The oxidation peak for this reaction was found to occur at -0.15 v (+0.09 V referenced to the SHE) compared to the literature value[5] of +0.10 V (SHE). The midpoint between the reduction and oxidation peaks was -0.18 V, hence this was used as the origin for impedance studies using $Ru[(NH_3)_6]^{3+}$ as the active species.

3.8 PM-IRRAS

A Bruker Vertex 80v FTIR formed the core of the PM-IIRAS system. A light beam from the spectrometer's interferometer was sent through an exit port to the PEM. The PEM, cell and detector along with their associated optics were located in an external box which could be sealed and purged with dry air. The PEM, the sample cell or stage, the detector and optics were enclosed in a perspex box which was purged with dry air in order to minimise the impact of atmospheric water vapour on the data.

A mercury cadmium telluride (MCT) detector was used, cooled to 77 K by liquid nitrogen. This device is sensitive to radiation between 5000 cm^{-1} down to 600 cm^{-1}.

A glow-bar – a ceramic element heated to approximately 1200 K – was the source. This is a broadband source which produces copious amounts of infrared radiation from approximately 10 000 cm^{-1} to 200 cm^{-1}.

The Bruker FTIR used a temperature stabilised helium-neon laser to measure the path difference by projecting a beam through the instrument's interferometer. This had the effect of generating a set of light fringes which were detected and counted. Every fringe represented movement of 632.8 nm (the wavelength of the red HeNe laser line) of the movable mirror.

The stabilised HeNe laser is a secondary frequency standard[6]: its frequency and hence wavelength is defined (strictly speaking, the 632.8 nm line is referenced back to the primary caesium standard). This means that acquired spectra are referenced to a known standard and thus have a very high degree of accuracy.

A model II/ZS50 PEM was supplied by Hinds Instruments. It had an operating frequency of 50 kHz and an effective bandwidth of approximately 250 cm^{-1}. The PEM was driven from a Hinds Instruments PEM-100 Controller. A GWC Technologies Synchronous Sampling Demodulator was used to extract the signal.

3.8.1 Methodology

Ex situ samples were prepared on gold coated glass slides. 99.999% gold was evaporated directly onto glass microscope slides. The thickness was approximately 25 nm.

Bilayers of various compositions were prepared using the LB-LS method, as described in Section 3.4.2. The Au coated glass slides were flame annealed before bilayer deposition. Compositions used were 10% DMPS in DMPE, 20% DMPS, 30% DMPS, 40% DMPS and 50% DMPS all in DMPE as mole fractions. The sample was then mounted onto a holder using double sided sticky tape. This may sound crude but provides a secure mount, yet allows for easy removal.

The MCT detector was positioned at an angle of 80^{o}. This is the optimum angle for *ex situ* PM-IRRAS on Au[7]. The sample stage was an adjustable optical mount. The position of the stage was adjusted to optimise the signal measured by the detector. The gain of the SSD was adjusted so that the p-polarised signal was of similar magnitude to the s-polarisation. This ensured that the difference signal was of a similar magnitude to the average signal.

The spectrometer was controlled by Opus: a custom software package provided by Bruker. Opus also stored the acquired interferogram and in cases where multiple scans were made to improve S/N, summed each scan to

produce the final interferogram. It was then used to execute a fast Fourier transform on the acquired data to recover the actual spectrum.

Three regions were of interest: the C-H stretching region at 2900 cm^{-1}, the carbonyl stretching region at 1600 cm^{-1} and the phosphate stretch vibrations at 1100 cm^{-1}. Spectra were acquired at all these regions at a resolution of 2 cm^{-1}. Typically, 4000 scans were used for each spectrum to ensure an acceptable signal to noise ratio.

3.9 Neutron Reflectometry

The electrochemical cell used in neutron reflectometry experiments consisted of several components[8]. The layout is shown in figure 3.9.

The size of the cell was determined by the fact that the neutron beam employed is rather large: hence, to maximise the signal, a large working electrode area was required. The working electrode was composed of a base substrate which was a polished single crystal block of quartz with dimensions 100 x 50 x 10 mm. Quartz has the advantage of being highly transparent to neutrons: less than 30% of neutrons will be absorbed in transit through 10 cm of quartz[9].

The surface was coated in an “adhesion layer”: 3-mercapto-(propyl)trimethoxysilane[10]. It is notoriously difficult to obtain good adhesion of

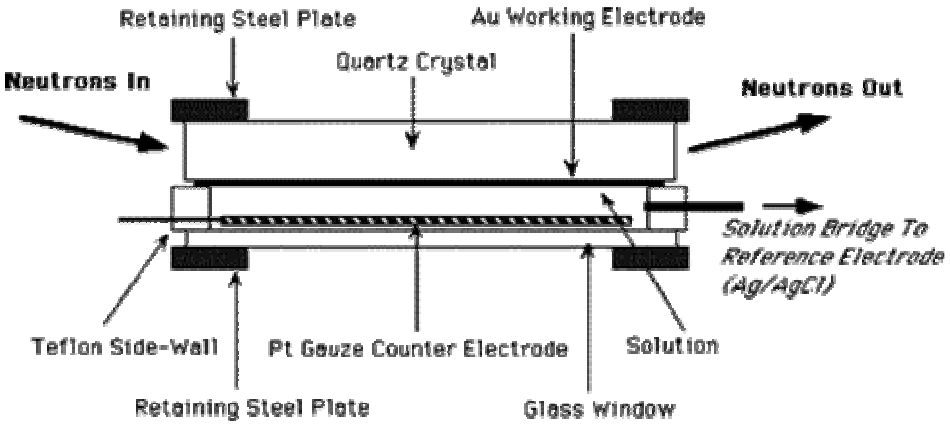

Figure 3.9: The neutron reflectivity cell. (After Glidle[8].)

gold to a quartz surface: this adhesion layer ensures good cohesion with the substrate. A 200 Å thick layer of gold was then evaporated onto the block.

Neutrons pass through the back of the block: reflection takes place at the quartz/adhesion layer, adhesion layer/gold, gold/bilayer and bilayer/electrolyte interfaces.

A PTFE collar was placed upon the working electrode. The electrolyte compartment was sealed with a glass block on top of the collar. The collar set the area of the working electrode as 30 cm^2. A platinum gauze electrode next to the glass block served as the counter electrode. A glass side arm attached to the cell allowed the electrolyte compartment to be filled and provided a convenient port for the Ag/AgCl reference electrode. All potentials are therefore quoted with respect to this reference ($E^{\ominus}$ = 0.2223 V).

The cell was then placed in the reflectometer and aligned. A potentiostat was attached so that the cell voltage could be held to the desired value. Data were gathered at a range of cell potentials: +0.35 V, +0.15 V, -0.15 V, -0.35 V, -0.55 V and -0.75 V so that any change in the bilayer structure could be determined. These potentials were chosen on the basis of DC data. +0.35 V is just beyond the PZC when the surface pressure is falling, +0.15 V is close to the PZC at maximum surface pressure, -0.15 V is in the regime that a stable bilayer can be expected to be adsorbed onto the substrate, -0.35 V close to a phase transition and -0.75 V is a potential that the chronocoulometry data for bilayers formed via vesicle fusion are desorbed from the surface.

Data were gathered at two detector angles, 0.7^{o} and 2.2^{o}, so that a sufficient range in *Q* was acquired for analysis. Neutron counting was integrated for 1800s for 0.7^{o} and 2700s for 2.2^{o} in order to ensure a good signal to noise ratio.

3.9.1 Materials

The bilayers investigated were DMPE/DMPS mixtures with a ratio of 9:1 DMPE to DMPS, a value close to that observed in biological systems. The phospholipids came in normal hydrogenous and deuterated varieties, where all the hydrogen atoms in the tail were replaced by deuterons and were supplied by Avanti Polar Lipids.

Four contrasts were used: hydrogenous lipids in H_2O, deuterated lipids in H_2O, hydrogenous lipids in D_2O and deuterated lipids in D_2O.

Vesicles were prepared as outlined in Section 3.4.1. A 0.05 M solution of NaF (Suprapur grade, Merck) was used as the electrolyte. Water was obtained from a Millipore MilliQ water purifier with a TOC < 5 ppb and greater than 18 MΩ cm resistivity. D_2O was supplied by Aldrich. Upon removal from the sonicator, the vesicle solution was introduced into the neutron electrochemical cell and left to incubate at open circuit potential in an oven at 40^{o}C for a minimum of 2.5 hours. This was to allow the vesicles sufficient time to adhere and spread on the Au electrode.

3.9 References

1. Grant T100 Refrigerated Thermostatic Circulating Bath datasheet

2. S. L. Horswell, private communication

3. Clavilier, J., Nguyen van Huong, C., (1977), *J. Electroanal. Chem.*, **80**:101

4. Sofonov, V. A., Choba, M. A., Krivenko, A. G., Manzhos, R. A., Maksimov, Yu. M., (2012), *Electrochim. Acta*, **61**:140

5. CRC Handbook of Chemistry and Physics, 74th edition

6. Zamlynny, V., PhD Thesis, University of Guelph (2002)

7. US Federal Standard 1037C, 1991

8. Glidle, A., Hadyoon, C. S, Gadegaard, N., Cooper, J. M., Hillman, A. R., Wilson, A. R., Ryder, K, S., Webster, J. R. P., Cubitt, R., (2005), *J. Phys Chem B*, **109**, 30:14335

9. Penfold, J., Thomas, R. K., (1990), *J. Phys – Condensed Matt*, **2**:1369

10. Goss, C. A.; Charych, D. H.; Majda, (1991) M. *Anal. Chem.* **63**:85

4. Polarisation Modulated Infrared Reflectance Spectroscopy

4.1 Data Processing

Background spectra were acquired with the detector angle set to 0^{o} with no sample emplaced. A polariser was placed directly after the PEM, set to admit p-polarised light.

An Opus macro supplied by Bruker was used to extract the average and difference signals from the acquired spectrum. These data were then imported into Igor Pro, along with the background data. A macro was employed to recover the PM-IRRAS spectrum using Equation 2.58 and then correct for PEM distortions using the background spectra. The macro is based on the procedure outlined in Section 2.5.3, originally developed by Zamlynny[1]. This procedure would typically result in a spectrum such as that in Figure 4.1. Further manipulation was required before quantitative information could be extracted.

The data were then imported into Origin Pro 8. The features of this software package, such as background subtraction and peak finding, are very useful for dealing with spectra. The background contains absorption lines of water and carbon dioxide. The first step was to subtract a spline so as to flatten the

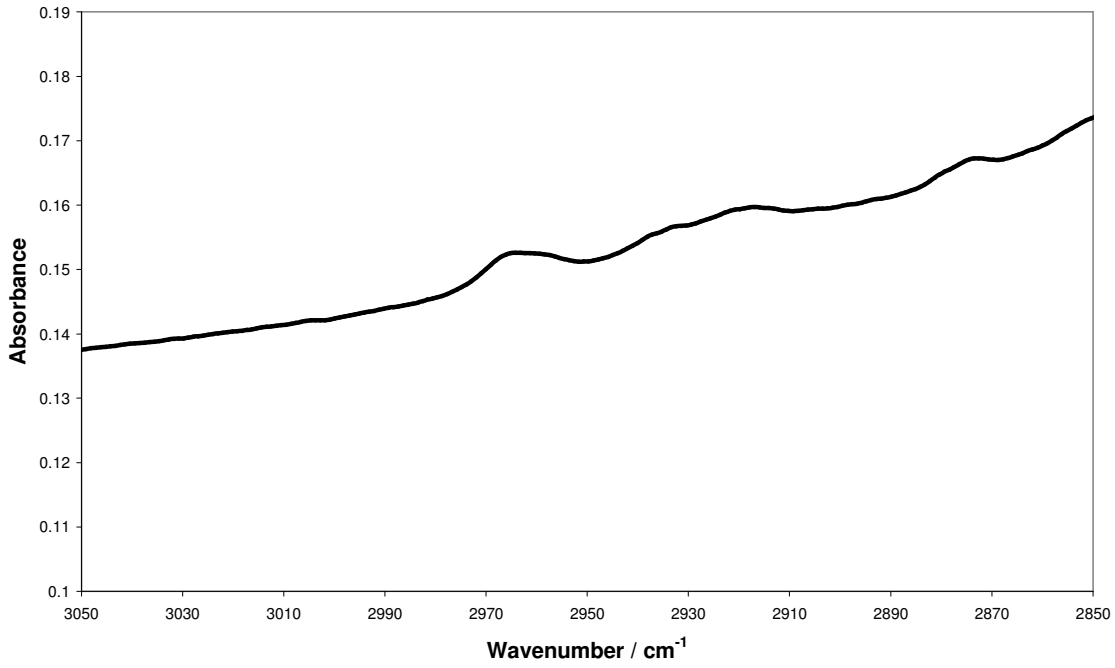

Figure 4.1: Raw PM-IRRAS spectrum after background subtraction, but before any data processing. The sloping baseline is an artefact produced by the PEM.

the spectrum. Once this was deconvolution was used to resolve individual peaks (Figure 4.2).

4.2 Results and Discussion

The Peak Finding suite of Origin Pro was employed to fit lines using a Voigt line shape for maximum flexibility. This line shape combines properties of both Gaussian and Lorentzian line shapes. Line shape is dependent upon the

Peak Analysis

Data Set:[Book1]Sheet1!C Date:30/11/2011

Baseline:Spline

Chi^2=3.44566E-008 Adj. R-Square=9.90588E-001 # of Data Points=234.

SS=7.92503E-006 Degree of Freedom=230.

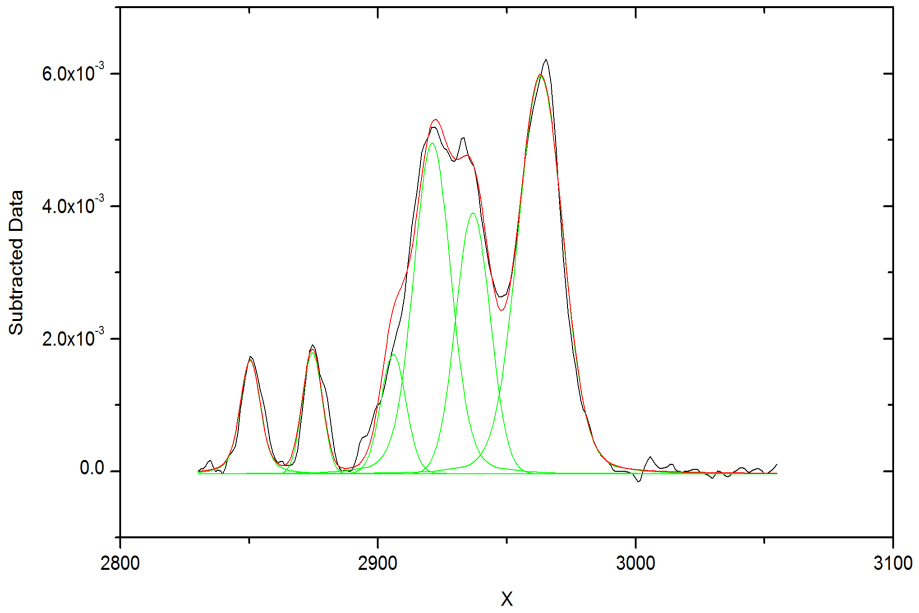

Fitting Results

Peak #	Peak Type	Area Intg	FWHM	Max Height	Center Grvty	Area IntgP
1.	Voigt	0.00921	9.31588	0.00171	2850.41853	2.71629
2.	Voigt	0.00779	9.12931	0.00183	2874.53396	2.29653
3.	Voigt	0.08669	17.0738	0.00499	2921.03879	25.56619
4.	Voigt	0.05579	15.6922	0.00394	2936.81671	16.45329
5.	Voigt	0.1284	20.58701	0.006	2963.06821	37.86708
6.	Voigt	0.01274	11.57349	0.0018	2905.94612	3.75842

Figure 4.2: Deconvolution of the CH stretching region. This is an example of the output by the peak finding program in Origin 8 Pro, for a 40% DMPS bilayer in the CH stretching region. The black line is the PM-IRRAS spectrum after subtraction of a spline to flatten the spectrum. Deconvoluted lines are shown in green. The red line is the sum of the green deconvoluted lines.

broadening mechanism[2]: a Lorentzian line shape is produced by homogeneous line broadening processes which affect all molecules equally. Pressure or collision broadening is one such example[2]. A Gaussian line shape is broader then the Lorentzian shape and is the result of inhomogeneous line broadening processes which introduce a frequency shift of differing magnitude to each molecule: the broadened line is the result when the contributions of all molecules are summed. Doppler broadening is the most important example of an inhomogeneous line broadening mechanism[2]. The Voight line shape was chosen so that the deconvolution software would use line shape as one of the variables to be fitted. In practice, all lines were fitted to Lorentzian line shapes, which suggests that pressure broadening is the dominant line broadening process.

Deconvolution and line fitting was repeated several times for each acquired spectrum. Thus a range of values for each deconvoluted line was calculated. This allowed an estimate of the errors introduced by the deconvolution process to be made. The uncertaincy in the line position was estimated to be ±2 cm^{-1} with errors in the line intensity and line width of 10%.

There are three regions of interest: at 2900 cm^{-1} where the CH stretching lines are located, 1600 cm^{-1} where bands due to the headgroup carbonyl moieties are observed and at 1100 cm^{-1} which features absorption bands due to the phosphate group. Each region will be considered in turn.

4.2.2 The 2900 cm^{-1} CH Stretching Region

Spectra from the 2900 cm^{-1} CH stretching region after baseline removal are shown in Figure 4.3 for all compositions. Lines and their assignments are listed in Table 4.1.

Figure 4.4 shows the line position of the methyl and methylene stretch bands. The CH_3 and CH_2 stretching bands show very little change with composition in line position: changes lie within the 2 cm^{-1} resolution of the FTIR. There is no evidence of systematic shifts in position. This is unsurprising, given that these lines arise from the hydrocarbon tail, which is identical for both DMPE and DMPS. This indicates that packing is similar for all compositions. Since the limiting molecular area of DMPE (38 $Å^2$) is similar to that of DMPS (41 $Å^2$) this is not unexpected (see Section 7.1.4).line is the resultant simulated spectrum produced by the superposition of the modelled deconvoluted lines.

Table 4.1: Line assignments in the C-H stretching region[3-7].

Frequency / cm^{-1}	Assignment
2964	CH_3 anti-symmetric stretch
2937	Fermi band, CH_3 anti-symmetric stretch
2922	CH_2 anti-symmetric stretch
2908	Fermi CH_2 anti-symmetric stretch
2876	CH_3 symmetric stretch
2851	CH_2 symmetric stretch

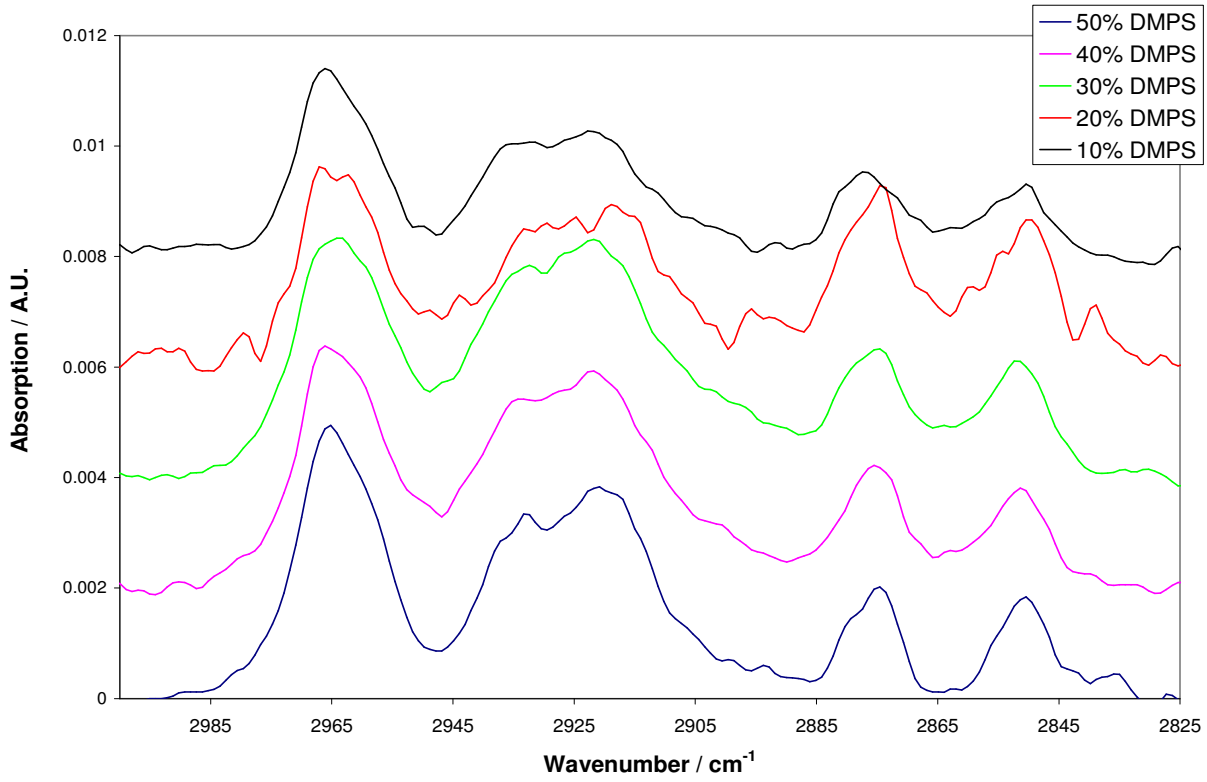

Figure 4.3: The CH stretching region for bilayers with the stated mole fractions of DMPS in DMPE. Spectra are offset for clarity, from 50% DMPS (bottom) to 10% DMPS (top).

The methylene symmetric stretch appears at 2851 cm^{-1}. ATR investigations of egg phosphatidylcholine (egg PC is derived from natural sources – egg – and hence contains a mixture of tail groups) indicated that this band appeared at 2853.7 cm^{-1} when hydrated but shifted downwards to 2851.7 cm^{-1} upon dehydration[8]. It can thus be inferred that the tail groups are dehydrated.

Figure 4.5 charts the dependence of line FWHM with composition. With the exception of the 2964 cm^{-1} methyl anti-symmetric line, there is a trend towards

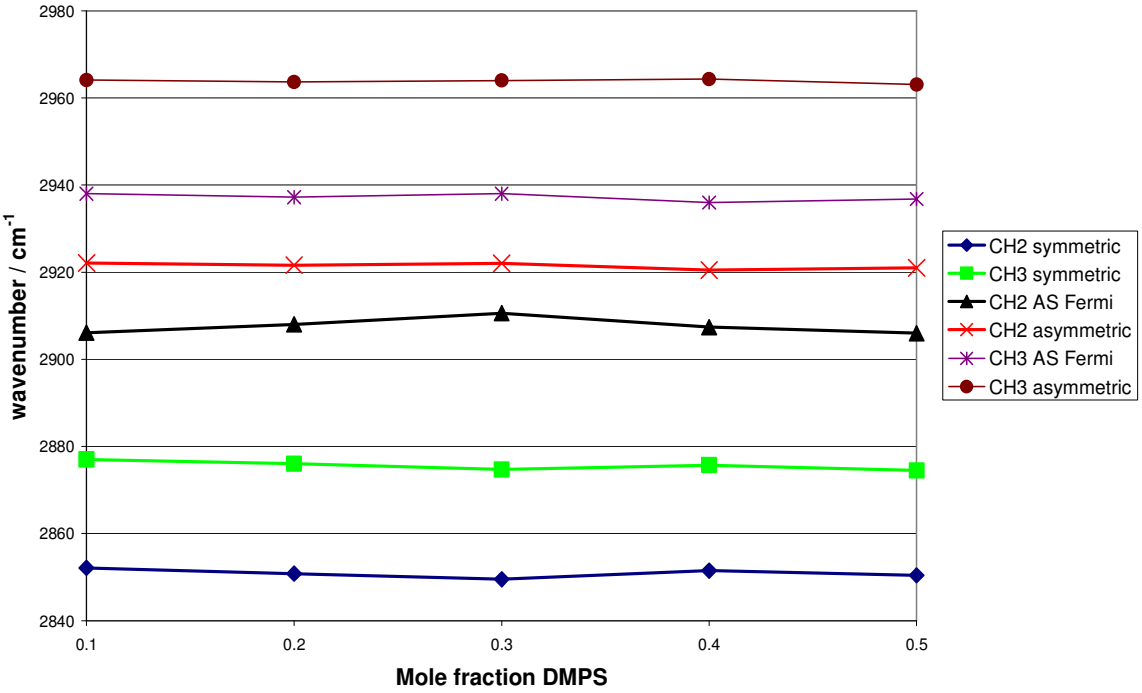

Figure 4.4: Effect of bilayer composition on position of the CH stretching bands. There is little systematic change in line position with composition.

decreased line width as the concentration of DMPS increases. With the exception of the methylene AS line, the 30% DMPS bilayer shows a lower FWHM than other compositions. The methyl AS shows the opposite trend – an increasing FWHM with DMPS, but again the 30% DMPS shows a minimum.

A change in line width indicates a change in organisation in the acyl tails. A decrease indicates that there is an increase in order[9]. The 30% DMPS bilayer seems to be particularly favoured in this respect: quite why is unclear though it is possible to hypothesise that there is a “magic ratio” of DMPS to DMPE molecules that results in a more ordered structure which, to 30% DMPS.

The absorption intensities of the CH stretching lines are graphed in Figure 4.6. Absorption intensities are dependent on the orientation of the transition dipole moment: a dipole moment that is orientated parallel to the substrate will not give rise to an absorption band. Both DMPS and DMPE possess the same tail groups. Hence any change in the line intensity will be the result of changes in direction that the vectors of the dipole moment that give rise to the absorption lines. Considering first the CH_3 asymmetric (AS) line, it can be seen that the intensity is at a minimum at 10% DMPS, increases at 20% DMPS then falls back before peaking at 50% DMPS. The CH_3 symmetric line intensity also increases going from 10% to 20% DMPS, but falls thereafter. The intensity of both lines thus vary similarly between 10% and 30% DMPS. The dipole moment of the methyl AS stretch is perpendicular to the methyl symmetric stretch. A change in tilt angle – the angle at which the moiety is tilted with respect to the bilayer normal – will therefore cause the intensity one line to increase and the other to decrease. That both lines vary in step suggest that the CH_3 group rotates with respect to the rest of the acyl chain. The intensity of both lines change in opposite directions as the mole fraction of DMPS rises from 0.4 to 0.5, indicating that the lipid tilt angles have changed. The dipole of the methyl symmetric stretch is in line with the acyl chain: for a molecule standing vertically on the substrate, this dipole moment would be perpendicular to the surface. The methyl asymmetric stretch dipole moment would thus be parallel to the surface. Therefore the decrease in intensity of the symmetric stretch coupled with the increase in intensity of the asymmetric

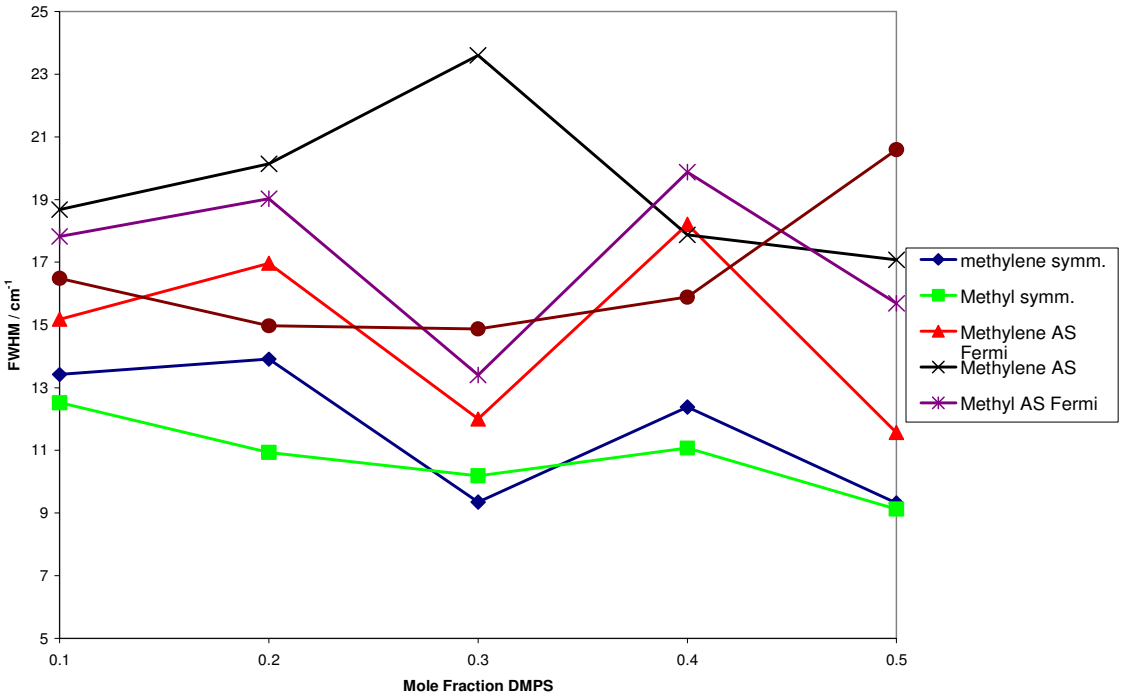

Figure 4.5: The variation of FWHM values with composition for the CH stretching bands. AS is short for asymmetric.

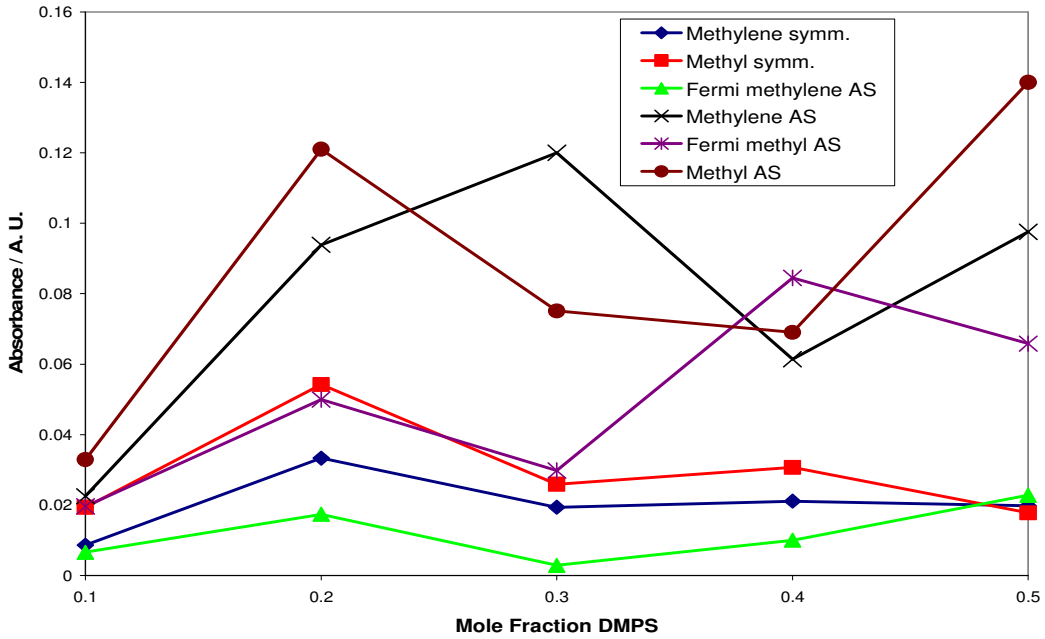

Figure 4.6: The CH Stretching band intensities of bilayers of different composition from 10% DMPS to 50% DMPS.

stretch is an indication that the tilt angle of the 50% DMPS bilayer is greater than the 40% DMPS and lower bilayers.

The symmetric and asymmetric methylene lines both show a similar rise in intensity from 10% to 20% DMPS. The intensity of the CH_2 asymmetric line remains high as the concentration of DMPS increases from 20% to 50% while the CH_2 symmetric line decreases slightly in intensity over the same region. Changes in tilt angle can be expected to affect both lines in a similar manner, so this is unlikely to be the explanation for these observations. It is possible that the chains are rotating into a different conformation.

4.2.2 1600 cm^{-1} carbonyl region

Figure 4.7 shows PM-IRRAS spectra acquired in the 1600 cm^{-1} region. This region is dominated by the C=O stretch of the ester group. The narrow peaks observed are not actually noise but absorption lines of atmospheric water superimposed onto the PM-IRRAS spectra. Line assignments are listed in Table 4.2.

The appearance of this region is qualitatively similar for all compositions. Line positions are charted in Figure 4.8 against bilayer composition. As with the CH stretching region, there is little evidence of systematic shifts of line position with composition, with the exception of the 1538 cm^{-1} band which is attributed to the NH_3^+ symmetric bend. This line moves to longer wavelengths as the

Table 4.2: Line assignments in the 1600 cm^{-1} region[3-7].

Frequency / cm^{-1}	Assignment
1738	C=O stretch (ester moiety)
1650	$-CO_2^-$ anti-symmetric stretch (DMPS only)
1538	NH_3^+ symmetric bend[10,12]
1464	CH_2 scissoring

mole fraction of DMPS is increased. Line positions for this band have been plotted in Figure 4.9 so that this shift can be seen more clearly.

The ester carbonyl groups have a pronounced absorption band at 1738 cm^{-1} due to the C=O stretching vibration. The 1650 cm^{-1} band is attributed the carboxlyate antisymmetric stretch in DMPS. The 1738 cm^{-1} ester band has been observed by Lewis[11] who determined it was composed of two separate lines, one at 1743 cm^{-1} being due to the free ester and the second at 1728 cm^{-1} due to the ester group being hydrated. The high frequency of this ester band suggests that this functional group is in an environment free from water. This is consistent with the position of the CH_2 symmetric stretching band which also indicated that the bilayers were dehydrated. However, the line shape is not symmetrical in any of the bilayers, with a definite tail extending to low frequencies. This suggests that there may be a small hydrated ester band present at 1728 cm^{-1} – which implies that there is a small population of molecules with hydrated ester groups.

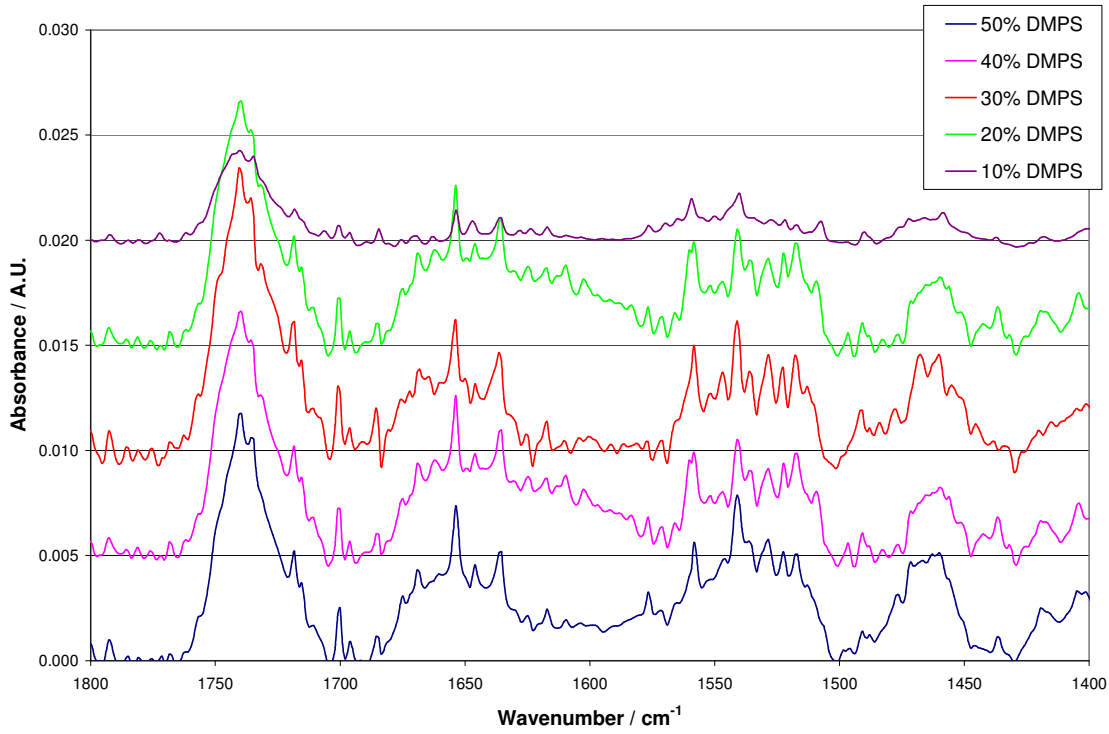

Figure 4.7: PM-IRRAS spectra at 1600 cm^{-1} for bilayers with the given mole fraction of DMPS in DMPE Spectra are offset for clarity with 10%, 20%, 30%, 40% and 50% DMPS consecutively from bottom to top.

Line widths are shown in Figure 4.9 as a function of composition. The NH_3^+ symmetric bend line shows a consistent fall in FWHM as the DMPS concentration is increased. The FWHM of the carboxylate stretching line is much larger when DMPS is at 10% mole fraction. This suggests that the DMPS head groups are in a significantly different environment at these low concentrations. It can be speculated that at higher concentrations, neighbouring DMPS atoms become sufficiently close as to

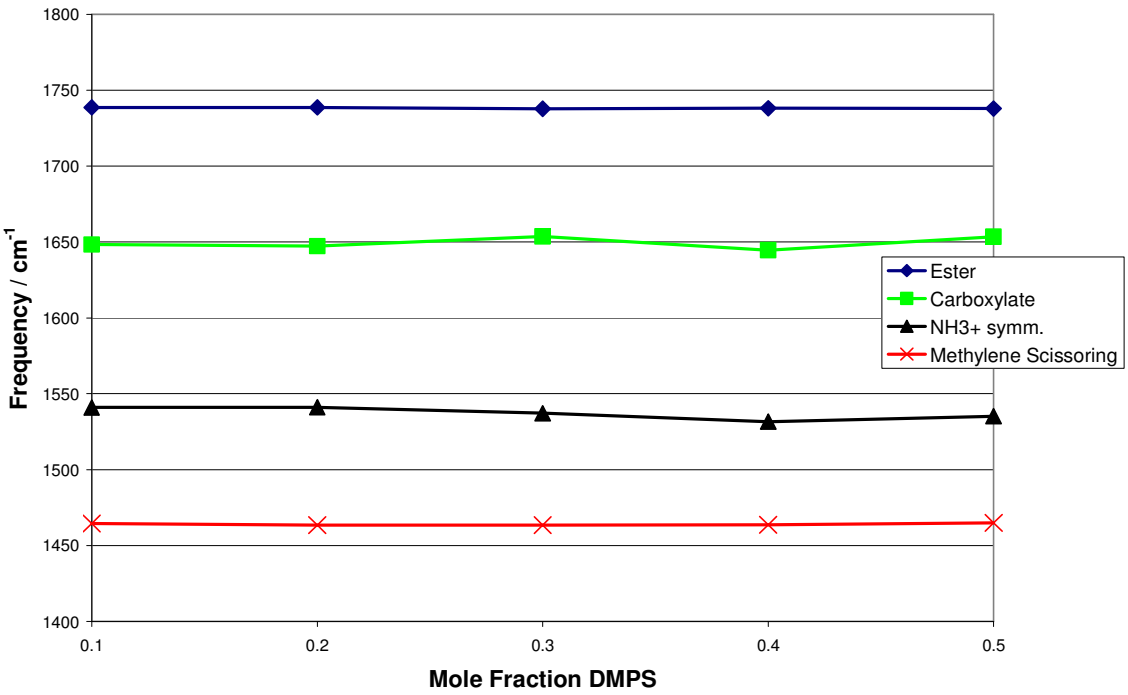

Figure 4.8: The effect of bilayer composition on line positions in the 1600 cm^{-1} region. There is little variation with the exception of the NH_3^+ symmetric bend absorption, which is shown in greater detail below.

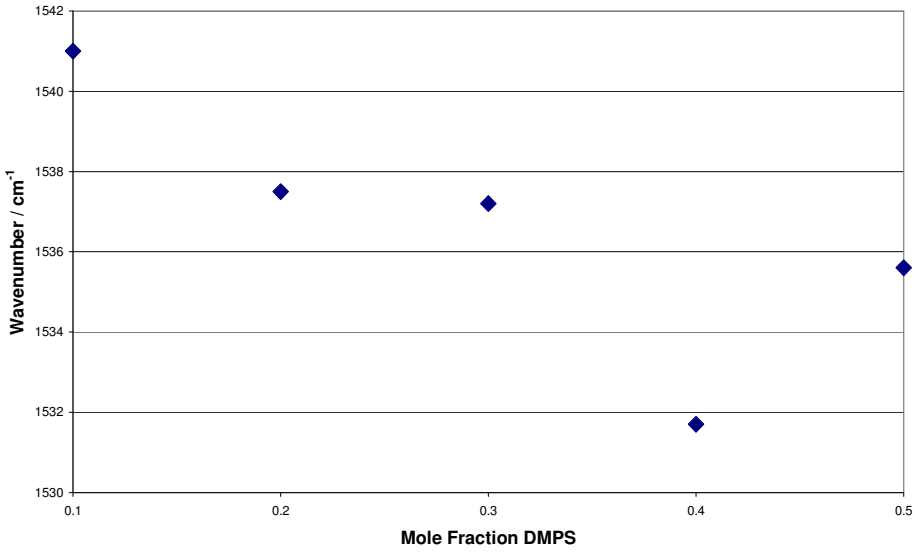

Figure 4.9: Effect of composition on the NH_3^+ symmetric bend absorption frequency. There is a general red shift with DMPS concentration.

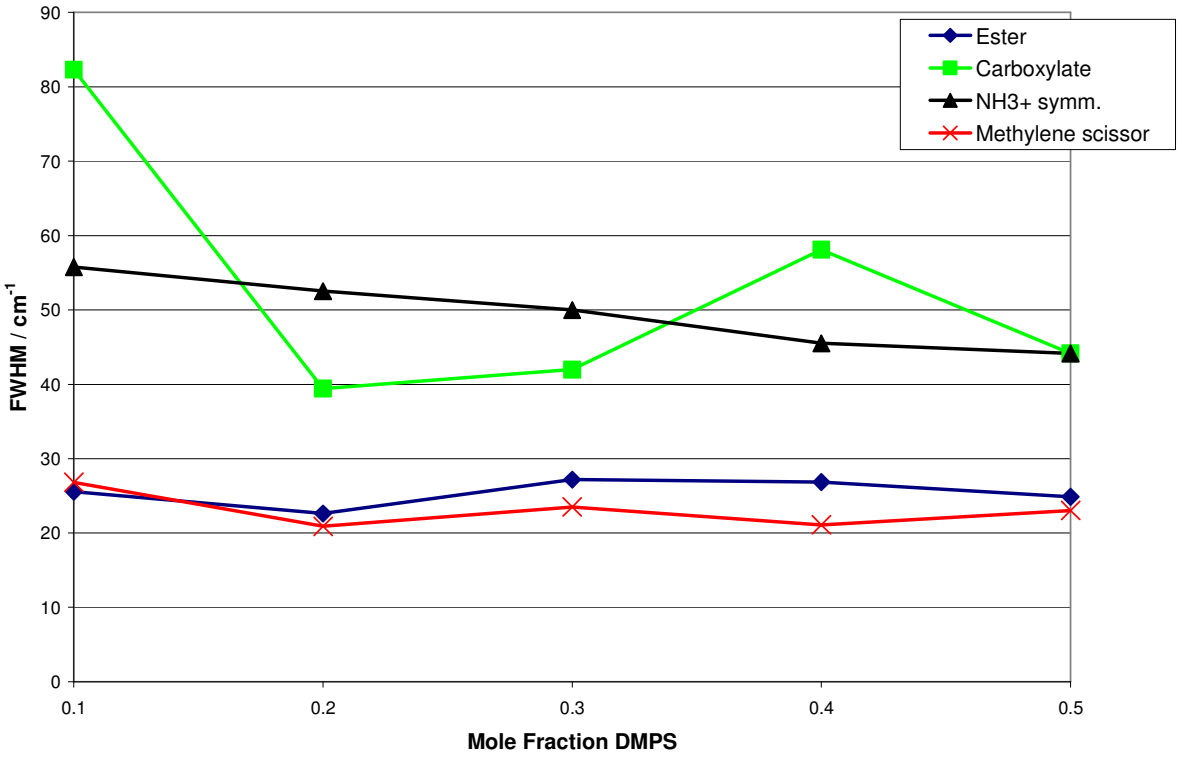

Figure 4.10: The variation of FWHM values with bilayer composition for lines in the 1600 cm^{-1} region. NH_3^+ and COO^- lines show a decrease in FWHM with DMPS mole fraction.

influence or restrict the conformational freedom on the DMPS head groups, presumably by virtue of their electric charge.

The 1538 cm^{-1} does show significant variation, in both position and line width (Figures 4.9 and 4.10). This line has been assigned to the symmetric bending mode of the NH_3^+ functional group[12]. Its frequency increases as the mole fraction of DMPE is increased. Similarly, line width increases with step with the concentration of DMPS. Both DMPS and DMPE have this moiety: undoubtedly this band is a sum of contributions from both molecules.

Line width is inversely proportional to the lifetime of the excited state[13]. A transition with a long lifetime will have a small line width compared to a transition with a short lifetime. The decrease in line width of this line as the concentration of DMPS increases means the lifetime of this transition increases.

Collisions with other molecules and atoms are a major line broadening process. If one imagines the exposed head groups free to wave around on the surface of the bilayer as a result of thermal fluctuations – Brownian motion – it is easy to conceive that collisions with neighbouring head groups will occur often. The decrease in line width means fewer collisions – the NH_3^+ moiety must be in a more ordered local environment. This is suggestive that the addition of DMPS serves to increase the degree of ordering in the head groups. The observed red shift of the NH_3^+ line may be related to this process.

The position of the CH_2 scissoring band (1464 cm^{-1}) is sensitive to packing[13]. Triclinic packing gives rise to a band frequency of 1473 cm^{-1} whilst 1468 cm^{-1} indicates hexagonal packing. The observed band frequency is consistently below either value. Triclinic packing can thus be ruled out. This suggests that the bilayer packing is predominately hexagonal in nature. The low frequency of this band may indicate either an absence of solvent or that packing may be less organised.

Figure 4.11 charts the variation of line intensity with composition. Qualitatively, there is a similarity in the shape of all curves. The absorption intensities of all

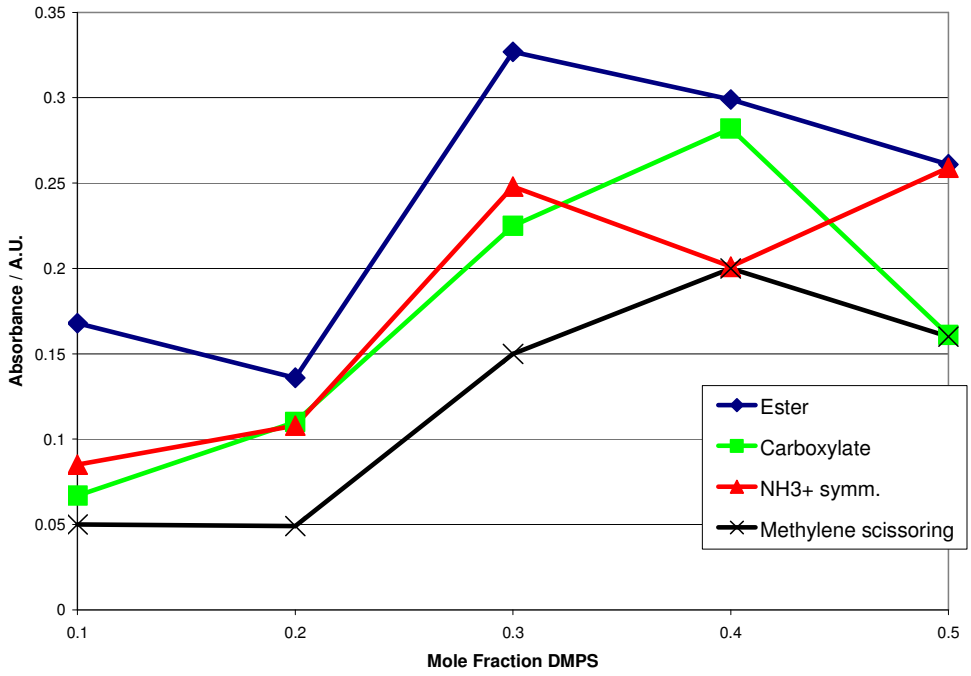

Figure 4.11: The effect of bilayer composition on the line intensities in the 1600 cm^{-1} region.

lines are small at low molar ratios of DMPS. Above 20% DMPS, there is a sharp increase in amplitude: bilayers containing 30% or more DMPS all display stronger absorption lines.

The carboxylate stretching band is most interesting. This band due to DMPS alone and thus its intensity might be expected to be proportional to the fraction of DMPS contained in the film. This is indeed broadly true up to 40% DMPS. At 50%, however, the intensity undergoes a substantial fall. As PM-IRRAS is sensitive to the alignment of the transition dipole with respect to the surface normal: the fall in intensity can be explained by the carboxylate group shifting

in alignment at the highest DMPS concentrations to one that is directed more parallel to the supporting Au substrate.

Casal *et al.* reported this line to have a frequency of 1640 cm^{-1} in the anhydrous state and 1621 cm^{-1} when hydrated[5]. The high frequency observed here is consistent with the bilayer being anhydrous. This is consistent with the ester and CH_2 symmetric stretch band positions. It should be noted that Casal *et al.* observed that POPS carboxylate moieties would bind with Li^+ (aq) ions, losing their water of hydration in the process[15]. Observed line positions were at 1640 cm^{-1}, hence close association with a positive charge could also account for the carboxylate band appearing at 1650 cm^{-1}.

The ester stretch, NH_3^+ asymmetric stretch and CH_2 scissoring bend lines all display a similar theme: line intensities are low at low concentrations of DMPS but undergo an abrupt increase at 30% DMPS. Absorption strengths remain high up to 50% DMPS. It was concluded from the behaviour of the CH stretching lines that this phenomena is unlikely to be caused by a major shift in the orientation of the lipid molecule. The increase in intensity of the CH_2 scissoring bend line is most likely due to a reordering of the acyl chains rotating to a new conformation. The changes seen in the intensities of the CH stretching lines supports this hypothesis, as they must be a result of conformational changes also.

4.2.3 1100 cm^{-1} phosphate region

Figure 4.12 shows the PM-IRRAS spectra acquired in the 1100 cm^{-1} region for bilayers of different compositions. Line assignments are tabulated in Table 4.3. The variation of line position with composition is shown in Figure 20. The narrow lines appearing above 1300 cm^{-1} are due to water vapour. These water vapour lines have FWHM values of 2-3 cm^{-1}. This is an indication that the true resolution of the Bruker FTIR spectrometer was in this range (absorption lines in the gas phase are typically considerably less than 1 cm^{-1}, thus the broadening effect is due to the spectrometer response).

Line positions of these absorptions is given in Figure 4.13. Since the 984 cm^{-1} C-NH_3 stretching band is only observed in three of the spectra, this line will not be considered further: it is inadvisable to attempt to discern trends with only three data points. No systematic shifts in line position are observed with composition. Figure 4.14 charts changes of absorbance with composition.

Table 4.3: Assignments in the phosphate region[5,15].

Frequency / cm^{-1}	Assignment
1231	PO_2^- anti-symmetric stretch
1108	PO_2^- symmetric stretch
1078	C-O[P] anti-symmetric stretch
984	C-NH_3 stretching

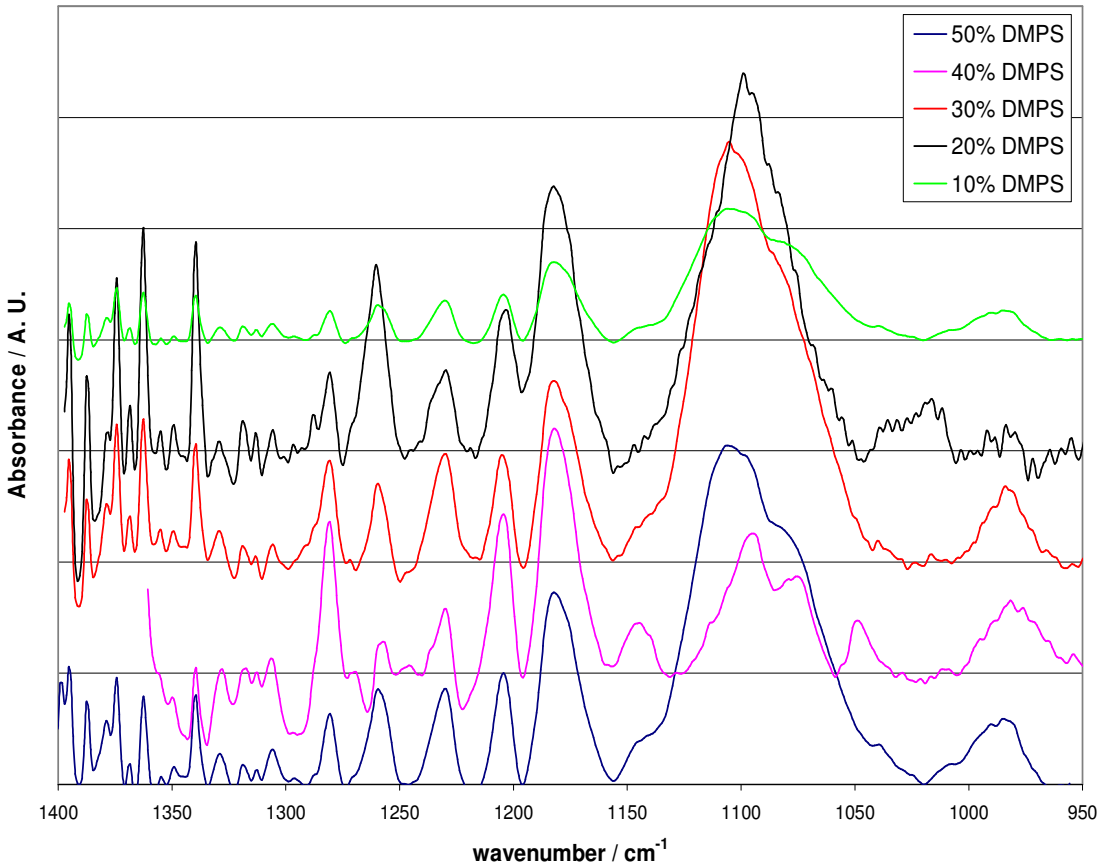

Figure 4.12: The phosphate stretching region. Spectra acquired for differing bilayer composition are shown, offset for clarity. 10% DMPS mole fraction appears at the top with the 50% DMPS bilayer at the bottom. The narrow lines observed above 1300 cm^{-1} are due to atmospheric water vapour.

The PO_2^- antisymmetric line was observed at 1231 cm^{-1}. Selle and coworkers observed that the position of this line varied with hydration: from 1228 cm^{-1} when hydrated to 1246 cm^{-1} when dehydrated[16]. The position of the PO_2^- antisymmetric line has been observed at 1240 cm^{-1} when complexed with Li^+, 1230 cm^{-1} when complexed with NH_4^+ and 1220 cm^{-1} when hydrated[5,15]. It

does not seem likely that the phosphate group is hydrated. DMPS was supplied as the sodium salt, so the presence of the ammonium ion seems unlikely. While complexation with Na^+ may at first sight seem an attractive propostion, an explanation must be sought as to why the position of this line will shift for both DMPS *and* DMPE molecules. At low DMPS concentrations, there are far more DMPE molecules than Na^+ ions. If complexation with Na^+ were the cause, in these circumstances we would expect to see two populations – one whose line had shifted due to complexation and another which was composed of uncomplexed PO_2^- groups. The absence of two lines or even a broadening of this line at low DMPS concentrations rules out complexation with Na^+.

That this line appears so close to that reported by Casal seems to be no coincidence: the NH_3^+ moiety is rather similar to the ammonium ion. It hence seems plausible that the phosphate group is complexed with the NH_3^+ moiety of a neighbouring molecule. The NH_3^+ moiety of DMPE is at the tip of the head group: hence the DMPE head group must be lying flat parallel to the surface for it to complex with the phosphate group of a neighbouring lipid. The effects of composition on line width are shown in Figure 4.15. No obvious trend with regards to film composition is apparent.

The phosphate symmetric stretching line appears at 1108 cm^{-1}. This line is rather broad (Figure 4.15), suggesting that the phosphate group retains considerable rotational freedom (rotational freedom will result a large number

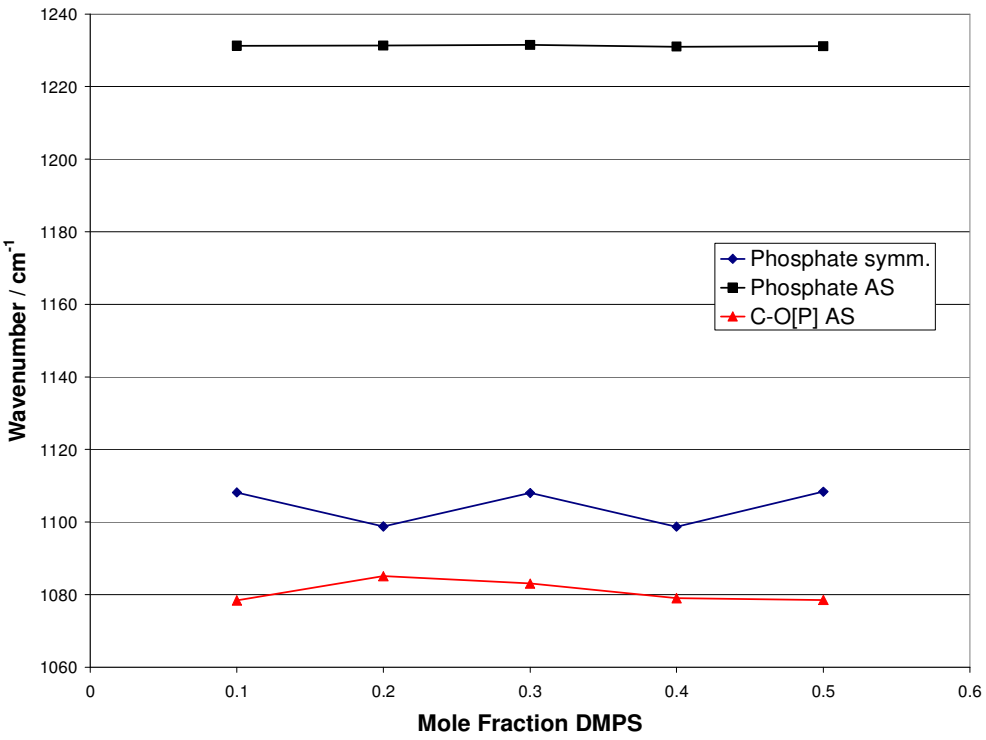

Figure 4.13: The variation of line positions with composition in the 1100 cm^{-1} region for the phosphate anti-symmetric (phosphate AS), phosphate symmetric (phosphate symm.) and C-O[P] anti-symmetric (C-O[P] AS) bands.

of rotational modes being energised and hence extensive P and R branches. The low resolution of the FTIR coupled with collision broadening processes mean the individual vib-rotational lines will appear as one broad band).

The intensity of both symmetric and anti-symmetric phosphate lines does not vary in any systematic way with composition. It can thus be concluded that the tilt angle of the phosphate group is not significantly shifted by changes in bilayer composition.

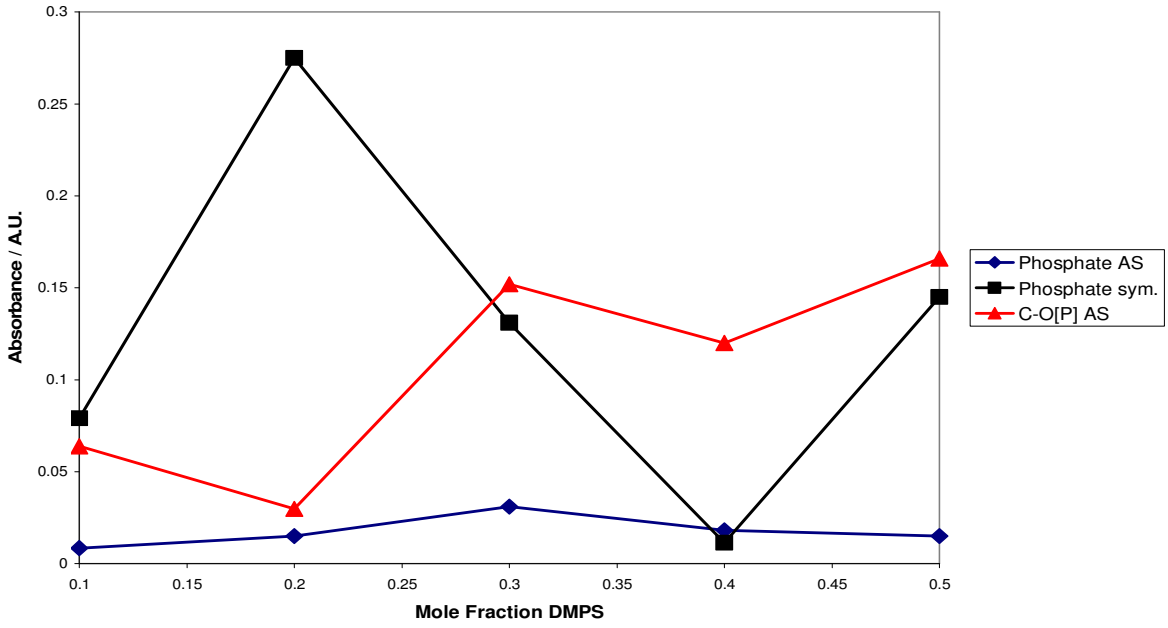

Figure 4.14: The variation of absorption intensities of the phosphate AS, phosphate symmetric and C-O[P] AS bands with bilayer composition.

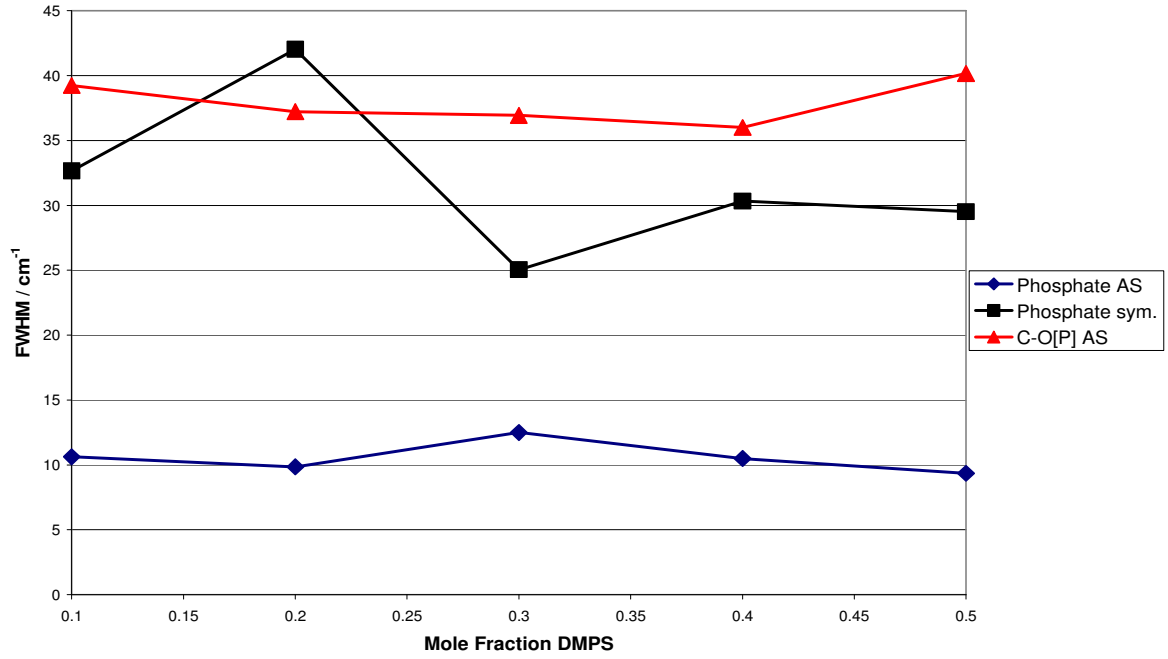

Figure 4.15: The effect of bilayer composition on the line widths of the phosphate AS, phosphate symmetric and C-O[P] anti-symmetric bands.

Appearing as a shoulder on the phosphate symmetric stretching line is the anti-symmetric stretching line of C-O[P]. This is another broad band which also implies that the phosphate group is relatively unrestrained in its conformational motion. Interestingly, the intensity of this band is small at low DMPS concentrations, but considerably enhanced at 30% DMPS and above (Figure 4.14). This indicates that the phosphate group adopts a more upright conformation at high DMPS mole fractions. It is rather surprising that this line should show changes in intensity while the phosphate stretching lines do not. This can be explained if it is hypothesised that the PE head group changes in orientation with respect to the phosphate, which itself does remains in the same conformation regardless of membrane composition. To explain the increase in intensity, the dipole of the C-O[P], and presumably the PE head group, must adopt a more vertical orientation with respect to the substrate when the DMPS concentration is 30% or greater.

4.3 Conclusions

Absorption lines due to the tail groups do not show any significant or systematic changes in position due to bilayer composition. Given that the tail groups are identical in both molecules this is perhaps not surprising. The position of the CH_2 scissoring absorption suggests that lipid molecules are ordered hexagonal close packed. However, the lower than expected frequency suggests that ordering is not complete. This, again, is not

surprising. The LB/LS bilayers were deposited at 42 mN m^{-1} pressure in the gel phase: the lipid molecules can be expected to be tightly packed and hexagonal packing is the most efficient in terms of space utilised. The line position indicates some disorder in the packing – this is again understandable as a LB/LS film is likely to have significant numbers of defects; the deviation of this line is evidence of this effect.

The abrupt increase in line width of the carboxylate stretch at 10% molar fractions of DMPS suggests a significant fraction of the DMPS head groups are not complexed, which is the case at higher mole fractions. It can be speculated that this is due to DMPS molecules forming close aggregations when the concentration is high.

Up to 40% DMPS, the intensity of the carboxylate line has a linear dependence on DMPS concentration. Above this concentration, the abrupt fall in intensity can only be explained by a change in the orientation of the carboxylate moiety, with this group becoming nearly parallel to the substrate. This can be explained if we hypothesise that at this high concentration, the DMPS head groups become aligned in order to pack more efficiently. It is entirely plausible to suggest that the carboxylate head may at high DMPS concentrations adopt a conformation where it can approach the NH_3^+ moiety of a neighbouring molecule, thereby decreasing energy and increasing packing. This would explain why the NH_3^+ group continues to show a decrease in tilt angle at the highest concentrations of DMPS while all other lines show an *increase* in tilt angle: at low DMPS fractions the NH_3^+ group

would likely associate with the phosphate group, but as the concentration of DMPS increased the probability of an association with the carboxylate group would increase. Molecular dynamics simulations of PE have indicated that the PE head group has a tendency to adopt a conformation that is parallel to the bilayer (perpendicular to the bilayer normal)[17,18]. In contrast, molecular dynamics simulations of DPPS indicated that the serine head group had a tendency to adopt a vertical conformation[19]. This is the opposite to what the line intensity of the carboxylate group for the 50% DMPS bilayer indicates: its fall in intensity can only be explained by a shift in the conformation of this group to a more horizontal conformation.

The NH_3^+ symmetric bend absorption line shows a systematic red shift and decrease in line width as the mole fraction of DMPS is increased. This decrease in line width is suggestive of an increase in order of the phospholipid head groups at high concentrations of DMPS. It is an indication that the NH_3^+ functional group has a tendency to complex with neighbouring lipid molecules – presumably DMPS molecules – as the DMPS concentration increases. This observation could be explained by hypothesising that DMPS molecules form small aggregations at high concentrations but have a tendency to be more randomly distributed throughout the bilayer at low concentrations. Complexing in this fashion would also serve to decrease the energy of the absorption transition – and indeed the NH_3^+ symmetric bend line displays a tendency to shift to longer wavelengths as the fraction of DMPS is increased.

The trends displayed by the carboxylate and ammonium symmetric stretch lines can both be explained by hypothesising that DMPS rafts form in the bilayer at high DMPS concentrations. The decrease in line width observed in the CH stretch bands supports this – the acyl tails could be expected to be more ordered if DMPS has a tendency to form rafts rather than be randomly distributed.

The methyl and methylene stretching lines indicate some rotational changes occur in the acyl tails as the DMPS concentration increases. In particular, the methyl scissoring absorption shows a reordering involving rotational changes occurs when the DMPS concentration is 30% or more. The C-O[P] band also shows a stepwise change in ordering when DMPS concentrations reach 30%. This is suggestive that there is a critical threshold for the DMPS concentration which, if exceeded, results in a reordering of the bilayer. Interestingly, DMPS concentrations in biological membranes lie below this level: DMPS makes up typically 10% in the cell membrane of a bacterium[20] and 20-25% in the inner leaflet of a mammalian cell[21].

Examination of the symmetric and asymmetric CH_3 lines suggested the lipids underwent a increase in tilt angle as the mole fraction of DMPS increased from 40% to 50%. However, this observation was not mirrored by any other absorption, suggesting that the lipids do not change in tilt angle. This infers that the methyl groups instead undergo a local change in conformation – this links to the observation of the methylene lines that the acyl tails undergo conformal changes.

Line positions of the methylene symmetric, ester and phosphate asymmetric groups indicate that the bilayers contained little water regardless of composition. However, the broadness of the 1738 cm^{-1} ester band may be due to a small population of hydrated molecules. Interestingly, Bach and Miller have reported that DPPS bound 3.5 water molecules per lipid molecule using differential scanning calorimetry[22]. There is evidence for rotational and conformal changes in the tail groups. Similar changes have been observed in DMPC/cholesterol systems[23].

It should be noted that each individual leaflet is in a different environment: the inner leaflet has its head groups in contact with the substrate while the head groups of the outer leaflet are freely exposed to the air. Though little evidence of the existence of two separate environments can be seen in the data, this possibility cannot be discounted. Zawisza *et al*. reported differences between the inner and outer leaflets of a DMPC bilayer on an SiO_2 coated gold substrate[24]. The outer leaflet, freely exposed to air had a tilt angle of 55^o while the tilt angle of the inner leaflet was estimated to be 20^o. Garcia-Araez reported a similar finding with a DMPC bilayer adsorbed onto Au (111)[25]: the bottom leaflet in contact with the gold surface was tilted 10^o less than the top leaflet which was in contact with 0.1 M NaF solution. This issue warrants further investigation.

4.3 References

1. Zamlynny, V., PhD Thesis, University of Guelph (2002)

2. Hollas, J. M., 1987, *Modern Spectroscopy*, Wiley

3. Brumfeld, V., Bach D., Miller I. R., (1991), *Eur. Biophys. J.*, **19**:287

4. Hubner, W., Mantsch H. H., Paltauf, F., Hauser, H., (1994), *Biochemistry*, **33**:320

5. Casal, H. L., Mantsch, H. H., Hauser, H., (1987), *Biochemistry*, **26**:4408

6. Choi, S., Ware, W., Lauterbach, S. R., Phillips, W. M., (1991), *Biochemistry*, **30**:8563

7. Hull, M. C., Cambrea, L. R., Hovis, J. S., (2005), *Anal. Chem.*, **77**:6096

8. Wolkers, W. F., Oldenhof, H., Glasmacher, B., (2010), *Cryobiology*, **61**:108

9. Tuchtenhagen, J., Ziegler, W., Blume, A., (1994), *Eur. Biophys. J.*, **23**:323

10. Bach, D., Miller, I. R., (2001), *Biochim Acta Biophys,* **1574**:318

11. Lewis, R. N. A. H., McElhaney, R. N., (2000), *Biophys. J.,* **79**:2043

12. Suzuki, S., Ohshima, T., Tamiya, N., Fukushima, K., Shimanouchi, T., Mizushima, S., (1959), Spectrochimica Acta, **11**:969

13. B. H. Stuart, 2004, *Infrared Spectroscopy: Fundamentals and Applications*, Wiley

14. Horswell, S. L., Zamlynny, V., Li, H-Q, Merrill, A. R., Lipkowski, J., (2002), *Faraday Discuss*. **121**:405

15. Casal, H. L., Martin, A., Mantsch, H. H., Paltauf, F., Hauser, H., (1987), *Biochemistry*, **26**:7395

16. Selle, C., Pohle, W., (1998), *Biospectroscopy*, **4**:281

17. Pink, D. A., Belaya, M., Levadny, V., Quinn, B., (1997), *Langmuir*, **13**:1701

18. Damodaran, K. V., Merz, K. M., Gaber, B. P., (1992), *Biochemistry*, **31**:7656

19. Pandit, S. A., Bostick, D., Berkowitz, M. L., (2003), *Biophys. J.,* **85**:3120

20. Alberts, B., Johnson, A., Lewis, J., Raff, M., Roberts, K., Walter, P., 2002, *Molecular Biology of the Cell*, 4th edition, Garland Science, US

21. Kiessling, V, (2009), *Biochim Acta Biophys-biomembranes*, (2009), **1788**:64

22. Bach, D., Miller, I. R., (2005), *Chem. Phys. Lipids*, **136**:67

23. Brosseau, C. L., Bin, X., Roscoe, S. G., Lipkowski, J., (2008), *J. Electroanal. Chem.,* **621**:222

24. Zawisza, I., Wittstock, G., Boukherroub, R., Szunerits, S., (2008), *Langmuir*, **24**:3922

25. Garcia-Araez, N., Brosseau, C. L., Rodriguez, P., Lipkowski, J., (2008), *Langmuir*, **22**:10365

5. Electrochemistry

A number of techniques are available to investigate the properties of species adsorbed onto an electrode surface. Differential capacitance reveals the presence of phase transitions – which are usually related to the processes of adsorption/desorption and reorganisation of the layer structure. Chronocoulometry examines the surface energy of an adsorbed film to be determined while impedance spectroscopy is can be used to measure the permeability of the adsorbed layer.

5.1 Differential Capacitance

As outlined in Section 2.2, the interface between electrode and electrolyte is a region that experiences charge separation and hence capacitance. Differential capacitance (DC) allows this property to be measured. The capacitance is affected by adsorbed species, making DC a good technique to use to characterise adsorbed films.

5.1.1 Results

Bilayers formed through vesicle fusion and LB/LS deposition were deposited onto the surface of an Au (111) electrode. The differential capacitance of bilayers formed by each method will be considered in turn.

Bilayers formed by vesicle fusion

The differential capacity of various compositions of phospholipid bilayers was investigated. Figure 5.1 shows a typical scan for a 10% DMPS in DMPE bilayer as the potential is ramped positive. Typical day to day variations in the curves was of the order of 3 μF cm^{-2}. A number of features are apparent. The capacity is lower than that for bare gold. This is to be expected: DMPE and DMPS are largely composed of the hydrocarbon chain which has a dielectric constant of approximately 2-4[1]. This is smaller than the dielectric constant of the water that is displaced. Hence the capacitance should be lower, as is observed.

Water has a dielectric constant of 80 at room temperature[1]. It should be noted that experiments suggest that water molecules when subjected to the large electric fields present close to the electrode assume a more ordered ice-like structure[2] with a substantially lower ε_r. Even taking account of this effect, the dielectric constant of these entrained water molecules is larger than the values measured for hydrocarbons.

The peak observed at -0.4 V is similar to that seen with DMPC bilayers[3]. DMPC was observed to undergo a phase change where the lipid molecules became reordered. It is hence likely that a similar process is occurring here. There is a similar peak close to 0 V which may be caused by another reordering of the bilayer.

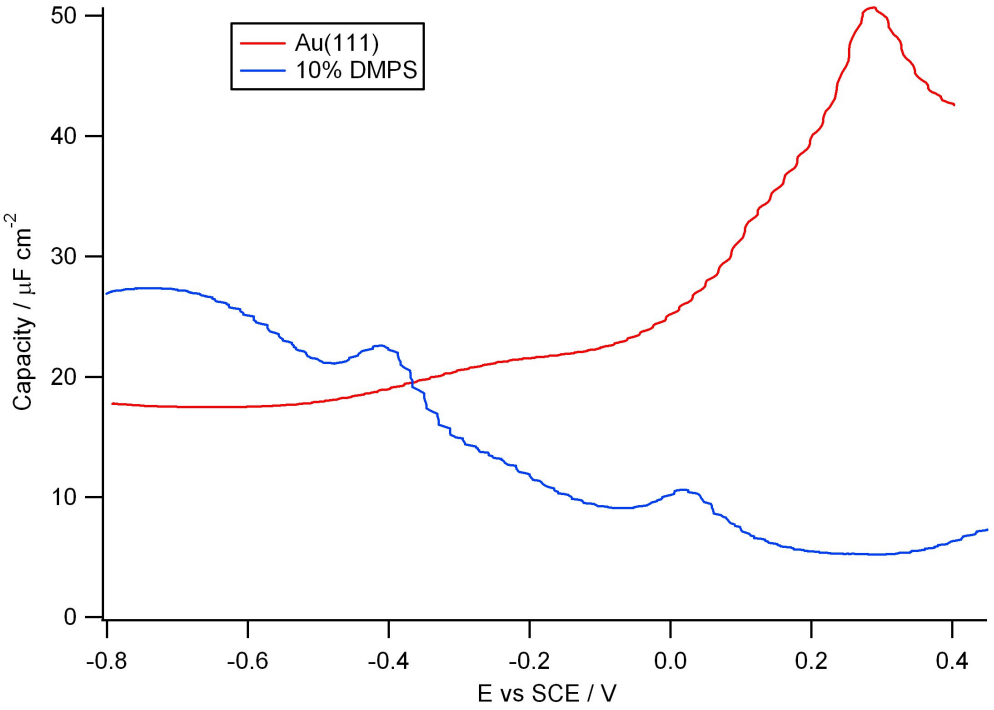

Figure 5.1: Capacities of the bare gold (111) electrode and a 10% DMPS in DMPE bilayer formed through vesicle fusion.

The PZC for Au (111) is 0.288 V relative to the SCE[4]. This point corresponds to the minimum capacity. At this point, the bilayer can be expected to adhere to the substrate most strongly. At potentials other than this, a substantial electric field exists between electrode and solvent: this can be expected to drive water molecules into the bilayer, increasing capacity. Indeed, this is observed: capacity increases slightly as the potential becomes more positive and substantially as the potential is driven more negative than the PZC.

Figure 5.2 shows the capacitance curves for bilayers of several different compositions. A number of trends can be discerned. The phase transition at

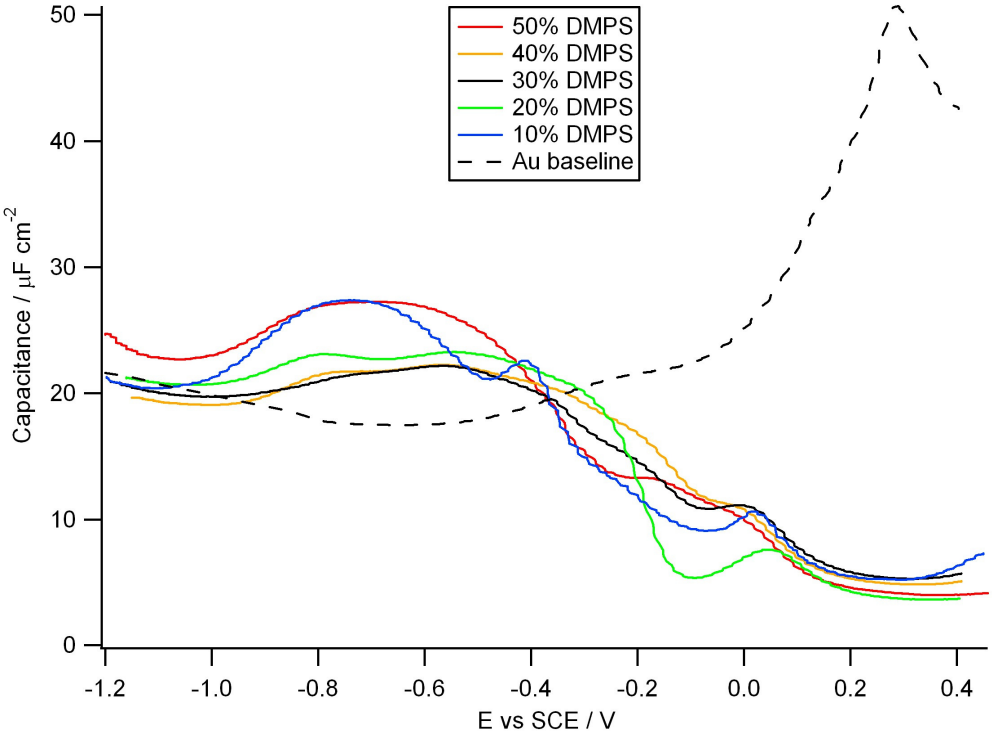

Figure 5.2: Capacities of bilayers of varying compositions formed by vesicle fusion. The features observable in the 10% DMPS bilayer capacity curve at 0 V and -0.4 V are phase transitions. These become less prominent as the concentration of DMPS is increased.

-0.4 V becomes less pronounced, merely appearing as a change in gradient in lipid mixtures of greater than 10% DMPS. With the exception of the 50% DMPS bilayer, there is a regular progression for this feature to appear at less negative potentials. The O V feature also displays a similar trend to become less prominent as the fraction of DMPS is increased.

Langmuir-Blodgett Langmuir-Schaeffer Bilayers

Figure 5.3 shows the capacity of LB/LS bilayers. The scans were limited to a

maximum negative potential of -0.8 V as a precaution in order to preserve bilayer integrity.

A pure DMPS bilayer has a higher capacity than any of the mixed composition or DMPE bilayers. DMPS presents less of a barrier to the underlying electrode. This is possibly due either to the overall negative charge on the molecule disrupting the organisation of the bilayer or the charge allowing solvent molecules greater access through the film.

The DMPE bilayer exhibits a capacity minimum close the PZC. It has the lowest overall capacitance of any of the films characterised here. Isotherms of DMPE monolayers show that a pure DMPE monolayer compresses to form a tightly packed film (see Section 7.1.4), as a consequence of the small cylindrical shaped head group. The low capacity observed here is a reflection of this and supports the idea that DMPE forms well organised mono and bilayers. Infrared spectroscopy of DMPE monolayers shows that the molecules form well packed films with few gauche conformations in the tails[5].

DMPS displays a phase transition peak at -0.45 V: DMPE has an analogue at -0.65 V. The position of this peak shifts with the composition of the bilayer. Mixed bilayers which have a mole fraction of less than 20% DMPS behave similarly to DMPE with a peak at -0.65 V. Mixtures with between 30% and 50% DMPS exhibit a phase transition peak at -0.55 V.

Both DMPS and DMPE show a feature at around +0.05 V (for DMPS) and

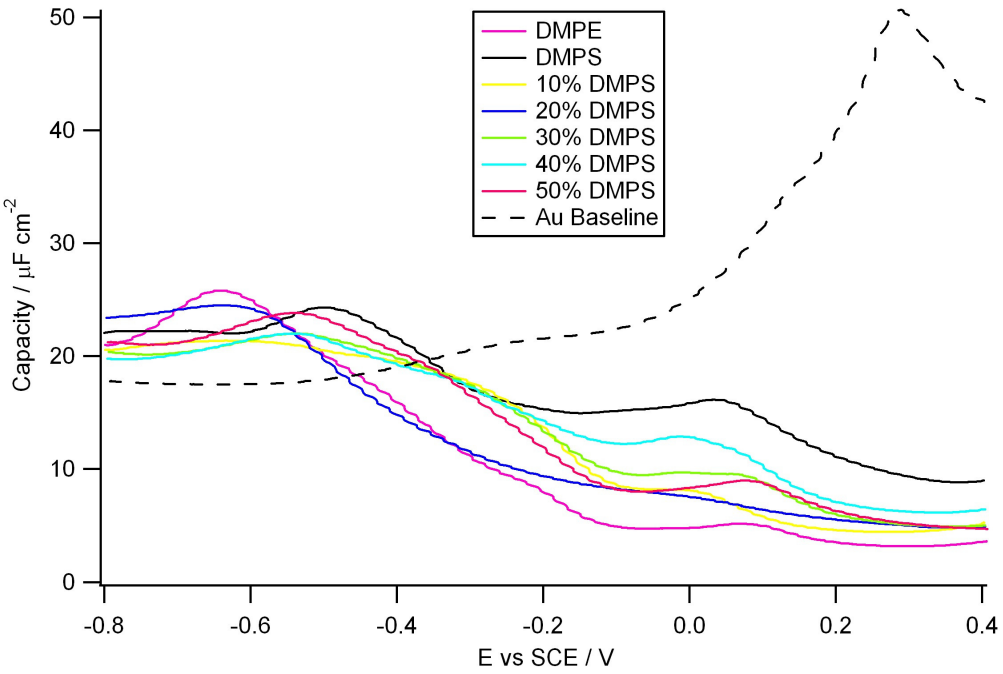

Figure 5.3: Capacities of LB/LS bilayers with differing compositions. As with the bilayers formed through vesicle fusion, the peaks at 0 V and -0.4 V are due to phase transitions within the film.

+0.08 V for DMPE. A mixed bilayer with 50% DMPS exhibits a similar peak at +0.1 V. This peak then shifts to 0 V for all other lipid compositions. Interestingly, bilayers containing 40% and 30% DMPS also show evidence of a peak at +0.1 V.

5.1.2 Discussion

Minimum capacitance values range from approximately 4 µF cm^{-2} for DMPE to 8 µF cm^{-2} for DMPS. Rubinstein *et al.* measured the capacities of a

trishydroxamate binder monolayer on gold to be 4 μF cm^{-2} using EIS[5]. The equivalent capacity for a bilayer would be 2 μF cm^{-2}. Lindholm-Sethson when investigating multiple layers of dipalmitoylphosphatidic acid (DPPA) on Au with EIS quoted a value of 1.2 μF cm^{-2} per monolayer[6] (0.6 μF cm^{-2} for a bilayer). Interestingly, measurements of DPPA bilayers indicated two separate capacitance values (capacities were measured using EIS). These films had the hydrophilic head groups facing the gold substrate so the possibility exists that there is solvation water associated with the head groups at the electrode surface. The second, larger, capacitance value was attributed to charging of a double layer in the water at the electrode surface.

The minimum capacities determined in Section 5.1.1 are thus somewhat high. A possible explanation for this is water entrained in the bilayer. In light of the observations noted by Lindholm-Sethson[6], water surrounding the head groups facing the Au substrate would seem to be a plausible explanation.

Surface coverage, θ, can be calculated from the formula[7]:

$$\theta = \frac{C_0 - C_1}{C_0 - C} \qquad [5.1]$$

C_0 is the capacity of the bare electrode, C_1 the capacity of the film coated electrode without defects and C the capacity of the coated electrode with defects. At a potential of 160 mV, C_0 is 36 μF cm^{-2}. The capacity of a defect free bilayer is in theory[8] 0.8 μF cm^{-2}. From these data points, the coverage of films formed *via* vesicle fusion is approximately 80% and that of the LB/LS bilayers is 85%. This value for the vesicle formed bilayers agrees well with

published values[3,9], though Oleson noted higher coverage values - 85% - for more hydrophilic substrates such as fused silica and sapphire[10]. The LB/LS coverage seems rather low: however, the theoretical capacity of a bilayer assumes water is absent. The lower than expected coverage value is most likely an indication that the LB/LS bilayers contain significant water entrained within their structure, as noted.

The feature close to 0 V is at a potential where the bilayer is adsorbed onto the substrate. Similar features have been observed in the differential capacity curves of other adsorbed membranes. The cationic surfactant N-decyl-N,N,N-trimethylammonium triflate (DeTATf) exhibits such a feature when adsorbed onto an Au (111) substrate[11], which has been attributed to a phase transition caused by a rearrangement of the orientation of the adsorbed molecules. Likewise, the rearrangement of *N*-dodecyl-*N*,*N*-dimethyl-3-ammonio-1-propane sulfonate to a hemicylindrical morphology on an Au (111) substrate also features a peak in the capacity[12]. DOPC monolayers on Hg are known to undergo two structural reorientations which are demarked by two pseudocapacitance peaks[13]. An adsorbed monolayer of 1-pyridin-4-ly-hexadecan-1-one on a gold (111) substrate exhibited a phase transition between loosely and more densely packed states[14]. Again, this transition was indicated by a peak in the differential capacity curve. In light of these observations, it is likely that the 0 V pseudocapacitance peak is indicative of a phase transition where the adsorbed bilayer adopts a different configuration.

LB/LS bilayers show a clear trend where mixtures with over 30% DMPS

exhibit similar properties to those of pure DMPS while compositions with 20% or less mole fraction of DMPS appear to behave similarly to DMPE. Hence it is possible to conjecture that bilayers of different compositions appear to be "DMPS-like" or "DMPE-like" at high concentrations of DMPS and DMPE respectively. This leads to the suggestion that there are two possible states: "DMPS-like" and "DMPE-like".

In one state the bilayer properties are determined by DMPE and appear similar to those of pure DMPE. There are sufficient numbers of DMPE molecules to screen out the effects of the negative charge of DMPS. The "DMPS-like" state, however, has so many DMPS molecules that interactions between them (presumably Coulombic in nature) are no longer insignificant, instead becoming a major determinant of bilayer properties.

The "0 V" phase transition peak is especially intriguing in this light. At high DMPS concentration, this peak appears at +0.1 V. At lower DMPS concentration, this peak shifts to 0 V. However, bilayers containing 40% and 30% DMPS display evidence for peaks at *both* positions. This behaviour could be explained if we hypothesise that mixtures of these compositions are composed of regions or domains that are themselves "DMPS-like" or "DMPE-like". In other words this could be evidence that at these concentrations there is a tendency for the bilayer to form DMPE rich and DMPS rich phases.

The question arises: why should this peak shift at all? The obvious difference between DMPE and DMPS is the negative charge. Both potentials are below

the PZC, but at +0.1 V the charge density is closer to zero – DMPS molecules will experience a smaller electric field in this case. This raises the intriguing possibility that this peak is a result of the rearrangement of the head groups. With the negatively charged carboxylate group at the tip of the DMPS molecule, it is reasonable to expect the head group to have the tendency to assume a vertical orientation when subjected to the large negative electric fields observed at potentials below the PZC. A fall in the intensity of the carboxylate stretching line at high DMPS concentrations was attributed to this group pairing up with the NH_3^+ group of a neighbouring molecule (Section 4.10). This 0 V peak may be caused by this rearrangement of the DMPS head groups. This idea lends credence to the idea that this 0 V peak is related to a phase transition induced by a rearrangement of the bilayer.

DMPE-rich bilayers (those with 10 – 20% DMPS) show lower capacities than do DMPC bilayers[3] when both were formed *via* vesicle fusion. This is suggestive that these films contain less solvent than bilayers consisting of DMPC. This in turn implies that the DMPE-rich mixtures have fewer defects and/or higher coverage.

It is interesting to note that the capacities of all bilayer compositions investigated exceeds that of the Au substrate at potentials more negative than -0.6 V. This phenomenon has also been observed for DMPC bilayers[15]. Figure 5.4 illustrates this effect. Burgess *et al.* observed a similar feature with DMPC/cholesterol mixtures[16], sodium dodecyl sulphate[17] and DeTATf[11].

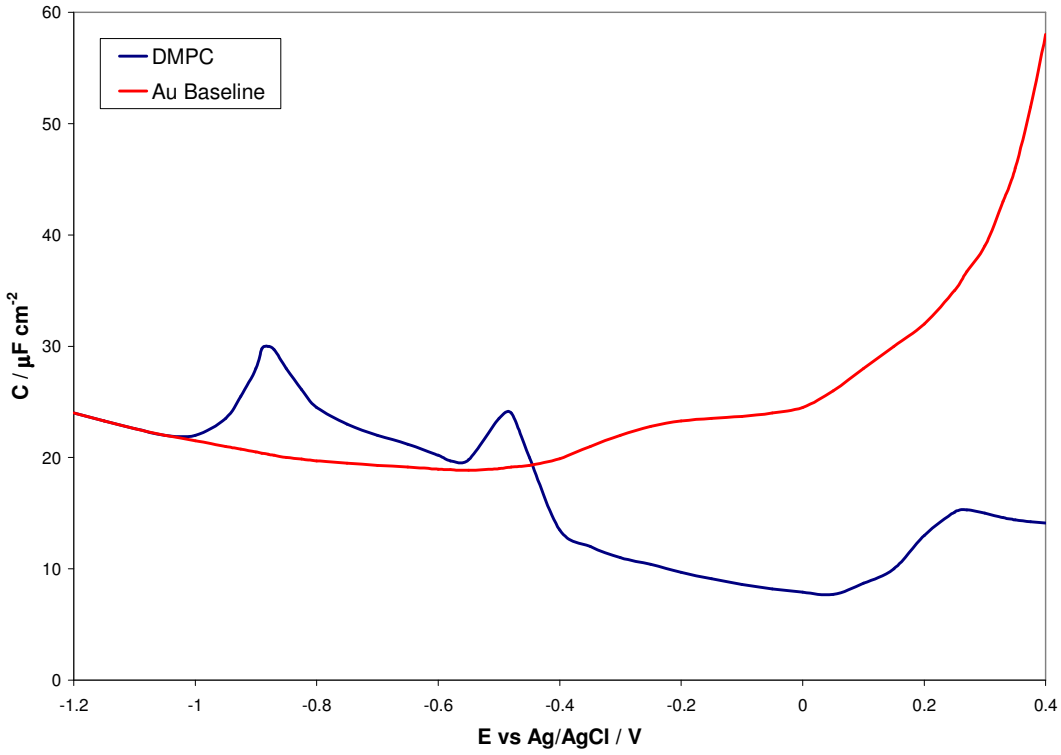

Figure 5.4: The differential capacity of a DMPC bilayer formed by vesicle fusion on an Au (111), as measured by Bin *et al*[15]. The desorption phase transition at -0.9 V can be clearly seen.

At potentials more negative than -1.0 V, the DC curve converges with the Au baseline. This is observed for all mixtures as well as for the systems referenced above. Lipkowski and coworkers have attributed this peak to desorption of the film from the electrode surface[11,15,16]. Bin *et al*. noted that the capacity of a DMPC bilayer formed *via* vesicle fusion showed a peak at -0.4 V after which it remained above the Au baseline until -1.0 V whereupon it converged with the baseline[15]. This was believed to be a phase transition heralding the onset of desorption at -0.4 V, the desorption process becoming

complete as the potential was swept to -0.9 V. Given the similarity of these phospholipid mixtures to the DMPC bilayers investigated by Bin, it seems reasonable to propose a similar underlying cause: the peak observed occurring between -0.4 V (DMPS) and -0.7 V (DMPE) also indicates the onset of desorption of the bilayer from the substrate. This peak will be called “Peak A” to ensure clarity in the following discussion. Table 5.1 lists the position of this peak for differing bilayer compositions. There is a clear trend for this peak to occur at greater negative potentials as the mole fraction of DMPE is increased. Note that, apart from the 10% DMPS bilayer, vesicle formed bilayers have a quite poorly defined Peak A compared to those of LB/LS bilayers.

Similar desorption peaks have been observed in phospholipid monolayers adsorbed onto a Hg substrate. Bizzotto and Nelson attributed a pseudocapacitance peak at -1.3 V vs Ag/AgCl (sat) to the desorption of a DOPC monolayer from the mercury electrode[13]. This desorption process was further investigated by Stoodley and Bizzotto[18] by imaging the adsorbed DOPC monolayer using epi-fluorescence. Fluorophores within the DOPC would fluoresce in the stable environment of an adsorbed monolayer. This fluorescence was progressively quenched as the applied potential approached the phase transition at -0.95 V vs SCE. Nelson interpreted this to be caused by the DOPC head groups moving inward along with electrolyte to the electrode surface. In the light of this, a similar mechanism can be postulated to explain the extended nature of the observed desorption phase transition.

Table 5.1: Position of Peak A: this peak is possibly related to the onset of desorption of the bilayer.

Bilayer Composition	Peak A Position, LB/LS Bilayer / V	Peak A Position, Vesicle Bilayer / V
DMPS	-0.5	
50% DMPS	-0.55	-0.4
40% DMPS	-0.55	-0.55
30% DMPS	-0.55	-0.55
20% DMPS	-0.6	-0.55
10% DMPS	-0.65	-0.6
DMPE	-0.7	

From Figure 5.2, it is apparent that while the capacities of the bilayers converge with that of the bare Au surface, they do not coincide exactly. It was noted that some small variation of capacities could be caused by raising or lowering the height of the working electrode thereby stretching or relaxing the meniscus attaching the electrode to the surface. It is likely that this failure to achieve an exact union with the Au (111) DC curve is a result of this effect, as the differences are very similar to those caused by electrode height. It seems unlikely that any phospholipid will remain adsorbed at these large negative potentials – full desorption is certainly observed with other lipid systems[11,15,16]. However, these seemingly random variations do allow an estimation of the errors to be made: the difference in capacity between the highest and lowest measured bilayer in this region (below -1.0 V) is 5.5 μF cm^{-2}. Hence the error can be estimated to be ±3 μF cm^{-2}.

5.1.2 Conclusions

Burgess (2004) proposed a model to explain the behaviour of a mixed DMPC/cholesterol bilayer system, by combining electrochemistry observations similar to those described above with neutron reflectivity data[16] (neutron reflectometry is described in Chapter 6). It was proposed that a mixed cholesterol and DMPC bilayer that is adsorbed on a Au (111) substrate will first swell and incorporate water into its structure as the electrode potential is swept from positive to negative potentials (relative to the SCE). It is notable that Peak A occurs just before the onset of this rise in bilayer capacity. This phenomenon was related to electroporation of the bilayer leading to water absorption as the electric field strength increases[20]. It seems reasonable to suggest the same effect leads to the increase in capacitance observed with DMPS/DMPE bilayers. Peak A thus may represent a reorganisation of the bilayer which itself allows the absorption of water. Below – 0.7 V, the bilayer detaches from the substrate, allowing water to form a thin layer of approximately 1 nm in thickness between electrode and bilayer. Figure 5.5 is a pictorial representation of the process.

The similarity between DMPC/cholesterol and DMPS/DMPE bilayers allows this mechanism to be proposed as a hypothesis to explain the differential capacitance data. Between 0 V and -0.4 V, the increase in bilayer capacity can be explained by the incorporation of water into the film as a result of water's greater dielectric constant. A peak in capacitance is observed when the bilayer detaches and a thin layer of water interposes itself between bilayer

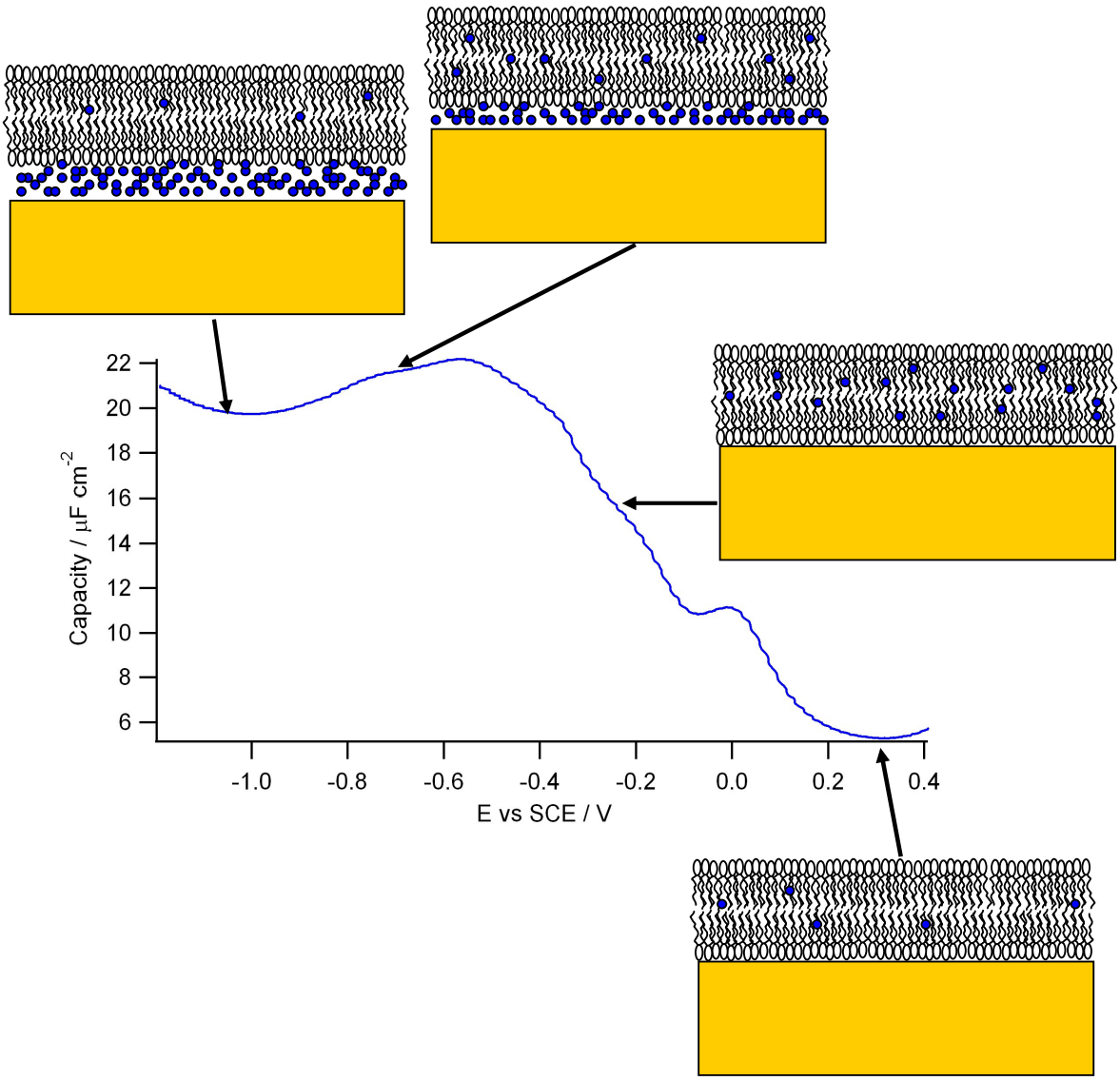

Figure 5.5: A representation of the changes that an adsorbed phospholipid bilayer undergoes in response to changes in potential. The blue dots represent water molecules. As the potential becomes more negative, the layer first incorporates more solvent into its structure until at large negative potentials a thin layer of water forms between the substrate and bilayer.

and substrate. At more negative potentials, the capacity converges towards the bare Au (111) value. It can be speculated that this is caused by a progressive thickening of this water layer as the potential is swept to greater negative potentials.

It may be expected that the negative charge of the DMPS molecule would predispose it to desorb at lower negative potentials than for the zwitterionic DMPE due to Coulombic repulsion. This is indeed observed. Furthermore, there is an orderly decrease in desorption potential as the concentration of DMPS is increased (Table 5.1), suggesting that the bilayer becomes less stable at negative potentials as the mole fraction of DMPS increases.

5.2 Chronocoulometry

Chronocoulometry differs from differential capacitance in that it is a stepped technique. The potential of the working electrode is stepped: the resultant current pulse is measured over time. This technique is very sensitive to the presence of adsorbed species.

5.2.1 Results and Discussion

Chronocoulometry of mixed bilayers formed by vesicle fusion and LB/LS deposition were investigated. Figure 5.6 shows the charge density profiles of bilayers formed by vesicle deposition. As can be seen, charge density values

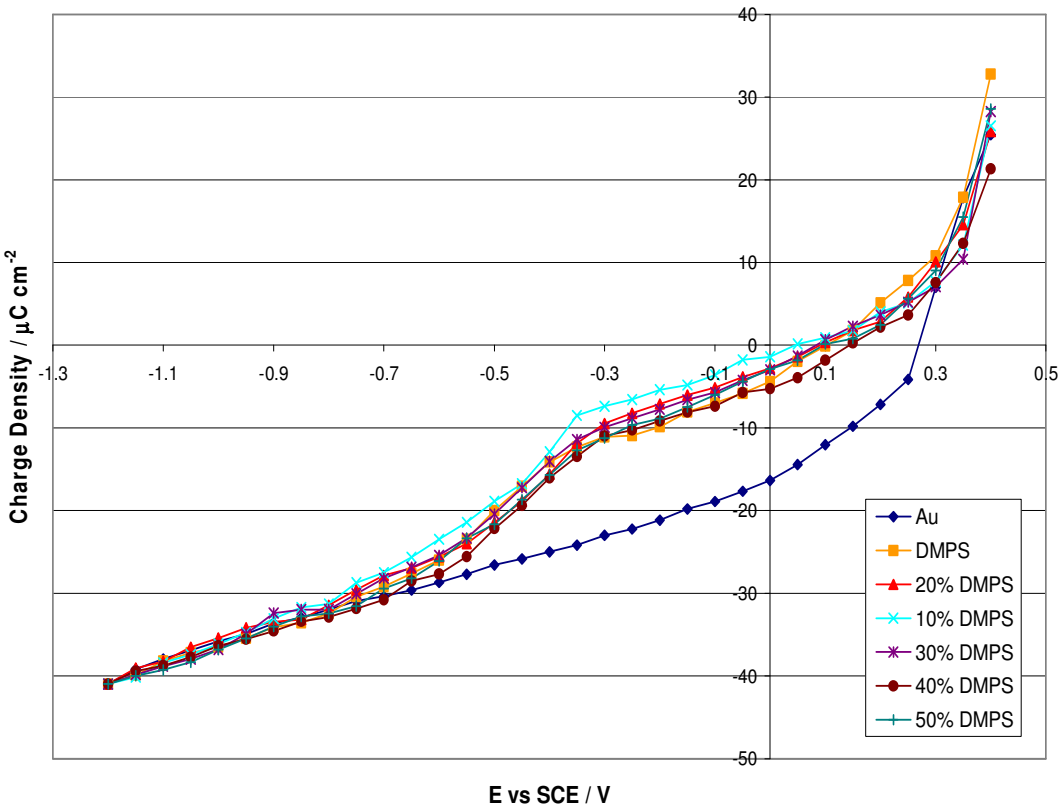

Figure 5.6: Charge density profiles of bilayer of varying composition formed via vesicle fusion. All curves have a similar aspect.

rise sharply at potentials of around -0.7 V. The phase transition at -0.7 V revealed by DC indicates that the bilayer becomes attached to the electrode at this potential. An attached bilayer acts as a barrier between electrode and electrolyte – as seen in the differential capacitance where the adsorbed bilayer can be observed to reduce the capacitance at positive potentials. In other words, charge storage in this system is less than that seen for a bare Au (111) surface. Therefore the fact that the charge density for an adsorbed bilayer is less than that of the substrate is unsurprising.

The PZC of this Au (111) electrode has been measured as 0.288 V (relative to the SCE)[4]. At this point, the charge density of all bilayers increases sharply and can be observed to track closely that seen for the bare Au surface. However, the charge density remains lower than that of the bare gold surface, thus it can be inferred that the bilayers still adhere to the electrode at potentials more positive than the PZC. The sole exception to this is DMPS, which retains a higher charge density above the PZC than the substrate.

The PZC can be determined from the charge density curves in Figure 5.6: it is the point where the charge density is zero and thus the point where the curve crosses the x-axis. Table 5.2 lists the PZC for all bilayers. The PZC of all supported bilayers is shifted towards less positive values. Below the PZC, which occurs at +80 mV for most bilayers (except 20% DMPS at +40 mV and +140 mV for 40% DMPS, see Table 5.2) a trend can be discerned where bilayers containing less DMPS lie closer to the x-axis: the charge density is less negative. This effect varies with the mole fraction of DMPS: hence a bilayer with 10% DMPS lies positive of the 20% DMPS bilayer, which in turn is above that for 30% DMPS. Bilayers with a greater concentration of DMPS possess the most negative charge density: these curves are all similar and are very close to each other. Hence it is possible to say that the magnitude of the charge density is affected by the concentration of DMPS where the potential applied to the bilayer coated electrode is negative of the PZC and for DMPS mole fractions of less than 40%.

These observations are consistent with the idea that the presence of DMPS destabilises the membrane at negative potentials: the more stable membranes possess charge densities closer to zero. As the mole fraction of DMPS increases, stability decreases - to a limiting value of 40% DMPS. Bilayers with this concentration or higher of DMPS all behave in a similar manner. This behaviour reflects that seen with vesicle-formed bilayers in DC experiments where bilayers with more than 40% DMPS possessed "DMPS-like" properties. Some caution needs to be exercised, though, as the differences are not much larger than the random errors estimated for this experiment (3 μC cm^{-2} maximum, estimated from repeat runs).

This possible effect can be understood in terms of electrostatic repulsion. Coulombic repulsion between the negative charge on the DMPS molecule and the negatively charged substrate will act to oppose the cohesive forces between substrate and bilayer. Increasing the concentration of DMPS in that bilayer can be expected to increase the magnitude of Coulombic repulsion. Hence the energy of adsorption at any given potential less than the PZC will decrease as the DMPS mole fraction increases.

It is thus possible to predict that that desorption should take place at less negative potentials as the DMPS concentration in the bilayer increases. Referring back to the DC data, Table 5.1 clearly shows such a trend. This supports the suggestion that Peak A is indeed associated with bilayer desorption. However, desorption is a process that is extended over a considerable range of potential, as shown in Figure 5.2. It can thus be

postulated that desorption is a gradual process. If electroporation leads to pores being opened in the bilayer at potentials between 0 V and -0.4 V, it is likely that these pores would act as sites where full desorption would be initiated. During the desorption process, these pores would allow water to reach the substrate. This water layer will force the bilayer away from the supporting electrode, thus a situation where most of the bilayer is directly adsorbed onto the surface, but with pockets of water standing the bilayer off the substrate here and there. As desorption continued, these pockets could be expected to grow until, finally, they merged and the film was fully desorbed.

DMPE-rich bilayers have charge densities closer to zero below the PZC than do similar DMPC bilayers[3,21]. A similar effect was noted with DC (Section 5.1.3). Again, this difference can be attributed to DMPE-like bilayers possessing fewer defects. DMPE has a smaller head group than DMPC. Hence it is able to pack more densely. Better packing may account for the observations implying fewer defects.

Surface pressure plots are given in figure 5.7. It is immediately apparent that all pressure profiles follow the same general form. The surface pressure begins to rise significantly at around -0.6 V (the point at which the bilayer can be expected to begin to adhere to the electrode surface) and reaches a maximum at around +0.3 V, close to the PZC for the Au (111) surface.

Maximum surface pressures range between 89 mN m^{-1} for 20% DMPS and 122 mN m^{-1} for 40% DMPS bilayers. Measurements of DMPC bilayer by chronocoulometry have yielded surface pressures of 45 mN m^{-1} (Horswell, 2002)[9] and 62 mN m^{-1} (Zawisza, 2004)[22]. DOPC bilayers have been found[23] to have a surface pressure of 48.5 mN m^{-1} (Zawisza, 2003)[23]. The surface pressure of these DMPE/DMPS films are thus somewhat greater than those of the equivalent phosphatidylcholine bilayers. Interestingly, 30% cholesterol in DMPC mixtures exhibited higher surface pressures -125 mN m^{-1}- than pure DMPC[24], which in this instance was measured to be 105 mN m^{-1}.

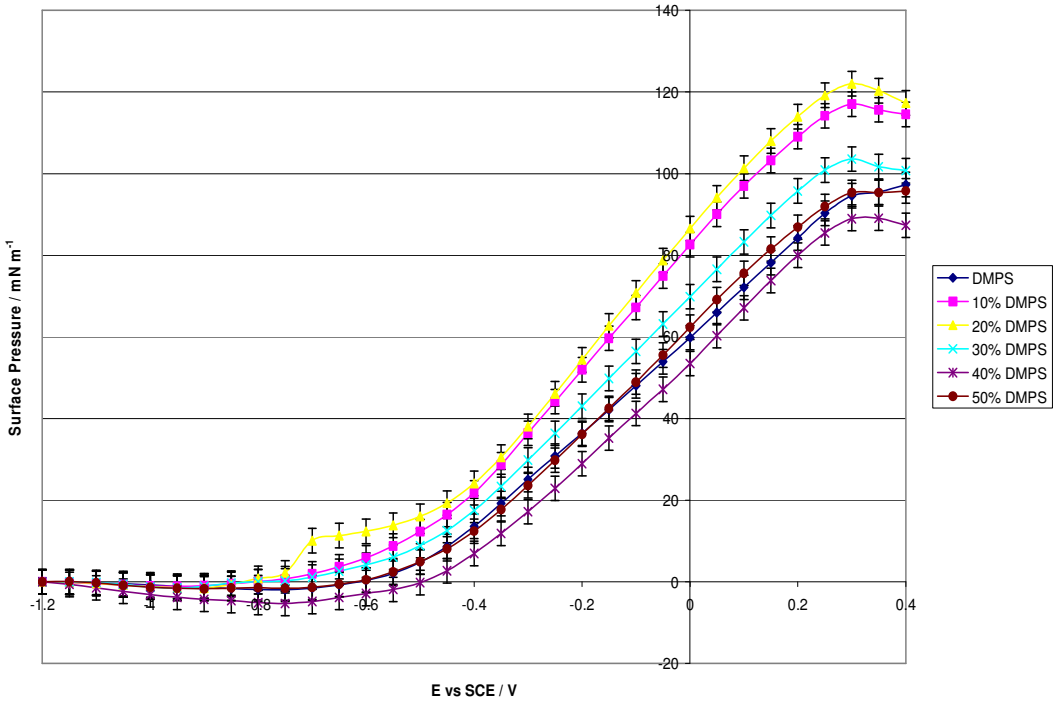

Figure 5.7: Surface pressure of vesicle fusion formed bilayers of varying compositions. As with charge density, the surface pressure curves have a similar appearance.

Beyond this potential, there may be a difference due to composition. The bell shaped curve observed is typical for amphiphiles[3]. Mixtures with large fractions of DMPE experience a fall in surface pressure as the potential becomes more positive while DMPS and 50% DMPS mixtures behave similarly – both continue to exhibit a rise of surface pressure, albeit at a diminished gradient than before.

This behaviour can be explained quite simply with reference to the negative charge on DMPS: simply put, the Coulombic attraction between DMPS and the positively charged substrate is a favourable interaction which is reflected in the surface energy, which increases with the potential. Mixtures with larger fractions of DMPE are not stabilised by this effect as the potential rises above the PZC. Neutral adsorbants display a fall in surface pressure above the PZC as the increasing electric field is able to drive increasing numbers of water molecules into the bilayer[3].

This behaviour is only observed at potentials above +0.3 V – for two data points only. It is reasonable to ask whether this is a real effect or merely a random artefact. Considering the data points at +0.4 V, two out of six values show an increase. There are fourteen unique variations in this set of six curves whereby two curves increase in magnitude while the four others decrease (e.g. the 50% and 30% curves could increase, or the 50% and 20% curves increase, and so on). Thus the probability of both bilayers with the highest DMPS concentration exhibiting this behaviour at random is 1 in 14. The probability of this observation being caused by a real effect as opposed to

chance is 0.93 – which is a little short of the 0.95 probability required for statistical significance.

However, this pattern is also observed at +0.35 V. Indeed, the bilayer with 40% DMPS also exhibits an increase in surface pressure. There are twenty unique combinations possible in this set of six curves. The probability of the three bilayers with the highest concentrations of DMPS exhibiting this behaviour as a result of a genuine effect is 0.95, which is statistically significant.

It is a simple exercise to evaluate the probability of *both* the +0.35 V and +0.4 V data points being due to chance: the probabilities are multiplied. This yields a probability of this pattern being reproduced purely by chance to be 0.0035, which is highly significant. Thus a gradation in properties is observed from DMPS which shows behaviour typical for that of an anionic adsorbant through the 50% and 40% DMPS bilayers which display intermediate properties, though not as strongly as for DMPS to bilayers containing 30% DMPS or less which show typical behaviour for an amphiphile. The 50% DMPS bilayer displays similar properties to that of DMPS, though less pronounced while the 40% DMPS bilayer displays a fall in surface pressure at +0.4 V and thus is intermediate in behaviour between anionic and amphiphilic bilayers. This is similar to the DC observations that bilayers with high concentrations of DMPS behave in a similar fashion to DMPS itself.

However, a note of caution must be sounded. The very simplistic statistical analysis assumes that each unique combination is equally likely, which may not necessarily be the case. Furthermore, with such few data extreme outliers can be expected to have a major impact. Hence this analysis should be considered to be somewhat speculative. These data need to reproduced in order to lend confidence to these speculations.

Both mixtures with the lowest fraction of DMPS (10% and 20%) also behave quite similarly, with larger surface pressures than the other compositions. We can speculate that this is a result of the bilayer having a smaller negative electric charge: the absence of such charge at the surface will mean the bilayer will have a smaller solvation shell of entrained water molecules associated with it. It is also possible to explain this observation if these bilayers possess better surface coverage. Better packing could also account for the observations that DMPE-rich bilayers (10% and 20% DMPS) have higher surface pressures.

Similar DMPC bilayers formed via vesicle fusion have been investigated by Bin *et al* [3]. These studies showed that DMPC exhibits a similar charge density curve to DMPE/DMPS mixtures, albeit with a considerably more abrupt transition at around -0.4 V. DMPC was also observed to possess a bell shaped surface pressure curve with maximum pressure close to the PZC. This behaviour is expected for an amphiphile and mirrors what has been described for mixed bilayers with a high mole fraction (70% or more) of DMPE. This supports the hypothesis that bilayer mixtures with low

concentrations of DMPS behave in a similar manner to that of a pure amphiphile bilayer.

AFM studies of DMPC membranes formed by vesicle fusion showed that the bilayer contained many defects and could be regarded as an “assembly of rafts” separated by fissures that contained solvent[3]. The surface coverage of these DMPE/DMPS bilayers was estimated to be 80% (Section 5.1.4) from the capacity data. It is therefore reasonable to expect these membranes to exhibit similar morphology.

Figure 5.8 shows the charge density plots for bilayers formed via LB/LS deposition. The general profile is very similar to that already seen with the vesicle bilayers, but there are differences. Charge density begins to rise (towards zero) at a larger negative potential – approximately -0.9 V. Coverage of DMPE/DMPS LB/LS bilayers were calculated as being 85% (Section 5.1.4), higher than the equivalent value for vesicle bilayers. This is most probably the minimum value. A more complete bilayer can be expected to exhibit a larger effect on the charge density: this may account for the observations that an effect can be seen at more negative potentials when compared to vesicle formed bilayers. A plausible mechanism for this is that desorption is likely to proceed by water penetrating the film at defects. With fewer defects, a stronger electric field will be required to initiate the desorption process.

Interestingly, the charge density does not track the Au (111) plot once the

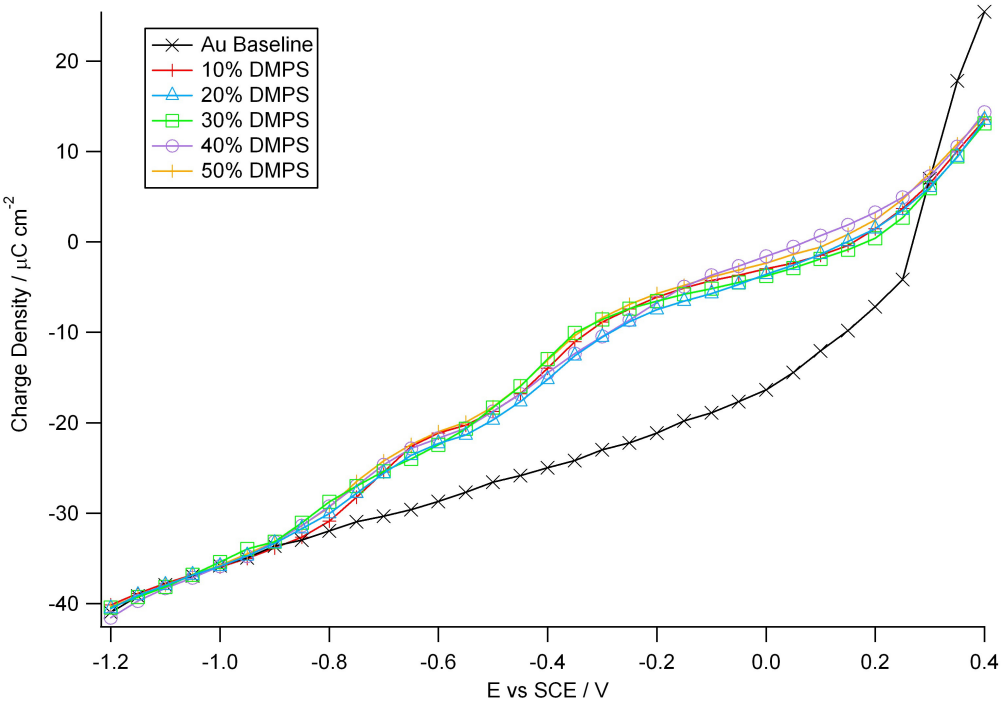

Figure 5.8: Charge density curves for LB/LS bilayers of differing compositions. All compositions exhibit similar curves, tracking the Au baseline until approximately -0.9 V. Errors are estimated at ±2 µC cm^{-2}: error bars are omitted for clarity.

PZC has been reached. The charge density remains at a lower value throughout for all compositions studied. This behaviour is different to that seen with the vesicle formed films (Figure 5.6).

A speculative explanation for this observation is to consider the difference in coverage between bilayers formed by LB/LS deposition and vesicle fusion. A bilayer formed through LB/LS will have higher coverage than its vesicle formed analogue. The end result of this is that which bilayers formed by vesicle fusion, parts of the electrode surface are exposed to the electrolyte,

and so will accumulate charge in the normal way that any similar Au (111) surface will. At the PZC, the charge density of Au increases sharply – as is observed. A LB/LS bilayer with its greater surface coverage more effectively shields the electrode so this effect will not be seen.

An alternative explanation is to postulate bilayers formed by vesicle fusion are more hydrated than LB/LS bilayers. PM-IRRAS investigations of DMPC bilayers formed both by LB/LS deposition and vesicle spreading indicated that the vesicle bilayers were more hydrated[3,21]. In the light of this, it is likely that a similar effect is the explanation here.

That the charge density remains very close to that seen for a bare Au (111) surface up to -0.9 V (and indeed higher for vesicle formed bilayers) indicates that the assumption that the bilayer is desorbed at a potential of -1.2 V is valid.

A close examination of the charge density curves reveals no convincing evidence for a systematic variation with bilayer composition. The curves all lie close to each other. Random errors have been estimated to be ±2 μC cm^{-2} from repeat experiments: the curves all lie within this distance of each other. Hence the small differences observed can be explained by natural variations.

The PZC varies between +90 mV (40% DMPS) and +180 mV (30% DMPS).There is evidence of a small positive shift in the PZC when compared

Table 5.2: PZC values for different bilayers.

Composition	PZC of vesicle-formed Bilayers on Au / mV	PZC of LB/LS formed Bilayers on Au / mV
10% DMPS	40	160
20% DMPS	80	140
30% DMPS	80	180
40% DMPS	140	90
50% DMPS	90	130
Average	86	140

with bilayers formed via vesicle fusion. A comparison between the PZC observed for vesicle-formed bilayers and LB/LS bilayers can be seen in Table 5.2. It is clear from these data that there is a positive shift in the PZC for LB/LS bilayers, calculated to be 54 mV.

Comparing vesicle and LB/LS membranes, it can be seen that the PZC for all compositions is less than that of the bare Au (111) surface. LB/LS bilayers consistently show a higher PZC than their vesicle equivalents – with the exception of the 30% DMPS film.

The change in the PZC, ΔE_{pzc}, is due to polar water molecules being displaced by the adsorbed bilayer and can be found from the following relation[25,26]:

$$\Delta E_{pzc} = \frac{\Gamma_{\max}\left(\mu_{org} - n\mu_{w}\right)}{\varepsilon} \qquad [5.2]$$

where Γ_{max} is the surface coverage, μ_{org} and μ_w the permanent dipole moments perpendicular to the surface, n the number of water molecules displaced by a single adsorbant molecule and ε is the permittivity of the inner layer.

The negative shift in the PZC indicates that water molecules have been replaced by negatively charged or polar molecules which have their dipole directed so that the negative end is pointing towards the electrode surface. All these films contain negatively charged DMPS, so such a shift is to be expected.

However, surface coverage of the LB/LS bilayers is greater than that of the vesicle formed bilayers – yet the PZC of the LB/LS films has shifted considerably less on average. There are two possible explanations for this. The first is that there is a difference in the conformation of the head groups between vesicle and LB/LS bilayers such that the vesicle films have the dipole moments of their constituent molecules orientated closer to perpendicular to the surface. The other option is that the process of formation preferentially favours the placement of DMPS in the bottom leaflet during vesicle formation. The spontaneous formation of asymmetric phospholipid bilayers has been reported by Wacklin and Thomas[27]. It was observed that vesicles of mixed compositions (di-palmityl-phosphatidylcholine (DPPC) and di-oleyl-phosphatidylcholine (DOPC)), the inner leaflet next to the supporting bilayer had a higher concentration of DPPC than the outer leaflet. It is unfortunate that there is insufficient data to favour one explanation over the other.

5.3 Electrochemical Impedance Spectroscopy

5.3.1 Frequency Response Analyser

Any electrical system will exhibit a characteristic response subjected to an input sine wave of a particular frequency. This response will be composed of a phase shift of the input signal along with high frequency harmonics (at multiples of the input frequency). This response can be used to acquire information about the system being investigated such as its impedance. Moreover, this response is very often dependent upon the frequency of the input excitation. Measuring the system's response at a number of different frequencies therefore allows its frequency response to be determined.

This response of an electrical system can be measured by a frequency response analyser (FRA)[28]. A FRA applies a sinusoidal reference signal to the electrochemical system under investigation and measures the response. The response is multiplied by the sine and cosine of the reference signal. This is then integrated over one or more cycles in order to extract the real and imaginary components of the output signal:

$$\mathrm{Re}(E) = \frac{1}{T}\int_0^T E\sin(\omega t + \phi)\sin(\omega t)dt = \frac{E}{2}\cos(\phi) \qquad [5.3]$$

$$\mathrm{Im}(E) = \frac{1}{T}\int_0^T E\sin(\omega t + \phi)\cos(\omega t)dt = \frac{E}{2}\sin(\phi) \qquad [5.4]$$

where T is the measurement time, ϕ the phase shift and E amplitude of the signal in Volts.

The FRA has the advantage of rejecting harmonics (that is, multiples of the excitation frequency) and it is also capable of reducing noise[28]. Longer measurement times will result in greater noise reduction.

It must be emphasised that the analysis outlined in Section 2.4 assumes that the electrochemical system under investigation is linear. This clearly is not true: one of the fundamental equations of electrochemistry, the Butler-Volmer Equation shows that the current response to applied potential is exponential. The response of a nonlinear system to a single frequency excitation is to generate harmonics at multiples of the fundamental frequency.

To work around this problem, it is necessary to use a small amplitude AC signal so that the response of the electrochemical cell becomes approximately linear. Typically amplitudes of 5-10 mV rms are employed. A FRA is advantageous in this situation in that it is insensitive to any harmonics that may still be produced by residual nonlinearities.

5.3.2 Results and Discussion

Cyclic voltammograms were done to confirm the presence of an adsorbed bilayer. Figure 5.11 shows the CV for the uncoated electrode. The reduction peak at +0.12 V and oxidation peak at +0.24 V can clearly be seen. The equivalent CVs for DMPS and DMPE can be seen in Figures 5.11 and 5.12 respectively. It is clear that the oxidation and reduction peaks have been

significantly reduced in magnitude. Since peak height is related to the rate of diffusion to the electrode surface, this indicates that diffusion has been reduced. This can be expected to occur as the bilayer will act as a barrier restricting access to the electrode. Hence this confirms that a bilayer is present on the electrode surface.

A typical Nyquist plot can be seen in Figure 5.9. This was obtained for a bilayer deposited by Langmuir-Blodgett / Langmuir-Schaeffer deposition.

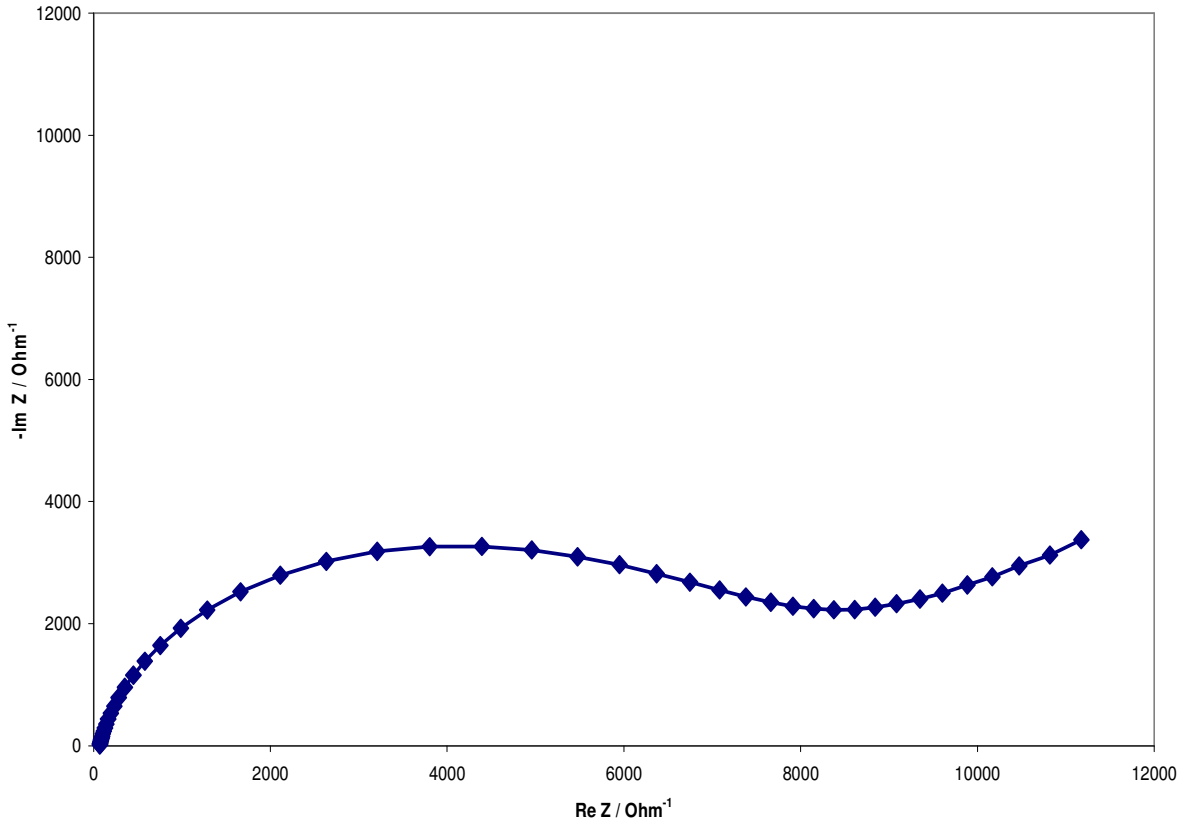

Figure 5.9: Impedance spectrum of a 50% DMPS in DMPE bilayer, deposited using LB/LS. The applied cell potential was 180 mV and ferrocyanide concentration was 1 mM in 0.1 M NaF. The AC component was 10 mV rms.

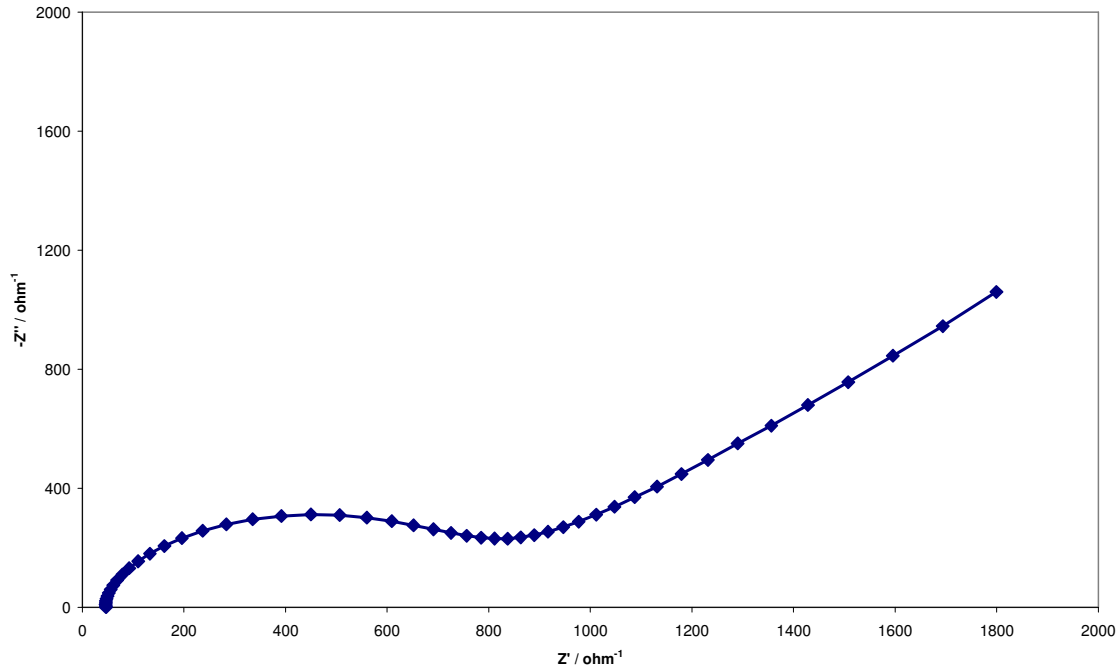

Figure 5.10: A 50% DMPS bilayer produced by LB deposition at a potential of 180 mV with 1 mM ferrocyanide in 0.1 M NaF electrolyte. An AC signal of 10 mV rms amplitude was used.

There are several regions of interest. The first point to note is that the Nyquist plot looks very similar to that of the Randles cell with an extended near linear tail.

As a very quick check, projecting the semicircle to the x-axis yields R_{ct} = 9000 Ω. The equivalent figure for an uncoated Au electrode was estimated to be 140 Ω. Clearly this is rather crude and proper modelling must be done to establish more reliable values, but even with this crude check it can be seen that the presence of the film sharply decreases the rate at which the ferrocyanide ion is able to gain access to the electrode. The oxidation of

ferrocyanide possesses fast reaction kinetics and hence low transfer resistance. The large increase is caused by the bilayer which blocks access to the Au electrode to the ferrocyanide ions except through small defects and pores. These pores constitute only a very small surface area of the electrode so only very few ions gain access. This is the cause of the observed increase in R_{ct}.

Hence, it is possible to use EIS to evaluate the quality of the bilayer in terms of defects such as pores. This was done to evaluate the quality of bilayers produced by Langmuir-Blodgett and Langmuir-Blodgett / Langmuir-Schaeffer bilayers. Figure 5.10 shows a typical Nyquist plot obtained for a LB bilayer. The most striking thing is the observed semicircle – and hence R_{ct} – is very noticeably smaller than LB/LS bilayers, by close to an order of magnitude. This pattern was observed for all bilayer compositions. It is abundantly clear that bilayers obtained by LB deposition are very much the poorer relation to those acquired by LB/LS deposition. Why might this be so? One very plausible explanation is that the second step, where the substrate is raised out of the Langmuir Trough, the surface tension of the sub-phase acts to smear and remove some of the phospholipids already sitting on the surface[21]. This will act to substantially reduce coverage and degrade the organisation of the lipids that remain, introducing further defects. X-ray and neutron reflectometry studies of multi-bilayers of barium stearate deposited by the Langmuir-Blodgett technique demonstrated that the topmost layers only had 40% coverage[29] which was attributed to the film preparation, similar to what has been observed with this EIS data.

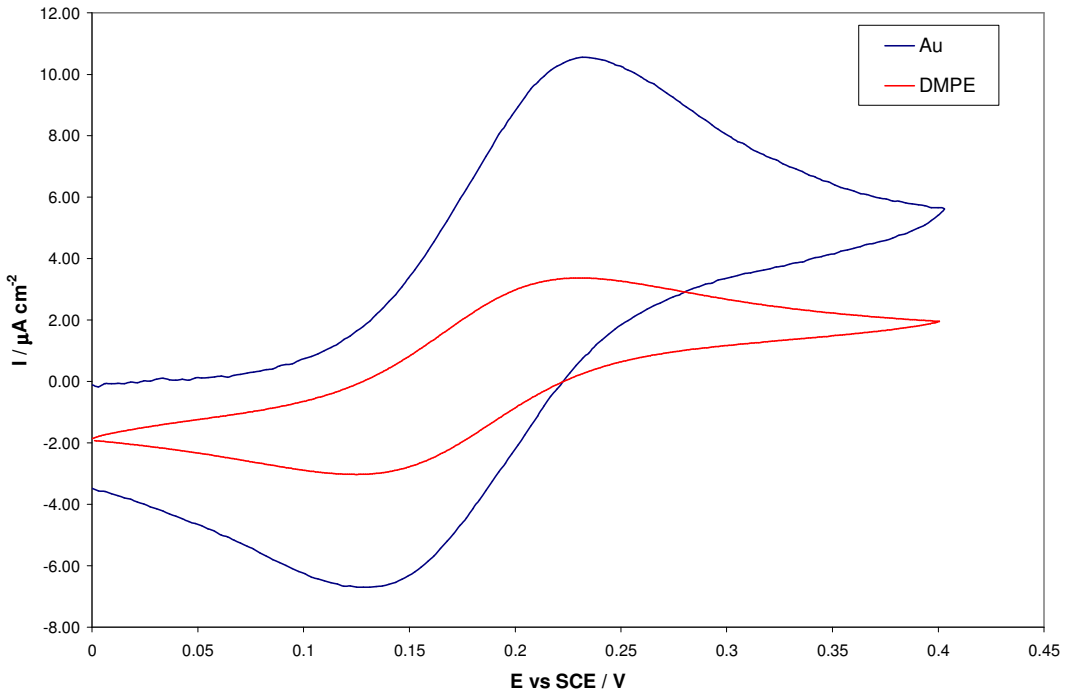

Figure 5.11: Cyclic voltammograms of a polycrystalline Au electrode (blue) and the same electrode with an adsorbed DMPE bilayer (red). The scan rate was 50 mV s^{-1}.

Figure 5.11 compares the cyclic voltammogram of bare gold with that of a DMPE layer. The oxidation and reduction peaks can clearly be seen, at 0.24 V and 0.12 V respectively. The DMPE CV has peaks that are markedly smaller in magnitude which indicates that the DMPE bilayer is impermeable to the electroactive anions to some extent and restricts their access to the electrode. Figure 5.12 shows the CV obtained for a DMPS bilayer on polycrystalline gold. The oxidation and reduction peaks are smaller than magnitude than even the DMPE layer, implying that the DMPS layer is less permeable to ferrocyanide than DMPE.

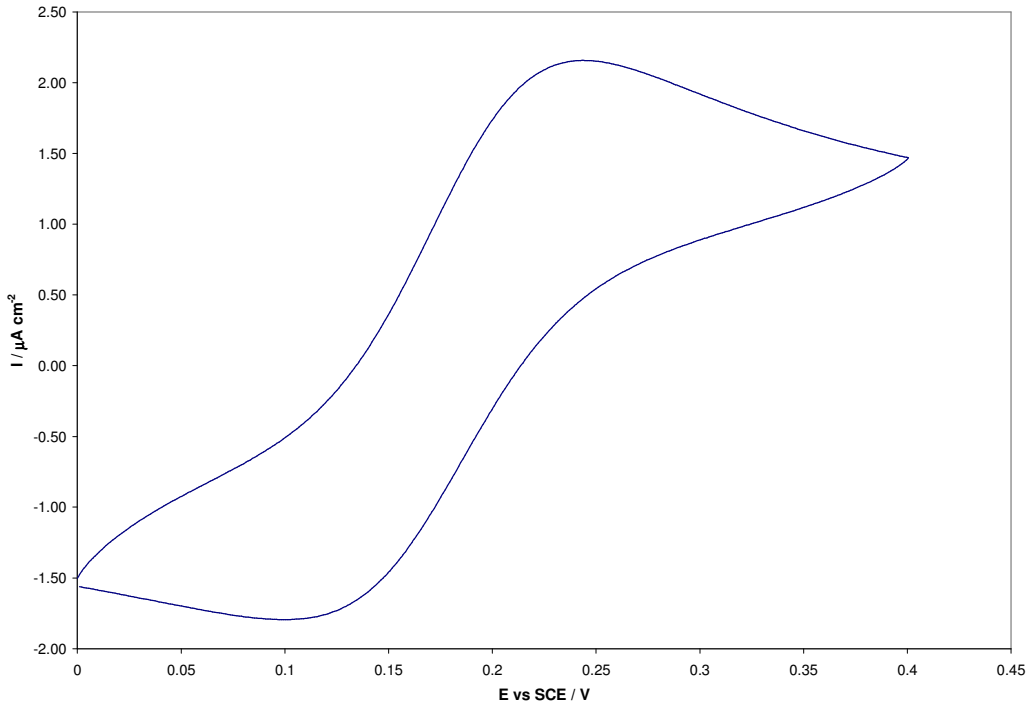

Figure 5.12: Cyclic voltammogram of DMPS on a polycrystalline Au substrate. The electroactive species was ferrocyanide. Note the magnitude of the peaks is less than the equivalent DMPE CV in Figure 5.11.

Figure 5.13 is a Nyquist plot for bilayers of varying compositions. It is readily apparent that there is a considerable spread in properties. That this spread does not show any discernable pattern with respect to composition compels us to conclude that variation in the quality – in terms of pores and defects within the film – of the formed bilayer is sufficiently large as to swamp any effects due to composition. DMPE is an exception. All the bilayers possess an overall negative charge with the exception of DMPE. Coulombic repulsion might be expected to act to reduce the access that negatively charged ferrocyanide ions have of the electrode surface below, and this does indeed

seem to be the case. However, there is no systematic increase in R_{ct} with DMPS composition. This suggests that it is the simple fact that the bilayer possesses an overall negative charge is of importance rather than its magnitude. This is not surprising when it is considered that the solvent, with an $\varepsilon_r = 80$, acts very effectively to screen electric field over long range.

The evidence suggests that it is defects and pores in the bilayer that control access to the electrode surface. The number of pores will be considerably fewer than the number of DMPS molecules, even in bilayers that have 10%

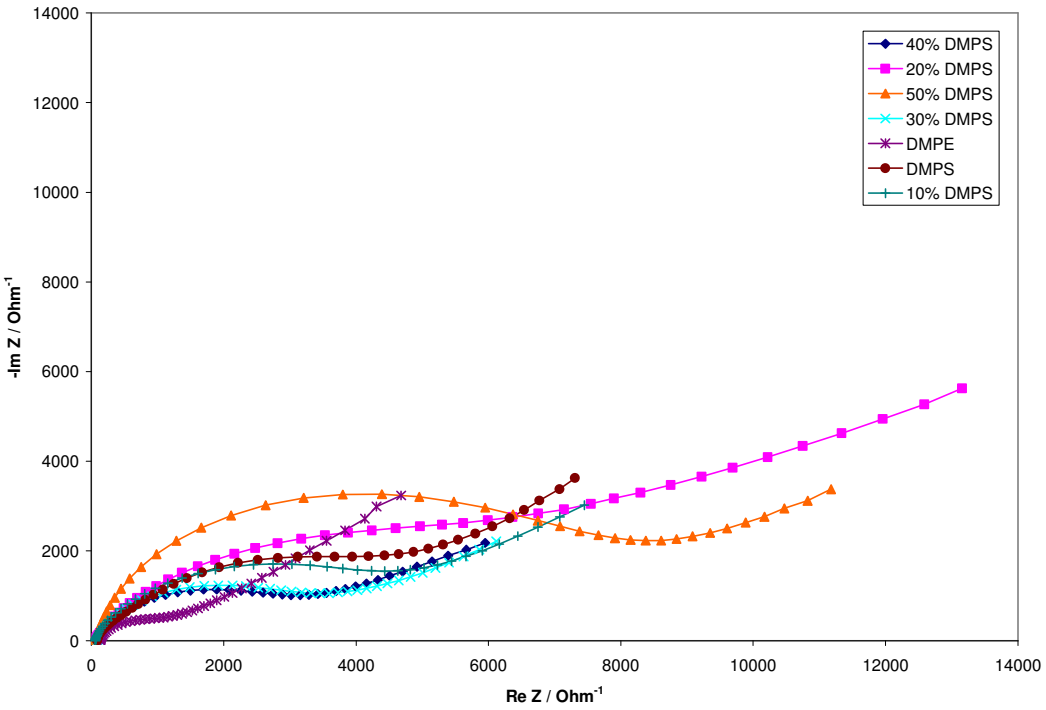

Figure 5.13: Impedance spectra for LB/LS bilayers of varying compositions. The electrolyte was 1 mM ferrocyanide in 0.1 M NaF. A 10 mV rms excitation signal was used.

mole fraction DMPS. Hence most pores can be expected to have a negatively charged DMPS molecule in close proximity whose charge will act as a gate keeper to any ferrocyanide ion as a result of Columbic repulsion between charges. Increasing the concentration of DMPS will not appreciably alter this situation.

The FRA software is capable of modelling the acquired impedance spectrum. Given that the impedance plots appear very similar to the theoretical impedance plot of a Randles cell with diffusion, it is of little surprise that the equivalent circuit in Figure 2.7 (Randles cell with Warburg CPE) proved to be the best fit. The equivalent circuit is shown in Figure 5.14 Table 5.3 summarises the results.

The solution resistance, R_s, should be the same for all compositions given that the same stock solution was used for all. The variation may therefore be used to estimate errors. The mean value is 14.6±1.9 Ω cm $^{-1}$ The error value is therefore 13%, which can be applied to all fitted parameters. Much of this is

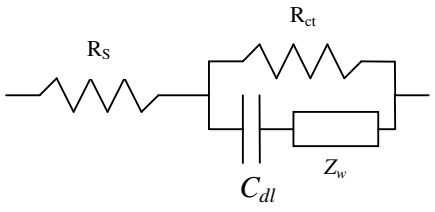

Figure 5.14: Equivalent circuit used for fitting EIS data. A standard Randles circuit was used with a Warburg CPE.

due to the fitting procedure: natural noise in the data means that the acquired fit will not be perfect. However, some variation can be attributed to differences in the surface roughness of the polycrystalline Au substrate.

Values of R_{ct} show some scatter, as expected from the Nyquist plots. However, it is evident that DMPE presents less of a barrier to the ferrocyanide ion than any bilayer incorporating DMPS.

The fitted bilayer capacitance is higher than that seen in the DC experiments – but this can be explained by the differences in substrate. Polycrystalline gold has a slightly higher differential capacity at this potential – 0.18V vs SCE[30] (Figure 3.8 and Section 3.7). The Au (111) surface has lower energy than an

Table 5.3: Modelled parameters for bilayers of various compositions.

Composition	R_s / Ω cm^2	R_{ct} / Ω cm^2	C / μF cm^{-2}	CPE / 10^{-4} Ω^{-1} cm^{-2}	ϕ
DMPE	15.9±2	215±14	10.1±2	3.49±0.49	0.82±0.08
10% DMPS	14.4±4	923±79	12.2±5	5.91±0.66	0.78±0.17
20% DMPS	12.7±3	738±71	6.0±2	6.30±0.23	0.86±0.10
30% DMPS	17.0±3	744±56	7.1±3	3.25±0.79	0.82±0.09
40% DMPS	14.3±2	837±67	11.9±2	3.27±0.50	0.79±0.14
50% DMPS	14.9±3	1190±94	28.3±7	7.32±0.35	0.73±0.11
DMPS	12.1±2	881±83	14.8±3	5.22±0.21	0.80±0.12
Au (no lipid)	15.1±2	18±2	25.9±6	6.35±0.54	1.00±0.03

annealed polycrystalline surface, and it is less rough. The PZC for polycrystalline gold is -0.05 V, referenced to the SCE[31], which is significantly lower than for Au (111). Taken together, these effects can be expected to disrupt the bilayer organisation somewhat, leading to higher capacity values.

The CPE exponent, ϕ, contains information as to the roughness of the surface. An exponent of 1.00 indicates a smooth surface – a lowered value can be interpreted as being caused by surface roughness. A value of 0.5 indicates the presence of an infinite Warburg impedance[28]. The exponent of the Au surface is 1.00, indicating that the electrode surface was very smooth. This is a pleasing result that shows it is possible to obtain smooth polycrystalline gold surfaces using evaporation as the method of coating. The bilayers all display lower values, indicating that the surface is less smooth than the Au substrate. This could indicate the presence of defects and pores in the bilayer structure. There is, however, no readily discernable pattern with regards to bilayer composition. Whitehouse *et al.* measured the related parameter β (see p. 49) for DOPC monolayers on mercury[32] to be between 1.0 (indicating a smooth surface) and 0.991. It is clear that these bilayers on polycrystalline Au are considerably rougher in comparison.

It is possible to calculate the reaction rate of the electroactive probe[33]. It can be shown that the rate constant of the electroactive probe, J_{ea}, is given by the following equation:

$$J_{ea} = \frac{B}{nFR_{ct}} \qquad [5.5]$$

B is dependent upon the Tafel slope of the electroactive probe and can be found using the following relation:

$$B = \frac{b_a \times b_c}{2.303(b_a + b_c)} \qquad [5.6]$$

b_a is the anodic Tafel slope and b_c the Tafel slope of the cathodic reaction.

In instances where the reaction is diffusion limited, the rate constant is limited by the diffusion rate. The reduction of the ferrocyanide ion and the oxidation of the ferricyanide ion are both reactions with very fast electron transfer kinetics. The rate determining step is the diffusion of ions to the electrode surface.

For an electrode that has an adsorbed bilayer, since the same electroactive probe is used, any differences observed between J_{ea} for the coated electrode and uncoated electrode can as an approximation be caused by a reduction in the surface area of the electrode as a result of its adsorbed film. (It should be noted that this ignores any contribution to diffusion of the electroactive probe through the bilayer itself. This assumption is thus reasonable for an ionic species such as the ferri/ferrocyanide couple but not for an organic species which possesses a high degree of lipid solubility.)

Hence surface coverage, θ, can be calculated by using the relation:

$$\theta = 1 - \frac{J_{ea}[Au]}{J_{ea}[Bilayer]} \qquad [5.7]$$

$J_{ea}[Au]$ is the rate constant for the electroactive probe as measured on a bare gold electrode while $J_{ea}[bilayer]$ is the rate constant for the sample

electroactive probe in the presence of an adsorbed bilayer. Rate constants and coverage values are listed in Table 5.4.

It is clear from the calculated coverage values that the LB/LS bilayers are quite uniform, with the notable exception of DMPE. Errors have been calculated to be ±0.01, assuming an error of 14% in R_{ct}. It seems reasonable to postulate that the little electrode surface that remains accessible to the electroactive probe ions is through pores and other defects in the bilayer. These values are greater than the coverage value calculated from the differential capacitance (0.85). It was commented that this coverage appeared

Table 5.4: Rate constants and coverage values for bilayers of different compositions as measured using the ferri/ferrocyanide couple as an electroactive probe.

Composition	J_{ea} as measured using EIS / $cm^2\ s^{-1}$	Estimated Coverage	J_{ea} as measured using CV / $cm^2\ s^{-1}$
Au	3.28×10^{-8}	0	4.81×10^{-7}
DMPE	2.75×10^{-9}	0.92	1.40×10^{-8}
10% DMPS	6.40×10^{-10}	0.98	4.43×10^{-8}
20% DMPS	8.00×10^{-10}	0.98	2.09×10^{-8}
30% DMPS	7.95×10^{-10}	0.98	2.39×10^{-8}
40% DMPS	7.06×10^{-10}	0.98	3.90×10^{-8}
50% DMPS	4.96×10^{-10}	0.98	1.48×10^{-8}
DMPS	8.67×10^{-10}	0.97	1.70×10^{-8}

to be somewhat low (Section 5.1.2). These data from EIS experiments implies that the actual coverage is greater – and thus the high capacity of the bilayer as measured by DC is not a result of low coverage. A high degree of coverage has been observed for other supported phospholipid layer systems: Starr and Thompson observed full coverage of LB/LS deposited DOPC bilayers on fused silica and single crystal TiO_2 and $SrTiO_3$ surfaces[34]. Charitat and coworkers determined that LB/LS bilayers of DPPC and distearylphosphatidylcholine (DSPC) deposited on a Si substrate had a somewhat lower coverage of 80-85% using AFM and neutron reflectometry[35] (though coverage immediately after transfer of the lipids onto the substrate was estimated to be at least 93%).

Charitat measured the water content of their DPPC and DSPC bilayers by neutron reflectometry to be in the range 10-23%[35]. Water entrained within the film or hydrating the headgroups is thus a good candidate for explaining the high capacitance and lower than expected estimates for coverage derived from the DC data.

In cyclic voltammetry, it can be shown that, for a reversible reaction, the peak current, I_{peak} of a species undergoing an electron transfer reaction can be found from[36]:

$$I_{peak} = 0.4463nFAC\left(\frac{nF\nu D}{RT}\right)^{1/2} \qquad [5.8]$$

C the species concentration, D the diffusion constant and ν the scan rate. This equation is derived from Nicholson and Shain (1964)[37]. It is thus possible to

compare values of J_{ea} obtained by CV and EIS for the same bilayer. This has been tabulated in Table 5.4. Disappointingly, there is a considerable difference between the rate constants derived from the CV data and the EIS data, with the CV rate constants consistently being an order of magnitude larger. The CV rate constants do however show that these phospholipid bilayers act as a barrier to the passage of anions to the substrate. Curiously, DMPE has the *lowest* rate constant: this is the opposite to the EIS data. Both sets of data were gained under different conditions: the CV data was collected first (as CV was used to confirm the presence of a bilayer on the electrode) while the potential at which the impedance spectroscopy was performed was +0.18 V as opposed to the anodic peak of +0.24 V for the CV. While some deterioration of the layer is possible in the interval between running the CV and EIS experiments, it must be pointed out that a set of 5 cycles was always run which showed very little difference between each cycle (otherwise the bilayer would have been discarded and the experiment repeated). Though the difference in potential could account for some differences, an order of magnitude difference seems rather high: alas, an error in the analysis must be suspected.

The coverage of the DMPE bilayer is interesting: it possesses a lower coverage than the other bilayer systems. DMPE is a neutral molecule. Chronocoulometry data showed that the surface pressure of DMPE decreased at potentials greater than the PZC. Since the PZC is -0.05 V for polycrystalline gold, the substrate could be expected to have a significant positive charge. Thus DMPE may be expected to be less firmly attached to

the substrate and contain more defects and pores. This would account for the observed decrease in coverage. Bilayers containing DMPS can be expected to have a negative electric charge which will act to stabilise the film at potentials greater than the PZC. Hence coverage would be higher.

However the chronocoulometry data indicated that bilayers containing low mole fractions of DMPS also become less stable at potentials higher than the PZC while those containing 50% DMPS or more *possibly* become more stable at these large positive potentials. Data in Table 5.4 do not mirror the chronocoulometry observations: all bilayers containing DMPS have markedly higher coverage than pure DMPE.

Hexaaminеruthenium(III) Chloride

To investigate the permeability of phospsholipid bilayers to positve ions, the reduction of hexaaminеruthenium (III) chloride was investigated. An electrolyte of 1 mM $Ru(NH_3)_6^{3+}$ in 0.1 M NaF was used.

Representative cyclic voltammograms are shown in Figures 5.15 to 5.16. As was observed with the ferrocyanide electroactive probe, the oxidation and reduction peaks are much reduced in the presence of a bilayer. Again, this

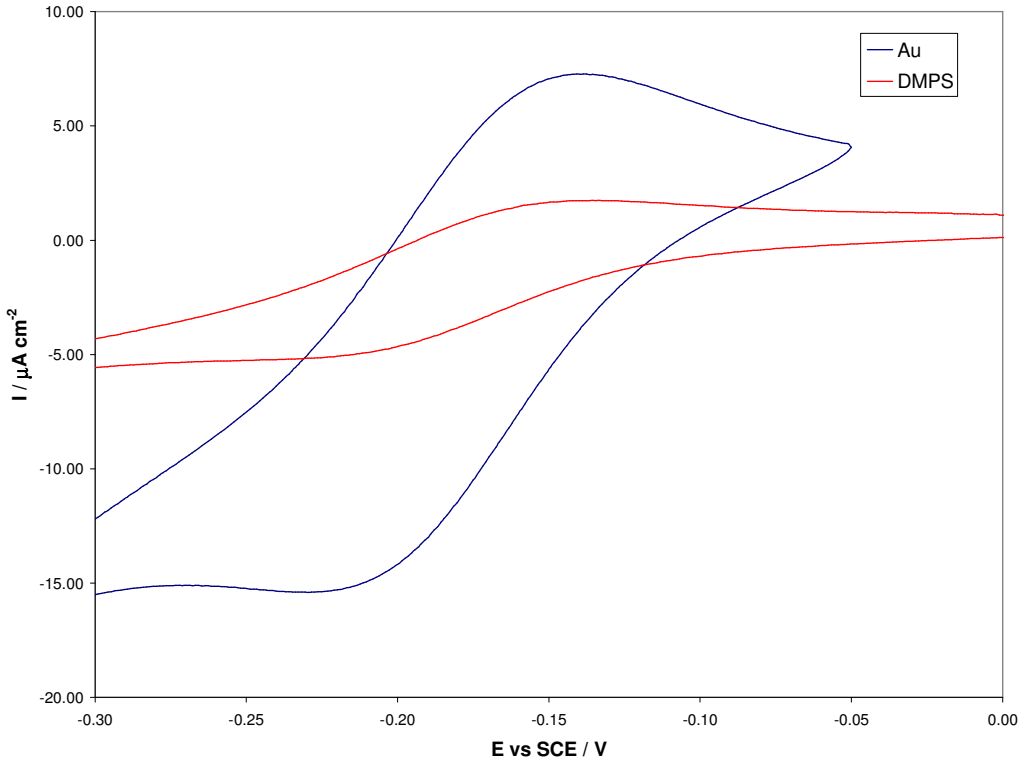

Figure 5.15: CV of Au substrate and DMPS with $Ru(NH_3)_6^{3+}$ as the electroactive probe.

observation can be attributed to the barrier that the bilayer interposes between electrolyte and electrode.

Impedance plots are shown in Figure 5.17. It is clear from the data that the bilayers behave rather differently to cations than anions. Bilayers containing DMPS pose considerably less of a barrier to cations than anions. In contrast, DMPE itself displays increased impedance to the passage of $Ru(NH_3)_6^{3+}$ than ferrocyanide ions.

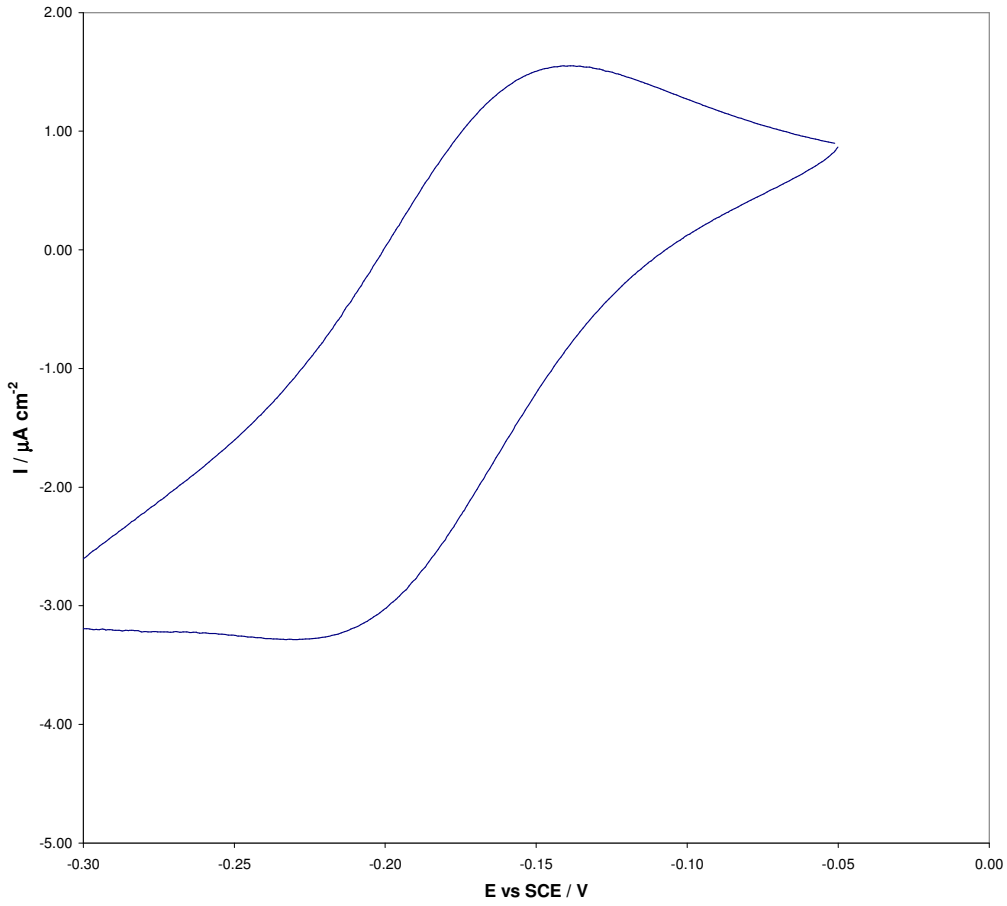

Figure 5.16: CV of 20% DMPS in DMPE bilayer. $Ru(NH_3)_6^{3+}$ was used as the electroactive probe.

The results of modelling the EIS data are tabulated in Table 5.5. As with the ferrocyanide data, a Randles cell with Warburg CPE was used. The equivalent circuit is shown in Figure 5.14.

Turning first to R_s, again there is some scatter in this value. Taking the average of this, 13.4±1.9 Ω cm^{-1}, errors can be evaluated as 14%. Again, this can be attributed to the fitting procedure: the equivalent circuit used to fit the results is merely a simplistic model of the physical processes.

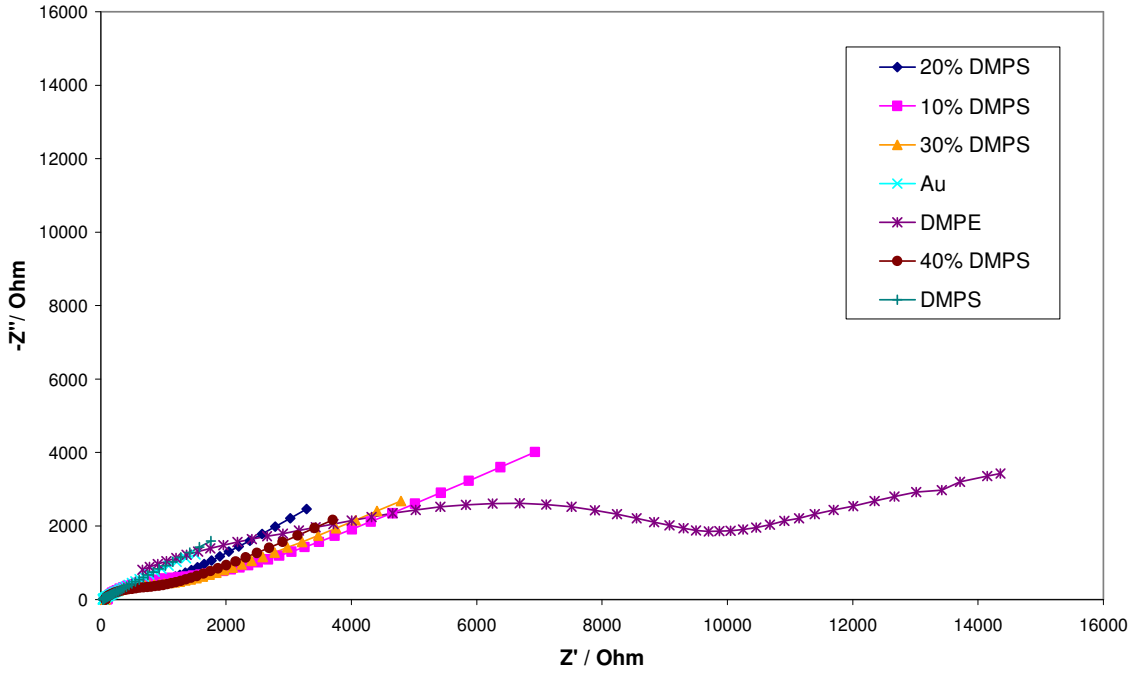

Figure 5.17: Impedance spectra of bilayers of varying compositions using 1 mM $Ru(NH_3)_6^{3+}$ in 0.1 M NaF at a potential of -0.18 V. An AC signal of 10 mV rms was used.

R_{ct}, though higher than that of the bare Au surface, is substantially less than what was seen with the ferrocyanide anion. The exception is DMPE: its transfer resistance has increased to a value considerably higher than that estimated for ferrocyanide. DMPE presents a more substantial barrier to the passage of cations than any of the bilayers containing DMPS.

Bilayer capacities are higher than that observed in DC. Again, caution should be exercised in direct comparison as the DC data were on a different

Table 5.5: Fitted data to the impedance spectra of bilayers using $Ru(NH_3)_6^{3+}$ as an electroactive probe.

Composition	R_s / Ω cm^2	R_{ct} / Ω cm^2	C / μF cm^{-2}	CPE / 10^{-4} Ω^{-1} cm^{-2}	ϕ
DMPE	15.9±3	683±74	25.9±5	5.5±0.6	0.79±0.12
10% DMPS	15.1±3	72.5±16	20.8±4	4.8±0.4	0.88±0.09
20% DMPS	12.7±2	220±33	9.3±2	4.2±0.4	0.82±0.12
30% DMPS	12.4±2	173±20	19.4±5	5.1±0.3	0.81±0.15
40% DMPS	13.7±3	133±14	16.5±3	5.4±0.7	0.84±0.11
DMPS	11.9±2	43.1±9	25.9±4	5.5±0.5	0.54±0.19
Au (no lipid)	12.2±2	30.1±7	39.8±6	6.8±0.4	1.00±0.04

substrate that can be expected to produce a better bilayer and hence lower capacities.

Also notable is the high value of C_{dl} for the uncoated electrode: it is substantially higher than the equivalent figure in the ferrocyanide series of impedance spectra. This is an indication of a deterioration of the electrode surface. Flame annealing the electrode before LB/LS deposition was an essential step to guarantee cleanliness, but no matter how gently this is done it is still very hard on the electrode. It is likely that the surface became roughened as a result. Attempting to clean the electrode by immersion in hot acid or piranha solution was met merely with the loss of gold from the surface.

Examination of ϕ suggests that the bilayer coated electrode is rougher than the bare substrate, and substantially rougher than phospholipid monolayers formed on mercury[32]. This, as with the ferrocyanide electrochemical probe, suggests that the bilayer contains defects and pores. If the reaction is assumed to be diffusion limited, the same procedure that was used to calculate rate constants for the ferri/ferrocyanide ion (Table 5.4) can be used here to estimate surface coverage. Results are tabulated in Table 5.6.

It is notable from Table 5.6 that coverage is significantly lower than that calculated for the ferrocyanide probe at +0.18 V. The single exception to this trend is DMPE which exhibits a higher coverage. Strikingly, DMPS has a very

Table 5.6: Calculated rate constants and coverage for bilayers with differing compositions using $(NH_3)_6^{3+}$ (aq) as an electroactive probe.

Composition	J_{ea} as measured using EIS / $cm^2\ s^{-1}$	Estimated Coverage	J_{ea} as measured using CV / $cm^2\ s^{-1}$
Au	1.96×10^{-8}	0	5.78×10^{-7}
DMPE	6.65×10^{-10}	0.96	1.81×10^{-8}
10% DMPS	8.15×10^{-9}	0.58	5.06×10^{-8}
20% DMPS	2.69×10^{-9}	0.86	2.52×10^{-8}
30% DMPS	3.41×10^{-9}	0.82	4.20×10^{-8}
40% DMPS	4.44×10^{-9}	0.77	3.68×10^{-8}
DMPS	1.37×10^{-8}	0.30	7.00×10^{-8}

low coverage. DMPS was repeated twice more with $Ru(NH_3)_6^{3+}$: all runs produced very similar results hence this low coverage is unlikely to be down to accident.

As with the ferrocyanide data, rate constants derived from CV data is very much higher than those calculated from R_{ct}. As before, a set of 5 cycles was always run prior to EIS data acquisition which showed little if any deterioration in bilayer quality. Thus again an error in data analysis must be suspected. It is fascinating to note, however, that the CV rate constants do demonstrate that the bilayers act as a substantial barrier towards cations more so than would be suggested by the EIS data – this is especially true for DMPS. The rate constant for DMPS suggests a surface coverage of 89%.

The electrode potential, -0.18 V, was below the PZC and hence a negative charge would have been present on the substrate. This can be expected to reduce the stability of any bilayer containing negatively charged DMPS. Indeed, a pattern can be seen with coverage falling in a regular manner as the mole fraction of DMPS is increased. This postulate is marred somewhat by the anomalously low coverage calculated for the 10% DMPS bilayer. However, there is sufficient evidence to propose that the presence of negatively charged DMPS enhances or promotes the passage of positively charged ions compared to DMPE while the opposite is true for negatively charged ions.

A bilayer containing negatively charged lipids will have a different surface potential than one whose component lipids are neutral. This altered surface potential can be expected to alter the concentration of an ionic species at the surface, $C_{surface}$, with respect to its bulk concentration, C_{bulk}. The ratio of surface to bulk concentration can be found using Gouy-Chapman theory[38]:

$$\frac{C_{surface}}{C_{bulk}} = \exp\left\{\frac{-nF\psi}{RT}\right\} \qquad [5.9]$$

Recalling Equation 2.10, which related the surface charge to surface potential of an interface in a 1:1 electrolyte:

$$\sigma = \sqrt{8k_B T C_{bulk}\varepsilon_r\varepsilon_0}\,\sinh\left(\frac{ne\psi}{2k_B T}\right) \qquad [5.10]$$

This equation can be rearranged to solve for the surface potential, ψ.

$$\psi = \frac{2k_B T}{ne}\sinh^{-1}\left\{\frac{\sigma}{\sqrt{(8k_B T\varepsilon_r\varepsilon_0 C_{bulk})}}\right\} \qquad [5.11]$$

Equation 5.11 can be used to determine the theoretical surface potential of charged bilayers. As a first approximation, if the surface potential of a DMPE bilayer is somewhat arbitrarily set to zero – which ignores the substantial dipole moment the DMPE head group possesses, then the *difference* in surface potential of a charged phospholipid bilayer and DMPE can be calculated. This quantity is denoted $\Delta\psi_{BL-DMPE}$. Results are tabulated in Table 5.7. Also shown are the ratios of surface to bulk concentrations for both positive and negative ions.

It cannot be overstated that this is a rather crude model. The dipole moment of DMPE has been ignored, as have solvation effects on both DMPS and

DMPE. Moncelli and coworkers have suggested that the charge of DMPS lies buried within the head group and hence may not be strictly considered as a purely surface charge[39]. Notwithstanding these reservations, it is still instructive to examine the EIS data in light of this model.

10% DMPS in DMPE has a surface charge density of -0.025 e/Å with full coverage. This is the same surface charge density as measured for chick ventricle cells. The surface potential was measured[40] to be -40 mV, which is close to the -48 mV calculated for a 10% DMPS film with full coverage. This is close enough to suggest that this model, despite its simplicity, is not

Table 5.7: Calculated surface potentials. A surface coverage of 90% was used in the calculations, except where noted.

Composition	$\Delta\psi_{BL-DMPE}$ / mV	Positive ion surface concentration to bulk ratio	Negative ion surface concentration to bulk ratio
DMPE	0	1	1
10% DMPS	-44	5.65	0.177
20% DMPS	-73	17.7	0.0566
30% DMPS	-92	37.3	0.0268
40% DMPS	-106	64.7	0.0155
50% DMPS	-117	99.8	0.0100
DMPS	-153	411	2.43×10^{-3}
DMPS (30% coverage)	-96	43.7	0.023

unreasonable at least at small values of surface charge. Note also that the decrease in calculated to measured values of σ would be expected if the negative charge on DMPS is buried as is suggested by Monocelli[39].

The application of Gouy-Chapman theory suggests that the surface concentration of anions is less for bilayers containing DMPS than for pure DMPE bilayers. This decrease in anion surface concentration increases as the mole fraction of DMPS increases. The opposite is true for cations: here cation surface concentration is increased as compared to DMPE and the cation surface concentration increases as the mole fraction of DMPS increases.

Turning first to the hexaaminеruthenium(III) chloride, it can be seen that values of R_{ct} and hence calculated values for J_{ea} and coverage show a clear trend towards lower values as the mole fraction of DMPS is increased, with the exception of 10% DMPS in DMPE. This mirrors quite well the expected increase in the surface concentration of $Ru(NH_3)_6^{3+}$ (aq) with the increase in DMPS mole fraction. The observed increase porosity of these DMPE/DMPS bilayers to $Ru(NH_3)_6^{3+}$ (aq) can thus be explained by the increasing surface charge density caused by DMPS. It also seems reasonable to conclude that the low values of coverage calculated is at least partly due to this enhanced porosity of cations: surface coverage is likely to be higher than calculated.

Gramacidin is a amphiphilic peptide with the ability to open channels in phospholipid membranes[41]. Nelson demonstrated that bovine-PS monolayers incorporating gramacidin had a 9 fold increase in permeability to Tl^+ ions than

the equivalent DOPC monolayer with gramicidin[42]. This was attributed to the negative surface potential of the PS monolayer increasing the surface concentration of Tl^+, analogous to the increase in the layer permeability to $Ru(NH_3)_6^{3+}$ observed here. Likewise, the permeability of a bovine-PS monolayer on mercury to the cations Tl^+, Cd^{2+}, Cu^{2+} and Pb^{2+} was shown to be greater than for a DOPC monolayer on the same surface[43].

The ferrocyanide anion behaves somewhat differently. Here there is observed a stepwise increase in R_{ct}, D_{ea} and coverage from a pure DMPE bilayer to ones containing DMPS. Bilayers containing DMPS are less permeable to anions, but the expected regular pattern of decrease in porosity to anions with DMPS is not observed. It is clear that this simple model cannot fully account for these observations.

Impedance spectra of self-assembled monolayers (SAMs), often alkanethiols, and bilayers have been reported in the literature. Pandey *et al.* investigated a system where a 2-naphthalenethiol SAM was deposited onto a gold surface[44]. R_{ct} for the ferrocyanide redox system was reported as 592.1 Ω cm^2, compared to 7.60 Ω cm^2 for bare Au. This value increased to 19.57 kΩ cm^2 when a cholesterol monolayer was deposited by LB on top of the SAM. A LB deposited cholesterol bilayer on top of the SAM had a high R_{ct} of 2.406 MΩ cm^2. From this, even allowing for the effect of the 2-naphthalenethiol SAM, it can be seen that all of the phospholipid bilayers in this work have higher numbers of defects than cholesterol bilayers.

Finkles *et al.* reported what they termed "weakly blocking" SAMs of octadecanethiol on Au with $Ru(NH_3)_6^{3+}$ in 0.2 M Na_2SO_4 as the redox system[45]. R_{ct} in this case was 150 Ω cm^2. From these values, it can be seen that the phospholipid bilayers here are all weakly blocking. Mixed DMPS/DMPE bilayers display charge resistances similar to that of octadecanethiol on the same surface. DMPS is rather lower while DMPE is substantially higher. Thus both octadecanethiol and mixed DMPE/DMPS bilayers can be expected to have similar numbers of defects.

Thiols have a high affinity for mercury, and form highly organised SAMs on the mercury surface[46]. A R_{ct} of 108 MΩ cm^2 was reported for a octadecanethiol SAM on Hg with 1 mM $Ru(NH_3)_6^{3+}$ in 0.1 M KNO_3 [15]. This is five orders of magnitude higher than any value in Table 5.3, which is a good indication how well octadecanethiol is organised on mercury as opposed to octadecanethiol or phospholipids on Au. Mercury, by virtue of its liquid state, is capable of forming a very flat surface with few defects, explaining the extremely high R_{ct}. Thus it is likely that the low values observed in this section for R_{ct} are a reflection of the quality of the electrode surface. It is thus interesting to compare these results to those obtained by Lindholm-Sethson[6] who investigated multilayers of dipalmitoylphosphatidic acid (DPPA) deposited onto a polycrystalline gold surface. It was found that in many cases with films possessing fewer than five layers that the layer resistances were low when the DPPA head groups faced the Au substrate. This was attributed to the first deposited layers of DPPA being disorganised and with looser packing than subsequent layers. This disorder is a direct consequence of the imperfections

present in the polycrystalline gold substrate. It seems reasonable to postulate that a similar phenomenon can explain the low values of R_{ct} recorded in Tables 5.3 and 5.5.

Though EIS studies without an electroactive probe are not directly comparable with these studies it is nevertheless an interesting exercise to compare the two. Kendall *et al*. have used the technique to evaluate tethered bilayers of a polar lipid extract from the bacterium *E. coli* using a triethyleneoxythiol cholesterol tether to attach the bilayer to a sputtered Au substrate[47]. The tethered bilayer resistance was measured to be 11.7±4.6 MΩ cm^{-2}. Interestingly, this film resistance was more than halved on the addition of valinomycin, a peptide which forms channels which can conduct K^+ ions across a lipid membrane.

5.3.3 Conclusions

Films containing DMPS act as more effective barriers to the ferrocyanide anion than pure DMPE. The opposite is found for the $Ru(NH_3)_6^{3+}$ cation where DMPE is the superior barrier. It was hypothesised that the negative charge on the DMPS lipid would exert a controlling effect on the permeability of the bilayer to anions. The negative charge on DMPS molecules neighbouring pores and defects can be expected to repel anions, thereby reducing permeability. This hypothesis allows us to make the prediction that the opposite will occur for cations: mutual attraction between DMPS and cation will increase permeability. DMPS will therefore act as a gatekeeper.

Such voltage gated pores have indeed been observed. Melittin is a small amphiphilic peptide that can be incorporated into phospholipid membranes and will open pores within that membrane[48]. Melittin is positively charged. Pores opened by melittin have been observed to conduct anions in preference to cations[49,50].

In this light, a re-examination of the variation of R_{ct} with composition and electroactive probe is warranted. As the mole fraction of DMPS was increased, there was a marked trend for the bilayer permeability to $Ru(NH_3)_6^{3+}$ cations to increase in step. In contrast, the bilayer permeability to the anion ferrocyanide diminished sharply compared to pure DMPE with even low concentrations of DMPS. Furthermore, this fall in permeability does not depend on the mole fraction of DMPS, merely that DMPS is present in the bilayer. This does suggest voltage gating behaviour is occurring in addition to effects due to increased negative surface potential.

As a thought exercise, if it is postulated that voltage gating is caused by the presence of at least one DMPS molecule next to a pore in the bilayer, it is possible to come up with a crude estimate of the pore diameter necessary for a DMPS molecule to reside on the pore wall. The DMPE and DMPS head groups have a diameter of approximately 10 Å. Assuming the lipids are packed in a hexagonal arrangement, a pore which is 30 Å across will be bordered by 12 lipid molecules on each leaflet – 24 in total. For a 10% DMPS bilayer, the probability of there being at least one DMPS molecule in that

border is 0.92. It is thus highly likely that a pore of this dimension would exhibit voltage gating. A similarly dimensioned pore in a 20% DMPS bilayer would have a 0.995 probability of at least one DMPS molecule. This difference is smaller than the reproducibility of the bilayers in this work, hence it is unlikely that any variation of permeability would be resolved. Interestingly, the pores opened in phospholipid bilayers by melittin have been measured as having a diameter of 44 Å by neutron diffraction[51] and 10 – 60 Å using vesicle leakage rates[52,53]. Thus this admittedly crude estimation produces a pore size that is reasonable.

Caution must be exercised with this conclusion, however. $Ru(NH_3)_6^{3+}$ was measured at a potential of -0.18 V, a point where the charge density is negative. Ferrocyanide was measured at a potential of +0.18 V, close to the PZC and where the film will be most stable. In particular, a negative charge density might be expected to exert a particularly deleterious effect to bilayers containing DMPS. The possible result of this would be more pores and defects – hence a greater permeability to any ion. This is in fact what is observed. We thus are unable to distinguish between either explanation.

5.4 References

1. CRC Handbook of Physics and Chemistry, 74th edition

2. Toney, M. F., Howard, J. N., Richer, J., Borges, G. L., Gordon, J. G., Melroy, O. R., Wiesler, D. G., Yee, D., Sorensen, L. B., (1994), *Nature*, **368**:444

3. Bin, X., Zawisza, I., Goddard, D., Lipkowski, J., (2004), *Langmuir*, **21**:330

4. S. L. Horswell, private communication

5. Gafni, Y., Weizman, H., Libman, J., Shanzer, A., Rubinstein, I., (1996), *Chem. Eur. J.,* **2**:759

6. Lindholm-Stethson, B., (1996), *Langmuir*, **12**:3305

7. Damaskin, B. B., Petrii, O. A., Batrakov, V. V., *Adsorption of Organic Compounds at Electrodes,* Nauka, Moscow, 1968

8. Castellana, T., Cremer, P. S., (2006), *Surf. Sci. Rpt.*, **61**:429

9. Horswell, S. L., Zamlyynny, V., Li, H-Q., Merrill, R., Lipkowski, J., (2002), *Faraday Discuss.*, **121**:405

10. Oleson, T., A., Sahai, N., Wesolowski, D. J., Dura, J. A., Majkrzak, C. F., Giuffre, A. J., (2012), *J. Colloid Interface Sci*, **370**:192

11. Brosseau, C. L., Sheepwash, E., Burgess, I. J., Cholewa, E., Roscoe, S. G., Lipkowski, J., (2007), *Langmuir*, **23**:1784

12. Xu, S. M., Chen, M. H., Cholewa, E., Szymanski, G., Lipkowski, J., (2007), *Langmuir*, **23**:6937

13. Bizzotto, D., Nelson, A., (1998), *Langmuir*, **14**:6269

14. Uematsu, K., Sagara, T., (2008), *J. Electroanal. Chem.*, **623**:109

15. Bin, X., Zawaisza, I., Goddard, J. D., Lipkowski, J., (2005), *Langmuir*, **21**:330

16. Burgess, I., Li, M., Horswell, S. L., Szymanski, G., Lipkowski, J., Majewski, J., Satija, S., (2004), *Biophys. J.* **86**:1763

17. Burgess, I., Zamlynny, G., Szymanski, G., Lipkowski, J., (2001), *Langmuir*, **17**:3355

18. Stoodley, R., Bizzotto, D., (2003), *Analyst*, **128**:552

19. Nelson, A., (2007), *J. Electroanal. Chem.*, **601**:83

20. Bizzotto, D., Zamlynny, V., Burgess, I., Jeffry, C. A., Li, H. Q., Rubinstein, I., Galus, Z., Nelson, A., Pettinger, B., Merill, A. R., Lipkowski, J., 1999, *Interfacial Electrochemistry, Theory, Experiment and Applications*, ed. A. Wieckowski, Marcel Dekker, New York

21. Zawisza, I., Bin, X., Lipkowski, J., (2007), *Langmuir*, **23**:5180

22. Zawisza, I., Bin, X., Lipkowski, J., (2004), *Bioelectrochem.*, **63**:137

23. Zawisza, I., Lachenwitzer, A., Zamlynny, V., Horswell, S. L., Goddard, J. D., Lipkowski, J., (2003), *Biophys. J.*, **85**:4055

24. Bin, X., Horswell, S. L., Lipkowski, J., (2005), *Biophys. J.*, **89**:592

25. Lipkowski, J., Stolberg, L., 2002, *Adsorption of Molecules at Metal Interfaces*, VCH

26. Trasatti, S. J., (1974), *J. Electroanal. Chem*. **53**:335

27. Wacklin, H. P., Thomas, R. K., (2007), *Langmuir*, **23**:7644

28. Lasia, A., 1999, *Electrochemical Impedance Spectroscopy and Its Applications, Modern Aspects of Electrochemistry*, ed: B E Conway, J Bockris, R E White, Vol. 32, Kluwer Academic/Plenum p143

29. Kepa, H., Kleinwaks, L. J., Berk, N. F., Majkrzak, C. F., Berzina, T. S., Troitsky, V. I., Antolini, R., Feigin, L. A., (1998), Physica B, 241:1048

30. Sofonov, V. A., Choba, M. A., Krivenko, A. G., Manzhos, R. A., Maksimov, Yu. M., (2012), *Electrochim. Acta*, **61**:140

31. Clavilier, J., Nguyen van Huong, C., (1977), *J. Electroanal. Chem.*, **80**:101

32. Whitehouse, C., O'Flanagan, R., Lindholm-Sethson, B., Movaghar, B., Nelson, A., (2004), *Langmuir*, **20**:136

33. Stern, M., Geary, A. L., (1957), *J. Electrochem. Soc.*, **104**:56

34. Starr, T. E., Thompson, N. L., (2000), *Langmuir*, **16**:10301

35. Charitat, T., Bellet-Amalric, E., Fragneto, G., Graner, F., (1999), *Eur. Phys. J. B*, **8**:583

36. Bard, A. J., Faulkner, L. R., 2001, *Electrochemical Methods, Fundamentals and Applications*, 2nd edition, John Wiley

37. Nicholson, R. S., Shain, I., (1964), *Anal. Chem.*, **36**:707

38. Bockris, J. O'M., Reddy, A. N., 1970, *Modern Electrochemistry*, Plenum, New York

39. Moncelli, M. R., Becucci, L., Buoninsegni, F. T., Guidelli, R., (1998), *Biophys. J.,* **74**:2388

40. Kell, M. J., Defelice, L. J., (1988), *J. Membr. Bio.*, **102**:1

41. Prenner, E. J., Lewis, R. N. A. H., McElhaney, R. N., (1999), *Biochim Biophys Acta*, **1462**:201

42. Nelson, A., (1993), *Faraday Trans.*, **89**:2799

43. Nelson, A., (1993), *Faraday Trans*, **89**:3081

44. Pandey, R. K., Suresh, K. A., Lakshminarayanan, V., (2007), *J. Colloid and Interface Sci.*, **315**:528

45. Finkles, H. O., Snider, D. A., Fedyk, J., Sabatani, E., Gafni, Y., Rubinstein, I., (1993), *Langmuir*, **9**:3660

46. Cohen-Atiya, M., Nelson, A., Mandler, D., (2006), *J. Electroanal. Chem.*, **593**:227

47. Kendall, J. K. R., Johnson, B. R. G., Symonds, P. H., Imperato, G., Bushby, R. J., Gwyer, J. D., van Berkel, C., Evans, S. D., Jeuken, L. J. C., (2010), *ChemPhysChem*, **11**:2191

48. Chen X., Wang J., Kristalyen C. B., Chen Z., (2007), *Biophys. J.*, **93**:866

49. Tosteson M. T., Tosteson D. C., (1981), *Biophys J.*, **36**:109

50. Pawlak M., Stankowski S., Schwarz G., (1991), *Biochim Biophys Acta*, **1062**:94

51. Yang L., Harroun T. A., Weiss T. A., Ding L., Huang H. W., (2001), *Biophys. J.,* **81**:1475

52. Rex S., (1996), *Biophys. Chem.,* **58**:75

53. Matsuzaki K., Yoneyama S., Miyajima K., (1997), *Biophys. J.,* **73**:831

6. Neutron Reflectometry of Phospholipid Bilayers

Neutron reflectometry is a powerful technique capable of probing the vertical structure of interfaces at the nanometre scale. The D17 neutron reflectometer at the Institut Laue Langevin (ILL) in Grenoble, France was used to investigate a 10% DMPS in DMPE bilayer supported on gold.

6.1 The D17 Neutron Reflectometer

A neutron reflectometer is composed of five essential components:

1. A neutron source.
2. A monochromator. Some means of selecting for neutron frequency is necessary to generate the required monochromatic beam
3. Collimation optics. This collects and focuses a beam of neutrons onto the sample
4. The sample in a sample holder. The sample holder can be moved in three dimensions to aid alignment.
5. Detection: there must be some means of recording the reflected neutrons.

The D17 neutron reflectometer at the Institut Laue Langevin (ILL) in Grenoble, France, was used to probe the structure of a lipid bilayer composed of a

mixture of DMPS and DMPE. It is described by Cubitt and Fragneto, 2002[1]. Figure 6.1 is a diagram of D17 as it was used.

The neutron source at the ILL was a D_2O moderated nuclear reactor operated at 50 MW thermal power. D17 was operated in time of flight mode. A pair of choppers acted to select wavelength. Only neutrons travelling in a narrow range of velocities, and hence wavelengths, were able to pass through in the time interval that both choppers were open. This gave a wavelength range of 2-20 Å.

Collimation was provided by a focusing supermirror guide. A supermirror is a sandwich of alternating thin layers (approximately 500 Å thick) of Ti and Ni: the large SLD contrast between these elements increases the critical angle by as much as a factor of four over Ni. This makes the supermirror guide more efficient in collimating neutrons. A neutron flux of 9.6×10^{10} neutrons cm^{-2} s^{-1} was achieved at the sample stage[1]. The sample stage can be moved in three directions in order to ensure correct alignment. The two slits at each end of the supermirror guide were to stop any off-axis neutrons reaching the sample stage, thus improving collimation.

Detection was by means of a ^3He multidetector with a size of 250 x 500 mm. The multidetector is composed of an array of detecting elements that allow a spatial picture of the specular and off-specular reflections to be built up. This has the advantage that the background, which consists mostly of off-specular reflection, is captured concurrently with the specular data.

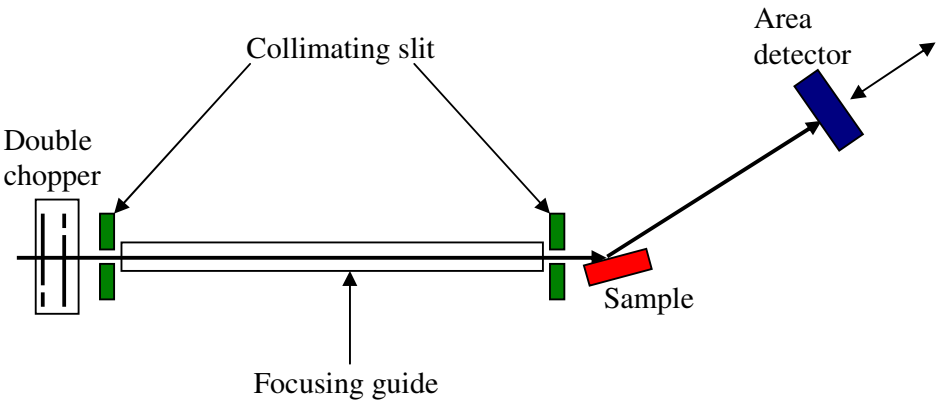

Figure 6.1: A representation of the D17 Reflectometer layout[2]. Not shown is the reactor neutron source.

6.2 Data Analysis

As was discussed in Section 2.6, data from the reflectometer is a Fourier transform of the vertical structure of the sample. It must be processed in order for useful information to be gained.

The raw data of each run were composed of a data file for each angle. Use was made of the in-house Large Array Manipulation Program (LAMP) software for data reduction. LAMP combines both data files and outputs a file with reflectivity versus Q. Figure 6.4 shows a typical reflectivity curve versus Q. This particular instance was of a deuterated lipid bilayer in D_2O solvent.

Motofit was used to fit the experimental data[3]. This is a sophisticated fitting program that can be used to obtain data on layer thickness and SLD, interface roughness and degree of solvent penetration.

There are two methods available: genetic fitting and Levenberg-Marquardt fitting. Genetic fitting produces a population of possible fits generated from user selected parameters. The members of this population which have the best fit to the experimental data as determined by the χ^2 value are allowed to "mutate" while the rest are discarded. This process is repeated for a number of generations (usually 100) with the survivors from each generation being selected for the lowest χ^2 value. Genetic fitting has the advantage that it can find a good fit even when the initial first guess is poor. However, the eventual solution may not have a valid physical meaning even though it has an excellent χ^2 value.

The Levenberg-Marquardt method is an algorithm developed for the fitting of non-linear equations. It minimises the χ^2 value. It is efficient at finding a minimum in the given function, but unless the initial guess is close to the global minimum, there is a high probability the method will converge on a local minimum.

Motofit has the option to use both fitting methods. Fitting neutron reflectivity data may be regarded as a problem of finding a solution in what could be termed "solution phase space". Each parameter that is being fitted, such as layer thickness, will have its own dimension in solution phase space. The

number of dimensions in solution phase space is thus equal to the number of parameters that are being fitted, plus an extra one for the χ^2 value. In this case, sixteen parameters were being fitted for the four layer model (the properties of thickness, SLD, roughness and solvent content were variables that were fitted for each layer). Hence solution phase space had seventeen dimensions, meaning a large volume had to be searched. In practice, genetic fitting was used to generate a population of models which would span this volume. The genetic fitting algorithm was then left for 100 generations to evolve a solution with the lowest χ^2 value. This solution was then used as the initial parameters for Levenberg-Marquardt fitting in order to ensure the final fit had the lowest χ^2 value.

The fitting procedure rarely produces on unique solution. Rather, there are a number of possible solutions, each of which possess a similar χ^2 value. Some of these modelled solutions can be ruled out as they have unrealistic parameters such as an excessively large bilayer thickness. However, there will remain a number of plausible solutions, each of which will vary slightly in their individual fitted parameters. Therefore it must be emphasised is that the fitting procedure will arrive at one of a family of possible solutions, each with similar χ^2 values. Each member of this family will have broadly similar attributes, but variations in the values of individual parameters. This variation is typically 10% and is a major source of uncertaincy. It is therefore possible to define the error in the data arising from the fitting procedure to be 10%.

6.2.1 Choice of Model

The model used has a crucial bearing upon the outcome of the fitting procedure. In order to get meaningful information from this technique, an accurate model is needed. In other words, some knowledge of the system being investigated is required. It is for this reason that neutron reflectivity is best used to glean collaborative data about a system. A four layer model was employed for fitting (figure 6.2):

Layer 1: quartz substrate

Layer 2: polymer adhesion layer

Layer 3: bilayer

Layer 4: electric double layer

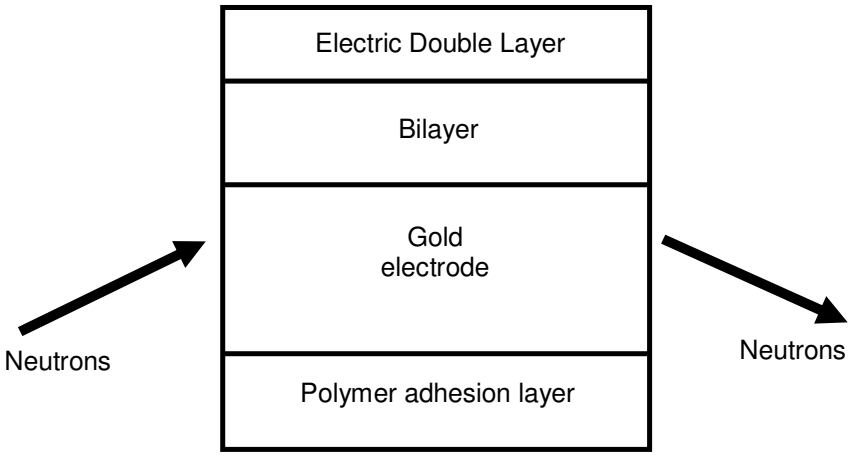

Figure 6.2: Four layer model. The bilayer is sitting directly on the substrate. This model was used to fit data at all potentials of -0.55 V and greater.

The wavelength of the neutrons source (2-20 Å) means that it is unlikely that the head group region will be resolved as a separate region in the bilayer structure. The bilayer was hence modelled as one layer. This model was based on the data from the DC and chronocoulometry experiments which indicated that a bilayer formed by vesicle fusion of this composition can be expected to be adsorbed onto an Au surface. Further support for this model come from studies of mixed DMPC/cholesterol bilayers which have broadly similar structural properties to the system under investigation[4].

There is evidence that at high negative potentials, similar systems where the bilayers are composed of cholesterol in DMPC become detached from the substrate and allows a thin solvent layer to interpose itself between substrate and bilayer[4]. Furthermore, DC data for 10% DMPS in DMPE show a rise in capacitance at potentials more negative than -0.4 V which is consistent with this hypothesis. Chronocoulometry data shows that the charge density for a 10% DMPS in DMPE bilayer that has been formed *via* vesicle fusion is similar to that of the bare electrode, suggestive of a desorbed bilayer. Hence, at -0.75 V, this effect was introduced into the model (figure 6.3):

Layer 1: quartz substrate

Layer 2: polymer adhesion layer

Layer 3: solvent layer

Layer 4: bilayer

Layer 5: electric double layer

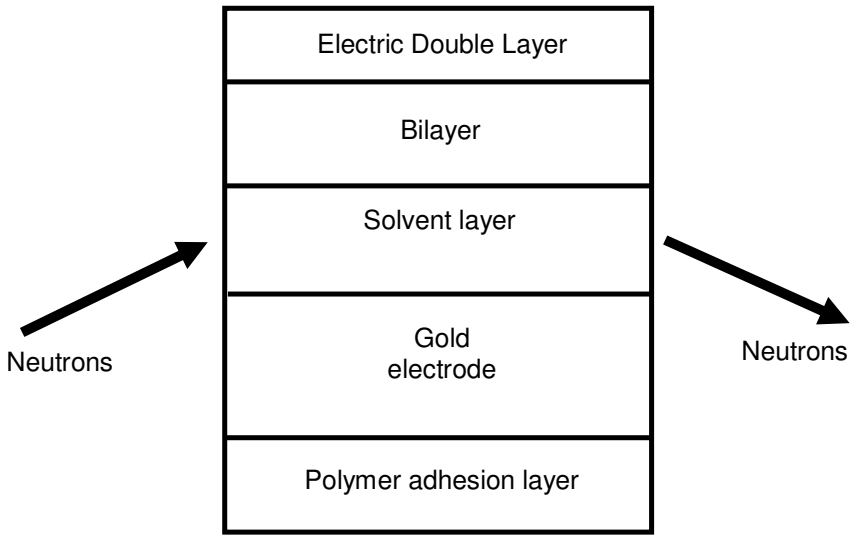

Figure 6.3: Five layer model used at -0.75 V potential. In this model, the bilayer has become detached from the substrate, allowing a thin solvent layer to interpose itself between the gold electrode and bilayer.

6.3 Results and Discussion

Fits generated by *Motofit* for all four contrasts are shown in Figures 6.4 to 6.7 along with the raw data. The potential for was +0.15 V for all contrasts. Figure 6.8 shows how the reflectivity data changes with the applied potential.

The five layer model used at -0.75 V proved to provide an improved fit to the data than the four layer model at this potential, as judged by the resultant χ^2 value: 0.015 for the four layer model versus 0.004 for the five layer model.

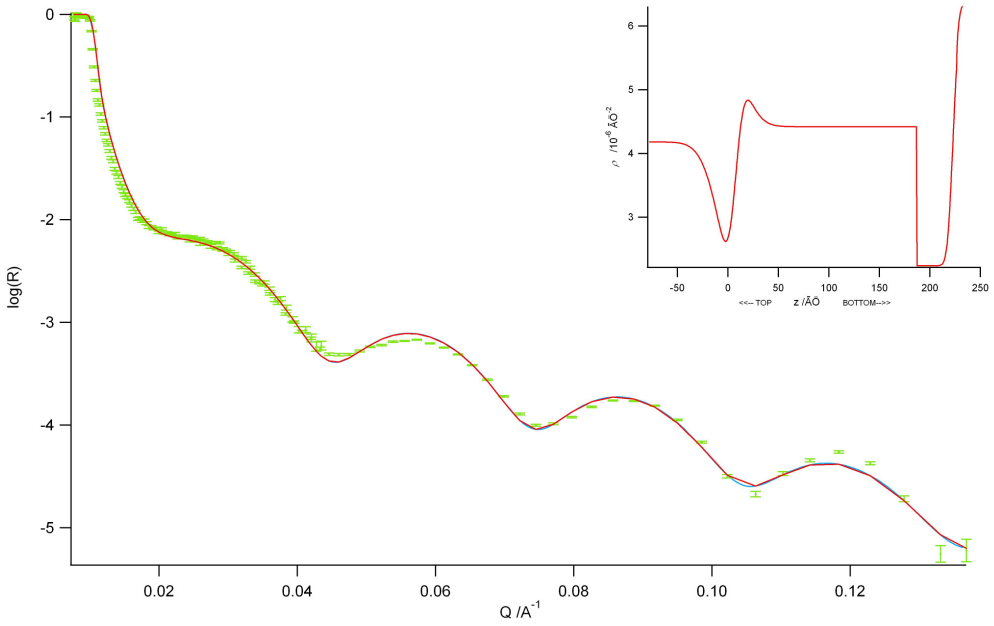

Figure 6.4: Neutron reflectivity profile for deuterated lipid in D_2O at an applied potential of +0.15 V. Green points with error bars are the raw data. The red line is the fit.

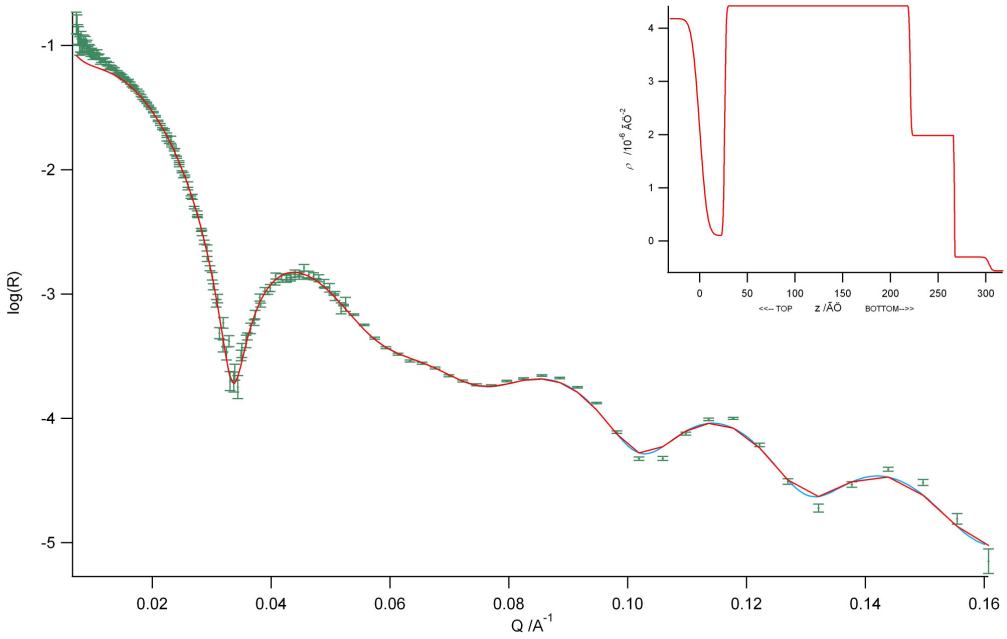

Figure 6.5: Neutron reflectivity profile for deuterated lipid in H_2O at an applied potential of +0.15 V. Green points with error bars are the raw data. As before, the red line represents the fitted data.

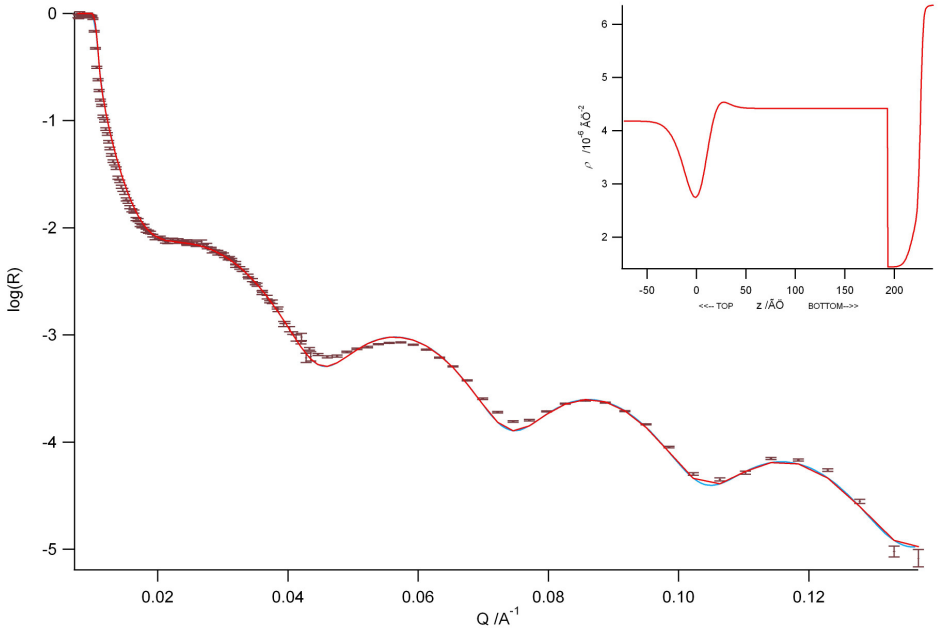

Figure 6.6: Neutron reflectivity profile for hydrogenous lipid in D_2O at an applied potential of +0.15 V. Purple points with error bars are the raw data. The red line is the fit.

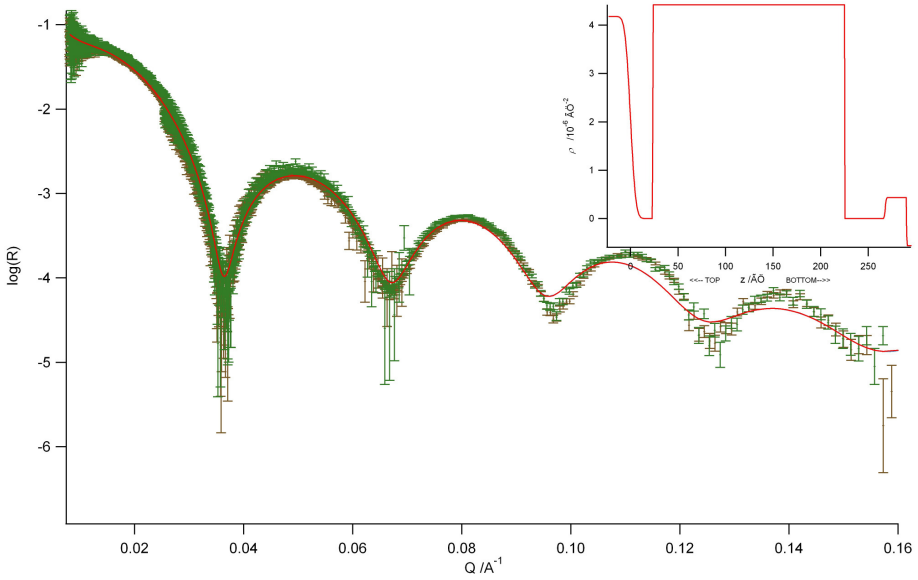

Figure 6.7: Neutron reflectivity profile for hydrogenous lipid in H_2O at an applied potential of +0.15 V. Green points with error bars are the raw data. The red line is the fit. The fit is poorer in this case as the contrast between hydrogenous lipid and H_2O is low.

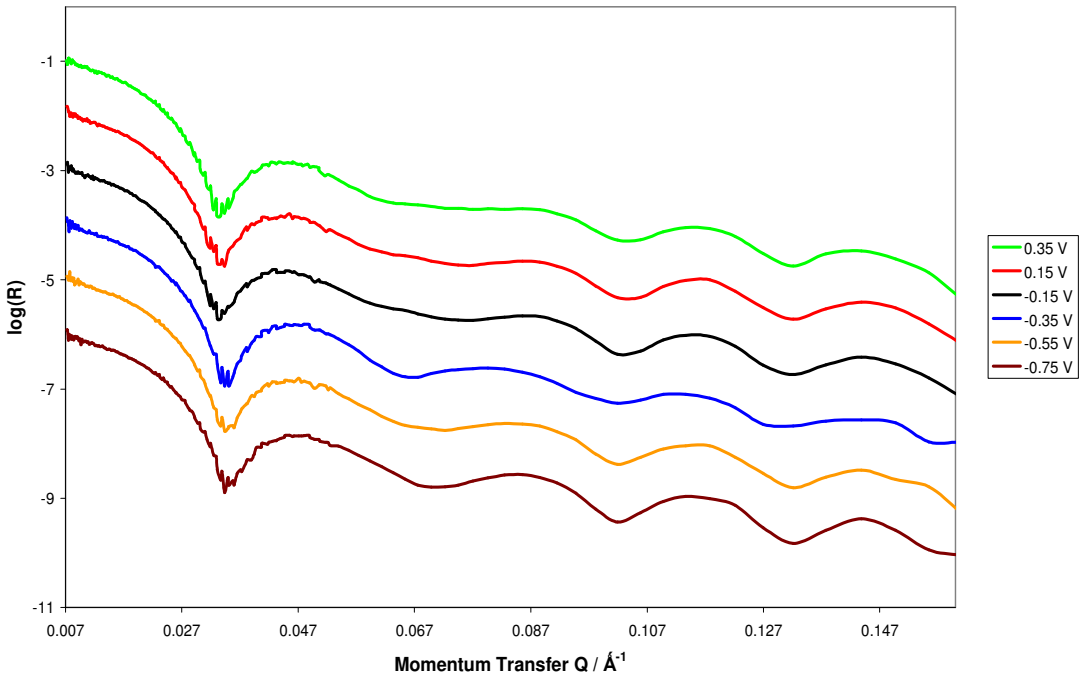

Figure 6.8: Neutron reflectivity profiles for deuterated lipids in H_2O. Each profile is offset by a one decade for clarity.

All four contrasts display the expected sharp fall to the fourth power of intensity with Q. Hillman[5] examined the off-specular signal on the detector for these data and concluded that there was in fact little off-specular reflection. This is a good indication that the bilayers formed at all four contrasts had good surface coverage.

Figure 6.9 displays the results of the *Motofit* fit for four contrasts, showing how bilayer thickness varies with potential. Bilayer thicknesses fall within the range of values reported for similar systems. Burgess *et al.* reported thicknesses of 26 Å to 37 Å in neutron reflectometry studies of mixed DMPC/cholesterol

bilayers[4]. These thicknesses varied with potential, with the smallest thickness at positive potentials and becoming progressively thicker as the potential was changed to more negative values. Majewski *et al*. reported a thickness of 31.9 Á for DMPC on a silica substrate[6] while Johnson *et al.* reported a somewhat higher thickness of 46 Á for the same system[7] (DMPC on silica). Neutron reflectometry studies of DMPE bilayers adsorbed onto a polyelectrolyte multilayer[8] (itself adsorbed on a silica substrate) produced a thickness of 45 Á.

Three of the contrasts display a trend for the bilayer to increase in thickness as the potential becomes more negative going to -0.55 V. The swelling becomes more pronounced as the applied potential becomes negative (from -0.15 V to -0.55 V). Such swelling of phospholipid bilayers with application of a negative potential have been observed using PM-IRRAS in DOPC[9] and DMPC[10]. The fourth contrast (deuterated lipid in H_2O) shows no such trend: if anything, it displays a tendency towards decreasing thickness as the potential becomes increasingly negative.

All contrasts, however, show a marked decrease in thickness at -0.75 V. At this potential, the bilayer can be expected to have desorbed from the substrate. It is not, then, unexpected that some changes are seen.

Motofit is able to model the degree of solvent penetration into the bilayer. It may be expected that some variation of solvation may be the result of altering the applied electric field. Figure 6.10 displays the solvation fit.

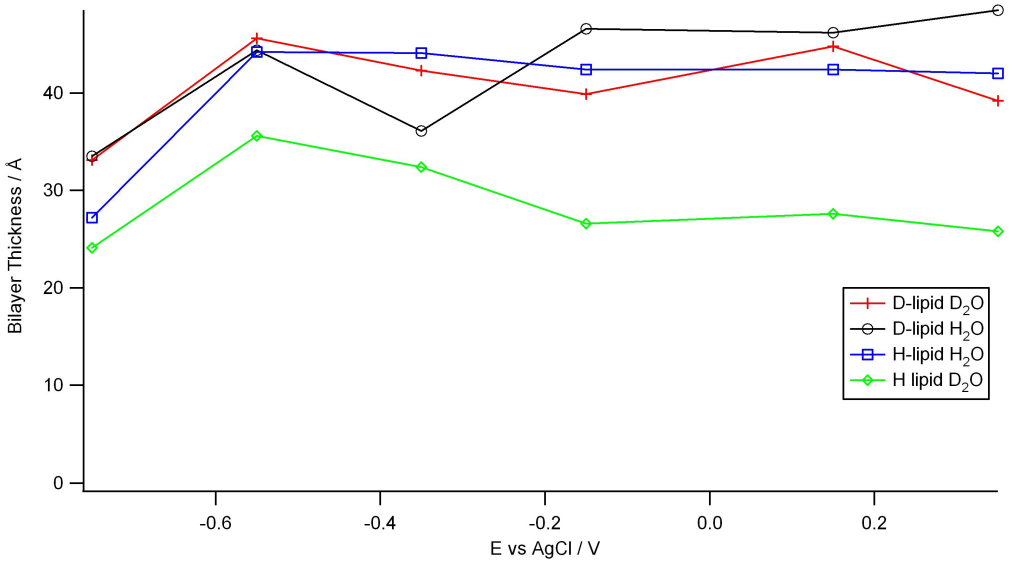

Figure 6.9: Variation of film thickness with potential

Again, there is some variation in the fit between contrasts. However, a clear trend can be discerned. All four bilayers have increased solvent penetration at potentials below -0.15 V. In fact, these data mirror reasonably well the bilayer thickness plots. There is relatively little change in solvent content at the positive potentials, a region where little change in thickness is noted. In this region, water content is in the range 3-18%. This agrees reasonably well for neutron reflectometry studies of DPPC on sapphire, where solvation was estimated to be 20%[11]. The bulk of the change occurs at negative potentials, particularly going from -0.15 V to -0.55 V. Again, this is similar to the thickness data. Finally, a fall in solvation can be observed when the bilayer becomes detached from its substrate. A change in solvent content in response to applied potential has been observed in other thin film systems such as polyvinylferrocene films[12].

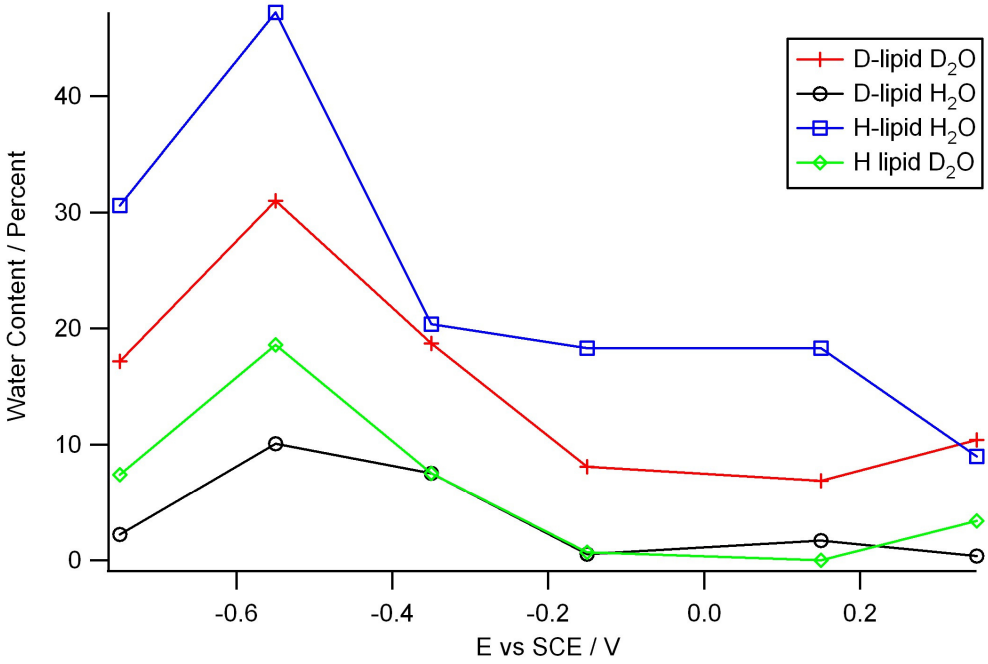

Figure 6.10 Fitted results for the variation of bilayer solvent content by mass with potential.

The similarities between the bilayer thickness and solvation data leads almost inevitably to the hypothesis that they are linked. In fact, it is possible to propose that the degree of solvent penetration controls the bilayer thickness – with more solvent entrained in the bilayer, it is reasonable to conclude that the bilayer swells as a direct consequence. Indeed, this behaviour was observed for cholesterol in an DMPC mixed bilayer[4]. Hydrogels also show this behaviour of increasing film thickness with increasing water content[13].

It was proposed that subjecting a phospholipid bilayer to a strong electric field acts in such a way as to allow the ingress of water at least past the head groups in order to explain the surface pressure profile of vesicle formed DMPE/DMPS bilayers (Section 5.2.2). The fitted neutron data, most

particularly the solvation data supports this hypothesis. That the solvent content falls sharply at -0.75 V, when the bilayer detaches from the electrode (and thus experiences a fall in the electric field) would support this conclusion. Mixed DMPC/cholesterol bilayers have been shown to behave in this manner[4].

Capacitance data shows that the capacitance of an adsorbed phospholipid bilayer increases as the substrate becomes more negative (Section 5.1). Water has a higher relative permittivity (80) than lipid (2-3). This increase was postulated to be as a result of increasing hydration of the bilayer. That the fitting data above shows exactly such a trend of increasing solvent content offers support to this hypothesis. Moreover, the biggest change in capacitance is observed at between -0.3 and -0.7 V, the region where the largest increase in water content is seen. At potentials of -0.15 V and above, both the neutron reflectometry data and the DC results are in agreement: little change in either solvation or capacitance.

Chronocoulometry of bilayers formed by vesicle fusion indicate such layers have little cohesion to the substrate at potentials more negative than -0.7 V. A five layer model with the bilayer detached from the surface was found to be a better fit than the four layer model at a potential of -0.75 V. Separation between substrate and bilayer is small – averaging 8 Å for the four bilayers (Table 6.1). Burgess *et al.* concluded that when the DMPC/cholesterol bilayer detached, a 10 Å solvent layer separated the bilayer and Au substrate[4].

Table 6.1: Modelled solvent layer thickness at -0.75 V

Contrast	Solvent layer thickness / Å
D-lipid in H_2O	7.2
D-lipid in D_2O	8.1
H-lipid in H_2O	11.2
H-lipid in D_2O	5.2

Other investigations of phospholipid bilayers have revealed that the bilayer is not directly adsorbed onto the surface but instead sits on a cushion of solvent. Typically the substrate is hydrophilic. Miller *et al*. showed using X-ray reflectometry that a DOPC bilayer was separated from its quartz substrate by a 4 Å thick layer of water[15]. Neutron reflectometry by Johnson *et al*. of a DMPC bilayer on quartz revealed a solvent cushion 30±10 Å thick[7]. NMR studies[16] of DMPC bilayers adsorbed onto glass beads indicated that the bilayer was stood off from the glass surface by a solvent layer whose thickness was 17±5 Å. Thus the values for the solvent layer thickness in Table 6.1 are of a similar magnitude. It should be noted that the high values quoted by Johnson were believed to be caused in part by the surface roughness of the substrate.

It was found in both the chronocoulometry and DC experiments that once the bilayer had detached from its substrate at a large negative potential, it would readily re-attach once the potential was increased. This observation lends credence to the idea that the bilayer remains more or less intact a short distance from the electrode surface: if the bilayer were to fragment

immediately after desorption, it would take time (at least 10 minutes) to re-assemble on the substrate, which would exhibit charge densities and capacities much closer to that of bare Au (111). Instead, what was observed was the rapid re-attachment of a near complete bilayer as witnessed by the rapid fall in capacity as the potential increased above -0.7 V.

6.4 Conclusions

Observations using differential capacitance led to the proposal that DMPE/DMPS bilayers absorb water and finally desorb from the electrode at large negative potentials (Section 5.1.2). This model was based on observations by Burgess *et al*[4]. How well is this model supported by neutron reflectometry data?

The neutron reflectivity data collaborates much of the electrochemistry data. These data support the hypothesis that the bilayer is directly adsorbed onto the Au substrate at a potential of -0.55 V or greater. This is in agreement with the DC and chronocoulometry data. When a five layer fit was attempted for all potentials at one contrast (deuterated lipid in H_2O) it was the resultant fits all had significantly higher χ^2 values (0.2 versus 0.006 for the four layer model). More damningly, the calculated bilayer thicknesses were significantly smaller – 25 Á compared to 40 Á. These values are considerably lower than the thicknesses measured for biological membranes[14] or those measured by Burgess *et al.* for DMPC/cholesterol[4]. It is thus reasonable to conclude the

five layer model with its solvent cushion separating the substrate from bilayer is unlikely at potentials of -0.55 V and above.

In contrast, at a potential of -0.75 V, the five layer model proved to provide a better fit as compared to the four layer model. Thicknesses of all contrasts decreased, probably as a result of the loss of solvent. The thickness of the h-lipid in D_2O is rather low at 24 Á. However, this contrast displayed low thicknesses, consistently lower than the other three, at all potentials. It is possible that this low thickness can be attributed to incomplete coverage.

Chronocoulometry shows that charge density values are close to the Au baseline for all bilayer compositions formed by vesicle fusion at potentials below -0.7 V (Section 5.2.1). This suggests that the bilayer is desorbed from the substrate at this potential. Fits to the neutron reflectometry data is improved when it is assumed the bilayer is desorbed at -0.75 V and hence supports this idea. This also supports the suggestion that peaks seen in the DC data close to this potential are associated with desorption.

It was proposed that the increase in capacitance observed between 0 V and -0.4 V was caused by the bilayer aborbing water (Section 5.1.2). The neutron reflectometry fit shows that water in the bilayer increases as the potential decreases and hence supports this hypothesis.

Thus the neutron relfecometry analysis supports the model suggested in

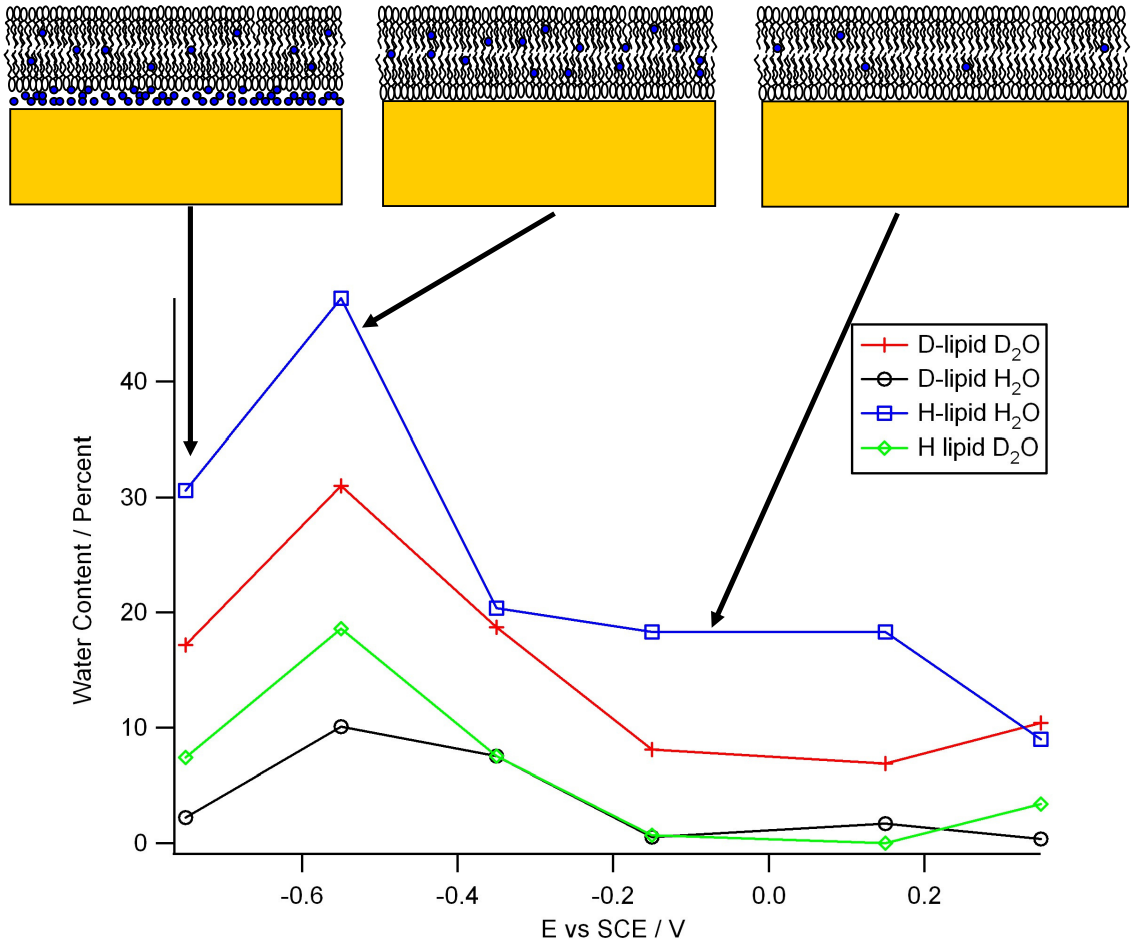

Figure 6.11: Schematic representation of the changes that adsorbed bilayers undergo with changes in potential. The blue dots represent water molecules. Below 0 V, water is incorporated into the film. Once desorption occurs, a thin layer of water forms at the electrode surface.

incorporates more water and finally detaches from the substrate entirely once the potential has reached -0.7 V. This process is shown pictorially in Figure 6.11.

6.5 References

1. Cubitt, R., Fragneto, G., (2002), *Appl. Phys. A*, **74**:S329

2. ILL website, http://www.ill.eu/d17/home, retrieved 02/11/2011

3. Nelson, A, (2010), *J. Phys.: Conf. Ser.* **251** 012094

4. Burgess, I., Szymanski, G., Li M., Horswell, S., Lipkowski, J., Majewski, J., Satija, S., (2005), *Biophys. J.*, **86**:1763

5. Hillman, A. R., Ryder, K. S., Madrid, E., Burley, A. W., Wiltshire, R. J., Merotra, J., Grau, M., Horswell, S. L., Glidle, A., Dalgleish, R. M., Hughes, A., Cubitt, R., Wildes, A., (2010), *Faraday Dis.*, **145**:357

6. Majewski, J., Wong, J. L., Park, C. K., Seitz, M., Israelachvili, J. N., Smith, G. S., (1998), *Biophysical J.*, **75**:2363

7. Johnson, S. J., Bayerl, T. M., McDermott, D. C., Adam, G. W., Rennie, A. R., Thomas, R. K., Sackmann, E., (1991), *Biophysical J.*, **59**:289

8. Chen, J., Kohler, R., Gutberlet, T., Hohwald, H., Krastev, R., (2009), *Soft Matter*, **5**:228

9. Zawisza, I., Lachenwitzer, A., Zamlynny, V., Horswell, S. L., Goddard, J. D., Lipkowski, J., (2003), *Biophys. J.*, **85**:4055

10. Horswell, S. L., Zamlyynny, V., Li, H-Q., Merrill, R., Lipkowski, J., (2002), *Faraday Discuss.*, **121**:405

11. Oleson, T., A., Sahai, N., Wesolowski, D. J., Dura, J. A., Majkrzak, C. F., Giuffre, A. J., (2012), *J. Colloid Interface Sci*, **370**:192

12. Hillman, A. R., Hughes, N. A., Bruckenstein, S., (1992), *J. Electrochem. Soc.*, **139** 1:74

13. Wang, W., Metwalli, E., Perlich, J., Troll, K., Papadakis, C. M., Cubitt, R., Mueller-Buschbaum, P., (2009), *Macromol. Rapid Commun.*, **30**:114

14. Alberts, B., Johnson, A., Lewis, J., Raff, M., Roberts, K., Walter, P., 2002, *Molecular Biology of the Cell*, 4th edition, Garland Science, US

15. Miller, C. E., Majewski, J., Gog, T., Kuhl, T. L., (2005), *Phys. Rev. Lett.*, **94**:238104

16. Bayerl, T. M., Bloom, M., (1990), *Biophysical J.*, **58**:357

7. Isotherms and Molecular Dynamics Simulations

7.1 Isotherms

7.1.1 Thermodynamics

The amphiphilic nature of lipids means that the molecules have a tendency to form a film on the air/water interface in order to reduce the surface energy. Favourable interactions between the aqueous sub-phase and the phospholipid head groups means there is a strong tendency for the molecule to rotate so that the head group is in direct contact, and hydrated by, water.

Interactions between water and air are weak, hence this mechanism will act to reduce total surface energy of the system (e.g. weak air-water associations are replaced by strong water-head group interactions). For a liquid, surface energy is equivalent to surface tension or pressure. Pressure is expressed in two dimensions: Newtons per metre as opposed to Newtons per metre squared. Two dimensional pressure is force acting along a unit length.

Insoluble amphiphiles will remain on the air-water surface, and given time, the molecules will spread out, forming a film one molecule thick. It requires considerably more energy to move molecules perpendicularly with respect to the plane of the film as it does within the plane[1]. Hence a lipid monolayer on water may be considered to be a two dimensional environment.

Interactions between lipid molecules to a large extent determine the film properties. The strength of this interaction is dependent upon the average molecular separation.

Under compression, a phospholipid monolayer can be observed to undergo several distinct phases, separated by distinct phase transitions. This behaviour is analogous to that seen in normal three dimensional substances[2].

An example of this is shown in Figure 7.1. This is the isothermal phase diagram of DMPE under compression. Four distinct phases can be observed. At the lowest pressure, separation between phospholipids molecules is large, interactions are therefore weak and the layer is highly compressible as a result. The monolayer is behaving as a two dimensional analogue of a gas: thus this is known as the gas phase.

At higher pressures, two liquid phases appear. The first at lower pressure is the expanded liquid phase. This is characterised by limited short range cohesion between molecules. At higher pressure there appears a condensed liquid phase. In this phase, behaviour is influenced by greater forces between molecules.

At high pressure, the lipid molecules line up to form a relatively ordered state – similar to that of a three dimensional solid, but in two dimensions. The

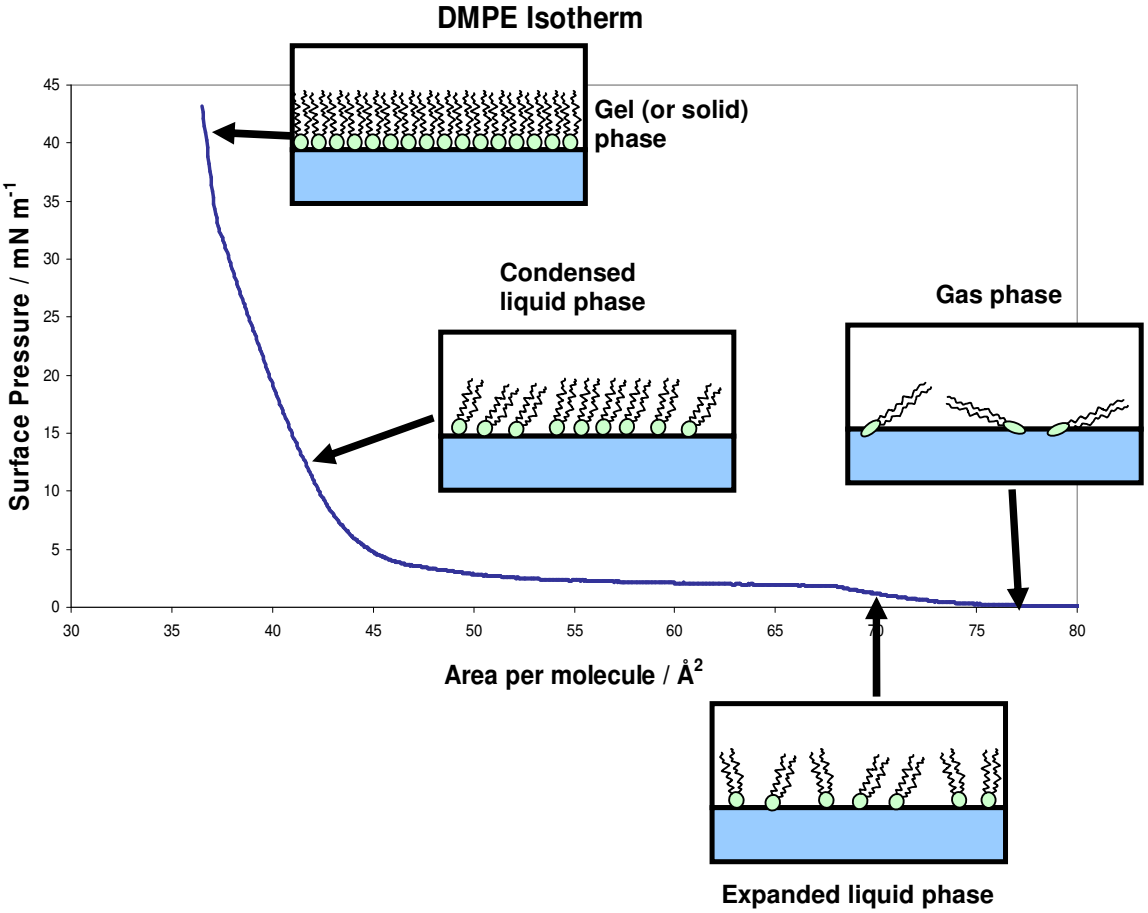

Figure 7.1: The isotherm of a monolayer of DMPE compressed on a Langmuir Trough with the phases highlighted. The inset cartoons depict the organisation of the lipid molecules in each phase.

molecules are likely to be packed in a hexagonal arrangement, as this is the most efficient packing scheme. This is the gel (or solid) phase. Molecules still have considerable mobility, so are not fixed to a particular location as might be expected: hence the monolayer behaves more like a gel than a true solid[2].

If compression is continued past this point, molecules will be forced out of the plane of the monolayer both into the aqueous sub-layer but most particularly on top, forming rafts where two or more layers of molecules are stacked on top of each other. This process is irreversible: these rafts persist even if the pressure is subsequently reduced. At this point, the monolayer is said to have undergone collapse. In order to produce and deposit stable monolayers and bilayers, collapse must be avoided.

It should be noted that DMPE displays different behaviour in the expanded to condensed liquid phase transition and the condensed liquid to gel transition. Specifically, the former phase transition is clearly visible as an extended plateau where the pressure is almost constant while the latter appears as a sharp kink in the isotherm.

The expanded to condensed liquid phase transition is a first order transition: latent energy is exchanged with the surroundings. Energy from the barrier is absorbed in producing liquid condensed domains within the monolayer. Hence during the phase transition both the condensed liquid and expanded liquid phases coexist, and the phase transition appears on the isotherm as a plateau parallel to the x-axis.

The DMPE liquid to gel phase transition is an example of a second order phase transition[3]. A second order phase transition has no latent energy exchange between the system and its surroundings but very often a change in

order is involved[4]. A good example of a second order phase transition is the transformation of a ferromagnet to a paramagnet at its Curie temperature, which involves no latent energy but does see the abrupt decrease in order as the magnetic domains are lost.[5] The isotherm at this phase transition shows a change in the gradient, but no plateau as was the case with the first order change from expanded liquid to condensed liquid phases. Hence there is no energy being exchanged between the phospholipid monolayer and its surroundings.

7.1.2 The Langmuir Trough

A Langmuir Trough is composed of a large trough constructed of some hydrophobic material, a movable barrier also of hydrophobic material and a pressure transducer which is used to measure the surface pressure.

For aqueous work, the trough is filled with high purity water. Insoluble amphiphilic molecules, when introduced to the water/air surface, will spread out over the interface and form a monolayer.

Most commonly, a Wilhelmy Plate is used for pressure measurement. A Wilhelmy Plate is a plate (either of platinum or paper) which is partially immersed in the aqueous sub-phase. The force, F, on the plate is measured by an electrobalance and is dependent upon the weight, surface tension and buoyancy[2]:

$$F = m_p g + 2(t_p + w_p)\gamma \cos(\theta) - \rho_l V_p g \qquad [7.1]$$

where m_p is the mass of the plate, g is the acceleration due to gravity, t_p the plate thickness, w_p is the plate width, γ the surface tension, θ is the contact angle, ρ_l is the liquid density and V_p is the volume of the plate immersed in in the liquid. The weight of the plate is a constant. (Some allowance may have to be made to account for capillary action, which will cause water to travel up a paper plate. In practice, waiting for 30 minutes for the system to stabilise was found to be sufficient to allow for this factor.)

If the immersion depth is also constant, the buoyancy force will not change during the course of the experiment. Hence Equation 7.1 can be simplified:

$$F = 2\left(t_p + w_p\right)\gamma_{LV}\cos\left(\theta\right) + C \qquad [7.2]$$

where C is a constant due to contributions from weight and buoyancy forces.

In the measurement of insoluble monolayers, it is the *change* in surface tension that is of interest, as this is related to the surface pressure, π:

$$\pi = \gamma_0 - \gamma \qquad [7.3]$$

γ_0 is the surface tension of the pure subphase while γ = surface tension of the pure subphase + monolayer.

Hence, as γ_0 is also constant, if the balance is set to zero with the pure subphase, any changes observed on the force experienced by the Wilhelmy plate will directly yield the pressure of the monolayer[2].

The monolayer can be compressed by moving the barrier so that the area is decreased. Measuring the surface pressure during compression yields the isotherm.

7.1.3 DMPE and DMPS

Figure 7.2 compares the isotherms of DMPE with DMPS. There are some differences. DMPE exhibits a first order phase transition between the expanded and condensed liquid phases, as has already been discussed. In contrast, DMPS does not have an expanded liquid phase.

Both lipids have a second order phase transition between the liquid and gel phases. This occurs at a higher pressure for DMPE (32 mN m^{-1}) than DMPS (26.5 mN m^{-1}). Such behaviour has been seen for other phospholipids: palmitoyl-ceramide monolayers exhibit a first order phase transition upon compression from the expanded liquid phase to condensed liquid phase and a second order phase transition from the condensed liquid to gel phase[6]. Similarly, DPPC monolayers were found to have a second order phase transition when compressed from the condensed liquid to gel phase[7].

Both lipids collapse when the pressure is close to 55 mN m^{-1}. Hoda *et al*. noted a collapse pressure of 51 mN m^{-1} for DMPE, but this was measured with a 0.15 M NaCl subphase[8].

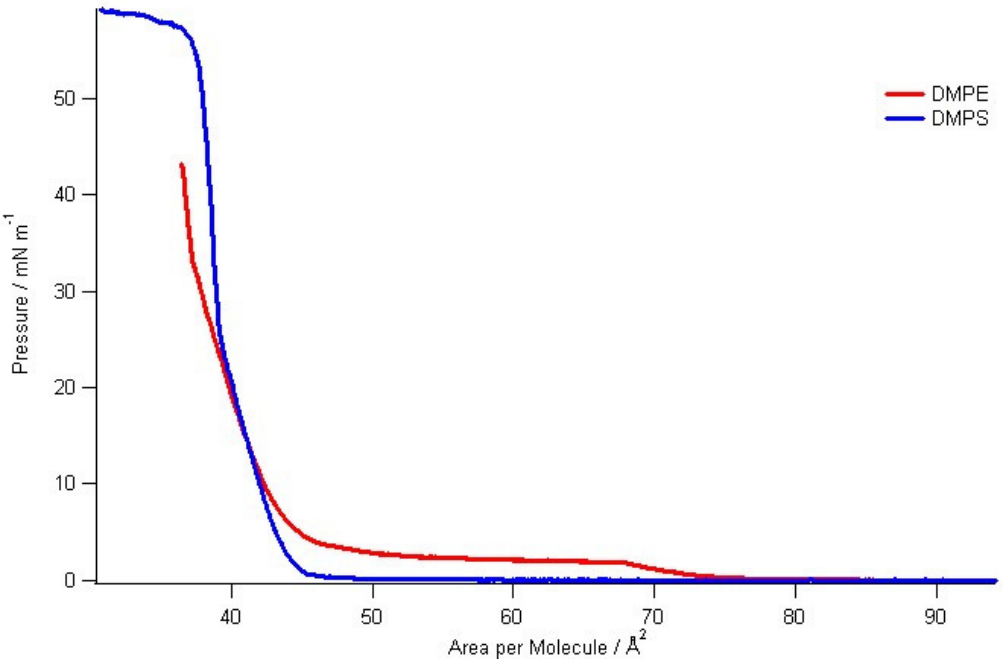

Figure 7.2: Isotherms of DMPE and DMPS.

The major difference between DMPE and DMPS lies in the head group: both have identical tails. DMPS has a net negative charge whereas DMPE is neutral, overall. It is therefore reasonable to hypothesise the differences in their isotherms is related to this fact.

To investigate this, it was decided to add some NaF to the aqueous sub-phase to see how this affected the DMPS isotherm. Adding counter ions to the charged DMPS could be expected to have the effect of screening out the charge on the headgroup. Na^+ (aq) ions in close proximity can be expected to

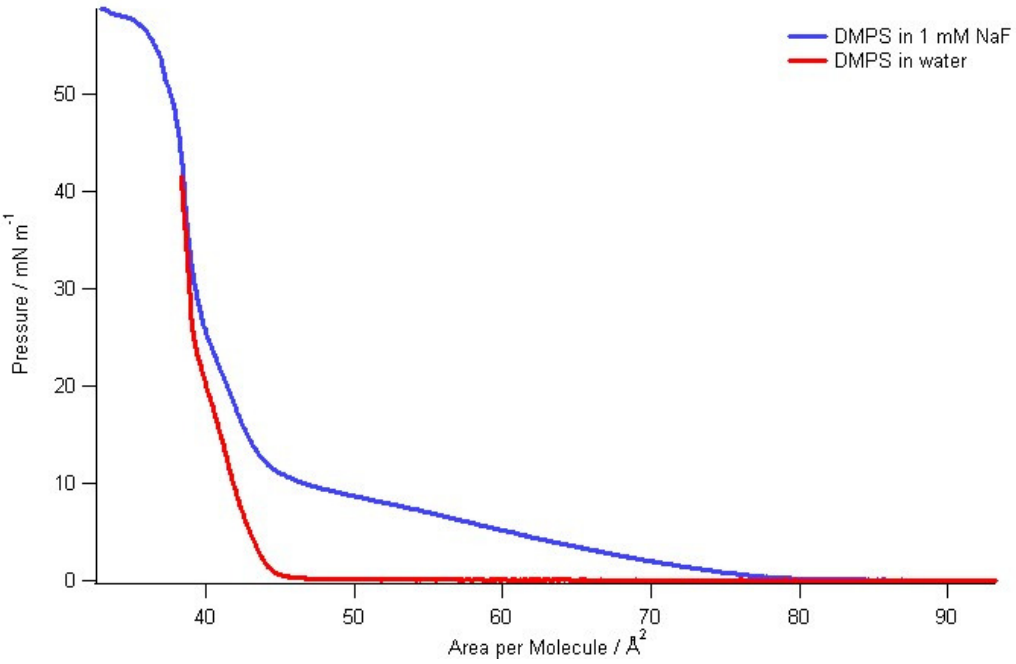

Figure 7.3: The effect of adding sodium counter ions to DMPS. The sub-phase was 1 mM NaF. The expanded liquid phase can be seen between molecular areas of 75 to 45 $Å^2$ $molecule^{-1}$.

reduce the electrostatic repulsion over long range. Physically, the Na^+/DMPS charge pair can be likened to a dipole: the electric field of a dipole decreases as r^3 rather than the more familiar r^2 for Coulomb interactions.

A DMPS isotherm was recorded as a baseline. Immediately afterwards, sufficient NaF was added so as to make the sub-phase concentration 1 mM NaF. A second isotherm was then taken.

Figure 7.3 compares the two isotherms. It can clearly be seen that the addition of positive counter ions has a substantial effect on the DMPS

isotherm. Most prominently, there is the appearance of a distinct expanded liquid phase, similar to that observed for DMPE. It is thus reasonable to hypothesise that Coulomb repulsion between DMPS molecules is of sufficient strength to inhibit the formation of an expanded liquid phase.

Similar observations have recently been reported by Luna *et al* with DMPS and K^+ and Na^+ ions[9]. Both ions triggered the appearance of an expanded liquid phase, but sodium had the greater effect. This was attributed to sodium ions having a higher affinity for DMPS. Ermakov *et al*. reported the existence of an expanded liquid phase for DMPS when the sub-phase was 10 mM KCl[10].

7.1.4 DMPE/DMPS Mixtures

The isotherms of mixtures of DMPE and DMPS were investigated. The isotherms have been collected and are shown together in Figure 7.4.

Table 7.1 lists the limiting molecular area for each of the lipid mixtures. The literature values[3,11] for DMPE are 43 $Å^2$, though Hoda reported a molecular area of 40 $Å^2$ (36 $Å^2$ at the onset of collapse)[8]. Li *et al*. also determined[3] the molecular area of DMPE to be 40 $Å^2$. The molecular area for DMPS has been reported[12] as being 45 $Å^2$. Ermakov published a molecular area of 43 $Å^2$ for DMPS[10].

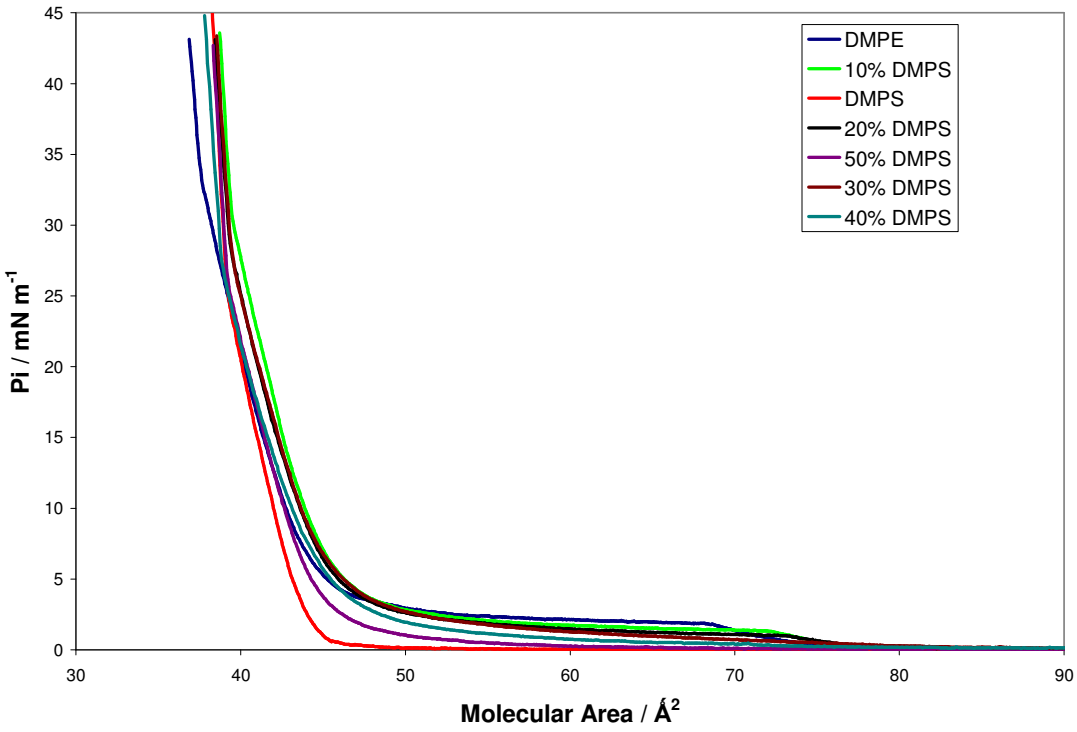

Figure 7.4: Isotherms of mixed lipid monolayers. There is a consistent change in properties from DMPS, which lacks an expanded liquid phase to DMPE, whose expanded liquid phase is pronounced.

It can be seen that mixtures with high mole fractions of DMPE have isotherms that appear similar to that of DMPE itself. Likewise, mixtures that have high mole fractions of DMPS behave similarly to DMPS.

The expanded liquid phase becomes less pronounced as the mole fraction of DMPS increases, disappearing entirely at 40% DMPS mole fraction. This pattern is mirrored in the expanded liquid to condensed liquid phase transition which likewise is present only at DMPS mole fractions below 40%. This effect was observed to have a steady progression: that is, 20% DMPS mixtures had

a less pronounced expanded liquid phase and the phase transition occurred at a lower pressure than the 10% DMPS mixture. The 30% DMPS mixture displayed an even weaker expanded liquid phase.

Table 7.1: Limiting molecular areas

Composition	Molecular Area / Å^2
DMPE	38.1
10% DMPS	42.2
20% DMPS	41.3
30% DMPS	41.1
40% DMPS	39.4
50% DMPS	39.9
DMPS	40.3

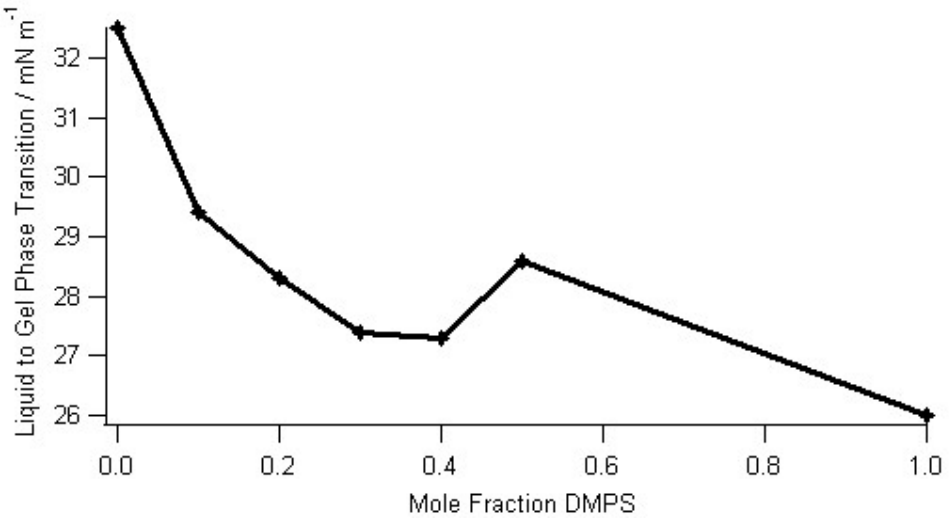

Figure 7.5: The effect of monolayer composition on the position of the gel to condensed liquid phase transition.

This effect has been noted for other mixed phospholipid systems. Hoda *et al*. noted that mixtures of DMPE and a ganglioside phospholipid (DSG-1) obtained from a species of sea urchin, *Diadema Setosum*, displayed isotherms whose appearance was intermediate between those exhibited by the pure lipid[8]. The expanded liquid phase increased in prominence as the concentration of DMPE was increased, similar to that in Figure 7.4. Mixtures of DPPC and DSG-1 displayed the same trend. Ermakov *et al*, whilst investigating mixtures of DMPS with DMPC also reported that the expanded liquid phase showed properties intermediate to that of the pure lipid[10].

The liquid to gel phase transition occurs at 32.5 mNm^{-1} for DMPE and 26.0 mNm^{-1} for DMPS. DMPE/DMPS mixtures have phase transitions that lie in between these two values. Again, there is a regular progression towards lower phase transition pressure as the fraction of DMPS increases (Figure 7.5).

The question can be asked as to whether the binary mixture separates into two phases – DMPE rich and DMPS rich. Researchers have noted that many lipids are miscible with phospholipids, exhibiting ideal mixing. Hoda found that DSG-1 was miscible with both DPPC and DMPE at all concentrations examined[8]. Likewise, X-ray diffraction studies by Quinn[13] showed miscibility between DPPC and the sphingolipid glucosylceramide. X-ray diffraction studies of DMPS/cholesterol mixtures demonstrated miscibility of the two lipids at ratios of 2:1 or less for the gel phase and 1.7:1 for the condensed liquid phase[14].

To this investigate this further, two isotherms of a 40% DMPE/DMPS mixture were acquired. The first was premixed in before being spread onto the Langmuir Trough. The second was after the correct quantities of each lipid was spread *separately* onto the trough. This spreading was done at a molecular area of 120 $Å^2$ / molecule. This is in the regime where both the gas phase and expanded liquid phases coexist. This monolayer was left for 30 minutes to allow the solvent to evaporate and some diffusion to take place. Hence at this point the monolayer consisted of domains of pure lipid in the expanded liquid phase surrounded by a mixed gas of DMPE and DMPS – though this gas would not necessarily be of uniform composition.

Figure 7.6 shows the resultant isotherms. The premixed monolayer, as before, is similar to that of DMPS with a very subdued expanded liquid phase. Strikingly, the monolayer with significant pure lipid domains appears very similar to that of DMPE itself: the isotherm exhibits a substantial expanded liquid phase. It is very clear that the DMPE domains that would exist on that monolayer exerted a controlling influence on its properties. Hence significant DMPE domains (and by inference, DMPS domains) cannot have existed in any of the monolayers prepared from premixed lipid mixtures, as they too could have been expected to show behaviour very similar to that of DMPE. This suggests that DMPE and DMPS are miscible and behaviour close to ideal mixing can be expected in the case of a pure water sub-phase. Differential scanning calorimetry studies by Silvius and Gagne[15] of vesicles composed of mixtures of DMPE and DMPS showed that in water, mixing of

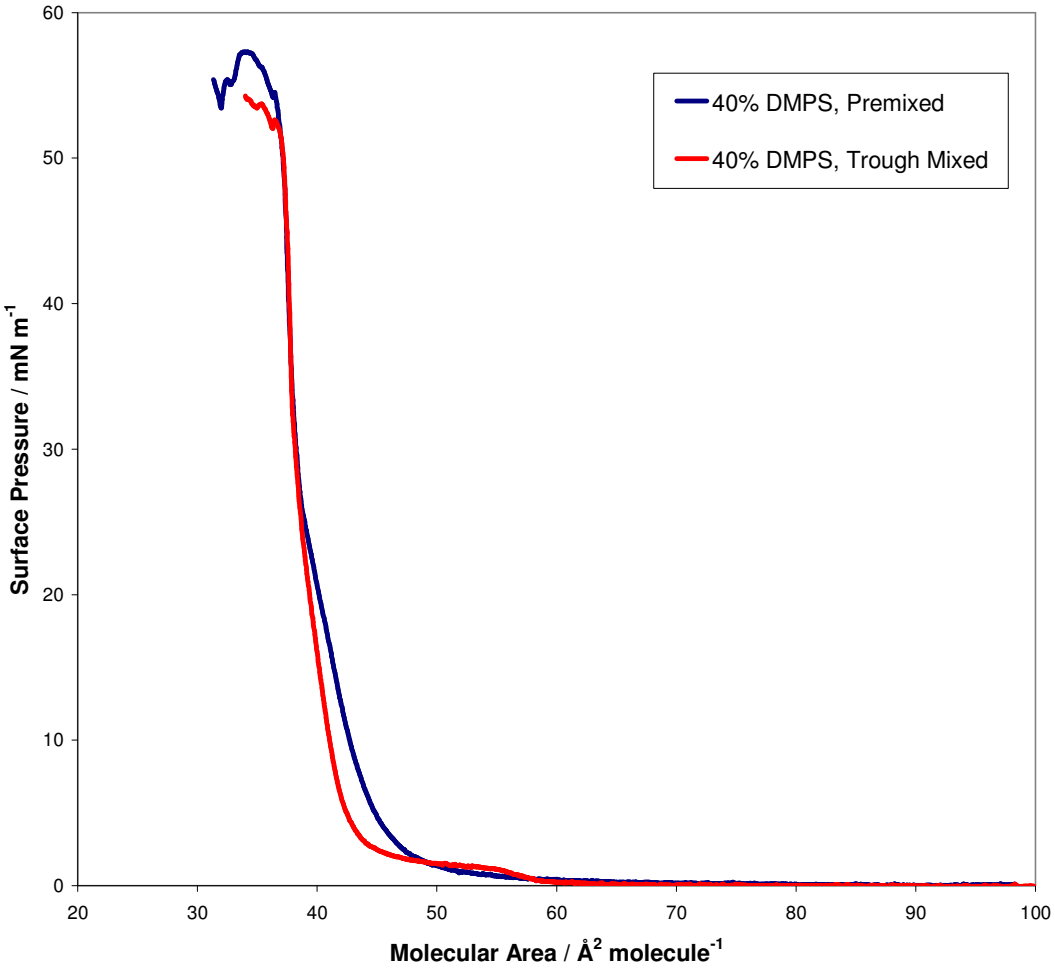

Figure 7.6: The effect of incomplete mixing. The "premixed" isotherm was produced from a DMPE/DMPS mixture that had been thoroughly mixed before spreading. The "Trough Mixed" isotherm was an incompletely mixed monolayer. Note that collapse occurs at a surface pressure of approximately 55 mN m^{-1}.

the two lipids was ideal. Interestingly, phase separation of the two components was observed in 30 mM Ca^{2+} (aq).

7.1.5 Conclusions

DMPE has a smaller molecular area than DMPS or any of the mixed monolayers; the effect of even 10% DMPS is to increase this value somewhat. Mixtures and DMPS all show quite similar molecular areas.

The data show that there is a gradual gradation of properties of monolayers from DMPE to DMPS. The prominence of the expanded liquid phase, and its associated phase transition decrease gradually as the DMPS fraction is increased. 10% DMPS mixtures appear similar to that of DMPE while 40% and 50% DMPS mixtures behave similarly to DMPS.

Differential capacitance experiments suggested that binary bilayers with low concentrations of DMPS behaved similarly to that of pure DMPE while at high concentrations of DMPS the resultant bilayers had similar properties to that of DMPS. The isotherms in Figure 7.4 display a similar trend: at low mole fractions of DMPS, the monolayer isotherms have a similar shape to DMPE, with a prominent expanded liquid phase in evidence while at high DMPS mole fractions, the expanded liquid phase is not apparent, similar to the DMPS monolayer isotherm.

The regular change in the both the position of the condensed liquid to gel phase transition and prominence of the expanded liquid phase as the mole fraction of DMPS is changed is similar to the observations that the desorption

potential observed in the DC experiments also exhibited a regular change with DMPS mole fraction.

7.2 Molecular Dynamics Simulations

Advances in computational power over the last few decades means it is now feasible to model substantial molecular systems on an atom by atom basis. Small systems (typically simple single molecules such as toluene) can be modelled by quantum mechanical techniques. Larger systems need to be simplified. Molecular mechanics (MM) is used for this purpose. Molecular mechanics operate by calculating a force field and evaluating its effect on the atoms comprising the system. This discards most of the quantum intricacies but can make it possible to find solutions to otherwise intractable (large!) systems.

7.2.1 Molecular Mechanics Force Fields

The fundamental step of any MM simulation is the calculation of the potential energy of a given arrangement of atoms. The potential energy includes contributions from bonding, van der Waals forces and electrostatic forces. How this information is used depends on the type of simulation being run.

With a minimisation simulation, the aim is to reduce the potential energy of the system in order to find its lowest energy, and hence most stable, state. Thus an algorithm will be used that will shift the position of the atoms comprising the system in order to reduce potential energy.

A molecular dynamics (MD) simulation is different in that the atoms are given some kinetic energy so that the system has internal energy in order to simulate the effect of temperature. How the system responds to this thermal perturbation is recorded.

It can thus be seen that the force field is the largest approximation in MM. There is a selection of molecular mechanics force fields available, including AMBER[16], CHARMM[17], and CVFF[18]. AMBER is one of the most commonly chosen force field for MM simulations. It has the advantages of being simple, fast and accurate. These make AMBER well suited for simulations of large complex systems such as proteins – or lipid bilayers.

The AMBER force field, *V*, is given by[11]:

$$V = \frac{1}{2}\sum_{bonds}\left(K_b\left(b-b_0\right)^2\right)+\frac{1}{2}\sum_{angles}\left(K_\theta\left(\theta-\theta_0\right)^2\right)+\frac{1}{2}\sum_{dihedrals}\left(K_\phi\left(1+\cos\left[n\varphi-\gamma\right]\right)\right) + \sum_{nonbonded}\left[\frac{A}{r^{12}}-\frac{B}{r^6}\right]+\sum_{electrostatic}\frac{q_1q_2}{\varepsilon r} \qquad [7.4]$$

This includes terms for the bonds, bond angles, dihedrals (rotation round a bond), non-bonded interactions (principally van der Waals forces) and electrostatic interactions, which include contributions from ions and hydrogen bonding.

7.2.2 Molecular Dynamics

Applying this force field to each and every atom in the simulation allows AMBER to calculate the potential energy of each atom, its velocity and position. Hence this is a "whole atom" simulation.

The force field allows the force, F, experienced by every atom to be calculated. Applying Newton's second law on the i-th atom,

$$F_i = m_i a_i \qquad [7.5]$$

where m_i is its mass allows its acceleration, a_i to be evaluated. Integrating Equation 7.5 over time *t* gives the velocity of the atom. Hence this procedure allows the positions and velocities of every atom to be calculated over a time interval *t*. After this, the force field must be recalculated to take account of the changes in atom positions. The whole cycle is then repeated. Time *t* is thus the step size, and is usually in the range of 1 to 5 ps.

The simulation is left to run. Given enough time, it will eventually reach thermal equilibrium, provided the model does not contain major defects. Molecular processes all have their own characteristic time scales. Localised conformational changes such as rotation around a bond take place on the picosecond time scale. Larger scale movements such as the rotation of whole molecules is on the nanosecond time scale. Diffusion of molecules occurs over tens of nanoseconds. Large structural rearrangements such as protein folding take place on the micro to millisecond time scale.

7.2.3 Set Up

A model of the DMPE and DMPS molecule was created on ChemDraw. The file generated from this process was converted into pdb (protein databank) format so that it could be entered into an AMBER utility, XLeaP. XLeaP was then used to generate force field representations of DMPE and DMPS.

A program was written to randomly select either a DMPE or DMPS molecule and then randomly place it on a 100 by 100 Å surface. The monolayer generated by this program was quite packed, with an average molecular area of 35 $Å^2$.

This monolayer was then minimised using AMBER to ensure unfavourable interactions were negated. A cut-off of 12 Å was used, meaning non-bonded interactions between atoms separated by more than 12 Å were ignored. This greatly simplifies the problem, reducing the computational load to a manageable level. A 12 Å cut-off was used in all the minimisation and MD steps that follow. A periodic boundary condition (PBC) was applied: the monolayer was placed in a box of dimensions 100 x 100 x 30 Å. Any atom straying over the box boundary will be placed on the other side. This step ensures that the number of entities in the MD simulation remain constant, and that only a small set of coordinates needs to be handled by the program. This also reduces the computational load.

The minimised monolayer was then copied, and the copied version rotated in order to form a bilayer. Solvent molecules were then added to hydrate the system. The thickness of the water layer was 15 Å. A second minimisation run was then commenced to ensure the complete bilayer system had minimum energy. The PBC were increased to accommodate the enlarged system (105 x 105 x 110 Å).

MD simulations were then performed on the minimised bilayer systems. The same PBC parameters were used as the minimisation above. The simulations were left to run until approximately one nanosecond of simulated time had accrued.

7.2.4 Results and Discussion

Five bilayer systems were investigated: pure DMPE, 10% DMPS in DMPE, 30% DMPS in DMPE, 50% DMPS in DMPE and pure DMPS. There were 600 to 620 phospholipid molecules in each system, arranged in a bilayer. The simulated temperature was 300 K.

After one nanosecond simulation, a number of characteristics were noted in all five simulated systems. The water molecules remain about the head group and show little tendency to penetrate into the hydrophobic core. The lipid head groups adopt a horizontal configuration rather than projecting vertically upwards into the solvent. This behaviour has been observed in MD simulations of DMPC bilayers[19] and DPPC bilayers[20]. Pink *et al*. also observed similar behaviour with MD simulations of the PE head groups[21] (the tail groups were excluded from the simulation).

The average change in displacement of specific atoms in each lipid can be examined and averaged over the entire bilayer population. Over the time scales of the MD runs, there has been comparatively little movement: an examination of the positional change of the phosphate atom in all five systems is less than 3 Å, on average. The central carbon atom in the glycerol

backbone yields a similar figure. Interestingly, the carbon atom in the terminating methyl group of the tail groups shows slightly greater displacement, just over 4 Á. These data are tabulated in Table 7.2.

Movement in one nanosecond has been less than the spacing of a single molecule. There is no evidence of lipid rafting – where like molecules coalesce together to form aggregations within the bilayer. This is not surprising. Diffusion in similar DMPC bilayer simulations has been reported to take place on a timescale greater than 10 ns[22,23]. This lack of movement agrees well with the published literature.

Table 7.2: Average atomic displacements in MD simulations

Simulation	Average displacement / Å		
	Phosphate	C2 glycerol	Methyl C
DMPE	2.94	2.62	4.09
10% DMPS	2.61	2.68	3.84
30% DMPS	2.77	2.92	3.47
50% DMPS	2.48	2.71	4.35
DMPS	2.80	2.53	3.71

It is interesting that the carbon atom terminating the acyl tails should show more movement over this timescale. Being as it is at the end of a long chain of

atoms, this carbon can be expected to have greater freedom to more rapidly adopt a different conformation. This may be the explanation for this atom's greater mobility.

7.3 References

1. Aveyard, R., Haydon D. A., 1973, *An Introduction to the Principles of Surface Chemistry*, Cambridge University Press

2. Martin, P., Szablewski, M., 1995, *Nima Tensiometers and Langmuir-Blodgett Troughs Operating Manual*, 4th edition

3. Li, J., Miller, R., Mohwald, H., (1996), *Colloids And Surfaces*, **114**:123

4. Adkins, C. J., *Equilibrium Thermodynamics*, 1983, Cambridge University Press

5. Hook, J. R., Hall, H. E., *Solid State Physics*, 1991, Wiley-Blackwell

6. Fannani, M. L., Maggio, B., (2010), *Chemistry and Physics of Lipids*, **163**:594

7. Kim, K., Choi, S. Q., Zasadzinski, J. A., Squires, T. M., (2011), *Soft Matter*, **17**:7782

8. Hoda, K., Ikeda, Y., Kawasaki, H., Yamada, K., Higuchi, R., Shibata, O., (2006), *Colloids and Surfaces*, **52**:57

9. Luna, C., Stroka, K. M., Bermudez, H., Aranda-Espinoza, H., (2011), *Colloids Surfaces B*, **85**:253

10. Ermakov, Y. A., Kamaraju, K., Sengupta, K., Sukharev, S., (2010), *Biophysical J.,* **98**:1018

11. Honig, D., Mobius, D., (1991), *J. Phys. Chem*, **95**:4590

12. Pedersen, U. R., Leidy, C., Westh, P., Peters, G. H., (2006), *Biochimica Biophysica Acta – Biomembranes*, **1758** 5:573

13. Quinn, P. J., (2009), *Biochimica Biophysica Acta - Biomembranes*, **1788**:2267

14. Bach, D., Borochov, N., Wachtel, E., (1998), *Chem. Phys. Lipids*, **92**:71

15. Silvius, J. R., Gagne, J., (1984), *Biochemistry*, **23**:3232

16. Weiner, S. J., Kolman, P. A., Nguyen, D. T., Singh, U. C., Ghio, C., Alagona, S., Profeta, P., Weiner, P., (1984), *J. Am. Chem. Soc*., **106**:765

17. Brooks, B. R., Bruccoleri, R. E., Olafson, B. D., States, D. J., Swaminathan, S., Karplus, M., (1983), *J. Comp. Chem*., **4**:187

18. Dauber-Osguthorpe, P., Roberts, V. A., Osguthorpe, D. J., Wolff, J., Genest, M., Hagler, A. T., (1988), *Proteins: Struct. Funct. And Gen*., **4**:31

19. Cornell, W. D, Cieplak, P, Bayly, C. I, Gould, I. R, Merz, K, M. Jr, Ferguson, D. M, Spellmeyer, D. C, Fox, T, Caldwell, J. W, Kollman, P. A (1995), *J. Am. Chem. Soc.* **117**: 5179

20. Smondyrev, A., Berkowitz, M. L., (1998), *J. Comp. Chem.*, **20**:531

21. Pink, D. A., Belaya, M., Levadny, V., Quinn, B., (1997), *Langmuir*, **13**:1701

22. Pasenkiewicz-Gierula, M., Takaoka, Y., Miyagawa, H., Kitamura, K., Kusumi, (1999), *Biophysical J.*, **76**:1228

23. Flenner, E., Das, J., Rheinstadter, M. C., Kosztin, I., (2009), *Phys. Rev. E*, **79**:011907

8. Conclusions and Further Work

8.1 Putting it All Together…

A considerable amount of data have been presented in the preceding seven chapters. It seems reasonable to ask what trends, if any, have surfaced.

The differential capacitance experiments showed firstly that bilayers deposited by the LB/LS method were of better quality than their vesicle-formed counterparts. The lower capacities observed indicated the presence of fewer defects and more complete coverage. Coverage of bilayers formed by vesicle fusion were estimated to be 80% while those formed by LB/LS deposition had 85% coverage. Bilayer properties displayed changes when the composition was altered. With low mole fractions of DMPS, 0.2 or less, the bilayer exhibited a capacity curve similar to that of pure DMPE. When the DMPS mole fraction was 0.4 or 0.5, the bilayer properties resembled those of pure DMPS. At 30% DMPS, the film assumed features that were intermediate between DMPS and DMPE. A model was proposed whereby an adsorbed bilayer would first absorb water as the potential became more negative and then allow water to reach the substrate by electroporation before finally detaching with a thin (1 nm thick) layer of water between film and substrate.

PM-IRRAS studies of *ex situ* bilayers deposited on gold supplied evidence that the films change configuration with composition. Though the molecules do not exhibit any pronounced change in tilt angle of the tail group, evidence for a change in configuration of the tail groups was observed with one configuration at low concentrations of DMPS and another at high DMPS concentrations. The transition occurs at 30% DMPS, mirroring that seen with the DC experiments. A similar change in conformation was seen with the head groups, with the P-O-C head group backbone adopting a more vertical conformation at high DMPS concentrations. Again, the transition occurs at 30% DMPS.

Chronocoulometry data shows that the charge density of bilayers of all compositions rises above the Au baseline at -0.7 V for vesicle formed bilayers and -0.9 V for LB/LS bilayers. This corresponds to the desorption peak observed in the DC curves. The surface pressure of DMPS/DMPE mixtures with 30% or less DMPS falls once the PZC is reached. This is behaviour typical of a zwitterionic surfactant.

Isotherms of DMPS/DMPE mixed monolayers show a gradual transition from DMPE behaviour to DMPS behaviour as the DMPS mole fraction increases. As the DMPS concentration increases, there is a gradual decrease in the prominence of the expanded liquid phase and its associated phase change. A 10% DMPS monolayer shows similar features to pure DMPE while 40% and 50% DMPS monolayers are very similar to DMPS. 30% DMPS monolayers have properties intermediate between DMPS and DMPE.

All these observations point in the same direction: that films with a high concentration of DMPS, say 40% or greater, behave similarly to DMPS itself while below 20% DMPS the film will behave in a manner analogous to DMPE. 30% DMPS mixtures seem to have properties intermediate between DMPE and DMPS. Line widths of the CH stretching vibrations were observed to be lower for this composition than at other mixtures, indicating that the acyl tails are more ordered for this particular composition. It is interesting to note that biological membranes always have DMPS concentrations below this value.

It is easy to attribute these observations to the fact that DMPS is negatively charged while DMPE is zwitterionic. Both molecules have a similar limiting molecular area, so packing effects due to size differences are unlikely. At high concentrations, there are sufficient numbers of DMPS molecules so that their electric charge is sufficient to overwhelm any effect of DMPE, hence DMPS will dominate membrane properties. The observation that suppressing the effect of the charge on DMPS with Na^+ ions causes DMPS monolayers to behave somewhat similarly to DMPE (the appearance of an expanded liquid phase) supports this hypothesis.

The PM-IRRAS data offer another possibility, however. A change in the orientation of the DMPS carboxylate group was observed at high DMPS concentrations. The COO^- moiety adopted a more horizontal orientation. This suggests that this group is pairing with a neighbouring molecule. The NH_3^+ moiety is the most obvious candidate: Coulombic and hydrogen bond

interactions would make such pairing favourable. In DMPE films, the NH_3^+ moiety is likely to pair with the phosphate group of a neighbouring molecule – the positions of the phosphate stretching bands support this assertion. However, as the ratio of DMPS molecules increases, the probability of the NH_3^+ groups pairing with the DMPS carboxylate moiety will increase. The pairing of DMPE NH_3^+ groups with COO^- may thus result in the DMPE molecules taking on a conformation more like that of DMPS, and hence causing the film as a whole to behave more like DMPS.

Electrochemical impedance spectroscopy shows that bilayers containing DMPS act as a more effective barrier to anions than pure DMPE. The situation is reversed for cations. This raises the possibility that voltage gated channels exist in DMPS/DMPE mixtures. There is a relationship between the mole fraction of DMPS and permeability of the bilayer to cations. This implies that it is the surface potential that is responsible for this observation. However, no corresponding relationship between DMPS concentration (and hence surface potential) and anion permeability was found. The presence of DMPS in the layer alone is enough to reduce the anion permeability. It is likely that even small defects or pores would have at least one DMPS molecule nearby. It was proposed that the mutual repulsion of the DMPS molecule and the anion within the confines of the defect would be of a sufficient magnitude to markedly reduce anion transport through the defect.

Neutron reflectometry studies of 10% DMPS in DMPE bilayers suggest that the degree of hydration of the bilayers increase as the potential goes more

negative. This observation helps explain why the capacity of these bilayers also increase as the potential becomes more negative – water has a high dielectric constant so increased solvation will lead directly to increased capacitance. The data suggested that the bilayer detached at a large negative potential, thus lending support to the model derived from the DC experiments where the bilayer first absorbs water before finally desorbing.

Molecular dynamics simulations of model bilayers with different compositions show little diffusion over the time scale of one nanosecond. This is in agreement with other MD simulations of phospholipid bilayers.

8.2 Further Work

The electrochemical impedance data suggest that the quality of the substrate plays a critical role in the quality of the bilayer it supports. Repeating the impedance experiments but using an Au (111) single crystal electrode would be an simple way to test this observation.

The head groups of supported bilayers exist in two quite different environments. The head groups in the inner leaflet are adsorbed onto the substrate while the outer leaflet is exposed to the outside environment. The *ex situ* PM-IRRAS experiments averaged both environments – it is very difficult if not impossible to quantity the differences (if indeed there are any). Acquiring PM-IRRAS spectra of two monolayers of similar composition – one whose head groups were in contact with the substrate, the other reversed so that the

tail groups were adsorbed onto the surface or onto a self-assembled monolayer – would aid in determining the effects of this different environment have on the organisation and conformation of these films.

Clearly, acquiring PM-IRRAS of DMPE/DMPS bilayers *in situ* is desirable. Connection to a potentiostat would also allow the effect of electric field on these structures to be investigated as well the effect of composition. Further neutron reflectometry experiments with different compositions – 30% and 50% DMPS in DMPE in particular – might help elucidate any changes in structure that are caused by compositional changes and how these are affected by the applied electric field.